SCALAR AND VECTOR CORRELATIONS IN MOLECULAR COLLISION DYNAMICS

STEPHEN JAMES MCGURK

(Submitted for the Degree of Doctor of Philosophy)

HERIOT-WATT UNIVERSITY
SCHOOL OF ENGINEERING AND PHYSICAL SCIENCES
SEPTEMBER, 2014

Abstract

This thesis concerns the fundamental scalar and vector attributes of molecular collisions. A translationally relaxed sample of fully state-selected and rotationally anisotropic CN($A^2\Pi$, v = 4, $jF\varepsilon$) was prepared within a thermal bath (~298 K) of partner gas (either Ar, N_2, O_2 or CO_2) by ns-pulsed laser excitation. The collisional evolution of the prepared polarised rotational angular momentum was monitored using high-resolution frequency modulation spectroscopy (FMS). The total removal and depolarisation of oriented or aligned rotational angular momentum was measured in CN($A^2\Pi$, v = 4, j = 2.5, 3.5, 6.5, 11.5, 13.5, and 18.5, F_1e). The state-to-state rotational energy transfer (RET) and orientation transfer from CN($A^2\Pi$, v = 4, j = 6.5 F_1e or j = 10.5 F_2f) to $\Delta j \leq |5|$ was investigated. The results for the CN($A^2\Pi$)+Ar system generally agree very well with complementary exact quantum scattering (QS) calculations on the best available *ab initio* potential energy surfaces (PESs). For all systems, a three-level multiple-collision kinetic model satisfactorily reproduces the observed removal of population and polarisation. Elastic depolarisation is found to be a relatively minor pathway relative to population removal and inelastic depolarisation, as confirmed by complete master equation (ME) simulations for CN($A^2\Pi$, v = 4, j = 6.5 F_1e)+Ar. The total removal efficiencies lie in the order $CO_2 > N_2 > O_2 >$ Ar, loosely correlated with long-range attractive forces. O_2 and CO_2 exhibit rapid removal channels in addition to RET, likely to be electronic quenching to CN($X^2\Sigma^+$).

There are substantial parity-dependent alternations with Δj in state-to-state RET and polarisation transfer, sufficient for a striking change in sign of orientation for specific transitions. This is attributed to the near-homonuclear nature of CN($A^2\Pi$) and consequent even character of the PESs. QS calculations indicate that the dynamics of parity-conserving and changing transitions differ fundamentally. A preference for spin-orbit conservation, strongest for Ar, comes from the near-Hund's case-(a) character of CN($A^2\Pi$) at low-j. Despite the additional dimensions available, the qualitatively similar behaviour of the molecular partners with Ar suggests that these systems have comparable interaction potentials with CN($A^2\Pi$). Therefore, small centrosymmetric molecules, such as N_2, O_2 and CO_2, may approximately be treated as spherical targets. This is supported by recent spherically-averaged CN($A^2\Pi$)-N_2 PESs and associated QS calculations from the literature.

Acknowledgements

First and foremost, I would like to express my sincere gratitude to my primary academic supervisor, Dr. Matthew Costen, for introducing me to the FMS experiment and for his encouragement in persuing this research. His guidance, patience and boundless knowledge were the called upon innumerous times during the entirety of this PhD. His suggestions for improving the experiment, helping to fix temperamental lasers or when anything else went wrong, writing LabVIEW® routines, and thesis corrections are amongst many other examples for which I am extremely grateful. I also warmly acknowledge my second supervisor, Prof. Kenneth McKendrick, who initially introduced me to the quantised world and to broader aspects of Physical Chemistry through my first ever undergraduate lecture, almost 10 years ago. This set the scene for my fondness of this extraordinary subject and ultimately led to undertaking a PhD.

I have spent 6 enjoyable and fruitful years in the group and take away with me a wealth of research experience. I would like to extend my thanks to all other members of the group who I encountered along the way, particularly Drs. Grant Paterson, Kerry King and Muthulingham Suresh. Thanks also go to Prof. Joshua Halpern for help on the experiment during his sabbatical visit from Howard University, and likewise to David Georgiev during his final year BSc project. I am also indebted to our collaborators, Profs. Paul Dagdigian (Johns Hopkins University) and Millard Alexander (University of Maryland), whose theoretical calculations played a crucial role in this research. I duly acknowledge the electronic and mechanical workshops for repairs when equipment failed (or more likely when I broke something), and also the Chemistry stores for ensuring I had a plentiful supply of ICN. I am equally grateful to Heriot-Watt University for awarding an EPSRC DTA studentship that provided the means necessary to carry out this research.

I would like to thank the good friends I have made at Heriot-Watt, not limited to Sarah, Jack, Julien, Nuno, Piotrek, Ali, Demian, Jérôme and Alex, for amongst other things the much needed beer trips. Outwith the University, Anas, Yahya, OJ and Sophie have been a great source of support and inspiration. Finally, I offer a special thank you to my family, especially my parents, for all of their encouragement and support over the years.

Thank you all.

ACADEMIC REGISTRY
Research Thesis Submission

Name*:*	Stephen James McGurk		
School/PGI:	EPS / Institute of Chemical Sciences		
Version: *(i.e. First, Resubmission, Final)*	Final	Degree Sought (Award **and** Subject area)	PhD Chemistry

Declaration

In accordance with the appropriate regulations I hereby submit my thesis and I declare that:

1) the thesis embodies the results of my own work and has been composed by myself
2) where appropriate, I have made acknowledgement of the work of others and have made reference to work carried out in collaboration with other persons
3) the thesis is the correct version of the thesis for submission and is the same version as any electronic versions submitted*.
4) my thesis for the award referred to, deposited in the Heriot-Watt University Library, should be made available for loan or photocopying and be available via the Institutional Repository, subject to such conditions as the Librarian may require
5) I understand that as a student of the University I am required to abide by the Regulations of the University and to conform to its discipline.

* *Please note that it is the responsibility of the candidate to ensure that the correct version of the thesis is submitted.*

Signature of Candidate*:*		Date:	

Submission

Submitted By *(name in capitals):*	
Signature of Individual Submitting:	
Date Submitted:	

For Completion in the Student Service Centre (SSC)

Received in the SSC by *(name in capitals):*			
Method of Submission *(Handed in to SSC; posted through internal/external mail):*			
E-thesis Submitted **(**mandatory for final theses)			
Signature:		Date:	

Chapter 1

Introduction

1.1 Scope of this Thesis

The research presented in this thesis employs frequency modulated spectroscopy as a probe of molecular collision dynamics. Measurements of energy transfer pathways and the polarisation properties of rotational angular momentum in the prototypical $CN(A^2\Pi)$+Ar collision system are compared to high level quantum scattering calculations on new *ab initio* potential energy surfaces. The synergism between experiment and theory elucidates fundamental properties of the interaction and provides a test for the accuracy of predictive models. The experiments are extended to potentially reactive molecule-molecule encounters, namely $CN(A^2\Pi)$ with N_2, O_2 and CO_2, in order to reveal the effects of additional intermolecular forces and correlated nuclear motions, with an ultimate aim to provide a general overview of the scattering propensities of electronically excited open-shell $^2\Pi$ species.

Chapter 1 introduces important concepts of this thesis, including angular momentum, polarisation, rotational energy transfer, elastic depolarisation and polarisation transfer, followed by energy transfer models, potential energy surfaces and quantum scattering theory. A literature review then highlights recent advances in scalar and vector correlations of bimolecular collisions, concluding with previous work on the $CN(A^2\Pi)$ molecule. Chapter 2 outlines the experimental methodology utilised for measuring the phenomenological observables in later chapters. An introduction to frequency modulated spectroscopy, its underlying theory and the experimental data processing routine are given in Chapter 3. The total removal of rotational angular momentum and

elastic depolarisation in collisions of CN($A^2\Pi$) with Ar, N_2, O_2 and CO_2 are then investigated in Chapter 4. Also addressed here is the optimisation of the kinetic scheme used to fit to the processed experimental data by comparing the CN($A^2\Pi$)+Ar results to exact quantum scattering predictions on recent and new *ab initio* potential energy surfaces, and subsequent master equation modeling. Chapter 5 widens the measurements to full state-to-state rotational energy transfer and polarisation transfer, again comparing the CN($A^2\Pi$)+Ar results to exact quantum scattering calculations. The main conclusions of this thesis and future prospects are drawn in Chapter 6.

1.2 General Introduction

Atomic and molecular collisions are ubiquitous to many gas phase chemical environments, such as technological plasmas, combustion processes and the atmosphere.[1] Accurate modeling of these systems requires a detailed understanding of the collision dynamics that underpin them. The term *collision* refers to the encounter of two or more atomic or molecular species that experience a force as they approach, interact and depart from one another.[2] A possible outcome of such an encounter could be a chemical reaction, whereby molecular bonds are broken and new bonds formed. However, a much more likely outcome is the exchange of energy between the collision partners.[3] Correlation of the pre- and post-collision energies and the product angular distributions hence serves as a probe of the forces that acted during the collision.[2]

While atoms only possess electronic and translational nuclear motion, molecules additionally experience vibration and rotation of the internuclear axes. The associated energies of the electronic and nuclear motions are quantised, i.e. exist only in discrete energy levels. The separation of translational energy levels is small enough that they may be treated as continuous (classically). The separation of rotational energy levels in small molecules is ~10^{-2} kJ mol^{-1}, smaller than that of vibrational levels (~10 kJ mol^{-1}), which is in turn smaller than typical electronic energy spacings (~10^3 kJ mol^{-1}), as summarised in Figure 1.1.[4] Therefore, in each electronic level there are several vibrational levels, and in each vibrational level there are many rotational levels.

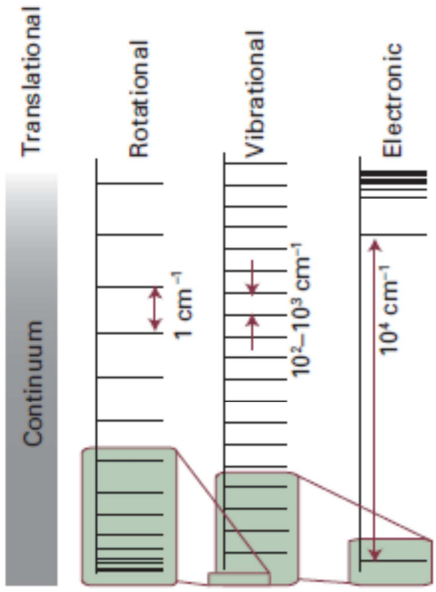

Figure 1.1 – Typical translational, rotational, vibrational and electronic energy level separations (in wavenumbers, cm^{-1}). Adapted from reference 4.

Collisions that transfer energy between translation and other internal degrees of freedom are termed *inelastic*. In order of decreasing complexity, this spans electronic energy transfer (EET), vibrational energy transfer (VET) and rotational energy transfer (RET), with combinations of these processes possible such that the total energy of the system is conserved. Collisions that only affect the velocity without redistributing the internal energy of the collision partners are termed *elastic*. Due to the size of the energy spacings compared to the room temperature thermal energy (~2.5 kJ mol^{-1}), RET and changes in translational motion are the most common forms of collisional energy transfer.

An intricate knowledge of energy transfer is therefore necessary to sucessfully model the above chemical environments and to develop predictive tools. Laser-based spectroscopic methods are particularly suited to interrogate these environments, as they are non-invasive and inherently sensitive to collisional phenomena. Of particular interest is the study of small open-shell molecules, such as CN, NO and OH, as they are amenable to experiment, easily produced and have well known and accessible spectroscopies. They also serve as prototypes that can be extrapolated to systems of higher degrees of freedom.

At a fundamental level, the most exact method of characterising interacting partners is the construction of a full dimensional *ab initio* (from quantum first principles) potential

energy surface (PES). This can be represented using a specific set of nuclear coordinates. The gradient of the interaction potential for a given set of coordinates is proportional to the force acting between the collision partners and dictates the dynamics of the encounter. The calculation of accurate PESs requires separately (adiabatically) the correlation of all electronic and nuclear motions within the system. Full quantum scattering (QS) calculations may then be performed on the PESs to predict energy transfer rate constants or cross-sections. Both the construction of the PESs and subsequent scattering calculations necessitate the use of dedicated software packages and powerful computer clusters. Collisions of small molecules, such as CN, NO and OH, with rare gases are used as paradigms for developing and testing theory, as they have few enough electrons and degrees of freedom that the interactions can be calculated at a very high level of theory, yet they also offer a rich dynamical complexity due to their open-shell electronic structure. Experimental measurements of energy transfer are therefore able to provide both a first-hand insight into the interaction dynamics and rigorously gauge the accuracy of the QS calculations and the PESs on which they are performed.[1, 5]

This thesis is concerned with rotationally elastic and inelastic collisions of the CN($A^2\Pi$) molecule with atomic and molecular partners. The rotation of a diatomic molecule is described by its rotational angular momentum, ***j***. The amount of rotational energy transferred in a collision is a *scalar* quantity, represented by the magnitude of *j*. For rotationally elastic collisions, the magnitude of *j* remains unchanged and there is only translational energy transfer (TET). For rotationally inelastic collisions, the magnitude of *j* changes. However, angular momentum is a *vector*, meaning *j* also has directional properties. Both rotationally elastic and inelastic collisions can change the direction of *j*. A preferred direction of *j* is called a *polarisation* or *rotational anisotropy*, two main forms of which are possible: a preferred *sense* of rotation, termed an *orientation*, or a preferred *plane* of rotation, termed an *alignment*. Inelastic and elastic directional changes in *j* are termed *polarisation transfer* (or *inelastic depolarisation*) and *elastic depolarisation*, respectively.

Measurement of vector properties hence provides an added layer of detail to conventional scalar measurements alone and helps build a wider picture of the dynamics. However, vector measurements are experimentally more challenging to perform, as for example collisions that are largely elastic in rotational level are harder to

separate from those molecules that have not undergone any collision. With regards to the PESs, scalar measurements, such as RET cross-sections, are generally a good test of the short range repulsive parts of the potential. Vector attributes on the other hand are more sensitive to the subtle long range regions of the PES that are mediated by weaker attractive forces.[6] Together, scalar and vector correlations serve to benchmark the full topographical landscape of the PES.

A vector $\boldsymbol{v}$ may be represented by unit vectors $\boldsymbol{i}$, $\boldsymbol{j}$ and $\boldsymbol{k}$ pointing along axes x, y and z, as shown in Equation 1.1 and Figure 1.2:[4]

$$\boldsymbol{v} = v_x\boldsymbol{i} + v_y\boldsymbol{j} + v_z\boldsymbol{k}$$

Equation 1.1

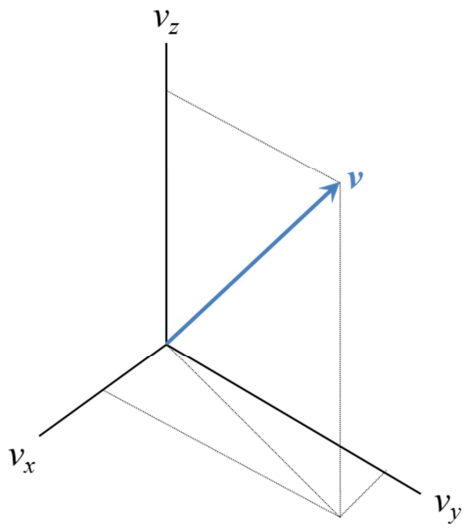

Figure 1.2 – A vector $\boldsymbol{v}$ *with component magnitudes* v_x, v_y *and* v_z *on the x, y and z axes, respectively. Adapted from reference 4.*

The magnitude of vector $\boldsymbol{v}$ is denoted by v:

$$v = \left(v_x^2 + v_y^2 + v_z^2\right)^{1/2}$$

Equation 1.2

To add or subtract vector $\boldsymbol{u} = (u_x\boldsymbol{i} + u_y\boldsymbol{j} + u_z\boldsymbol{k})$ from vector $\boldsymbol{v}$ (as previously defined in Equation 1.1):

$$\boldsymbol{v} \pm \boldsymbol{u} = (v_x \pm u_x)\boldsymbol{i} + (v_y \pm u_y)\boldsymbol{j} + (v_z \pm u_z)\boldsymbol{k}$$

Equation 1.3

If vectors ***v*** and ***u*** meet at angle θ, then the resultant addition vector, ***w*** = ***v*** + ***u***, is represented by Figure 1.3:

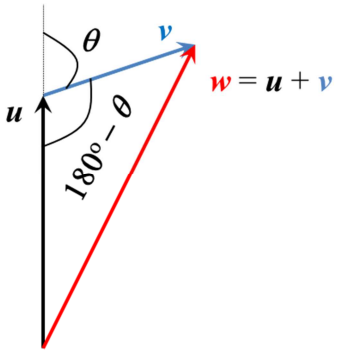

*Figure 1.3 – Vectors **u** and **v** add at angle θ to give the resultant vector **w** = **u** + **v**.*

The magnitude of ***w*** is determined by the *law of cosines*:

$$w^2 = v^2 + u^2 - 2vu\cos(180^\circ - \theta)$$

Equation 1.4

and so

$$w = (v^2 + u^2 + 2vu\cos\theta)^{1/2}$$

Equation 1.5

since

$$\cos(180^\circ - \theta) = -\cos\theta$$

Equation 1.6

The subtraction of vector ***u*** from ***v*** follows the same principle as Figure 1.3, but reversing the direction of ***u*** (i.e. ***v*** – ***u*** = -***u*** + ***v***).[4]

There are two methods of vector multiplication. Firstly, the *dot product* gives a scalar quantity:

$$\boldsymbol{u}\cdot\boldsymbol{v}=uv\cos\theta$$

Equation 1.7

where θ is the angle between the two vectors. The second procedure gives the *cross-product*, resulting in a psuedovector (***l***) normal to both the initial vectors, as defined in Equation 1.8 and Figure 1.4. The product is termed a *pseudovector*, as unlike a true vector, it changes sign under improper rotation or reflection.[4]

$$\boldsymbol{u}\times\boldsymbol{v}=\left(uv\sin\theta\right)\boldsymbol{l}$$

Equation 1.8

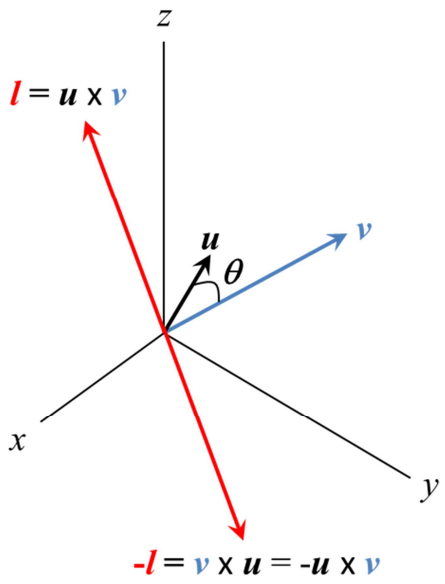

Figure 1.4 – The cross-product unit vector ***l*** *according to Equation 1.8 for* ***u*** × ***v*** *and* ***v*** × ***u****. The product vector is always perpendicular to the initial vectors, however its direction depends on the order in which the product is taken. Adapted from reference 4.*

In this regard, a diatom rotating in a plane may be thought of classically as a circle with radius (position vector) ***r*** rotating along a direction with velocity ***v***. The rotational angular momentum ***j*** can then be described as the cross-product ***j*** = ***v*** × ***r***, as shown in Figure 1.5(a), and so ***j*** is always perpendicular to the plane of molecular rotation and the internuclear axis, as seen in Figure 1.5(b).[4] Strictly speaking, this makes ***j*** a pseudovector. However, this thesis concerns the collisional transformation of ***j*** through

proper rotation against a fixed reference frame. Therefore, throughout this thesis, ***j*** is treated as a true polar vector.

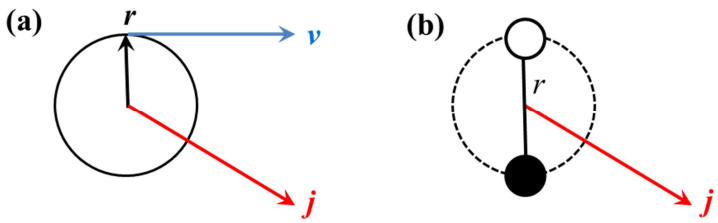

*Figure 1.5 – (a) The rotational angular momentum vector **j** represented as the cross-product **j** = **v** × **r** of the radius of a circle **r** moving along a direction with veclocity **v**. (b) A rotating diatom, where **j** is always perpendicular to the plane of rotation (dashed line) and the internuclear axis r.*

For consistency with standard typographical notation, vectors in this work are emboldened, whereas other labels, such as scalar quantities and quantum numbers, are not.

1.3 Intermolecular Forces

Weak intermolecular forces are electrostatic in nature and therefore governed by the presence and distribution of charge in the chemical species of interest. Molecules such as CN, H_2O and NH_3 are dipolar, whilst other molecules, such as N_2, O_2 or CO_2, are quadrupolar, or in the case of CH_4, octupolar.[7] Electrostatic interactions are described by the Coulomb potential:

$$V = \frac{q_1 q_2}{4\pi\varepsilon_0 r}$$

Equation 1.9

where q_1 and q_2 are point charges separated by distance r, and ε_0 is the vacuum permittivity. The interaction of two charges is shown in Figure 1.6.

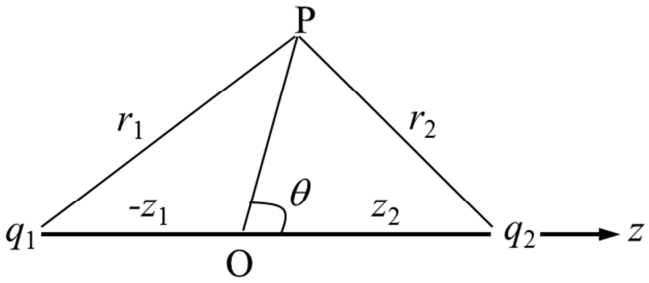

Figure 1.6 – The electrostatic interaction of two point charges, q_1 and q_2, along distance z. P refers to a point relative to the origin O.

The electrostatic potential at point P is given by:

$$\phi = \frac{q_1}{4\pi\varepsilon_0 r_1} + \frac{q_2}{4\pi\varepsilon_0 r_2}$$

Equation 1.10

which can be represented as a multipolar expansion:

$$\phi = \left(\frac{q}{4\pi\varepsilon_0 r}\right) + \left(\frac{\mu\cos\theta}{4\pi\varepsilon_0 r^2}\right) + \left(\frac{\Theta\left(3\cos^2\theta - 1\right)}{8\pi\varepsilon_0 r^3}\right) + \ldots$$

Equation 1.11

In Equation 1.11, the first bracket represents the charge term, the second bracket is the dipole term and the third bracket is the quadrupole term, with moments:

$$q = q_1 + q_2$$
$$\mu = q_2 z_2 - q_1 z_1$$
$$\Theta = q_1 z_1^2 - q_2 z_2^2$$

Equation 1.12

The interaction of two charge distributions is shown in Figure 1.7.

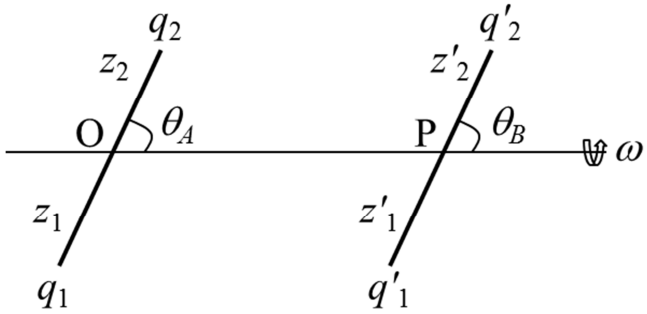

Figure 1.7 – The interaction of two charge distributions.

When averaged over the molecular orientations, the electrostatic interaction potentials become:

$$\langle V \rangle_{\mu\mu} = -\frac{2\mu_A\mu_B^2}{3k_BT(4\pi\varepsilon_0)^2 r^6}$$

Equation 1.13

$$\langle V \rangle_{\mu\Theta} = -\frac{\mu_A^2\Theta_B^2 + \mu_B^2\Theta_A^2}{k_BT(4\pi\varepsilon_0)^2 r^8}$$

Equation 1.14

$$\langle V \rangle_{\Theta\Theta} = -\frac{14\Theta_A^2\Theta_B^2}{5k_BT(4\pi\varepsilon_0)^2 r^{10}}$$

Equation 1.15

Here, k_B is the Boltzmann constant and T is the temperature of the system. The interactions are all attractive, where Equation 1.13 represents the dipole-dipole ($\mu\mu$) interaction, which decreases as r^{-6}. Equation 1.14 represents the dipole-quadrupole ($\mu\Theta$) interaction, which decreases as r^{-8}. Equation 1.15 represents the quadrupole-quadrupole ($\Theta\Theta$) interaction, which decreases as r^{-10}. The range of the interactions is therefore $\mu\mu < \mu\Theta < \Theta\Theta$.

The polarisation of the charge distribution in an atom or molecule by an electric field, E, can induce a dipole moment, μ_{ind}:

$$\mu_{ind} = \alpha E$$

Equation 1.16

where α is the polarisability (the ability of the charge distribution to be polarised). The dipole-induced dipole interaction is given by Equation 1.17, which is attractive and decreases as r^{-6}. Note, there is no temperature dependence.

$$\langle V \rangle_{\mu\mu_{ind}} = -\frac{\alpha\mu^2}{(4\pi\varepsilon_0)^2 r^6}$$

Equation 1.17

Since electrons in an atom or molecule are in constant motion, an instantaneous dipole can form in the charge distribution. This instantaneous dipole can induce a dipole in an adjacent atom or molecule. Such an interaction is termed the London dispersion force:

$$\langle V \rangle_{Disp} = -\frac{3\alpha^2 E_I}{4(4\pi\varepsilon_0)^2 r^6}$$

Equation 1.18

which is attractive and decreases as r^{-6}. The E_I in Equation 1.18 is the ionisation potential of the species concerned.

1.4 The Potential Energy Surface

The potential energy surface (PES) maps the potential energy of interacting collision partners as a function of all nuclear coordinates. Within the Born-Oppenheimer approximation of separated nuclear and electronic motions, the gradients of the PES describe the forces that act between the partners as they approach, collide and separate.[6] Small molecule systems are amenable to high level theory and experiments to yield state-resolved information. Scattering calculations utilise the PES to predict dynamical quantities, such as RET and elastic depolarisation rate constants. Aside from more general classical and quantal rigid body calculations, three main theoretical approaches include: quasi-classical trajectory (QCT) calculations, in which the scattering trajectories are treated classically, but with quantisation of the initial internal degrees of freedom; quasi-quantum treatment (QQT), a classical rigid body collision model, where

the PES is treated as being infinitely repulsive inside a given intermolecular distance as a function of incidence angle, but de Broglie interference is added between the scattered paths;[6] or quantum scattering (QS) calculations, the most exact form of which are termed close-coupled, or *cc*, that can be directly compared to experimental measurements. These are talked about in more detail in Section 1.6.1. Consequently, an abundance of theoretical and experimental effort has been spent characterising energy transfer in simple molecular encounters to encourage the calculation of more accurate PESs and associated scattering calculations, which in turn have driven more refined measurements of the scattering dynamics.

For a diatom interacting with a structureless atomic target, relevant to a large part of this thesis, the PES can be expressed as a function of three Jacobi co-ordinates: $\boldsymbol{r}$ – the diatomic internuclear separation, $\boldsymbol{R}$ – the vector connecting the centre of the atom and the centre-of-mass of the diatom, and $\boldsymbol{\theta}$ – the angle between the vectors $\boldsymbol{r}$ and $\boldsymbol{R}$. These are outlined in Figure 1.8.

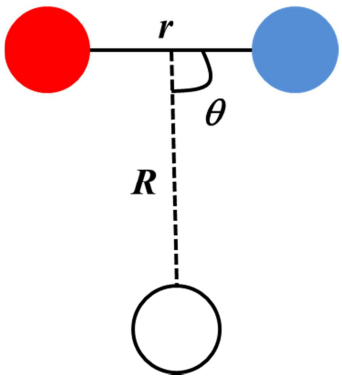

Figure 1.8 – The Jacobi co-ordinates describing a triatomic system, where $\boldsymbol{r}$ *is the diatomic internuclear separation,* $\boldsymbol{R}$ *is the vector connecting the centre of the atom and the centre-of-mass of the diatom, and* $\boldsymbol{\theta}$ *is the angle between the vectors* $\boldsymbol{r}$ *and* $\boldsymbol{R}$.

For the CN($A^2\Pi$)-Ar interaction potentials presented in this thesis, $\theta = 0^o$ corresponds to a linear Ar-N-C geometry, while $\theta = 180^o$ corresponds to a linear N-C-Ar arrangement. To reduce computational expense when calculating the PES and in subsequent scattering calculations, $\boldsymbol{r}$ is usually kept fixed at the equilibrium internuclear distance ($\boldsymbol{r_e}$) for a particular vibrational level. A finite grid of positions defined by $\boldsymbol{R}$ is then chosen, ranging in values of $\boldsymbol{R}$ that are sufficiently large enough to exceed likely collision energies and where the PES has approached the asymptotic limit, at which point the atom and diatom reach infinite separation. This is usually arbitrarily set to

zero. The angle, θ, is sampled at typically 10 – 20 discrete values between 0^o – 180^o. Established quantum-chemistry packages, such as MOLPRO[8] may be used to calculate the interaction potentials to a high level of theory, with different electronic structure approaches being applied depending on the precise electronic structure of the system. Long-range electrostatic terms are also included in the calculation, such as dipole and quadrupole moments and electronic polarisabilties.

For a $^2\Sigma^+$ diatom, only one PES (of $^2A'$ symmetry) is required to describe the interaction with a structureless target. This can be expanded into the separate radial and angular parts of the potential by:[9]

$$V_{\Sigma}(R,\theta) = \sum_{\lambda=0}^{\lambda=\lambda_{\max}} V_{\lambda 0}(R) d_{00}^{\lambda}(\cos\theta)$$

Equation 1.19

where $d_{00}^{\lambda}(\cos\theta)$ are the reduced rotation matrix elements, related to the Legendre polynomials, $P_{\lambda}(\cos\theta)$,[10] and $V_{\lambda 0}(R)$ are the radial expansion coefficients. Here, λ_{max} is limited to the number of angles, θ, for which the PES was initially calculated.

For a $^2\Pi$ system, the perturbation of an approaching partner lifts the asymptotic degeneracy of the diatomic π-orbitals, resulting in two adiabatic surfaces of $^2A'$ and $^2A''$ symmetry with respect to reflection of the electronic wavefunction in the triatomic plane,[11] analogous to the symmetry labels of the Λ-doublet levels in the isolated molecule. To perform scattering calculations it is convenient to represent the two surfaces in a diabatic basis by taking the following linear combinations:[11]

$$V_{sum}(R,\theta) = \frac{1}{2}\left[V_{A''}(R,\theta) + V_{A'}(R,\theta)\right]$$

Equation 1.20

$$V_{dif}(R,\theta) = \frac{1}{2}\left[V_{A''}(R,\theta) - V_{A'}(R,\theta)\right]$$

Equation 1.21

These are often referred to as the average and half-difference potentials, or more loosely, the sum and difference potentials. Again, these may be conveniently expanded into continuous functional forms of reduced rotation matrices:

$$V_{sum}(R,\theta) = \sum_{\lambda=0}^{\lambda=\lambda_{\max}} V_{\lambda 0}(R) d_{00}^{\lambda}(\cos\theta)$$

Equation 1.22

$$V_{dif}(R,\theta) = \sum_{\lambda=0}^{\lambda=\lambda_{\max}} V_{\lambda 2}(R) d_{20}^{\lambda}(\cos\theta)$$

Equation 1.23

where the $d_{20}^{\lambda}(\cos\theta)$ rotation matrix elements are related to the $P_{\lambda}^{2}(\cos\theta)$ associated Legendre functions by:[12]

$$d_{20}^{\lambda}(\cos\theta) = \left[\frac{(\lambda-2)!}{(\lambda+2)!}\right]^{1/2} P_{\lambda}^{2}(\cos\theta)$$

Equation 1.24

In the case of CN, where the separation of the neighbouring $X^2\Sigma^+$ and $A^2\Pi$ electronic states is small (~16000 cm^{-1}),[13, 14] an additional PES is required to describe the coupling between the $^2\Sigma(A')$ and $^2\Pi(A')$ PESs, termed V_1.[13]

Separation of the radial and angular parts of the potentials proves useful in subsequent QS calculations (see Section 1.6.1), as the potential energy of the system and its derivatives must be evaluable at any point on the PES. However, since the potential energy is only calculated at a limited number of places, a smooth analytical functional form is fitted to the points and then the energy may be returned for any arbitary set of coordinates. The rotation matrix elements or associated Legendre moments provide a useful basis for these analytical functions. The symmetry properties of the rotation matrix elements or Legendre moments are also found to couple specific channels of the scattering matrix. It becomes apparent that the lowest order spherical λ = 0 term can only mediate elastic collisions. The dipolar λ = 1 term is related to the difference between the two ends of the diatom and is able to induce RET in a heteronuclear diatomic molecule. The quadrupolar λ = 2 term distinguishes between the ends and

sides of the molecule, and is the lowest term that can cause rotational state changes in homonuclear diatomics. Inspection of these terms allows qualitative assessment of the strength and range of potentials governing rotationally elastic and inelastic collisions.[6]

The PES of a homonuclear diatom-rare gas interaction (such as N_2-Ar) is constrained by symmetry to possess only even-λ terms in the angular expansions.[15] Heteronuclear diatomics that can be described as "*near-homonuclear*", such as CN or NO, are then implicitly strongly even in character, which has a profound effect on the scattering amplitudes of subsequent QS calculations.

1.5 Rotational Anisotropy

1.5.1 Classical Description

The rotational angular momentum vector of a diatomic molecule, ***j***, possesses direction as well as magnitude. For an ensemble of molecules, the direction of ***j*** can be isotroptically or anisotropically distributed with respect to a reference frame. For this work, the reference frame is the either the propagation direction or electric field vector of the optical pump laser beam in the laboratory, which is termed the *laboratory* or *LAB* frame, denoted by ***z***. There are two limiting cases of rotational anisotropy: a dipolar distribution of ***j*** about ***z***, where classically there is a bias towards up *versus* down, called an *orientation*, or a quadrupolar distribution of ***j*** about ***z***, where classically there is a bias towards up-down *versus* side-to-side, termed an *alignment*. This is summarised in Figure 1.9. In terms of the rotational motion of the molecular ensemble, an oriented sample has a preferred *sense* of rotation (clockwise or anti-clockwise), while an aligned sample has a preferred *plane* of rotation, where in all cases the plane of rotation is perpendicular to ***j***.

In an isotropic collision environment, the position of ***j*** with respect to ***z*** can classically be defined by angle θ. The angular distribution of ***j***, $N(j,\theta)$, can then be conventiently represented by a weighted Legendre expansion with polynomial moments, $P_K(\cos\theta)$:[16]

$$N(j,\theta)=\frac{1}{4\pi}\begin{Bmatrix} A_0^{(0)}(j)+3A_0^{(1)}(j)P_1(\cos\theta)+\frac{5}{2}A_0^{(2)}(j)P_2(\cos\theta) \\ +7A_0^{(3)}(j)P_3(\cos\theta)+9A_0^{(4)}(j)P_4(\cos\theta)+\ldots \end{Bmatrix}$$

Equation 1.25

where the coefficients, $A_Q^{(K)}(j)$ (of rank K and projection Q) are the expectation values, or multipolar moments, of the distribution. Cylindrical symmetry imposes the constraint $Q = 0$, and $K = 0$, 1 or 2. The monopolar $A_0^{(0)}(j)$ moment then describes the population ($K = 0$) of the rotational state with angular momentum ***j***, $A_0^{(1)}(j)$ represents the orientation ($K = 1$) and $A_0^{(2)}(j)$ represents the alignment ($K = 2$), where

$$A_0^{(0)}(j)=1$$

$$A_0^{(1)}(j)=\langle P_1(\cos\theta)\rangle \quad \text{ranging from -1 to +1}$$

$$A_0^{(2)}(j)=2\langle P_2(\cos\theta)\rangle \quad \text{ranging from -1 to +2}$$

Equation 1.26

The ranges shown in Equation 1.26 are the high-j limiting cases that represent the maximum possible orientation or alignment. Generally, these parameters take values smaller in magnitude that tend towards one of the limits. When all the anisotropy parameters are zero, the ***j*** distribution is isotropic about ***z***.

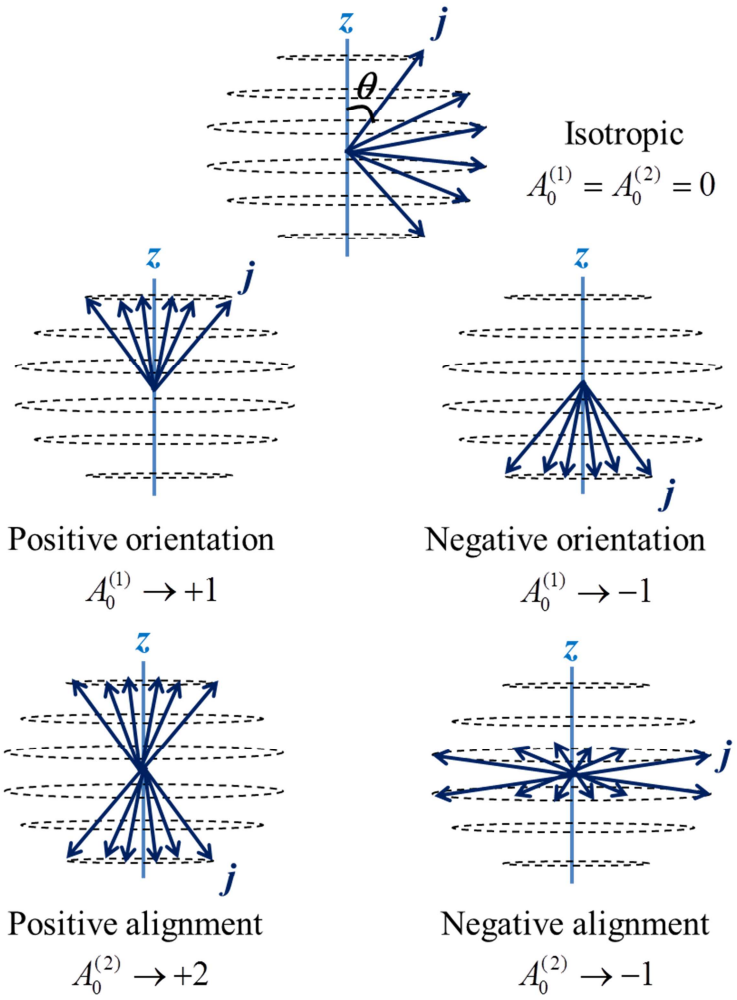

*Figure 1.9 – A schematic diagram of positively and negatively oriented and aligned distributions of **j** about **z** in the high-j limit. Adapted from reference 16.*

1.5.2 Quantum Mechanical Description

From a quantum mechanical view, rotationally resolved collisions are most naturally described in a $|jm\rangle$ basis, where j is the rotational angular momentum and m the projection of j onto a quantisation axis, such as the laser polarisation vector. A rotationally polarised ensemble is described by a density matrix, ρ, of $(2j+1)^2$ elements,[17] that gives a description of m-populations and the phase relationships between them. The matrix elements may couple to all other elements of the same j and accessible levels of different j, termed j'. The density matrix can be expressed in terms of spherical tensor operators, $T_Q^{(K)}$:[16, 17]

$$\rho = \sum_{K,Q} \rho_Q^{(K)} T_Q^{(K)}$$

Equation 1.27

Optical excitation with an axially symmetric polarised laser in a thermal (isotropic) bath of gas introduces low-order cylindrical symmetry to the density matrix. This means that only a few low-rank spherical tensor moments are sufficient to describe the density matrix. In such an environment, the spherical tensor moments are rotationally invariant and evolve independently (i.e. they cannot mix).[17] Optical detection is also similarly suited to description in a low-order spherical tensor basis.[10] The tensor moments are labelled $\rho_Q^{(K)}$, where K is the tensor rank and Q is the projection of K. The first few low rank moments relevant here are $K = 0$ (population), $K = 1$ (orientation) and $K = 2$ (alignment). Within a cylindrically symmetric system, such as that arising from optical excitation, only the diagonal elements of the density matrix are non-zero and consequently only those tensor moments with projection $Q = 0$ are non-zero, where the reciprocal relationship[10] between the tensor moments, $\rho_0^{(K)}$, and the matrix elements, ρ_m^j, is shown in Equation 1.28 and Equation 1.29.

$$\rho_0^{(K)}(j) = \sum_m (-1)^{j-m} [K]^{1/2} \begin{pmatrix} j & j & K \\ m & -m & 0 \end{pmatrix} \rho_m^j$$

Equation 1.28

$$\rho_m^j = \sum_m (-1)^{j-m} [K]^{1/2} \begin{pmatrix} j & j & K \\ m & -m & 0 \end{pmatrix} \rho_0^{(K)}(j)$$

Equation 1.29

Here, as throughout the rest of this work, $[n] = 2n + 1$ and the term in brackets, (:::), is a Wigner 3-j symbol.[10] The tensor moments depend on the populations of the individual matrix elements and are not normalised quantities. This is appropriate for discussing the time evolution of the density matrix for particular rotational states $|jm\rangle$, where population may flow in or out of the specified rotational level, j. When discussing rotational polarisation, it is more suitable to normalise the the density matrix tensor moment by the population, i.e. $(K \neq 0)/(K = 0)$.[16] This gives the alignment moments,

$A_Q^{(K)}$, with the same definitions and constraints on *K* and *Q* imposed by cylindrical symmetry as stated above. The population is then described by $A_0^{(0)}$, orientation by $A_0^{(1)}$ and alignment by $A_0^{(2)}$. The spherical tensor moments, $\rho_0^{(K)}$, are related to the alignment moments, $A_Q^{(K)}$, by:[3, 16]

$$A_Q^{(K)} = \rho_{-Q}^{(K)} \left[\frac{(-1)^Q c(K) \left(j \left\| J^{(K)} \right\| j' \right)}{\left\langle jm \left| J^2 \right| jm \right\rangle^{K/2} [K]^{1/2}} \right] = \frac{c(K)}{\left\langle jm \left| J^2 \right| jm \right\rangle^{K/2}} \left\langle J_Q^{(K)} \right\rangle$$

Equation 1.30

where

$$\rho_{-Q}^{(K)} = (-1)^Q \rho_Q^{(K)}$$

Equation 1.31

$$\left\langle J_Q^{(K)} \right\rangle = \sum_m \rho_{mm}^j \left\langle jm \left| J_Q^{(K)} \right| jm \right\rangle$$

Equation 1.32

Here, ρ_{mm}^j are diagonal elements of the density matrix, *J* is an angular momentum operator, $\left(j \left\| J^{(K)} \right\| j' \right)$ is a reduced matrix element,[11] and *c*(*K*) is a normalisation constant such that the moments with *Q* = 0 coincide with the classical high-*j* limits of the alignment moments from Section 1.5.1, where $c(0) = 1, c(1) = 1 \text{ and } c(2) = \sqrt{6}$.

The J^2 operator in Equation 1.30 gives the squared magnitude of *j*, i.e.:

$$\left\langle jm \left| J^2 \right| jm \right\rangle = j(j+1)$$

Equation 1.33

The $J_0^{(K)}$ are spherical-tensor angular momentum operators:[11]

$$\boldsymbol{J}_0^{(0)} = 1$$
$$\boldsymbol{J}_0^{(1)} = J_z$$
$$\boldsymbol{J}_0^{(2)} = \frac{1}{\sqrt{6}}\left(3J_z - J^2\right)$$

Equation 1.34

An orientation has a bias towards positive or negative values of *m*, while an alignment has a bias towards the absolute value of *m*. Furthermore, an aligned sample can exist that is unoriented, but an oriented sample is very often also aligned. All *m*-sublevels are equally populated in an isotropic distribution. Figure 1.10 shows example isotropic, oriented and aligned *m*-distributions for a molecular ensemble.

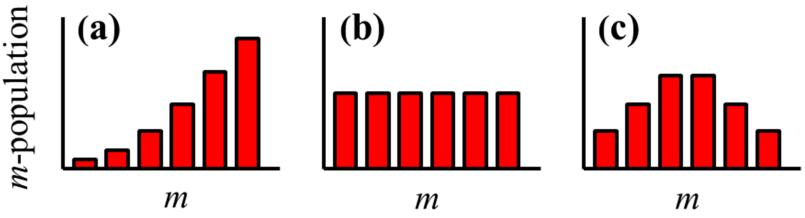

Figure 1.10 – Example m-sublevel distributions for (a) orientation, (b) isotropic and (c) alignment for j = 2.5. The quantisation axes are (a) the propogation vector of the pump laser and (c) the electric field vector of the pump laser.

1.6 Scalar and Vector Properties

Collisional energy transfer, such as EET, VET or RET, is a *scalar* quantity, as it shows for example the change in speed of vibration or rotation of a molecule. The key *vectors* in a collision between a diatom and a structureless target are outlined in Figure 1.11. Note, the unprimed terms represent pre-collision vectors and primed (′) terms present the post-collision vectors. The relative linear motion of the collision pair in the centre-of-mass frame is represented by $\boldsymbol{k}$, which is both parallel and proportional to the initial relative velocity, $\boldsymbol{v_{rel}}$. The magnitude of $\boldsymbol{k}$ is defined as:[6]

$$k = \frac{\sqrt{2E_T/\mu}}{\hbar}$$

Equation 1.35

where μ is the reduced mass of the collision pair with relative translational energy E_T. As noted in Section 1.2, the rotational angular momentum vector, ***j***, classically represents the speed and direction of rotation of the diatomic molecule and lies perpendicular to the plane of rotation, which contains the molecular axis, ***r***. The relative motion of the collision partners is represented by the orbital angular momentum, ***l***, whose initial magnitude is related to $\boldsymbol{v_{rel}}$ and the miss-distance between the colliding pair had there been no interaction, termed the impact parameter, *b*:

$$\boldsymbol{l} = \mu \boldsymbol{v}_{rel} b$$

Equation 1.36

The total angular momentum, ***J***, is conserved in the collision, such that:

$$J = j + l = j' + l'$$

Equation 1.37

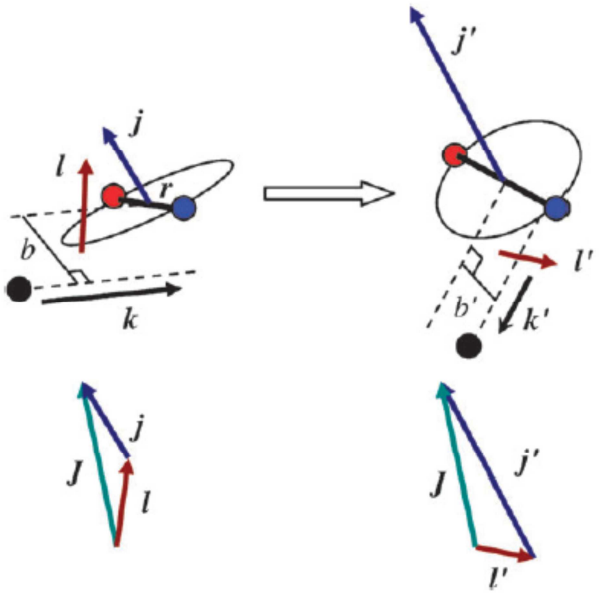

Figure 1.11 – The key vectors in an atom-diatom collision, as defined in the main text. Adapted from reference 6.

This thesis is concered with ***j.j′*** correlations, i.e. the magnitude and polarisation of ***j*** before and after collision. These may be evaluated by measuring RET, polarisation transfer and elastic depolarisation rate consants (or cross-sections), which are discussed in Section 1.6.1. Although not the topic of this work, the ***k.k′*** correlation is another important measurable quantity, termed the differential cross-section, or DCS. This

enables the scattering angle distributions to be resolved. Other higher-order correlations, such as ***k.k′.j′***, provide current state-of-the-art in molecular collision dynamics.

1.6.1 *j.j′* Correlations

For an ensemble of molecules under equilibrium conditions there is a Maxwell-Boltzmann distribution of relative velocities and internal state populations. The direction of rotational angular momentum is also isotropically distributed. In order to non-statistically populate a specific rotational level and create a rotational polarisation, the system must depart from equilibrium and a source of anisotropy introduced. This is usually performed by optical excitation using a polarised laser in a controlled experimental cell. The collisional evolution of the initial population and polarisation may then be monitored using a second laser, either by probing the prepared level or collisionally populated levels.

As stated in Section 1.2, the collisional transfer of energy between different rotational levels (Δj) is termed *RET*. The destruction of rotational anisotropy for non-state-changing ($\Delta j = 0$) collisions is termed *elastic depolarisation*, and for rotational state-changing collisions ($\Delta j \neq 0$) is called *inelastic depolarisation*. From a quantum mechanical view, depolarisation is the redistribution of anisotropically populated *m*-sublevels towards isotropy. Classically, this is a measure of the degree of tilt, $\theta_{jj'}$, suffered by the molecule during a collision, as shown in Figure 1.12.

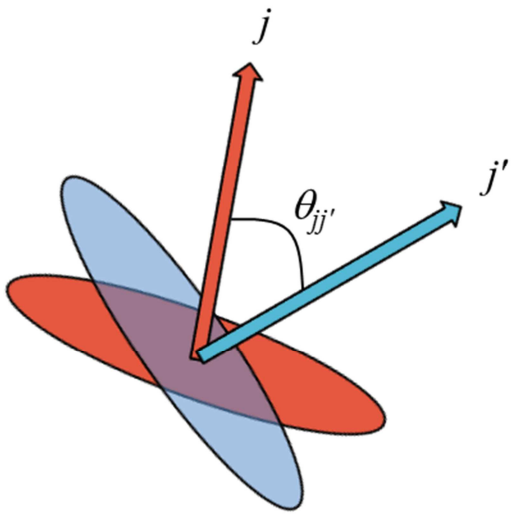

RET	$\boldsymbol{j} \neq \boldsymbol{j'}$	$\theta_{jj'}$ = unresolved
Elastic Depolarisation	$\boldsymbol{j} = \boldsymbol{j'}$	$\theta_{jj'} \neq 0$
Inelastic Depolarisation	$\boldsymbol{j} \neq \boldsymbol{j'}$	$\theta_{jj'} \neq 0$

*Figure 1.12 – The pre- and post-collision rotational angular momentum vectors of a diatomic molecule, **j** (red) and **j′** (blue), normal to the plane of molecular rotation (circles). For rotational energy transfer (RET), there is a change in the magnitude of **j**, i.e. **j** ≠ **j′**. The collisional tilt (depolarisation) of **j** is represented by $\theta_{jj'}$. A change the direction of **j** but not its magnitude (**j** = **j′**) is termed "elastic depolarisation". A change in both the direction and magnitude of j, i.e. **j** ≠ **j′**, is termed "inelastic depolarisation" or "polarisation transfer".*

When there is cylindrical symmetry, the classical distribution of the post-collision rotational angular momentum, ***j′***, about the pre-collision vector, ***j*** can be written as a Legendre expansion of the tilt angle:[18]

$$P\left(\theta_{jj'}\right) = \frac{1}{2}\sum_{K}\left[K\right]a^{(K)}P_K\left(\cos\theta_{jj'}\right)$$

Equation 1.38

where K is the tensor rank, $[K] = 2K+1$, and $a^{(K)}$ is equilvalent to the renormalised anisotropy moments, $A_Q^{(K)}$ in Equation 1.26, or the multipole transfer efficiency, $E^{(K)}(j,j')$, defined later in this section, depending on whether the process is elastic or inelastic.

Experiments traditionally measure rate constants or cross-sections of collisional energy transfer and depolarisation of rotational angular momentum over time. The rate constant

for state-to-state transfer of population from an initial level *j* to a product level *j′* is termed $k^{(0)}_{j\to j'}$. The total removal of population from level *j*, $k^{(0)}_{pop,j}$ is defined as the sum of the state-specific rate constants:

$$k^{(0)}_{pop,j} = \sum_{j'} k^{(0)}_{j\to j'}$$

Equation 1.39

The rate constants may be converted to velocity-averaged cross-sections, which accounts for the frequency of collisions:

$$\langle \sigma \rangle = \frac{k}{\langle v_{rel} \rangle}$$

Equation 1.40

where v_{rel} is the relative velocity of the collision pair:

$$\langle v_{rel} \rangle = \left(\frac{8k_B T}{\pi \mu} \right)^{1/2}$$

Equation 1.41

Here, k_B is the Boltzmann constant, T is the temperature of the system (T = ~298 K at thermal equilibrium), and μ is the reduced mass:

$$\mu = \frac{m_1 m_2}{m_1 + m_2}$$

Equation 1.42

The average relative velocity of each collision pair relevant to this work is listed in Table 1.1.

Table 1.1 – The average relative thermal velocity, $\langle v_{rel} \rangle$, of each CN($A^2\Pi$)-collider pair in this work.

Collider	$\langle v_{rel} \rangle$ / m s^{-1}
Ar	633
N_2	684
O_2	663
CO_2	621

The elastic depolarisation rate constant, $k_{dep,j}^{(K)}$, measures the collisional destruction of the prepared polarisation in level j back towards an isotropic distribution. Inelastic depolarisation is measured by the fraction of rotational anisotropy transferred from the initial level to a product state, which is termed the multipole transfer efficiency (MTE), $E^{(K)}(j,j')$.[19, 20]

The following sub-sections introduce collisional models of RET, elastic depolarisation and polarisation transfer.

Spin Spectator Model

For Hund's case-(b) molecules, such as OH($A^2\Sigma^+$), the electron spin may be treated to a very good approximation as a spectator during a collision with a spherical partner.[18] This means that changes in spin-rotation state, $j = N \pm S$, must be a result of reorienting the nuclear rotation N, followed by recoupling of the electron spin, S. This concept is outlined in Figure 1.13. The terminology used here is introduced in Chapter 2.

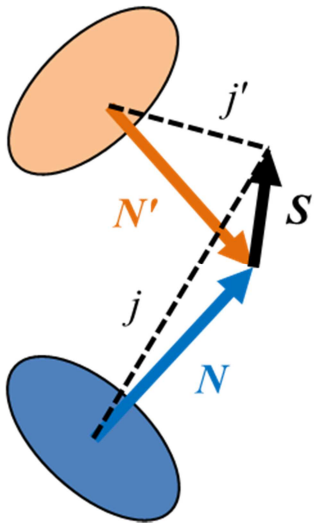

Figure 1.13 – Illustration of the spin spectator model. Uncoupling of the electron spin during a collision means that changes in spin-rotation state require significant reorientation of N. Adapted from reference 18.

Scaling Laws

There is an almost universal trend in RET studies of a strongly decreasing magnitude in state-to-state RET rate constant (or cross-section) with increasing Δj, often termed a *volcano* effect.[5] This arises due to the increasing energy gaps, $\Delta E_{jj'}$, between the initial, j, and final, j', rotational levels and from linear-to-angular momentum constraints (see next sub-section). Empirical statistical scaling models have been widely used to derive state-to-state (and hence also total) RET rate constants and their decline with increasing j'.[5, 21-25] Almost all of these models follow a power or exponential energy gap law, the basis of which resembles:[23]

$$\sigma_{j\to j'} = \alpha(2j'+1)(T/T')^{1/2}\left|\Delta E_{jj'}\right|^{\gamma}$$

Equation 1.43

or in the linear form:

$$\ln\left[\sigma_{j\to j'}(T/T')^{1/2}/(2j'+1)\right] = -\gamma\ln\left|\Delta E_{jj'}\right| + \ln\alpha$$

Equation 1.44

where $\sigma_{j\to j'}$ are the state-to-state transfer cross-sections, α and γ are fitting parameters and T and T' are the initial and final translational energies. The maximum classical limit

is given by a hard sphere-hard ellipse model, proposed by McCaffery and co-workers,[26, 27] as outlined later in this section. Popular modified scaling laws include the modified exponential gap (MEG) model:[24, 25]

$$k_{j\to j'} = \alpha \exp\left(\frac{-\beta\Delta E_{jj'}}{k_B T}\right)\left(\frac{1+\frac{2E_j}{\gamma k_B T}}{1+\frac{2E_j}{k_B T}}\right)$$

Equation 1.45

and the statistical power exponential gap (SPEG) model:[24, 25]

$$k_{j\to j'} = \alpha \exp\left(\frac{-\beta\Delta E_{jj'}}{k_B T}\right)\left(\frac{\Delta E_{jj'}}{B_v}\right)^{-\gamma}$$

Equation 1.46

where β is another adjustable parameter and B_v is the vibrational level-dependent rotational constant of the diatom.

Linear-to-Angular Momentum Model

In the classical impulsive limit, collision-induced rotational state change arises from the conversion of linear momentum to angular momentum at the anisotropic repulsive wall, $V(r,\theta)$, of a rigid ellipse. The rotation of the molecule is ignored in this type of model where a sudden approximation is assumed. The impact of an atom (hard sphere) at the surface of the stationary ellipse provides an instantaneous change in linear momentum, Δk. The transfer to angular momentum is given by the product of the torque, $-dV(r,\theta)/d\theta$, and the time for which it is applied. Only at the repulsive wall does the potential energy vary sufficiently enough with θ to generate the torque needed for effective RET.[26] Along the direction of momentum transfer and coinciding with the surface normal of the ellipse lies the kinematic apse, $\hat{a}_k$:[28, 29]

$$\hat{a}_k = \frac{k'-k}{|k'-k|}$$

Equation 1.47

where k and k' are the initial and final relative linear momenta. The magnitude of the tranferred angular momentum is given by the product of the kinematic apse and the torque arm of the effective impact parameter, b_n. This is defined as the perpendicular distance between the centre-of-mass of the molecule and the direction of the transferred momentum.

$$\Delta j = \mu v_{rel} b_n^{\max} = \hat{a}_k \times b_n$$

Equation 1.48

Here, μ is the reduced mass of the collision pair, v_{rel} is the relative velocity and $b_n^{\max}$ is the maximum value of the effective impact parameter. The transferred angular momentum, Δj, must obey total angular momentum conservation, such that:

$$\Delta j - \Delta(r \times k) = 0$$

Equation 1.49

where r is the distance between the centre-of-mass of the molecule and the spherical target. There is no change in r during the interaction, meaning:

$$\Delta j = r \times \hat{a}_k$$

Equation 1.50

It then directly follows that Δj is perpendicular to $\hat{a}_k$. This means that the apse frame projection, m_a, of the initial rotational angular momentum, j, is approximately conserved during the collision. This applies restrictions to the extent of m-changing collisions in the model. There are also kinematic constraints on the amount of linear momentum available for conversion to angular momentum. A vector representation of the linear-to angular-momentum model for an atom-diatom collision is shown in Figure 1.14.

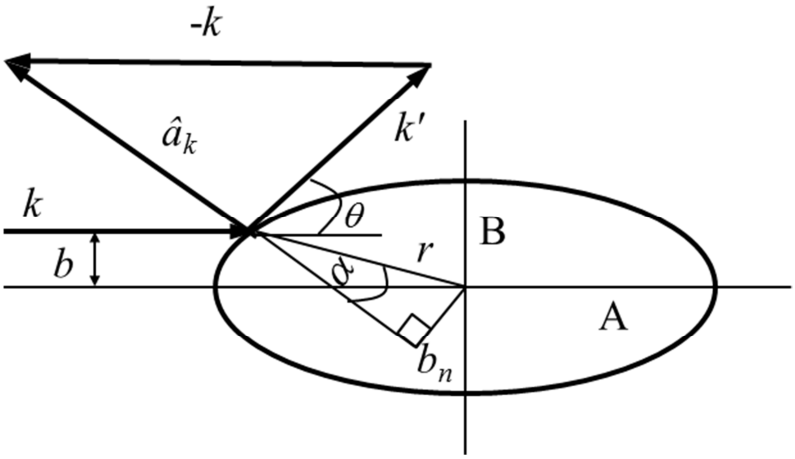

Figure 1.14 – The variables in a classical impulsive rigid ellipse representation of an atom-diatom collision. Adapted from reference 26.

McCaffery and co-workers extended their model to include transfer of translational motion to vibration as well as rotation of the diatom.[30, 31] This is represented by:

$$\Delta j = -\left(j+\frac{1}{2}\right)\sqrt{\left(j+\frac{1}{2}\right)^2 \pm \frac{\mu v_r^{\,2}}{2B} - E_v}$$

Equation 1.51

where B is the rotational constant of the molecule.

Models such as this have been successfully imployed in many RET studies,[32] however they are *a posteriori* and incapable of quantitative predictions.[33] They are unsuited to describing the scattering of open-shell species, where the attractive regions of the potentials become important and multiple PESs are needed to represent the system.

Quasi-Quantum Treatment (QQT)

The QQT approach aims at simplifying exact quantum treatments through use of semi-classical approximations. It provides a more general insight into the relationship between inelastic scattering and the repulsive anisotropy of the interaction and presents a basis for understanding the spatial stereochemistry of the collision. This model treats the scattering as defined by classical rigid body-rigid sphere kinematics, but allows for quantum interferences between paths that lead to the same final state and scattering angle that arise from impacts at different points on the ellipsoidal surface. The kinematic apse, $\hat{a}_k$, is quantised and used as the reference frame, along which angular

monentum is conserved. For given initial and final rotational states and a well-defined collision energy, the rotational anisotropy of the product is directly determined by the scattering angle, θ. This model has been successful in interpreting state-of-the-art inelastic scattering measurements.[34-36] However, while useful for qualitative interpretations, as stated previously, often such semi-classical approaches offer poor quantitative predictions, and so exact quantum scattering treatments may be employed instead of or alongside them.

Quasi-Classical Trajectory (QCT)

This method treats the scattering classically, then sorts the trajectories into quantum states. Traditionally, QCT has found prominence in the study of reactive systems, such as H + H_2 and F + H_2 amongst many other examples.[37-42] It has also been successfully applied to simple non-reactive scattering.[43-48] The use of classical trajectories greatly simplifies the theoretical description of the collision, the main reason being that the de Broglie wavelength associated with atomic or molecular motion is typically much shorter compared to the distance over which particles move during the scattering process.[42] The basic idea is to integrate over the classical equations of motion with quantisation of the internal degrees of freedom and averaging over different impact parameters, orientations and vibrational phases.

The classical equations of motion are most conveniently integrated using space-fixed Cartesian coordinates, where the *z*-axis lies along the direction of the initial relative velocity, *k* and the *x*-axis is defined by the initial orbital angular momentum, *l*.[40] If $r_{i\alpha}$ represents the α^{th} component ($\alpha = x,y,z$) of a vector r_i which locates the i^{th} atom (i = 1, 2 … N), then the equations of motion become:

$$\frac{dr_{i\alpha}}{dt} = \frac{p_{i\alpha}}{m_i}$$

Equation 1.52

$$\frac{dp_{i\alpha}}{dt} = -\frac{\partial V}{\partial r_{i\alpha}}$$

Equation 1.53

where $p_{i\alpha}$ is the momentum along $r_{i\alpha}$, m_i is the mass of atom i and V is the PES describing the system. For each trajectory, the final coordinates and momenta are analysed to obtain the product state distributions. Integration is carried out until product molecules have separated sufficiently that they no longer interact.

For rotationally inelastic ($N \rightarrow N'$) collisions at a fixed collision energy, E_{coll}, the expression for an inelastic RET cross-section is:[48]

$$\sigma_{N\rightarrow N'}(E_{coll}) = \pi b_{\max}^2 \frac{\aleph_{N'}}{\aleph_{tot}}$$

Equation 1.54

where $\aleph_{N'}$ is the number of trajectories ending in state N' and $\aleph_{tot}$ is the total number of trajectories (elastic plus inelastic). The $a^{(K)}(N,N')$ polarisation parameter may be calculated from the ensemble average of the Legendre moment of the classical tilt angle between the initial (N) and final (N') rotational angular momentum vectors, $P_K(\cos\theta_{NN'})$:[18]

$$a^{(K)}(N,N') = \left\langle P_K(\cos\theta_{NN'})\right\rangle = \frac{1}{\aleph_{N'}}\sum_{i=1}^{\aleph_{N'}} P_K\left(\cos\theta_{NN'}^{(i)}\right)$$

Equation 1.55

with summation over the ensemble of trajectories ending in a given N' rotational state.

Quantum Scattering (QS) Formalism

Collisions of small open-shell molecules, such as OH, NO or CN are readily amenable to exact QS calculations on accurate *ab initio* PESs and serve as prototypes for comparison of experiment and theory, providing fundamental tests of the development of scattering theory and of the PESs that underpin the scattering calculations. Open-shell molecules with non-zero orbital angular momenta, such as $^2\Pi$ systems, present additional dynamical complexity to scattering studies, as a result of spin-orbit (fine-structure) and Λ-doublet splittings of the rotational levels (see Chapter 2). The degree of Hund's case-(a) to (b) uncoupling also has significance in the interpretation of the scattering dynamics.[12]

The theoretical model for quantum scattering of a $^2\Pi$ molecule with a structureless target (rare gas atom) is well-established and has been discussed in detail in the literature, in particular by Alexander and co-workers.[49-51] The probability of scattering between the two rotational levels is found by solving a set of close-coupled (*cc*) differential equations that are directly related to the radial expansion terms, $V_{\lambda\mu}(R)$, of the V_{sum} and V_{dif} interaction potentials outlined in Section 1.4. For a pure Hund's case-(a) molecule, the potential matrix elements are expressed as:

$$\begin{aligned} V^{JM}_{j'\Omega'\varepsilon'L',j\Omega\varepsilon L}(R) &= \left\langle j'\Omega'\varepsilon'L'JM\middle|V\middle|j\Omega\varepsilon LJM\right\rangle \\ &= (-1)^{j+j'+J-\Omega}([L][L'][j][j'])^{1/2}\sum_{\lambda}\begin{pmatrix} L' & \lambda & L \\ 0 & 0 & 0\end{pmatrix}\begin{Bmatrix} j' & L' & J \\ L & j & \lambda\end{Bmatrix}F^{\lambda}_{j'\varepsilon',j\varepsilon} \\ &\times\left[\delta_{\Omega\Omega'}\begin{pmatrix} j' & \lambda & j \\ -\Omega' & 0 & \Omega\end{pmatrix}V_{\lambda 0}(R)-\varepsilon(1-\delta_{\Omega\Omega'})\begin{pmatrix} j' & \lambda & j \\ -\Omega' & 2 & \Omega\end{pmatrix}V_{\lambda 2}(R)\right] \end{aligned}$$

Equation 1.56

$$F^{\lambda}_{j'\varepsilon',j\varepsilon} = \frac{1}{2}\left[1-\varepsilon\varepsilon'(-1)^{j+j'+\lambda}\right]$$

Equation 1.57

where *JM* represents the total angular momentum and its laboratory-frame projection, *j* and *j′* are the initial and final rotational angular momenta of the diatomic, Ω and Ω' the initial and final spin-orbit angular momenta, ε and ε' the initial and final parity labels (symmetry indices), *L* and *L′* the initial and final orbital angular momenta of the collision pair, λ is the expansion index, $\delta_{\Omega\Omega'}$ is a Kroenecker delta and (:::) are Wigner 3-*j* symbols and {:::} are Wigner 6-*j* symbols that describe the vector couplings.[10]

The $\delta_{\Omega\Omega'}$ term in Equation 1.56 means that scattering within the same spin-orbit manifold ($\Omega = \Omega'$) is enabled by only the $V_{\lambda 0}(R)$ terms of the V_{sum} PES, while scattering between different spin-orbit manifolds ($\Omega \neq \Omega'$) is enabled by the $V_{\lambda 2}(R)$ terms of the V_{dif} PES. As a result of the phase factor, $F^{\lambda}_{j'\varepsilon',j\varepsilon}$, the scattering amplitude for rotational parity-*conserving* transitions arises only from the even-λ terms of the PESs, whilst the parity-*changing* transitions arise from the odd-λ terms.[49, 52] Consequently, pure Λ-doublet transfer is enabled only from odd-λ terms in the V_{sum} potential, and pure *elastic* ($j\Omega\varepsilon = j'\Omega'\varepsilon'$) collisions are enabled only from even-λ terms in the V_{sum} potential. As

shown in Chapter 2, whether a transition is parity or Λ-doublet conserving or parity or Λ-doublet changing ultimately depends on the parity and Λ-doublet label of the product level, $j'\Omega'\varepsilon'$, and therefore depends on whether Δj is even or odd. These propensities are summarised in Table 1.2. For a near-homonuclear molecule, such as CN, symmetry restrictions mean that interactions with rare gases are strongly even in character, making the scattering amplitudes for parity-conserving transitions substantially larger than for parity-changing transitions.[15]

Table 1.2 – Propensity rules for the contribution of different V_{sum} and V_{dif} PES Legendre components to the scattering into different product levels as a function of Δj and Λ-doublet symmetry index, ε.[12, 52]

	Δj = even	Δj = odd
Λ-conserving, $\varepsilon = \varepsilon'$	λ = even	λ = odd
Λ-changing, $\varepsilon \neq \varepsilon'$	λ = odd	λ = even

The 3-*j* symbol $\begin{pmatrix} L' & \lambda & L \\ 0 & 0 & 0 \end{pmatrix}$ in Equation 1.56 means that $L = L'$ when $\lambda = 0$, and so the isotropic part of the PES cannot change the orbital angular momentum of the system. Since the total angular momentum is conserved, this also means that the rotational angular momentum of the diatomic cannot change, either in projection or magnitude. Therefore, the $\lambda = 0$ term of the PES only contributes to totally elastic collisions, where $|jm\rangle$ is conserved. In a physical picture, the $\lambda = 0$ term is spherical, and so cannot provide a torque required to depolarise the molecule or cause energy transfer. Within the Hund's case-(a) limit, only the $\lambda \geq 2$ even terms of the V_{sum} potential contribute to elastic depolarisation.[12]

When the electron spin uncouples from the nuclear framework, spin-rotation coupling becomes significant (see Chapter 2) and the molecules are a mix of Hund's cases-(a) and (b) character. The potential matrix elements that describe the scattering now take the form:

$$V^{JM}_{j'\Omega'\varepsilon'L',j\Omega\varepsilon L}(R) = \left\langle j'F_i'\varepsilon'L'JM\middle|V\middle|jF_i\varepsilon LJM\right\rangle$$
$$= (-1)^{j+j'+J}([L][L'][j][j'])^{1/2}\sum_{\lambda}\begin{pmatrix} L' & \lambda & L \\ 0 & 0 & 0\end{pmatrix}\begin{Bmatrix} j' & L' & J \\ L & j & \lambda\end{Bmatrix}$$
$$\times F^{\lambda}_{j'\varepsilon',j\varepsilon}\left[A^{\lambda}_{j'F_i'\varepsilon',jF_i\varepsilon}V_{\lambda 0}(R) + B^{\lambda}_{j'F_i'\varepsilon',jF_i\varepsilon}V_{\lambda 2}(R)\right]$$

Equation 1.58

where the coefficients $A^{\lambda}_{j'F_i'\varepsilon'L',jF_i\varepsilon L}(R)$ and $B^{\lambda}_{j'F_i'\varepsilon'L',jF_i\varepsilon L}(R)$ are functions of the mixed spin-orbit character of the molecular wavefunction:

$$A^{\lambda}_{j'F_i'\varepsilon'L',jF_i\varepsilon L}(R) = C^{1/2}_{j'\Omega'\varepsilon'}C^{1/2}_{j\Omega\varepsilon}\begin{pmatrix} j' & \lambda & j \\ -1/2 & 0 & 1/2\end{pmatrix} - C^{3/2}_{j'\Omega'\varepsilon'}C^{3/2}_{j\Omega\varepsilon}\begin{pmatrix} j' & \lambda & j \\ -3/2 & 0 & 3/2\end{pmatrix}$$

Equation 1.59

$$B^{\lambda}_{j'F_i'\varepsilon'L',jF_i\varepsilon L}(R) = C^{3/2}_{j'\Omega'\varepsilon'}C^{1/2}_{j\Omega\varepsilon}\begin{pmatrix} j' & \lambda & j \\ -3/2 & 2 & -1/2\end{pmatrix} - C^{1/2}_{j'\Omega'\varepsilon'}C^{3/2}_{j\Omega\varepsilon}\begin{pmatrix} j' & \lambda & j \\ -1/2 & 0 & -3/2\end{pmatrix}$$

Equation 1.60

Here, $C^{\Omega}_{jF_i\varepsilon}$ are Wigner coefficients obtained by diagonalisation of the molecular Hamiltonian, defined as:

$$C^{\Omega}_{jF_i\varepsilon} = (-1)^{N-j+\Sigma}\left(jS\Omega - \Sigma\middle|N\Lambda\right)$$

Equation 1.61

such that

$$\left|JMF_i\varepsilon\right\rangle = \sum_{\Omega} C^{\Omega}_{jF_i\varepsilon}\left|JM\Omega\varepsilon\right\rangle$$

Equation 1.62

where $(\cdots\cdot|\cdot\cdot)$ is a Clebsch-Gordon coefficient,[52] S = ½ (CN electron spin), and $N = j \pm S$ (rotational angular momentum neglecting electron spin, as detailed in Chapter 2).

Spin-orbit conserving and spin-orbit changing transitions are now mediated by both the V_{sum} and V_{dif} PESs, weighted by the coefficients $A^{\lambda}_{j'F_i'\varepsilon,jF_i\varepsilon}$ and $B^{\lambda}_{j'F_i'\varepsilon,jF_i\varepsilon}$. Interference

between these two coefficients depends on the sign of ε for the initial level, resulting, for example, in uneven Λ'-populations from initially equal Λ-populations.[52] The $F^{\lambda}_{j'\varepsilon',j\varepsilon}$ term imposes the same parity propensities as discussed for a pure Hund's case-(a) molecule. The 3-*j* symbol again means the λ = 0 term enables only totally elastic scattering and the $\lambda \geq 2$ even terms of both the V_{sum} and V_{dif} potentials contribute to elastic depolarisation and energy transfer. The degree of Hund's case-(a) uncoupling for a $^2\Pi$ molecule is quantified by the ratio, $Y = A/B$, of the spin-orbit constant, A, and the rotational angular momentum constant, B. As seen from the values of these spectroscopic constants in the next chapter, CN($A^2\Pi$) is predominantly Hund's case-(a) for the low-*j* levels studied in this work.

Solution of the *cc*-equations using the potential matrix elements described in Equation 1.56 and Equation 1.58 results in the scattering matrix (*T*-matrix). The amplitudes and phases of the *T*-matrix elements, $T^{J}_{jF\varepsilon l,j'F'\varepsilon'l'}$, contain the complete information on the scattering process. They are related to the state-to-state tensor cross-section for molecules in a $^2\Pi$ electronic state:[53-56]

$$\sigma^{(K)}_{jF\varepsilon\to j'F'\varepsilon'} = \frac{\pi}{k^2_{jF\varepsilon}} \sum_{\substack{JJ'\\ ll'}} [J][J'](-1)^{l+l'-j-j'+2J} \begin{Bmatrix} j & j & K \\ J & J' & l \end{Bmatrix} \times \begin{Bmatrix} j & j' & K \\ J & J' & l' \end{Bmatrix} T^{J}_{jF\varepsilon l,j'F'\varepsilon'l'} \left(T^{J}_{jF\varepsilon l,j'F'\varepsilon'l'}\right)^{*}$$

Equation 1.63

Here, $k_{jF\varepsilon}$ is the wavevector of the initial level and the rest of the notation is as previously defined. The K = 0 tensor cross-sections are related to the integral cross-sections *via*:[53, 54]

$$\sigma_{j\to j'} = \left(\frac{[j']}{[j]}\right)^{1/2} \sigma^{(0)}_{j\to j'}$$

Equation 1.64

To calculate the thermal rate constants, the cross-sections are computed over a grid of collision energies and averaged over a room-temperature (T = 298 K) Maxwell-Boltzmann distribution of relative velocities:

$$k_{jF_i\varepsilon\to j'F'_i\varepsilon'}(T)=\left(\frac{8}{\pi\mu k^3T^3}\right)^{1/2}\int_0^\infty \sigma_{jF_i\varepsilon\to j'F'_i\varepsilon'}(E_{\text{coll}})E_{\text{coll}}\exp\left(-E_{\text{coll}}/k_BT\right)\mathrm{d}E_{\text{coll}}$$

Equation 1.65

The elastic depolarisation cross-section of rank K is given by the difference between the totally-elastic $K = 0$ cross-section and the elastic tensor cross-sections of rank K:[53, 54]

$$\sigma^{(K)}_{\text{dep},jF\varepsilon}=\sigma^{(K=0)}_{jF\varepsilon\to jF\varepsilon}-\sigma^{(K)}_{jF\varepsilon\to jF\varepsilon}$$

Equation 1.66

As introduced by Alexander and Orlikowski,[20] the measure of polarisation transferred in an inelastic collision for a $^2\Pi$ system is given by the MTE, $E^{(K)}(j,j')$, which can be defined in terms of the ratio of the cross-section for transfer of a moment of rank K of the angular momentum distribution, $\sigma^{(K)}_{j\to j'}$, to the population transfer tensor cross-section, $\sigma^{(0)}_{j\to j'}$ (or the equivalent ratio for rates or rate constants).[18, 19, 57]

$$E^{(K)}(j,j')=\frac{\sigma^{(K)}_{j\to j'}}{\sigma^{(0)}_{j\to j'}}$$

Equation 1.67

The MTE for the lowest orientation moment, $K = 1$, has the limits $-1 \leq E^{(1)}(j,j') \leq +1$, where the positive limit corresponds to complete conservation of the initial orientation and the negative limit corresponds to conservation of the magnitude, but change in the *sign* of orientation.

1.6.2 Optical Preparation and Detection of Polarised Rotational Angular Momentum

The symmetry properties of polarised laser light can be exploited to prepare and probe a polarised rotational quantum state from an initially isotropic ensemble. Light may be represented as a transverse electromagnetic wave comprised of mutually perpendicular electric and magnetic fields. Linear combinations of two orthogonal electric field components can be used to construct pure polarisation states of the light. Linearly polarised light consists of a $n\pi/2$ phase shift between the two components (where n is an

integer multiple), resulting in a product electric field oscillating sinusoidally in a plane along the direction of propagation. The plane of polarisation in this case is given by the direction of the electric field vector, ε. For circularly polarised light there is a $n\pi/4$ phase shift between the two components, where n = odd.[58] This results in a product electric field of constant magnitude rotating clockwise (σ^+) or anti-clockwise (σ^-) along the propagation direction, k, which in this case also serves as the symmetry axis. The linear and circular polarisations are shown in Figure 1.15. The polarisation of light may be rotated between these limiting cases using an optical wave-plate.[58]

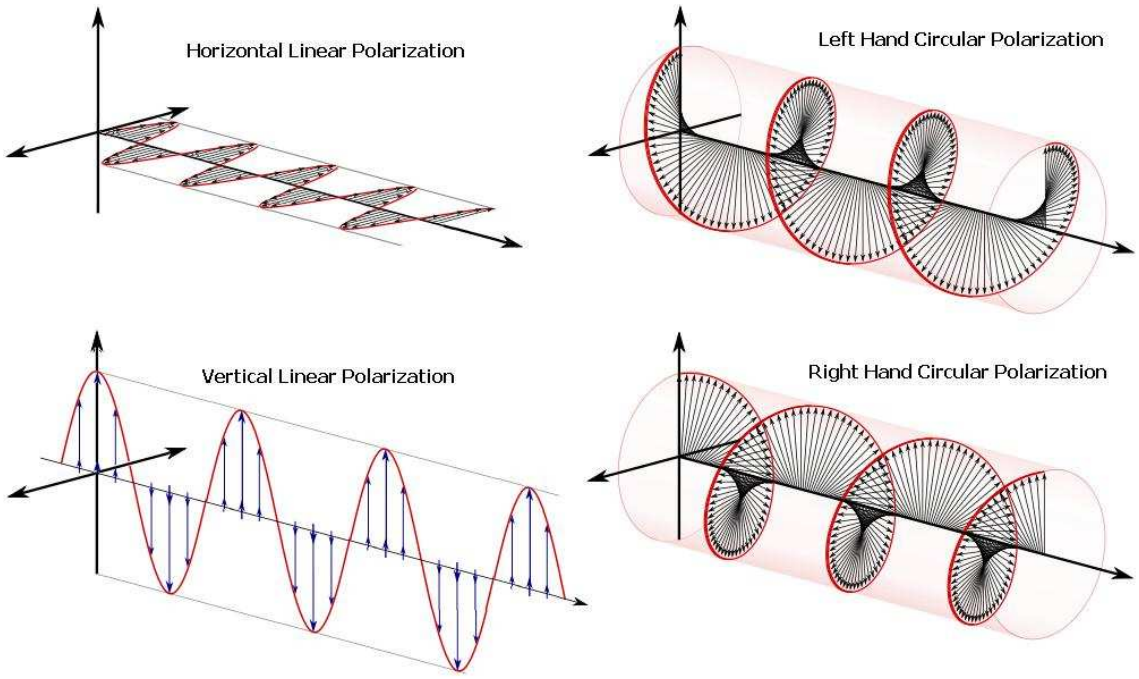

Figure 1.15 – Linearly and circularly polarised laser light. The red trace is the electric field vector, $\boldsymbol{\varepsilon}$. Adapted from reference 59.

The probability that a molecule absorbs or emits light is proportional to the (squared) projection of the electric field vector, $\boldsymbol{\varepsilon}$, of the polarised light, onto the transition dipole moment, μ, of the molecule. A $\cos\theta$ relationship between $\boldsymbol{\varepsilon}$ and $\boldsymbol{\mu}$ means that those molecules whose transition dipole moments happen to lie parallel to the electric field vector will be preferentially selected, as shown in Equation 1.68.[16]

$$\left|\boldsymbol{\mu}\cdot\boldsymbol{\varepsilon}\right|^2 = \left|\boldsymbol{\mu}\right|^2\left|\boldsymbol{\varepsilon}\right|^2\cos^2\theta$$

Equation 1.68

Since $\boldsymbol{\mu}$ is related to $\boldsymbol{j}$ through the molecular framework, the polarisation of the interacting light can be used to both prepare and probe a polarised rotational angular momentum. The relationships between $\boldsymbol{\mu}$, $\boldsymbol{j}$, the molecular axis (r), and the spectroscopic branches for a diatomic molecule in the high-j limit are shown in Figure 1.16.[16]

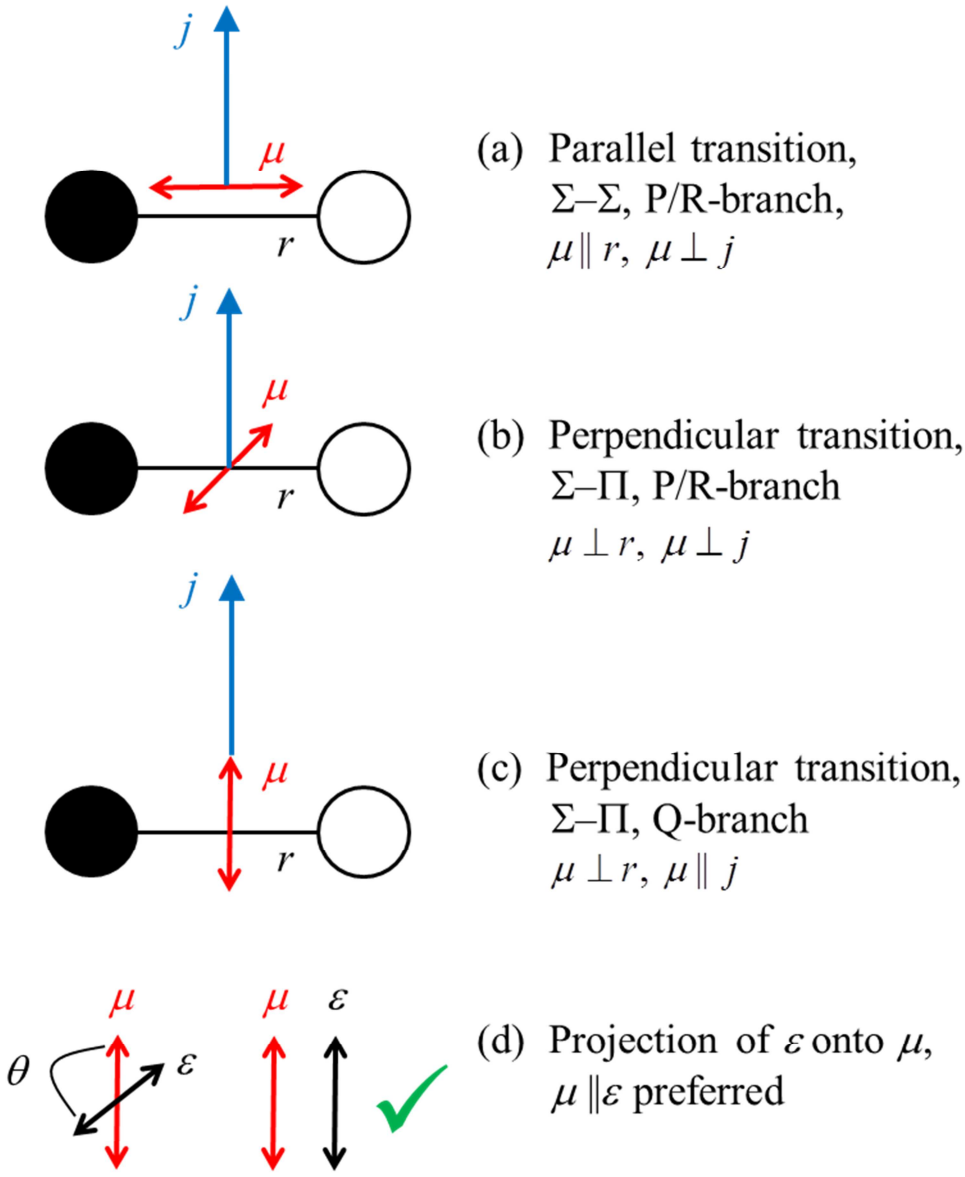

Figure 1.16 – The relationship between the transition dipole moment, $\boldsymbol{\mu}$, rotational angular momentum, $\boldsymbol{j}$, and the internuclear axis, r, for Σ-Σ and Σ-Π electronic transitions. Adapted from reference 16.

Both the preparation and probe steps usually follow a particular spectroscopic scheme between different electronic and vibrational levels using one or more photons of light. For a one-photon parallel (Σ–Σ) electronic transition, μ lies along r for P and R

rotational branches (there is no Q-branch), whereas for a perpendicular transition (Σ–Π), μ is always perpendicular to *r*.

In the perturbative limit, the maximum non-zero tensor rank, *K*, of the prepared population distribution is equal to twice the number of interacting photons. For one-photon excitation with cylindrical symmetry, a circular laser polarisation will generate a population (*K* = 0), orientation, (*K* = 1) and an alignment (*K* = 2). A linear polarisation will generate only even moments, in this case a population (*K* = 0) and alignment (*K* = 2). A triangular relationship between *Q* (= 0), *K* and *j* in the alignment moments, $A_0^{(K)}(j)$, means that *j* = 0 cannot be polarised, *j* = ½ can only possess an orientation (*K* = 1), and *j* = 1 is the lowest value of *j* that can be both oriented and aligned. For higher order systems, this trend can conceptually extend up to $K_{max} = 2j$.

For one-photon processes, the population and rotational anisotropy moments are commonly measured by recording the signal intensities (*I*) of two orthogonal pump-probe laser polarisations. This can be perfomed by periodically rotating either the pump or probe laser between vertical and horizontal linear polarisations, to give *parallel* ($I_{\parallel}$) and *perpendicular* ($I_{\perp}$) pump-probe geometries, or opposite helicities (σ^+ and σ^-) for circularly polarised light, to give *co*-rotating (I_{co}) and *counter*-rotating (I_{con}) geometries. The anisotropy is proportional to the difference of the two intensities, $I_{co} - I_{con}$ or $I_{\parallel} - I_{\perp}$, and the population is proportional to their sum, $I_{co} + I_{con}$ or $I_{\parallel} + 2I_{\perp}$, depending on which polarisations are used. The normalised orientation moment, $A_0^{(1)}$ is then proportional to the ratio *C*, and the alignment moment, $A_0^{(2)}$, to the ratio *P*, of these intensities, as shown in Equation 1.69 and Equation 1.70.[19]

$$C = \frac{I_{co} - I_{con}}{I_{co} + I_{con}}$$

Equation 1.69

$$P = \frac{I_{\parallel} - I_{\perp}}{I_{\parallel} + 2I_{\perp}}$$

Equation 1.70

For a Q-branch, the transition dipole moment points along *j* and does not rotate with the molecule, and so the plane of polarisation for circularly polarised light will be perpendicular to the plane of rotation of the molecule. There will clearly then be no difference between the two circular polarisation geometries experienced by the molecule, making a Q-branch insensitive to orientation at high-*j*. Conversely, for a P- or R-branch, μ is in the plane of rotation of the molecule, and so there is a rotating transition dipole moment and rotating electric field, making these branches sensitive to the sense of molecular rotation. Within the classical limits, P- and R-branches are therefore required for preparing and probing an orientation over Q-branches.[16, 19]

1.7 Experimental Techniques

Conventional methods to measure the scalar and vector properties of inelastic collisions generally fall into two categories – crossed-molecular beam (CMB) experiments and optical-optical double resonance (OODR) experiments.[6] Molecular beams are formed by expanding a gas mixture into a high vacuum chamber. Collisions within the expansion region cool the molecules' internal degrees of freedom and redistribute the energy into translation away from the expansion source.[60] This results in a well-defined superthermal velocity distribution, but confines the rotational energy to the lowest few levels, which gives good initial state definition, but restricts quantum state selectivity. In general, the relatively high collision energy resulting from crossing two supersonic molecular beams limits CMB methods to probing the repulsive regions of the PESs. However, recent experimental advances, such as Stark deceleration,[61, 62] offer a means to reduce the collision energy and hence also explore the attractive regions of the potential. The beams of the collider and target molecule are crossed in the chamber, often at 90^{o}, providing a precise collision axis. These attributes make CMB experiments well suited to DCS measurements.

Conversly, OODR experiments are usually performed with a small quantity of the molecule in an isotropic bath (bulb) of collider gas. The nature of the experiment means that the translational and other degrees of freedom can be easily thermalised to a Maxwell-Boltzmann distribution. This generally makes bulb experiments unsuitable for DCS measurements, although with notable exceptions.[63-74] The low collision energies involved provide access to the more subtle vector properties of the attractive regions of the PES.

A common starting point for most experiments is the introduction or generation of the molecule of interest. Stable species, such as NO, may be readily stored and delivered to the experiment, being suited to seeding in a molecular beam (usually in excess Ar or He buffer gas). However, radicals such as CN and OH are unstable and generally short-lived, and so are often produced *in situ* during the experiment *via* photodissociation of a photolabile precursor using intense laser pulses, for example at 266 nm (Nd:YAG laser) or 193 nm (ArF excimer laser). Photolysis usually produces radicals with a very non-statistical and anisotropic state distribution. In a bulb set-up, this nascent distribution is often allowed to thermalise to concentrate the population into a statistical range of levels.

There is usually then a requirement to prepare the target molecules in a specific set of quantum states with well-defined vector properties. Tunable lasers may be used to excite a fraction of the molecules to selected electronic, vibratonal and rotational (rovibronic) states, where the symmetry properties of the beam can create a desired rotational anisotropy with a convenient laboratory reference frame. The collisional evolution of the prepared molecules is then probed over time. The classic CMB approach is to use a rotatable time-of-flight mass spectrometer (TOF-MS),[6] however such a universal ionisation detector will not generally allow the measurement of product state-specific DCSs. Laser-induced flouresence (LIF) can be used to monitor the quantum state propensities,[75] but does not provide DCS information. The state-of-the-art in DCS measurements is velocity map imaging (VMI), as discussed Section 1.7.7.

Bulb experiments principally employ optical state-selection coupled with optical detection methods, such as LIF (Section 1.7.1) or resonance-enhanced multi-photon ionisation (REMPI), Section 1.7.6, hence the term optical-optical double resonance (OODR).[5, 76] The experimental techniques that have been employed to prepare or probe rotational population, orientation and alignment are outlined in the following sub-sections, where as will be seen, the number of photons in the pump and probe steps may vary and the experimental methods may be linear or non-linear.[19] Selected relevant results from these methods are used in later chapters when discussing the results of this thesis.

A detailed literature review of previous work on the CN radical is presented in Section 1.8. The frequency modulated spectroscopy (FMS) technique is introduced and discussed in Chapter 3.

1.7.1 Laser Induced Fluoresence (LIF)

Laser induced fluorescence is a highly sensitive resonance technique in which molecules are excited to a higher energy level by absorption of one or more photons, followed by emission (fluorescence) back down to the ground state. This method is readily employed in collisional energy transfer studies to measure state-specific populations. There are two different types of LIF, the first is purely as a detection method, with the initial state selection performed elsewhere,[77-82] or it can be used to prepare an excited state and the energy transfer observed using time-resolved dispersed fluoresence.[83-86] An example LIF spectroscopic scheme is shown in Figure 1.17. The basic experimental set-up consists of a tunable laser source and a photomultiplier tube (PMT), as shown in Figure 1.18, with the flourescence detected perpendicular to the laser axis. The polarisation of the fluoresence may also be resolved by using polarisation-sensitive optics.

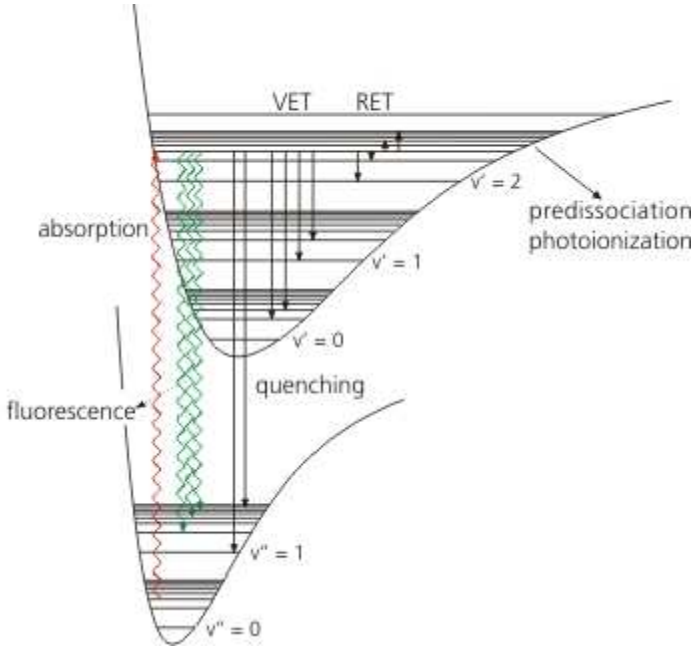

Figure 1.17 – An example energy level diagram for laser induced fluorescence (LIF). The molecule is excited on a particular rovibronic transition (red) using tunable laser light and the fluorescence from the excited level detected (green). Adapted from reference 87.

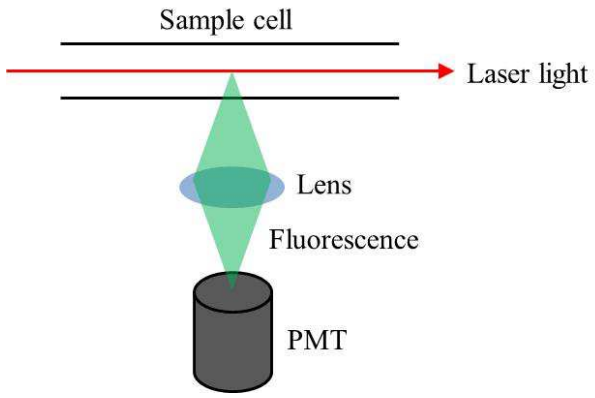

Figure 1.18 – An example LIF experimental set-up. Absorption of the laser light (red) excites the molecule to a higher rovibronic level. The fluorescence from this level (green) is then detected at 90° to the laser axis using a photomultiplier tube (PMT).

Some notable examples of LIF used in collisional energy transfer studies are listed next. Kliner and Farrow implemented LIF to monitor RET in collisions of rotationally hot OH($X^2\Pi_{3/2}$, v = 0, N'' = 1 – 12) in a thermal bath of Ar, N_2, O_2 and H_2O gases, fitting their results to an exponential gap model.[88] The RET rates were observed to be faster for low N'' compared to high N''. For H_2O, RET was around an order of magnitude faster than the other colliders, however the rate was less dependent upon N''.

Ter Meulen and co-workers used LIF as a powerful state-selective probe of Λ-doublet resolved RET. Firstly, they employed an electric field in a hexapole arrangement to prepare a beam of pure OH($X^2\Pi_{3/2}$, v = 0, j = 3/2, f) crossed with various partners, including Ar, He, H_2, CO, CO_2, HCl, HBr and HI.[77-79, 89-98] The two e (ε = 1) and f (ε = -1) Λ-doublets (see Chapter 2 for notation) experience different radial forces from the electrostatic field, resulting in the focussing of one Λ-doublet and divergence of the other, and hence selection of a single Λ-doublet level. In some experiments, the state-selected beam was then passed through a second homogeneous electrostatic field to physically orient the OH molecules, so that either the O-end or the H-end was presented to the collision partner. The orientation of the molecule for a particular inelastic transition is represented by the steric asymmetry ratio, $S_{i\to f}$, defined as:

$$S_{i\to f} = \frac{\sigma_{\text{C–HO}} - \sigma_{\text{C–OH}}}{\sigma_{\text{C–HO}} + \sigma_{\text{C–OH}}}$$

Equation 1.71

where σ_{C-HO} and σ_{C-OH} refer to RET cross-sections from level $i \rightarrow f$ when the collision partner, *C*, impinges on the H-end of the molecule or the O-end, respectively. A positive steric asymmetry ratio represents collisions with the O-end of the molecule, while a negative ratio represents collisions with the H-end.

The state-selected and oriented OH($X^2\Pi$)+Ar system[78, 79, 96, 98] showed a gross dependence of the amount of RET on which end of the OH molecule was struck. The O-end populated low-j' levels, whereas the H-end distributed population to the higher-j' levels. This has a simple explanation, as the H-atom is displaced further from the centre-of-mass of the OH molecule, and so it is easier for the collision partner to rotate the OH by hitting the lighter H-end than the heavier O-end.

In general, the CO and N_2 partners[77, 95] behaved similarly to Ar, where the inelastic cross-sections were dominated by energy gap law constraints and and with a preference for H-end collisions. Moreover, collisions at the O-end of the OH molecule lead to population of low rotational levels, whilst H-end collisions populated higher rotational levels. For N_2, CO and CO_2, the order of the rotationally inelastic cross-sections (sum over all state-to-state cross-sections) was OH+CO_2 > OH+CO > OH+N_2, which was explained in terms of the physical size of the collision partner.[77, 95] The CO_2 molecule is the largest out of the three, resulting in the largest total cross-section. The internuclear distance of CO is slightly longer than that of N_2, 1.13 Å *vs.* 1.10 Å, and also CO has a larger dipole and quadrupole moment compared to N_2, meaning the interaction at longer-range is stronger for OH+CO compared to OH+N_2. The three molecular partners also gave larger spin-orbit conserving cross-sections. The ratio between the total cross-sections for excitation out of the *e* or *f* Λ-doublets were 1.21 ± 0.12 $Å^2$, 1.71 ± 0.26 $Å^2$ and 1.84 ± 0.34 $Å^2$, respectively, which shows a marked preference for scattering out of the *e* state. From a quantum scattering perspective, these observations indicate that, in the mixed Hund's cases regime, the anisotropic terms in V_{dif} potentials are smaller than in V_{sum} for these colliders. The observed behaviour was also attributed to contributions from out-of-plane collisions.[77, 95]

Systematic differences between CO and N_2 were noted. Unoriented state-to-state RET cross-sections indicated the OH-N_2 PES to be more head-tail symmetric than for OH-CO, implying that the OH-N_2 interaction is more even and isotropic. CO had a larger magnitude of steric asymmetry, with a stonger preference for H-end collisions, which

for spin-orbit conserving transitions increased for higher j'. Conversely, N_2 showed a preference for H-end collisions in spin-orbit changing transitions. The origin of these differences was attributed to possible influence from reactive collisions and HOCO complex formation. Collisions that produce higher rotational excitation generally have smaller impact parameters, making complex formation more likely. The authors also investigated the effect of OH vibrational excitation. In comparison to OH(v = 0), the relative cross-sections for collisions of OH(v = 1) with N_2 were found to be smaller at low j' and larger for higher j'. This was ascribed to the larger equilibrium bond distance for the higher vibrational level, resulting in a more anisotropic potential. Also, the smaller rotational energy spacings for v = 1 would mean larger cross-sections due to the energy gap law.[77, 95]

For light collisions partners, such as He and H_2,[96-98] there was a preference for H-end collisions by He. In contrast, collisions of OH+H_2 preferred the O-end of the OH molecule when transferring to low j', with Λ-doublet selection in these transitions depending strongly on the rotational state of the H_2 partner. This dependence was shown to be much weaker for transfer to higher rotational states.[96-98]

With the halogen hydride (HX) collision partners,[89-93, 99] the amount of product rotational excitation decreased with increasing rotational quantum number. For HCl, 81 ± 2% of the scattered OH molecules were found in other internal states compared to 80 ± 2% for HBr collisions. For HI scattering, those OH molecules ending up in the f Λ-doublet had populated both Ω = 3/2 and 1/2 spin-orbit manifolds, whilst those molecules that had transferred to the e level were found to have undergone only parity changing transitions. The spin-orbit conserving cross-sections decreased faster with rotational excitation when scattered by HI compared to the other two colliders. A propensity for Ω = 3/2 f and 1/2 e for HI at low rotational excitation was also revealed, with overall 41.6 ± 1.3% of the scattered molecules ending up in the lower Λ-doublet. However, no Λ-doublet parity propensity was observed for collisions with HCl and HBr. This behaviour was attributed to the magnitude of the different OH-HX intermolecular interactions, where the electric quadrupole moment and polarisabilities are larger for OH-HI than for OH-HBr and OH-HCl.[89-93, 99] The quadrupole moments and polarisabilities for the HX species are all positive and increase from HCl to HI, whereas the dipole moments decrease in this direction.

For parity changing transitions, each of the HX molecules exhibited a preference for impacting the O-end of the OH molecule.[89-93, 99] Large negative steric asymmetries were observed for spin-orbit and parity conserving transitions, especially for HCl. All other transitions presented very small steric asymmetries. Measurement of the OH-HX interaction strengths suggested that the global minimum of the potentials decrease with the dipole moment of the halogen hydride for HCl and HBr.[89-93, 99] Aside from the type and strengths of the intermolecular interactions, the differences in results for the OH($X^2\Pi$)+HX systems could be linked to reaction, the different temperature dependencies thereof and the different vibrational distributions of the H_2O product. The reactions are of the form:

$$OH + HX \rightarrow H_2O + X$$

Reaction 1.1

The reaction species form a T-shaped HOH′X complex as they approach, which is principally attributed to a dipole-quadrupole interaction, while the global minimum of each system represents more of a dipole-dipole interaction. The spin-orbit conserving collisions with negative steric asymmetries represent encounters with the H-side of the OH molecule, which suggests the partners approach on a path that does not sample the complex formation region of the PES. For collisions with HBr and HI, a second, OHXH′ complex may become important, meaning both the H-end and O-end oriented molecules could be lost by reaction, resulting in smaller measured steric asymmetries.[89-93, 99]

Dispersing the LIF emission within a well-defined time frame provides information on collisional energy transfer pathways. Dagdigian and co-workers made extensive use of OODR dispersed LIF detection to monitor RET in CN($A^2\Pi$), as outlined in Section 1.8. Use of polarisation optics and different laser-detector geometries allows for preparation and probing of a polarised ensemble of molecules. This method was applied by McKendrick and co-workers to follow polarisation effects in electronically inelastic collisions of SiF($C^2\Delta \rightarrow B^2\Sigma^+$)+$H_2$.[83, 84, 86] The transferred population was found to be significantly less polarised than the initial level. Brinkman and Crosley also utilised the dispersed LIF method to study the collisional depolarisation of rotational alignment in OH($A^2\Sigma^+$, v = 0, j = 4.5) by He, Ar, N_2, O_2, CO_2 and H_2O.[100] Their results are summarised in Table 1.3 along with the total RET cross-sections cited by the authors.

As apparent, H_2O is the most effective collider for both RET and removal of the prepared polarisation. For depolarisation alone, Ar is faster than the remaining molecular partners, followed by N_2, CO_2 and O_2. However, Ar and CO_2 have the same ability to induce RET, but both are slower than N_2. The authors explained their results in terms of application to monitoring trace species in flame diagnostics.

Table 1.3 – Alignment depolarisation and total RET cross-sections for OH($A^2\Sigma^+$) from Brinkman and Crosley.[100] Units are in Å^2.

Collider	$\sigma_{dep}^{(2)}$	σ_{RET}	RET ref.
He	3	-	-
O_2	6	-	-
CO_2	9	62	101
N_2	15	93	101
Ar	20	62	102
H_2O	< 30	145	101

In a similar set-up, Troe and co-workers quantified state- and polarisation-resolved collisional energy transfer in NO_2 self-collisions.[103] Cross-sections derived from master equation analysis and angular momentum scaling expressions showed pure RET to dominate the collision dynamics, whereas rovibrational transfer was inefficient. Loss of polarisation was minimal, indicating a preference for small changes of *m*. These results are consistent with a direct RET mechanism, rather than one that follows complex formation.

McCaffery and co-workers made extensive use of dispersed polarised LIF and OODR-LIF using cw lasers to obtain elastic and inelastic depolarisation cross-sections for a wide range of diatomics,[32] including Li_2+Ar and He; I_2+I_2, O_2, He, Ar, CO_2, CHF_3 and Xe; Na_2+Rg; NaK+Rg; NaLi+He and Ar; and Se_2+Ar and Se. The depolarisation cross-sections were invariably small, around two orders of magnitude less than the total RET cross-sections. A general $\Delta m = 0$ propensity was observed, leading to minimal destruction of the prepared polarisation during RET.

Pibel and Moore used polarised OODR fluorescence detection to measure orientation removal during initial state-selected collisions of H_2, HD and D_2 ($B^1\Sigma_u^+$, $v = 0$, $j = 1$) with He, Ne, Ar and H_2($X^1\Sigma_g^+$).[104] Encounters of all three isotopologues with He and Ne resulted in cross-sections of around 30 Å^2. Collisions of HD and D_2 with Ar gave cross-

sections of around 10.6 Å^2 and 13.9 Å^2, respectively, and D_2 with $H_2(X^1\Sigma_g^+)$ around 7.6 Å^2. The smaller cross-sections were attributed to the dominant quenching abilities of Ar and $H_2(X^1\Sigma_g^+)$ for these systems.

Field and co-workers employed polarisation-sensitive LIF in an OODR set-up to study *m*-changing collisions of BaO($A^1\Sigma^+$, $v = 1$, $j = 1$) with Ar and CO_2, and CaF($A^2\Pi_{1/2}$, $v = 0$, $j = 0.5$, *f*, $m = 0.5$)+Ar.[105, 106] In these experiments, sequential excitation was used to probe the prepared and collisionally populated levels *via* different excited states. The BaO+CO_2 elastic depolarisation cross-section was around 20% smaller than the measured total removal cross-section, however Ar was in contrast very inefficient at depolarising BaO.[106] The authors discussed these results with respect to the importance of long-range intermolecular forces in *m*-changing collisions. For the CaF($A^2\Pi$)+Ar system, the $j' = 0.5$ *e*, 1.5 *f*, and 1.5 *e* RET product levels were probed with left- and right-handed circularly polarised cw-LIF. A strong final level dependence of the product orientation was observed, with the parity-conserving transfer ($j' = 1.5$ *f*) resulting in products with the same sign of orientation as the initial level, while the parity-changing transfer ($j' = 0.5$ *e* and 0.5 *e*) resulted in products with the opposite sign of orientation.[105] This corresponds to a positive MTE for the parity-conserving Δj transitions and a negative MTE for the parity-changing transitions, exactly as predicted earlier by Alexander and Davis.[56]

1.7.2 Zeeman Quantum Beat Spectroscopy (ZQBS)

Brouard and co-workers have developed this technique as an extension to dispersed polarisation-resolved LIF.[18, 44, 46-48, 107] It shares the same experimental attributes, but with the addition of a pair of Helmholtz coils that apply a small magnetic field to lift the degeneracy of the Zeeman fine-structure *m*-sublevels. The splitting of the Zeeman levels is in the 10 MHz range, making the transitions from individual Zeeman levels close to the original field free transition. The Zeeman states are therefore coherently excited during the optical pump stage, which results in oscillation of the prepared rotational anisotropy and convolutes a beat signal onto the observed fluorescence for a particular polarisation geometry. For this to happen, the polarisation of the excitation laser must break the cylindrical symmetry of the magnetic field by being orthogonal to the field direction. The beat signal is dependent on both the magnetic field strength and

gyromagnetic ratio of the level involved, and the magnitude of the beat signal depends on the amount of rotational anisotropy. The dampening of the Zeeman quantum beat is therefore proportional to the decay of the bulk polarisation (un-normalised tensor moments of the density matrix), independent of the population (fluorescence) decay. It is however difficult to separate elastic and inelastic depolarisation, as to do this requires the fluorescence to be dispersed, which dramatically reduced the signal-to-noise ratio. The ZQBS technique was recently applied to measurements of elastic depolarisation in OH($A^2\Sigma^+$) and NO($A^2\Sigma^+$).[18, 44, 46-48, 107]

For the OH($A^2\Sigma^+$)+Ar system, elastic scattering was found to comprise around 20% of the total (elastic plus inelastic) depolarisation rate at low *j*, with removal of alignment typically faster than of orientation.[44] Comparison to QS and QCT predictions on recent *ab initio* PESs revealed that depolarisation is comparable to or faster than RET.[18] This reflects the sizable depth of the potential energy well and is consistent with significant tilting of the plane of rotation, where classically the molecule is dragged around as the collider approaches. Overall, there was a reasonable level of agreement between experiment and theory and also with analogous depolarisation measurements using polarisation spectroscopy (PS) by McKendrick and co-workers (see Section 1.7.4). At low *j*, elastic depolarisation was of similar magnitude to OH($X^2\Pi$)+Ar, despite the different electronic character and a considerably shallower attractive well-depth in the latter. However, depolarisation in OH($A^2\Sigma^+$)+Ar appeared to be far more insensitive to the value of *j*, reflecting the difference in anisotropy of the PESs and the nature of depolarising collisions.

The depolarisation of rotational angular momentum in collisions of NO($A^2\Sigma^+$) with He and Ar has also been measured using ZQBS.[46] Again, the alignment decay was revealed to be more efficient than for orientation, although overall, collisional depolarisation was concluded to be very inefficient and a relatively minor process in the presence of much faster RET, alluding to the weak long-range forces of the systems. There was good agreement between experiment and QS and QCT calculations. Encounters with Ar were around 30% more efficient at removing the prepared polarisation compared to He, which was attributed to kinematic effects and differences in the PESs. Comparison of NO($A^2\Sigma^+$) and OH($X^2\Pi$) with either Ar or He partner shows that each respective rare gas system have similar degrees of attractive and repulsive character.[18, 44, 46-48] It therefore might be expected that the depolarisation cross-sections be similar, but this is

not the case. One major difference between the two molecules is their rotational energy spacings, which are much larger for OH($X^2\Pi$) *versus* NO($A^2\Sigma^+$). Consequently, elastic scattering is much more prominent in OH($X^2\Pi$) relative to NO($A^2\Sigma^+$).[18, 44, 46-48]

Brouard and co-workers have also evaluated the state-specific quenching and collisional depolarisation of rotational alignment of superthermal OH($A^2\Sigma^+$) by H_2O.[107] For the lowest rotational levels studied, the total depolarisation cross-sections were found to approach 100 $Å^2$, which is only slightly slower than the high-temperature RET cross-sections cited in their work. Overall, depolarisation was shown to be a dominant process.[107]

1.7.3 Stimulated Raman Pumping (SRP)

This is a non-linear optical preparation technique that employs a pump and dump laser set-up to generate a polarised rotational distribution in the ground electronic state.[80-82, 108-110] The two lasers differ in frequencies corresponding to the energy gap of the transition, but as with all Raman experiments, are not resonant with any allowed spectroscopic transition. The prepared level can then be monitored using a standard optical probe technique in an OODR set-up. Sitz and Farrow employed this method alongside [2+2]-REMPI detection (see Section 1.7.6) to prepare and probe a rotational alignment in $N_2(v = 1, j)$ self-collisions.[111, 112] Collisional depolarisation was indicated to be relatively slow compared with population removal. Substantial alignment was also preserved in state-to-state RET, inconsistent with the $\Delta m = 0$ propensity proposed by other authors.

Zacharias and co-workers implemented SRP to prepare separately oriented and aligned samples of $C_2H_2(\tilde{X}^1\Sigma_g^+, v_2 = 1, j)$ and then probed the elastic and inelastic evolution in self-collisions and in collisions with Ar using LIF.[80-82, 108-110] The measurements were well-described by a simple set of master equations, and the resulting rate constants compared favourably with theoretical calculations. The orientation and alignment decays were determined to be efficient processes, with no statistical difference between the two, although both declined with increasing j and were slower than the observed depopulation. The amount of rotational anisotropy that remained after an inelastic collision was found to depend on the value of $|\Delta j|$, although generally a significant amount was retained, even for large changes in the rotational angular momentum.

Around 80% of the inelastically scattered molecules underwent a change in the direction of the rotational angular momentum vector of less than 40^o, and nearly 50% of such molecules changed their direction by less than 20^o. Ultimately, the $\Delta m = 0$ rule was again found to be inconsistent with the observed results, and instead a model with an unrestricted change in m was proposed, where collisions perpendicular to the plane of rotation destroy the polarisation, while collisions in the plane result in RET.

1.7.4 Polarisation Spectroscopy (PS)

This is a third-order non-linear technique originally developed as a variant of high-resolution saturation spectroscopy and utilised as an analytical tool in flame and combustion research.[113-122] Three laser pulses interact through the third-order linear suceptibility, $\chi^{(3)}$, of the optical medium to generate a fourth signal wave.[123-125] Two spectroscopically resonant pump photons create a spatially uniform polarisation in the upper and lower levels. A probe beam then interacts with this prepared polarisation to generate a signal beam that travels along the probe direction. The component of the signal beam that is orthogonally polarised relative to the probe beam is separated *via* a linear polariser and subsequently detected. The observed PS signal depends on the bulk polarisation of the sample, and so varying the time delay between the pump and probe pulses allows the collisional evolution of the pump-induced polarisation to be monitored.

McKendrick and co-workers measured the bulk removal of rotational orientation and alignment in OH($X^2\Pi_{3/2}$, $v = 0$, $j = 1.5 – 6.5$, e) and OH($A^2\Sigma^+$, $v = 1$, $N = 1– 5$, f_1) in collisions with simple atomic and molecular partners using one-colour and two-colour polarisation spectroscopy (OCPS and TCPS, respectively).[3, 48, 124, 126-133] In OCPS, both the pump and probe beams are split from the same laser, whereas in TCPS the beams come from two separate lasers, allowing for better control of the laser timings and isolated quantum states to be studied.[3] The OH($X^2\Pi$) TCPS signal decay was investigated for a number of collision partners, namely He, Ar, Xe, N_2 and O_2. The atomic colliders were also compared to full QS calculations. For all species, the alignment depolarisation cross-sections were almost always twice as fast as the orientation depolarisation. The elastic depolarisation efficiencies for Ar and Xe were similar, in the region of ~20 $Å^2$, significantly faster than He. The total removal of the TCPS signal with the rare gases increased from Xe > Ar > He, consistent with the PESs

becoming progressively more anisotropic at longer range. However, the QS predictions revealed that the PESs overestimated the elastic depolarisation, with the largest discrepencies at low *j*. Competition between elastic depolarisation and Λ-doublet transfer was also exposed, which was explained qualitatively through the ranges of the even and odd expansion terms of the PESs. Overall, the V_{dif} potential was believed to play an important role in the elastic depolarisation dynamics. Out of the molecular colliders, N_2 was found to be more effective than O_2 at removing the prepared polarisation. Such behaviour has also been observed during inelastic spectroscopic line-broadening experiments by other authors.[134, 135]

The OH($A^2\Sigma^+$)+Rg rate constants were of similar magnitude to OH($X^2\Pi$)+Rg at low *j*, reflecting that the PESs of the two electronic states have comparable ranges. However, as *j* increased, the OH($A^2\Sigma^+$) rate constants were progressively larger than for OH($X^2\Pi$). Elastic depolarisation in OH($A^2\Sigma^+$)+Ar was insensitive to the initial *N* over the range $N = 1 - 10$ and shown to be a significant process, with removal of rotational alignment generally being faster than for orientation, although this was not the case for He. There was very good agreement between ZQBS results and QCT calculations.

McKendrick and co-workers extended their use of the PS experiment to investigate collisional depolarisation in NO($X^2\Pi$, $v = 0$, j, F_1e)+Ar and compared them to new QS calculations.[136] Experiment and theory agreed qualitatively with the *j*-dependence, however the predicted *K*-dependence was not observed. Elastic depolarisation was concluded to be a minor process in this collision system compared to the electronically similar OH($X^2\Pi$)+Ar.

Huennekens and co-workers incorporated a two-step PS-OODR fluorescence experiment in a heated pipe oven to gain information on the fate of population and orientation in NaK($A^1\Sigma^+$, $v = 16$, $j = 30$)+Ar and K.[137] Fitting their results to a rate equation model showed that collisions of NaK with K were more likely to transfer population and destroy orientation than collisions with Ar. Collisions with Ar exhibited a strong Δj = even propensity, alluding to interferences from the near-homonuclear symmetry of the system. Collisions with K had no such propensity, but instead a preference for Δj = positive over Δj = negative. As well as NaK($A^1\Sigma^+$)+K being strongly attractive and reactive compared to its Ar counterpart, this was suggested to be an effect of the non-zero angular momentum of the potassium atom's loosly bound outer valence

electron, and the difference in polarisabilities and molecule/atom mass ratios between the K and Ar systems.

In the late 1980s, Field and co-workers developed *polarisation-transient gain spectroscopy (PTGS).*[138] Here, after pulsed laser pumping, a single mode cw-dye laser probes the population and net spatial anisotropy of an excited state *via* stimulated emission to the ground state. This technique was implemented in elastic and inelastic depolarisation measurements of formaldehyde self-relaxation. Elastic depolarisation was observed to be far less efficient than any other collision-induced pathway and there was accordingly a tendancy to conserve the rotational anisotropy during collisional energy transfer, indicating a strong Δm propensity rule. These results were rationalised in terms of parity restrictions associated with intermolecular dipole-dipole interactions.

McCaffery and co-workers applied TCPS using circularly polarised cw-pump and linearly polarised cw-probe lasers to measure rotationally inelastic differential cross-sections in collisions of alkali dimers with rare gases, namely $Li_2(X^1\Sigma_g^+)$+Ar, Xe and $Na_2(X^1\Sigma_g^+)$+Ar, Xe. This technique was termed *velocity-selected laser polarisation spectroscopy (VSLP).*[139, 140] A narrow band tunable dye laser was used to excite and rotationally orient a velocity sub-group from a thermal sample, which was then probed with a second narrow-band dye laser using TCPS. The pump and probe transitions shared a common lower level[125] and detection was sensitive only to molecules carrying the polarisation label imparted to the parent level. The two alkali dimers exhibited strikingly different dynamics from one another. For Na_2, rainbow scattering was dominant in rotationally resolved transitions, characteristic of interactions at the anisotropic repulsive wall of the intermolecular potential. However, Li_2 showed evidence of long-lived Li_2-Li complex formation followed by mode-specific dissociation. All cases proceeded with some retention of molecular orientation from the initially polarised level.

1.7.5 Four Wave Mixing (FWM)

This technique is conceptually very similar to polarisation spectroscopy, but with some detail changes. It is again a non-linear method in which three laser pulses interact through the third-order non-linear susceptibility, $\chi^{(3)}$, of the optical medium to generate a fourth signal wave.[19, 123] However, the difference with FWM is in the physical

arrangement of the beams. Here, the pump photons come from two separate beams that cross at an accute angle, creating optical gratings of the population and polarisation dependent on the wavelength of the photons and the crossing-angle. This results in a polarisation of the upper and lower levels that is spatially non-uniform. The signal beam scatters in a discrete direction from the optical gratings prepared by the pump photons. Unfortunately, the gratings are destroyed on a ns-timescale by physical diffusion of the molecules from the interaction region, limiting this spectroscopic technique to faster pulsed laser systems.

1.7.6 Resonance Enhanced Multi-Photon Ionisation (REMPI)

This detection method implements stepwise resonance excitation of an atom or molecule *via* an intermediate spectroscopic level using *n* photons, preserving the initial velocity and spatial anisotropy. This is then followed by a *m* photon ionisation step, and is hence labelled [*n*+*m*]-REMPI. A prime on the ionisation step indicates that the ionisation photon is of a different frequency to the resonance photon, for example [1+1′]-REMPI at 226 nm + 308 nm. This technique is often used in conjunction with other detection methods, such as velocity map imaging (see Section 1.7.7).

McBane and co-workers incorporated [2+1]-REMPI detection in their CMB state-to-state RET experiments of $CO(X^1\Sigma^+)$ and $NO(X^2\Pi)$ colliding with rare gases, in some cases along with complementary IR-OODR measurements.[24, 25, 141-145] Their data were compared to complete master equation and energy gap law fitting. In all cases, marked parity-dependent oscillations in the Δj cross-sections were observed and related to the near-symmetry of the interaction potentials in the near-homonuclear limit. In earlier experiments, Zhang and co-workers resolved the rotational orientation in thermal collisions of $CO(A^1\Pi)$+He using OODR-REMPI. There was a propensity of increasing depolarisation with increasing Δj and decreasing initial j. The extent of depolarisation was asymmetric with respect to $\pm\Delta j$. The results were discussed in light of then-recent advances in quantum scattering theory.[56, 146]

1.7.7 Velocity Map Imaging (VMI)

Precision measurements of DCSs require full quantum state resolution. One recent approach to this problem is to apply REMPI-VMI detection,[147] where ionisation of the

post-collision product proceeds through a stable resonant intermediate to provide spectroscopic state resolution. The probe laser polarisation in the REMPI process also provides sensitivity to the rotational anisotropy of the scattered molecules. The resulting ion is accelerated and focussed through a set of ion optics at right angles to the scattering plane, formed from carefully controlled electric fields, towards a two-dimensional position-sensitive detector, where an image is then taken, usually with a CCD camera. The location of an ion in the image depends purely on its velocity, providing full state resolved correlation of the nuclear motions within the scattering plane. Importantly, for the context of this work, it is possible to determine the rotational angular momentum polarisation of the scattered molecules as a function of the scattering angle for individual product states.[6]

Chandler and co-workers applied the REMPI-VMI detection technique to CMB studies of RET in NO($X^2\Pi_{1/2}$, v = 0, j = 1/2, f)+Ar,[148, 149] with equal population of both Λ-doublets. Experiments with linear probe polarisations showed a strong product rotational alignment, with a striking scattering angle dependence. Small Δj transitions exhibited mainly forward scattering, with the product rotational angular momentum, j', tending to be parallel to the product velocity direction, v', ('propeller' motion), whereas larger Δj transitions were more backward scattered, with j' tending to be perpendicular to v' ('frisbee' motion). These results were in general agreement with QS calculations, although there was a slight over-prediction of the backward scattered alignment. Experiments performed with circular probe polarisations showed that the sense of product rotation switched between clockwise and anti-clockwise as a function of Δj and scattering angle, again reproduced by QS calculations.[148]

Very recently, Chandler and co-workers employed [1+1′]-REMPI with VMI detection to measure rotationally inelastic DCSs of excited state NO($A^2\Sigma^+$, v = 0, N = 0, j = 0.5) colliding with He, Ar and Ne.[150-152] The images and DCSs for NO($A^2\Sigma^+$)+He and Ar, ΔN = +2, +7 and +14, state-to-state RET illustrated the commonly observed shift from a tendancy for low-angle scattering for low ΔN to large-angle scattering for high ΔN. Comparison to QS predictions showed experiment and theory to agree well for NO($A^2\Sigma^+$)+He, but the experiments did not reproduce the degree of forward scattering predicted by theory for NO($A^2\Sigma^+$)+Ar. Scattering was shown to create collision-induced rotational alignment in the NO($A^2\Sigma^+$) products, which was discriminated by comparing images obtained using orthogonal linear probe polarisations. In contrast to scattering of

the NO($X^2\Pi$) state, which is well reproduced by rigid shell models, the NO($A^2\Sigma^+$)+Ne rotational alignment was found to have strong oscillatory behaviour in the forward hemisphere that was not predicted by classical rigid body models. Full QS calculations on the other hand were able to qualitatively reproduce the observed alignment, which was suggested to arise from 'soft' repulsive interactions in this excited state-Rg interaction.

In a conceptually similar set of experiments, Aoiz, Brouard, Stolte and co-workers utilised the hexapole state-selection method (introduced in Section 1.7.1) to prepare a single Λ-doublet level, NO($X^2\Pi$, j = 0.5 *e* or *f*) before collisions with Ar, He or D_2.[34-36, 153-158] In some cases, both spin-orbit conserving and changing collisions were also resolved. The DCSs of the fully state-selected NO again exhibited forward scattering for low Δj transitions and increasingly backwards scattering for high Δj transitions. A crucial result of these experiments, however, was that the observed DSCs depend sensitively on the rotational parity of the final level, as scattering into the two different product Λ-doublet levels of the same j' gave remarkably different DCSs. This cannot be an energetic effect, as the energy gap between the two Λ-doublet levels is much smaller than that between successive rotational levels and the collision energy of the system.

The rotational parity dependence is further exemplified by the intriguing results that the measured DCSs for scattering into neighbouring product states with the same rotational parity, p, and numbering index, n, were found to be nearly identical. The parity-changing transitions (n = odd) were shown to occur at larger scattering angles than parity-conserving transitions (n = even).[36] Here, n takes the form:

$$n = j' - \frac{\varepsilon\varepsilon'}{2}$$

Equation 1.72

Quantum scattering calculations were in quantitive agreement with the experimental observations and showed that the scattering distributions result from different partial cross-sections (cross-section as a function of total angular momentum, J), and scattering from the same range of total-J gives rise to different DCSs for each parity of the same j'. The number of peaks in the Λ-doublet resolved DCSs were directly linked to specific radial expansion terms in the interaction potential and reflect the near-homonuclearity of NO.[156]

Stolte and co-workers also turned to the QQT model to help rationalise their results.[34] The predicted shape of the DCS in this model depends on a Legendre polynomial of order $j' - (\varepsilon\varepsilon')/2$. As such, transitions into j' levels with the same value of n, termed '*parity pairs*', are determined by the same Legendre polynomial and hence exhibit similarly shaped DCSs. As outlined in Section 1.6.1, the QQT model treats the scattering as defined by classical rigid ellipse-rigid sphere kinematics on a purely repulsive PES, with quantum interferences between paths from different impact points on the ellipse that lead to the same j' and scattering angle, with conservation of angular momentum along the kinematic apse, $\hat{a}_k$. It was demonstrated that interferences between trajectories from impacts at the opposite ends of the ellipse lead to parity-changing transitions, whereas interference between end-on and side-on trajectories leads to parity conserving transitions.

The hexapole state selection method was additionally utilised by Stolte and co-workers in conjunction with Stark-induced focusing of the NO($X^2\Pi$) molecules within a homogeneous electrostatic field. This resulted in spatially oriented NO($X^2\Pi$) molecules, allowing for discrimination between collisions with rare gas atoms that occur at the N-end of the molecule or the O-end.[34, 36] The results revealed a remarkable alternation in the sign of the steric asymmetry between even and odd Δj transitions. QQT modeling again attributed the oscillations to quantum interferences between different orientations of the repulsive potential, due to phase differences between scattering from the two ends of the NO molecule.

1.8 Previous Work on the CN Radical

1.8.1 ICN Photodissociation

In this work, CN($X^2\Sigma^+$) is generated from the photolysis of ICN at 266 nm on the $\tilde{A} \leftarrow \tilde{X}$ band, followed by optical pumping to CN($A^2\Pi$). Cyanogen iodide, ICN, is a linear triatomic molecule with a vapour pressure of ~1 Torr and an I-CN bond dissociation energy of 26980 ± 100 cm^{-1}.[159] The ultraviolet (UV) photodissociation of ICN is a prototype of multiple surface dissociation dynamics and displays remarkable complexity.[159, 160] Photolysis at 266 nm produces CN($X^2\Sigma^+$) with a bimodal limiting translational anisotropy of β = 1.3 and 1.6, with corresponding initial speed components

of ~1400 m s^{-1} and ~2800 m s^{-1}.[161] These arise from two coincident spin-orbit iodine channels – ground state I($^2P_{3/2}$), termed *I*, and excited state I($^2P_{1/2}$), termed *I**, respectively, with a spin-orbit splitting of 7603 cm^{-1} and an *I*/*I** branching ratio of ~2/3. The CN($X^2\Sigma^+$) emerges vibrationally cold, with < 2% of the distribution from 266 nm dissociation populating the $v = 1$ and $v = 2$ levels.[162-164]

The ICN Ã band continuum extends from ~210 nm to ~320 nm, centering around 260 nm, and encompasses several optically bright states. *Ab initio* calculations by Amamatsu *et al*. showed that three of these states become important at 266 nm: $^3\Pi_{0+}(A')$, $^1\Pi_1$ and $^3\Pi_1$, respectively, each of which are bent in the Franck-Condon region, lifting the degeneracy of the $|\Omega| = 1$ levels.[159, 165, 166] The $^3\Pi_{0+}(A')$ state correlates diabatically to the *I**-channel and is populated by a parallel transition from the linear $\tilde{X}^1\Sigma^+$ ground state. The $^1\Pi_1$ and $^3\Pi_1$ states split into A' and A'' components and are populated by weaker perpendicular transitions that correlate diabatically with the ground state *I*-product. A conical intersection exists between the $^1\Pi_1(A')$ and $^3\Pi_{0+}(A')$ states outside of the Franck-Condon region, with the ICN bending angle playing an important role in the probability of curve crossing.[162] The CN product formed in coincidence with the *I*-channel may therefore be formed by excitation to any of these three excited state surfaces, however CN formed in conjunction with *I** can arise only from the two A' surfaces.[167] The relevant $^1\Pi_1(A')$ and $^3\Pi_{0+}(A')$ surfaces are shown in Figure 1.19.[168]

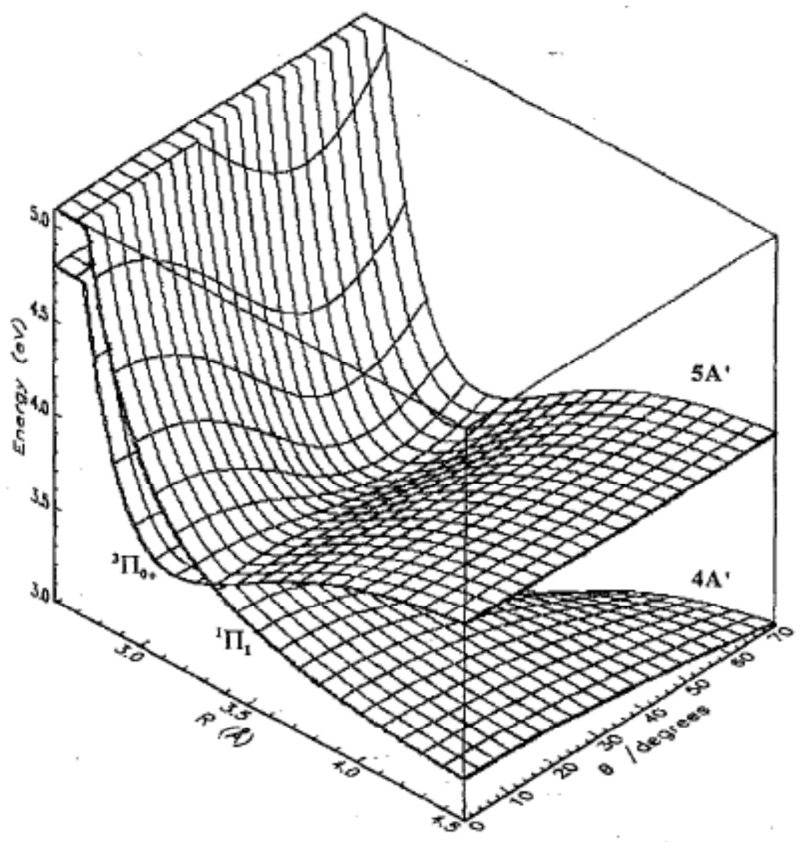

Figure 1.19 – A three-dimensional plot of the $^1\Pi_1(A')$ and $^3\Pi_{0+}(A')$ surfaces of ICN. Adapted from reference 168.

The CN product state distributions change substantially with photolysis wavelength, but exhibit little temperature dependence.[159] Hotter parent ICN generally leads to increasing *I**-branching and preferentially populates higher rotational states of CN, becoming more pronounced at longer photolysis wavelengths. The CN($X^2\Sigma^+$, v = 0, N'') rotational distributions from the 266 nm photolysis of 300 K ICN are shown in Figure 1.20, where a clear non-statistical multimodality is evident. Nadler *et al*. suggested that the overall N'' distribution from the *I*-channel is characteristic of dissociation from a nearly linear minimum energy pathway and that the lack of low N'' populations is indicative of a significant force that drives the nuclei towards a bent geometry during the rapid dissociation.[169] Spin-rotation resolved measurements of CN revealed the f_1 and f_2 components to oscillate with increasing N'', which has been attributed to interferences in the multiple surface dissociation.[159]

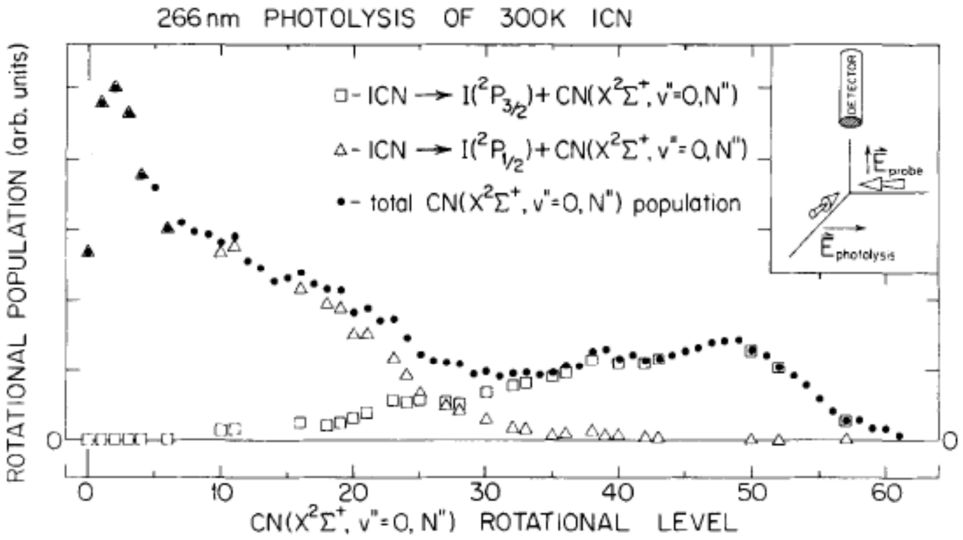

Figure 1.20 – Nascent CN($X^2\Sigma^+$, v = 0, N'') rotational distributions for the I and I product channels following the 266 nm photodissociation of 300 K ICN. Adapted from reference 169.*

Vector measurements of the dissociation indicate mixed parallel and perpendicular transitions. The velocity anisotropy shows a predominantly parallel nature, with the *I** channel generally closer to the limit of pure parallel dissociation, peaking at $\beta = 1.84$ for $N = 0$.[159] Rotational anisotropy measurements of the CN photofragments also point to mixed parallel and perpendicular absorption.[159] Low rotational motion emerges principally along the *I** exit channel and exhibits a negative alignment, where the rotational axis lies perpendicular to the photolysis polarisation direction, mediated by an almost pure A' origin.[159] However, this alignment diminishes towards zero for higher rotational levels, due to increasing A'' contributions from the *I*-channel.

Fragmentation of ICN with circularly polarised light produces a large velocity-dependent CN orientation in $v = 0$, which varies in both both sign and magnitude with product rotation, and more subtly with spin-rotation label, broadly following the rotational state dependence of the *I*/*I** branching ratio.[167] The orientation generally increases with CN rotational quantum number and is of opposite sign for the two *I* and *I** product channels. For the *I*-coincident channel below $N'' \approx 40$, the f_2 spin-rotation manifold is notably more oriented than the f_1 manifold. Furthermore, the orientation is distributed alternately parallel and anti-parallel to the angular momentum vector of the light as the product total angular momentum increases. This effect has again been accredited to quantum interferences between the different PESs leading to the same photoproducts. The CN orientation shows a marked vibrational dependence, being

considerably smaller in v = 1 and even changing sign in v = 2. Moreover, the orientation alternates as a function of spin-rotation manifold in the v = 2 level.[170]

Using the Doppler-resolved FMS technique, Costen and Hall have investigated the the coherent, γ_1, and incoherent, α_1, components of the CN orientation along the circularly polarised propagation axis.[167] These two components are characterised by their molecular frame axial ($\sin^2\theta_k$) and equatorial ($\cos^2\theta_k$) variation with the recoil direction, θ_k, respectively.[167] The orientation was observed to occur exclusively along the axial direction, alluding to a coherent dissociation mechanism. At high CN rotation (N'' > 5.5), this coherent orientation was shown to vary as a function of N'' and with photolysis wavelength, and again was of opposite sign for the different spin-orbit states of the coincident *I*-atom.[167] In a separate study, Costen and Hall also measured nuclear hyperfine quantum beats for the orientation and alignment of low-N'' CN($X^2\Sigma^+$) following UV photodissociation. They concluded that the electron spin cannot be viewed as a spectator during depolarisation of the photolytically generated rotational anisotropy.[171]

The non-statistical rotational distributions and diverse vectorial properties of CN($X^2\Sigma^+$) produced from the UV photofragmentation of ICN must be taken into account during polarisation-sensitive optical measurements of the CN radical. Specifically, they must be thermalised prior to experimentation in an isotropic collision environment, such as that presented in this thesis, in order to avoid signal-dependent correlations that could mask the desired dynamical information. Also, since the measurements in this thesis utilise the CN($A^2\Pi - X^2\Sigma^+$) (4,0) and (4,2) spectroscopic bands, the populations of these ground state vibrational levels should be considered during the experimental data analysis.

1.8.2 Collision Dynamics of the CN Radical

The CN radical is a prototypical candidate for studies of rotationally elastic and inelastic collisions, as it is amenable to both high level experiment and theory, with practical importance in many gas-phase environments. The two most important energy transfer processes relevant to CN are RET and EET, owing to the extensive overlap of the CN($A^2\Pi$) and CN($X^2\Sigma^+$) vibronic states, and to a lesser degree, the CN($B^2\Sigma^+$) state, as shown in Figure 1.21 and Figure 1.22.

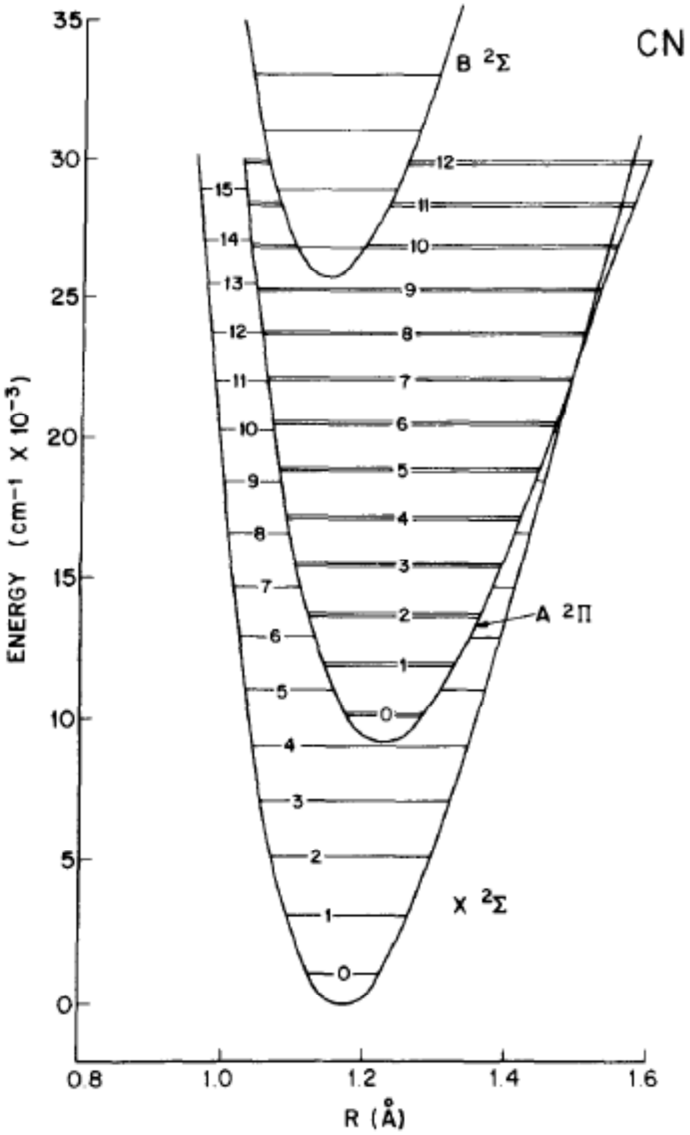

Figure 1.21 – Potential energy curves for the $X^2\Sigma^+$, $A^2\Pi$ and $B^2\Sigma^+$ states of CN. Adapted from reference 172.

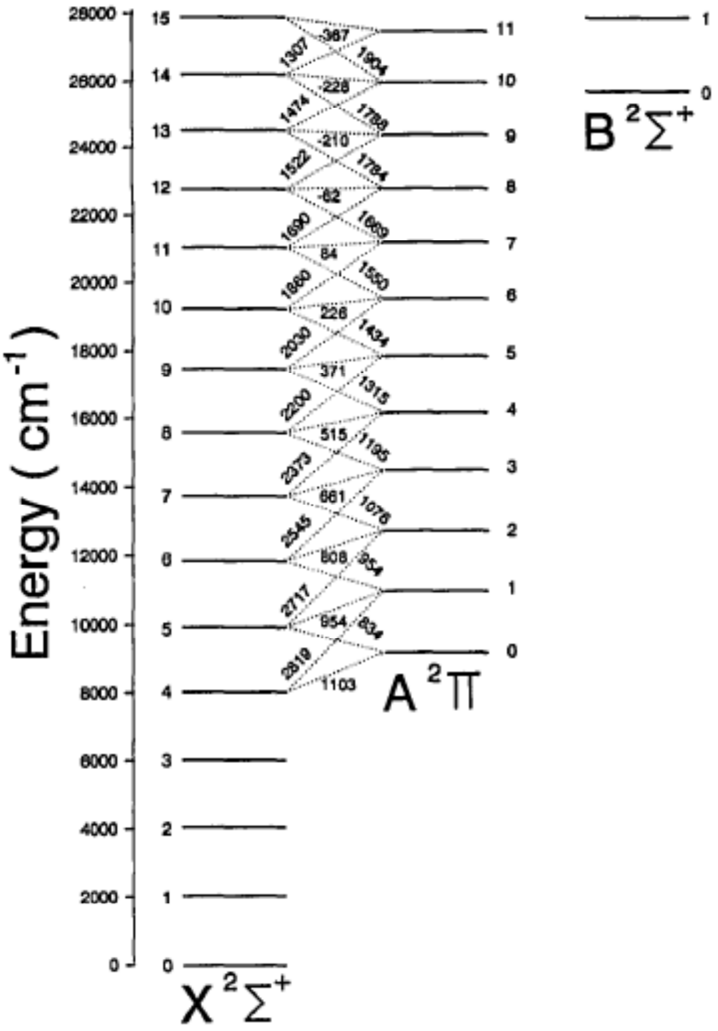

Figure 1.22 – Vibrational energy levels and energy spacings (in cm^{-1}) between the $X^2\Sigma^+$, $A^2\Pi$ and $B^2\Sigma^+$ electronic states of CN. Adapted from reference 110.

Several authors have determined the radiative lifetimes of CN($A^2\Pi$), both experimentally and theoretically, with the lifetime seen to decrease with increasing vibrational level. The radiative lifetimes of the $v' = 4$ level of CN($A^2\Pi$) are summarised in Table 1.4.

Table 1.4 – Radiative lifetimes of CN($A^2\Pi$, $v' = 4$). Adapted from reference 173.

τ_{rad} / μs	Method	Reference
3.83 ± 0.2	Expt.	173
4.70 ± 0.2	Expt.	174
2.5	Expt.	172
8	Expt.	175
3.98 ± 0.4	Expt.	176
6.58 ± 0.4	Expt.	177
7.25	Theory	178
7.2	Theory	179
5.3	Theory	180
6.9	Theory	181
7.2	Theory	182

Electronic Energy Transfer in CN + Rare Gases

As shown in Figure 1.21 and Figure 1.22, there is extensive overlap between the different vibronic manifolds of the CN $X^2\Sigma^+$ and $A^2\Pi$ states. As such, there exist near-degeneracies between rotational levels of the v_A and $v_X = v_A + 4$ manifolds.[183] Final rotational state specific A→X EET rate constants were found to be comparable to pure RET within CN($A^2\Pi$).[184] Two different mechanisms have been put forward to describe the collisional energy transfer between the different vibronic manifolds. The first is that electrostatic mixing of the two electronic states by approach of the collision partner facilitates EET.[185] The second proposed mechanism is termed the "*gateway*" model,[186] where transfer between the two electronic states is attributed to spectroscopic perturbations in the diatomic moiety. These perturbations sufficiently mix the two states such that collisions will allow EET transitions to borrow from the large cross-sections associated with rotationally inelastic scattering within a single electronic state.[1, 5, 183] However, these spectroscopic perturbations are weak, and so only those levels that happen to be nearly degenerate will mix adequately enough to serve as gateways between the two electronic states.

In the gateway model, the cross-section for collision-induced transitions, $\sigma_{Ej,E'j'}$, between specific initial and final rotational levels, j and j', in two different electronic states, E and E', respectively, can be expressed as:[76]

$$\sigma_{Ej,E'j'} \approx \sigma_{Ej,Ej'} C_{EE'}(j')^2 + \sigma_{E'j,E'j'} C_{EE'}(j)^2$$

Equation 1.73

where $\sigma_{Ej,Ej'}$ and $\sigma_{E'j,E'j'}$ are the cross-sections for pure collisional RET within the two respective electronic states, and $C_{EE'}(j')$ and $C_{EE'}(j)$ are the isolated-molecule E~E' mixing coefficients induced by the non-Born-Oppenheimer interactions.[76] Therefore, the magnitude of the cross-section for final rotational state specific EET is assumed to be equal to that for pure RET within the isolated electronic state reduced by the fractional mixing of the rotational level from the other electronic state.

To gauge the role of these mechanisms on EET, Dagdigian and co-workers performed experimental and theoretical investigations of state-resolved electronically inelastic collisions of CN($A^2\Pi$) with Ar and He.[183] The OODR-LIF technique was utilised to measure electronic transitions from low rotational levels of the v_A = 3, 7 and 8 vibronic manifolds.[184, 187-189] Here, the non-Born-Oppenheimer perturbations peak at around j = 13.5 F_1f, with the $X^2\Sigma^+$ character of the $A^2\Pi$ state reaching a maximum of 42.6%.[184] The final level rotational distributions displayed an even-odd alternation as a function of Δj for given fine-structure and Λ-doublet manifolds. This oscillation was attributed to the near-homonuclear nature of the CN($X^2\Sigma^+$, $A^2\Pi$) PESs, and in particular the V_1 coupling potential that mediates the A-X energy transfer. Unfortunately, in these studies, efficient non-perturbative electrostatic coupling and experimental difficulties masked any special role played by the perturbatively mixed gateway levels.

In another set of experiments, specific levels of CN($A^2\Pi$, v = 3, N = 60 – 63) were prepared by optical excitation, then product states collisionally populated by Ar and He in v_A = 3 and nearly isoenergetic v_X = 7 vibronic manifolds were probed using LIF. Crossing of the $A^2\Pi$ v = 3 F_1f rotational and fine-structure manifold with the $X^2\Sigma^+$ v = 7 F_2 levels at j = 62.5 acted as a gateway for collisional EET, as shown in Figure 1.23.[183]

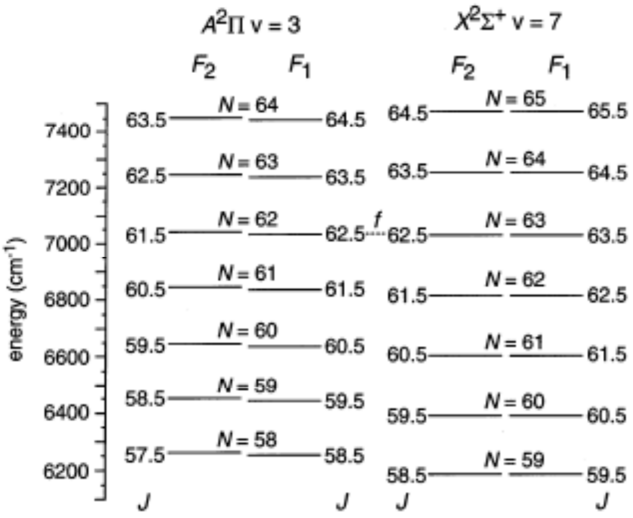

Figure 1.23 – An energy level diagram for the CN $A^2\Pi$ v = 3 and $X^2\Sigma^+$ v = 7 vibronic manifolds and their crossing at j = 62.5. Adapted from reference 183.

The even-odd Δ*j* oscillations observed for the low-*j* interelectronic energy transfer were not apparent in the high-*N* measurements, which was ascribed to the large rotational energy spacings and decreasing state-to-state transfer rate constants with increasing *N′*. Such a loss of alternation was also seen in high-*N* RET studies within CN($A^2\Pi$).[190] Overall, very good agreement was seen between experiment and QS calculations. In comparing the two colliders, Ar was much more efficient at inducing A→X transfer than He.[183] This points to the role of the V_1 coupling PES in enabling the EET, since the isolated diatom non-adiabatic mixing is independent of the identity of the collision partner. *Ab initio* calculations of the V_1 PES for each system accordingly showed that CN($X^2\Sigma^+$, $A^2\Pi$)-Ar has a considerably stronger coupling strength than CN($X^2\Sigma^+$, $A^2\Pi$)-He.[183] The authors concluded that both mechanisms have significance in collisional EET, where the relative importance of either depends on the extent of mixed electronic state character of the rotational levels involved.[183]

RET and Collisional Depolarisation in CN + Rare Gases

Fei *et al*. determined thermal RET cross-sections for collisions of CN($X^2\Sigma^+$, *v* = 2, *N*)+He and Ar *via* stimulated emission pumping and LIF probing.[191, 192] For He, the total removal cross-sections were found to decrease monotonically between *N* = 0 and *N* = 41 to around one third of their value at *N* = 0. Approximately two thirds of the total removal cross-sections for *N* = 2, 11 and 14 corresponded to changes in the rotational quantum number of $|\Delta N| \leq 3$, along with a strong propensity that favours changes in *N*

for $|\Delta N| \leq 4$. Overall, the total removal cross-sections for He were around half the size of those for Ar. The state-to-state cross-sections for both systems exhibited even-odd ΔN alternations, attributed to the near-homonuclear symmetry of CN. The sum of these state-to-state cross-sections agreed well with the total removal cross-sections and followed statistical power-gap and exponential energy-gap laws. The ΔN modulation was greater for Ar than He, suggestive of a more even and shorter range CN($X^2\Sigma^+$)-Ar interaction compared with CN($X^2\Sigma^+$)-He. Guo *et al*. measured the total and state-to-state RET and radiative lifetimes of CN($B^2\Sigma^+$, $v = 0$, $N = 0$, 4, 6, 7, 8, 11, 13)+He in a static cell.[193] They observed a weak propensity for odd jumps in N in the state-to-state RET for $N > 4$ and a modest variation with N_i for $0 \leq N_i \leq 19$.

The inelastic collision dynamics of the CN($A^2\Pi$)+Ar system has been the subject of several previous experimental and theoretical investigations by various research groups. The most relevant are those of Dagdigian and co-workers,[15, 190, 194] who, using OODR-LIF, measured fully state-resolved $jF\varepsilon \rightarrow j'F'\varepsilon'$ RET rate constants in the $v = 3$ vibrational state for both highly rotationally excited levels, at around $N = 60$, and levels near the peak of the thermalised Maxwell-Boltzmann distribution, around $j = 6.5$ F_1e. In 2000, Dagdigian and co-workers computed *ab initio* PESs for CN($X^2\Sigma^+$, $A^2\Pi$, $v = 3$)-Ar using the multireference configuration interaction (MCRI) method. These PESs are termed hereafter as the *Berning-Werner* or *B-W* PESs and their outline and detailed discussion with regards to the work in this thesis are deferred until Chapter 4. Dagdigian and co-workers then performed full close-coupled QS calculations on the appropriate diabatic PESs to calculate rate constants for rotationally inelastic scattering of CN($A^2\Pi$) with Ar.[15] These were compared to experimental state-to-state RET rate constants for a range of Δj out of $j = 6.5$ F_1e, $j = 6.5$ F_2e and $j = 7.5$ F_1f initial levels. Total removal RET rate constants from the initial levels were also recorded, showing an average value of $k_{pop} \approx 3.5 \times 10^{-10}$ cm^3 s^{-1}.[15]

The state-to-state rate constants showed a drop in magnitude with increasing Δj, attributed to the increasing ΔE energy gaps between the initial and final rotational levels. The final rotational distributions displayed an even-odd alternation as a function of Δj and fine-structure and Λ-doublet manifolds, with rotational parity conserving transitions favoured over parity changing transitions. This was ascribed to the near-homonuclear character of the CN-Ar interaction, which is clearly visible as near

forward-backwards symmetry in the PESs.[15] There was considerable probability for collision-induced change in the Λ-doublet symmetry label. Collisions within the F_1 fine-structure manifold saw roughly equal probability for *e*/*f* conservation and change, while within the F_2 manifold, the *e*/*f* changing transitions were somewhat less probable than *e*/*f* conserving transitions. Overall, there was a propensity to conserve the fine-structure label, the extent of which depended on the identity of the initial manifold – $F_2 \rightarrow F_1$ rate constants were around 80% the size of those for $F_2 \rightarrow F_2$, while $F_1 \rightarrow F_2$ were around 30% of $F_1 \rightarrow F_1$. These differences were explained in part by the fact that the F_1 manifold lies slightly lower in energy than the F_2 manifold. Within a Hund's case-(a) regime, spin-obit conserving transitions are mediated by the V_{sum} PES and spin-orbit changing transitions by the V_{dif} PES. The high probability for collision-induced changes in fine-structure label reflects the fact that the V_{dif} potential is significant compared to the V_{sum}.[15]

The experimental results were in good agreement with the QS calculations, suggesting that the repulsive core of the PESs is accurate. Recent spectroscopic studies by Heaven *et al.*[195, 196] on the CN($A^2\Pi$)-Ar van der Waals complex (discussed in greater detail below) confirmed that the general form of the B-W PESs are correct, with a T-shaped minimum. However, they suggested a dissociation energy of 125 cm^{-1}, substantially deeper than the calculated B-W V_{sum} well-depth of 75 cm^{-1}, meaning the PESs understate the attractive forces of the system. Subsquent empirical scaling of the PESs to reproduce the observed spectroscopy gave a modified well-depth of 138 cm^{-1}.

Dagdigian and co-workers have also studied collisions of highly rotationally excited CN($A^2\Pi$, v = 3, N = 60) with Ar.[190] They observed rate constants that were of significant magnitude only for a very small number of final states, due to the more widely spaced rotational ladders. The commonly observed ΔN oscillations were not seen at high N, presumably because of the rapid decrease in the rate constants with $|\Delta N|$. They also measured dramatic Λ-doublet propensities that depended on the reflection symmetries of the initial and final rotational levels, a common phenomenon for Hund's case-(b) molecules in Π electronic states.[52] Specifically, the rate constants for ΔN = -1 fine-structure conserving, Λ-doublet changing ($F_1f \rightarrow F_1e$ and $F_2e \rightarrow F_2f$) transitions were significantly larger than the corresponding fine-structure conserving, Λ-doublet conserving rate constants. The QS calculations attributed this to variations in the magnitude of the potential couplings between the different levels. Examination of the

partial cross-sections showed that these propensities arise from a "*helicopter*" orientation of approach, where the Ar approaches the CN plane of rotation perpendicular to the more attractive A' PES, followed by curve crossing to the A'' PES, correlating with different rotational asymptotes.

In contrast to Ar, when Dagdigian and co-workers extended their studies of highly rotationally excited species to CN($A^2\Pi$, v = 3, N = 60 – 62)+He, they revealed propensities to conserve *both* the fine-structure and Λ-doublet labels during state-to-state RET.[197] This difference in behaviour was credited to differences in the PESs of the two systems. The CN-He PESs are not sufficiently attractive to allow for facile crossings between the effective potential energy curves correlating to different rotational asymptotes. This demonstrates the importance of the interaction energies in determining the final fine-structure and Λ-doublet populations. The CN($A^2\Pi$)+He rate constants did not show a monotonic decline with ΔN, which could result from subtle differences between scattering on the two (A' and A'') PESs.[197] The total population removal rate constant from N = 62 F_1f was found to be around 20% larger than for the other N = 62 levels. This enhanced value was attributed to the N = 62 F_1f acting as a spectroscopic gateway facilitating CN $A^2\Pi \rightarrow X^2\Sigma^+$ EET, as discussed earlier in this section.

Previous work in our group utilised the FMS technique in a multi-pass optical set-up to probe the scalar and vector properties of the CN radical in both the $X^2\Sigma^+$ and $A^2\Pi$ electronic states with various atomic and molecular collision partners.[63, 64, 161, 198] Discussion of the molecular colliders is left until later in this section. FM Doppler profiles were acquired in different experimental geometries in order to isolate different speed, translational and rotational anisotropy signal components. Polarised photodissociation of ICN at 266 nm produced CN($X^2\Sigma^+$) radicals with a bimodal velocity distribution and well-defined rotational angular momentum distribution, as discussed in Section 1.8.1. The transfer of rotational and translational energy in nascent CN($X^2\Sigma^+$, v'' = 0, j = 0.5 F_1 and j = 27.5 F_1) colliding with Ar was dominated by backward scattering.[161] The initial photolytic speed distribution disappeared rapidly, over which time the large and positive translational anisotropy (***z*.v**) was maintained. The initial **v.*j*** (velocity and rotational angular momentum) correlation was close to the -0.5 limit, reflecting the perpendicular relationship of these vectors from a prompt triatomic photodissociation. The initial ***z*.*j*** correlation (laboratory-frame rotational

alignment) ≈ -0.3, representing a preference for ***j*** to be perpendicular to ***z***. The He collision partner displayed a different velocity distribution, where the initial speed relaxed much more slowly than for Ar. The translational anisotropy for collisions with He was also maintained for the fast component of the initial speed distribution, but a large positive anisotropy persisted for the slow speed component, even as it slowed further, although there was a positive correlation between speed and anisotropy. The differences between the Ar and He partners were attrubuted to differences in the CN($X^2\Sigma^+$) interaction potentials and are indicative of kinematic influences on the collision dynamics.[161]

Using the same experimental set-up, differential cross-sections (DCSs) for CN($A^2\Pi$, v' = 4)+Ar were measured.[64] Saturated optical pumping of nascent CN($X^2\Sigma^+$, v'' = 0) transferred the initial speed distribution without distortion to selected low j states of CN($A^2\Pi$, v' = 4). The products of RET within this upper vibronic manifold into j' = 0.5 F_2f (which cannot be rotationally aligned) were then probed using FMS. In all cases, the DCSs peaked in the forward direction, but also showed a clear trend towards sideways and backwards scattering for larger Δj, consistent with standard scattering theory.[64] Using the computed B-W potential anisotropy and a mean collision energy of 1720 cm^{-1}, a classical rotational rainbow of $\theta_R \approx 10^o$ was calculated for Δj = 3, which was the largest rotational AM transfer reported.[64]

The efficiencies of state and velocity-changing collisions of superthermal CN($A^2\Pi$, v' = 4, j = 0.5 F_2f) with He, Ar, N_2 and O_2 were also measured using the multi-pass FMS set-up.[198] The molecular partners will be addressed later. The second-order total removal cross-sections for the Ar collider was almost twice that measured for He (53 ± 3 $Å^2$ for Ar *vs*. 29 ± 1 $Å^2$ for He). The cross-section for He was in close agreement to the classical turning point of ≈ 3 Å from the *ab initio* CN($A^2\Pi$)-He PESs of Werner and co-workers,[13, 15] suggesting a purely repulsive interaction. The cross-section for Ar corresponds to a collision radius of ≈ 4.1 Å, which coincides closely with the location of the attractive minimum of the V_{sum} B-W CN($A^2\Pi$)-Ar potential.[15] The observed total removal cross-sections are therefore consistent with attractive forces contributing significantly for CN($A^2\Pi$)+Ar, compared to a substantially more repulsive CN($A^2\Pi$)+He system. Elastic scattering was concluded to occur almost exclusively in the forward hemisphere, and in all cases dominated by the long-range isotropic part of the interaction potential.[198]

Lastly in our group, the FMS technique was used in a multi-pass set-up for a preliminary study of the collisional loss and transfer of population and alignment in translationally thermalised CN($A^2\Pi$, v = 4)+Ar.[199] Rapid removal of both population and alignment was observed, with rate constants for both in the order of 10^{-10} cm^3 s^{-1} for j = 1.5 – 6.5, declining with increasing j and reaching zero for j = 23.5. This is surprising for a system with a relatively heavy rotor and modest attractive forces, and was suggested to be a result of the multiple PESs in the system.[12] There was good overall agreement between the experimental RET results and the QS theory of Alexander *et al*. for CN($A^2\Pi$, v = 3)-Ar.[15] Conversion of the population removal rate constants, k_{pop}, to thermally averaged cross-sections yielded $\sigma_{pop} \approx 62$ Å^2 for low-j, decreasing to ~41 Å^2 for j = 23.5. This implies a CN($A^2\Pi$)+Ar collision radius of ≈ 4.4 Å for the lowest j levels, which compares favourably with the previous results and the average attractive range of the B-W CN($A^2\Pi$)-Ar PESs,[15] but is considerably larger than that defined by the the repulsive core of the PESs. The alignment elastic depolarisation rate constants gave cross-sections of $\sigma_{dep}^{(2)} \approx 18$ Å^2 for low-j, indicating that most elastic collisions are not m-changing and instead points to a restricted change of Δm, where from a classical view point the rotor becomes harder to tilt as the angular momentum increases. Since the B-W V_{dif} CN($A^2\Pi$)-Ar potential has significant magnitude in the range of the V_{sum} attractive minimum, and the state-to-state RET cross-sections for spin-orbit transitions from Alexander *et al*.[15] were of similar size to spin-orbit changing transitions, it was speculated that the V_{dif} PES plays an important role in the elastic depolarisation of CN($A^2\Pi$) by Ar.[199]

The state-to-state population transfer rate constants ranged between $k_{j\rightarrow j'}^{(0)} \approx 1 - 3 \times 10^{-11}$ cm^3 s^{-1} for $\Delta j = \pm 3$ and decreased in magnitude with increasing Δj as a result of energy and linear-to-angular momentum restrictions. These results again agree well with those of Alexander *et al*.[15] There was substantial depolarisation of the transferred population out of j = 6.5 F_1e for the small range of Δj probed, with alignment multipole transfer efficiencies (MTEs) ranging from $E^{(2)}(j,j') = 0.55 \pm 0.066$ for Δj = -1 to $E^{(2)}(j,j') = 0.32 \pm 0.08$ for Δj = +3. This means that the product alignments were ~30 – 55% of the initial level. Conversion of the MTEs to a classical tilt angle gave $\theta_{jj'} = (33 \pm 3)^o$ for Δj = -1 and $\theta_{jj'} = (42 \pm 3)^o$ for Δj = +3, which shows a large change in direction of j during RET and implies that the magnitude of orbital angular momentum transferred in the collision is significant compared to the relatively low rotational angular momentum. Simple

vector analysis revealed the transferred orbital angular momentum to be consistent with a small $k.k'$ scattering angle, suggestive of strong forward scattering for small Δj.[199]

CN van der Waals Complexes

Spectroscopic studies of van der Waals complexes enable experimental exploration of the bound regions of interaction potentials. Additionally, observations of complex predissociation dynamics provide a complementary half-collision view of energy transfer pathways.[195] Predissociation of CN($A^2\Pi$)-*M* complexes (where *M* is the complexation partner, such as a rare gas) can be broken down into four distinct categories.[200] Firstly, spin-orbit (Ω) selected CN($A^2\Pi_\Omega$, v)-*M* complexes can dissociate into fragments of the other spin-orbit label, CN($A^2\Pi_\Omega$, v)+*M*. This is termed *spin-orbit* or *non-adiabatic predissociation* and is a relatively fast process enabled by the V_{dif} PES. *Electronic predissociation* is comparatively slower, where CN($A^2\Pi$)-*M* breaks apart to form CN($X^2\Sigma^+$)+*M*. This is mediated *via* the V_1 coupling PES. Complexes of high-j or N generally dissociate by transforming the rotational energy into the kinetic energy of the recoiling products. This process is known as *rotational predissociation*, and means that complexes populating higher diatomic rotational levels predissociate much faster than those in lower levels. Lastly, *vibrational predissocitation* can take place, where a complex of CN($A^2\Pi$, v') decays to release CN($A^2\Pi$, low v).

Heaven and co-workers utilised pump-probe spectroscopic techniques to characterise CN($A^2\Pi_{3/2}$, v = 3) and CN($X^2\Sigma^+$) fragments from the direct photodissociation and predissociation of CN($A^2\Pi$)-Ar.[195] The latter process showed a marked preference to populate positive parity diatomic rotational levels, related to the near-symmetry of the interaction potentials. Supporting bound state calculations obtained fitted PESs for CN($A^2\Pi$)-Ar, where an average potential well-depth of D_e = 137.8 cm^{-1} was inferred. From separate *ab initio* calculations of Alexander *et al*., it is known that this corresponds to a T-shaped equilibrium geometry.[15] The parity preference was strongest for predissociation from the zero-point level of CN($A^2\Pi$)-Ar and diminished with increasing vibrational excitation, indicating that the amplitude motions associated with increased vibration sampled less symmetric regions of the potentials. This also implies that the PES for the electrostatic mixing of the CN A-X states is also near-symmetric. In a separate study, Heaven and co-workers observed the CN-Ar complex on the $B^2\Sigma^+$-$A^2\Pi$ and $A^2\Pi$-$X^2\Sigma^+$ electronic transitions.[196] They noted a dissociation energy of D_0'' =

102 ± 2 cm^{-1} and a zero-point rotational constant of $B_0'' = 0.067 \pm 0.005$ cm^{-1} for CN(X)-Ar and a CN(A)-Ar dissociation energy of $D_0' = 125 \pm 2$ cm^{-1}.

The spectroscopy and non-adiabatic predissociation of CN($A^2\Pi$)-Ne has also been characterised.[201, 202] The upper spin-orbit component (Ω = 1/2) predissociated rapidly *via* non-adiabatic relaxation with no vibrational dependence. The lower spin-orbit component (Ω = 3/2) predissociated much more slowly through internal conversion (IC) from CN($A^2\Pi_{3/2}$, v)-Ne to CN($X^2\Sigma^+$, v+4)+Ne, with rates found to be exponentially dependent on the energy gap between the initial and final CN levels. The Ω = 1/2 spin-orbit predissociation was accompanied with a final state CN parity preference, however the excess energy from the electronic (IC) predissociation of the Ω = 3/2 component was released primarily into translational recoil and lacked any such parity propensity. These results were in good agreement with adiabatic and diabatic CN($X^2\Sigma^+$, $A^2\Pi$)-Ne PESs of Yang and Alexander.[200] Experimental anisotropy parameters[201] and *ab initio* calculations predicted a T-shaped equilibrium geometry for CN($A^2\Pi$)-Ne, akin to that of CN($A^2\Pi$)-Ar.

In contrast to CN-Ar, the lack of any clear parity propensity in the CN-Ne A→X predissociation was also mirrored in the CN-H_2 complex.[203, 204] However, collision-induced CN($A^2\Pi$)+Ne and H_2 A→X transfer did show symmetry preferences.[203, 204] This has bearing on the regions of the PES that mediate the observed process, since collisional energy transfer generally samples the repulsive walls, whereas predissociation is more sensitive to the bound wells. The larger amplitude bending motions of CN($A^2\Pi$)-Ne and CN($A^2\Pi$)-H_2 sample more asymmetric regions of the potentials, weakening the symmetry preference. The deeper, more anisotropic CN($A^2\Pi$)-Ar potentials restrict the bending motion, such that the predissociation is enabled by the symmetric regions of the PESs near the equilibrium geometry. The rotational endoergicity released to the CN($X^2\Sigma^+$) photofragment is also consistent with this homology. The lack of a predissociative parity propensity may also be indicative of a resonant scattering process in the half-collision, where the restricted initial geometry of the complex allows separation from a metastable state, which corresponds to resonances in the full-collision dynamics. This again implies that different regions of the PESs being sampled during the half- and full-collisional encounters.[203, 204]

Comparison of the CN-Ar and CN-Ne systems reveals trends that are expected when the topographies of the PESs are similar, but the strength of the interaction is greater for the heavier rare gas.[196] The rate of electronic predissociation of CN($A^2\Pi_{3/2}$)-H_2 was shown to be around three times faster than that of CN($A^2\Pi_{3/2}$)-Ne for $v_{CN(A)} = 3$. This implies that the electrostatic interactions for H_2 are significantly more effective in mixing the CN $A^2\Pi$ and $X^2\Sigma^+$ states than for Ne.[203] The PES of the CN($X^2\Sigma^+$)-H_2 van der Waals complex has also been studied.[205] The potential exhibits two minima, the first consisting of a linear H-H···N-C arrangement and the second a T-shaped H_2···CN geometry. Dipole-quadrupole and quadrupole-quadrupole interactions appeared to be the dominant electrostatic forces defining the anisotropy of the surface, with short-range repulsion and dispersion forces also significantly influencing the shape of the potential.[205]

Energy Transfer in CN + Molecular Partners

Molecules such as N_2, O_2 and CO_2 are abundant in combustion and atmospheric environments. The increased number of degrees of freedom with molecular colliders introduces an added complexity to both construction of full-dimensional interaction potentials and to the treatment of quantum scattering calculations. In addition to the energy transfer pathways available with rare gases, molecular partners offer resonant electronic energy exchange, correlated vibrational and angular motions, vibronic and reactive quenching, and long-range electrostatic interactions. There is also considerable interest in the astrophysics community to use molecule-molecule RET rate constants to model interstellar molecular encounters.[206, 207] Below is a summary of relevant literature on energy transfer.

Taherian and Slanger[174, 208] and Halpern *et al.*[110, 209] measured the vibronic quenching rates of CN($A^2\Pi$) in vibrational levels $v' = 0 - 5$ with a range of quencher gases, including Ar, N_2, O_2 and CO_2. The associated rate constants are shown in Table 1.5. The authors suggested that electronic quenching takes place *via* a cross-relaxation energy transfer mechanism to neighbouring CN($X^2\Sigma^+$) vibrational levels. This cascading effect is a result of the extensive overlap of the $X^2\Sigma^+$ and $A^2\Pi$ electronic states, as seen in Figure 1.22.

Table 1.5 – CN($A^2\Pi$, v') vibronic quenching rate constants, k_Q, for various quencher gases.

v'	k_Q / 10^{-11} cm^3 s^{-1}			
	Ar	N_2	O_2	CO_2
0	-	0.044 ± 0.005^a	3.0 ± 0.2^b	-
1	-	0.24 ± 0.015^b	3.1 ± 0.1^b	2.5 ± 0.15^b
2	0.51 ± 0.1^c	2.39 ± 0.2^c	-	5.3 ± 0.5^c
3	1.50 ± 0.2^c	2.36 ± 0.2^c	-	6.9 ± 0.7^c
4	2.63 ± 0.2^c	3.83 ± 0.3^c	-	13.1 ± 1.0^c
5	3.03 ± 0.3^c	4.43 ± 0.4^c	-	7.8 ± 0.8^c

[a] *Ref. 209.*
[b] *Ref. 208.*
[c] *Ref. 110.*

Table 1.5 shows that the general order of the quenching efficiencies is $CO_2 > O_2 > N_2 >$ Ar. Halpern *et al*. observed CO_2 to quench the the $v' = 4$ level particularly well, with a rate constant of $k_Q = (1.31 \pm 1.0) \times 10^{-10}$ cm^3 s^{-1}. A proposed explanation is that the anti-symmetric v_3 stretch of CO_2 is near-resonant with the energy gap between the CN($A^2\Pi$, $v' = 4$) and CN($X^2\Sigma^+$, $v'' = 7$) levels.[110]

A key difference between O_2, CO_2 and N_2 is the possibility of reactive channels with the oxygen-containing species. Studies of these have mainly focused on the $X^2\Sigma^+$ electronic ground state of CN. Only a limited number of authors have addressed the CN($X^2\Sigma^+$)+CO_2 reaction, shown below.[210-213]

$$CN(X^2\Sigma^+) + CO_2 \rightarrow CO + NCO \qquad \Delta H_0^0 = -6 \text{ kJ mol}^{-1}$$

Reaction 1.2

Reaction 1.2 is very slow up to temperatures of 1000 K, with an upper limit bimolecular rate constant of 4.2×10^{-15} cm^3 s^{-1}, and at room temperature is exothermic by only 6 kJ mol^{-1}.[213] The limiting step is believed to be the large activation energy required in breaking the C=O double bond, 114.6 kJ mol^{-1}, which proceeds *via* formation of a NCOCO complex. The reaction between CN($X^2\Sigma^+$)+O_2 is a prototypical radical-radical reaction that proceeds on an attractive potential without an entrance barrier.[214] The kinetics and dynamics of this reaction have been extensively studied by both experimental and computational methods between temperatures of 13 – 3800 K.[214] The three possible product channels are:[215]

$$CN + O_2 \rightarrow NCO + O \quad \Delta H_0^0 = -56 \text{ kJ mol}^{-1}$$

Reaction 1.3

$$\rightarrow CO + NO \quad \Delta H_0^0 = -456 \text{ kJ mol}^{-1}$$

Reaction 1.4

$$\rightarrow N + CO_2 \quad \Delta H_0^0 = -354 \text{ kJ mol}^{-1}$$

Reaction 1.5

The total reaction rate constant at room temperature was reported to be 5×10^{-11} cm^3 s^{-1}.[214] Under thermalised conditions, Reaction 1.3 is the only significant reactive channel. It is believed to proceed *via* a NCOO intermediate and has a strong dependence on the internal energies of the reactants,[216-220] with entrance channel rotation appearing as NCO product bending excitation. Taherian and Slanger measured the electronic quenching rates of CN($A^2\Pi$, v = 0, 1) by O_2, as seen in Table 1.5, and recorded total quenching rate constants of ~$(3 – 3.1) \times 10^{-11}$ cm^3 s^{-1},[208] which may or may not include loss due to reaction [as is so far unknown for CN($A^2\Pi$)]. The same authors also noted that EET to form $O_2(a^1\Delta_g)$, shown below in Reaction 1.6, is exothermic by only 13 kJ mol^{-1} for CN($A^2\Pi$, v = 0).

$$CN(A^2\Pi) + O_2 \rightarrow CN(X^2\Sigma^+) + O_2(a^1\Delta_g)$$

Reaction 1.6

Spin-pairing restrictions mean that only one out of three encounters with ground state $O_2\left(X^3\Sigma_g^-\right)$ can quench CN($A^2\Pi$), since the former has a spin S = 1 and the latter S = ½. These couple to form complexes with spins S = 1½ and S = ½, with respective multiplicities of $(2S+1)$ = 4 and 2, giving a total of 6. Therefore, 2/6 or 1/3 collisions can quench. Nontheless, the quenching of CN by O_2 appears to be a significant channel, and how this and the associated anisotropy affect the elastic and inelastic collision dynamics of CN($A^2\Pi$)+O_2 is an interesting question.

An important point to note is that the ground state $X^2\Sigma^+$ and first excited $A^2\Pi$ electronic states of CN are essentially different molecules, as they posses different electronic

energies and orbital angular momenta. Therefore, the reaction of CN($A^2\Pi$) with either O_2 or CO_2 may not necessarily proceed in the same manner as for CN($X^2\Sigma^+$). Indeed, no reaction may occur at all. However, since the reactions of CN($X^2\Sigma^+$) with O_2 or CO_2 are exothermic, it is clear that reactive pathways must be at least energetically accessible for both colliders with CN($A^2\Pi$). There may then be a possibility of strong anisotropic forces between the two colliders, which could influence the measurements. The FMS technique is unable to distinguish between electronic quenching of CN($A^2\Pi$) or quenching due to reaction.

Measurements of rotationally inelastic collisions of small molecules with CN have mainly focussed on its X and B $^2\Sigma^+$ electronic states. Sadowski and co-workers[193, 221] used resolved fluoresence spectroscopy to study RET of CN($X^2\Sigma^+$ and $B^2\Sigma^+$) with H_2, D_2, C_2N_2 and NO. They observed the total RET rate constants to decrease monotonically with increasing rotational quantum number, *N*, for every collider, except for CN($B^2\Sigma^+$)+H_2, which was found to be relatively independent of *N*. Smith *et al.*[222, 223] used IR-OODR to measure state-resolved collisions of CN($X^2\Sigma^+$, v = 2) with N_2 and C_2H_2. They concluded that the total removal RET rate constants were independent of the relative velocity of the collision pair and that it is purely the repulsive forces between the collision partners that is responsible for RET.

Our group has previously used Doppler-resolved FMS in a multi-pass optical set-up to probe the collisional evolution of the nascent CN($X^2\Sigma^+$) photofragment with N_2, O_2 and CO_2 (as well as He and Ar, as discussed earlier) partners after ICN photodissociation.[161] There was very little difference in the speed and translational anisotropy distributions for N_2, O_2 and CO_2, each displaying similar results to Ar. In all cases, the fast CN($X^2\Sigma^+$) speed component exhibited a decrease in $\mathbf{v}.\boldsymbol{j}$ (velocity-rotational AM) correlation, with essentially all correlation lost at later times for CO_2 and N_2. However, for O_2, a small $\mathbf{v}.\boldsymbol{j}$ moment of $\approx$ -0.2 persisted at late times. The initial $\boldsymbol{z}.\boldsymbol{j}$ (LAB-frame alignment) correlation of $\approx$ -0.3, representing a preference for $\boldsymbol{j}$ to be perpendicular to $\boldsymbol{z}$, was maintained in the fast speed component for CN($X^2\Sigma^+$)+N_2 as population was lost, whilst a decrease in alignment occurred for the slower component. Collisions which retain $\boldsymbol{z}.\boldsymbol{j}$, but depolarise $\boldsymbol{z}.\mathbf{v}$, must also depolarise $\mathbf{v}.\boldsymbol{j}$, as is the case for N_2. This is consistent with purely repulsive, sudden collisions giving broadly backward-scattered products in the centre-of-mass frame.

The ***z.j*** correlation for O_2 and CO_2 behaved similar to that for N_2, but the alignment was scrambled to a considerably greater extent. The rapid loss of ***z.j*** with O_2 and CO_2, but partial retention with N_2 suggests that there are differences in the PESs for the different molecular colliders,[161] consistent with more anisotropic potentials for O_2 and CO_2. This could be a result of reactive channels for the oxygen-containing species influencing the anisotropy of the interaction. Although the FMS experiment is only sensitive to unreactive collisions, the resulting strong anisotropic forces could tilt the plane of rotation of the CN molecule. Further support for this comes from the **v.*j*** correlation being retained for O_2, whilst being essentially lost in collisions with N_2 and CO_2, indicative of N_2 being dominated by repulsive interactions. In comparing O_2 and CO_2, any interaction that enforces planarity will result in a negative **v.*j*** correlation, as observed for O_2. The loss of all AM correlations for CO_2 suggests that there is no forced planarity in this system. A triple vector **v.*j*.*z*** correlation of ≈ 0.3 was measured for N_2, corresponding to the CN($X^2\Sigma^+$) radicals moving principally along the laboratory ***z***-axis with ***j*** perpendicular to both **v** and ***z***. This correlation underwent rapid decay and similar behaviour was observed for O_2 and CO_2.[161]

The FMS measurements were extended to study the efficiencies of state and velocity-changing collisions of superthermal CN($A^2\Pi$, $v = 4$, $j = 0.5$ F_2f) with N_2 and O_2 partners (and He and Ar, as discussed earlier in this section).[198] Aside from the different electronic state, rotational alignment was deliberately not possible with the rotational state selected. The measured total removal cross-sections are listed in Table 1.6.

Table 1.6 – Total removal cross-sections for superthermal collisions of CN($A^2\Pi$) with He, Ar, N_2 and O_2 from reference 198.

Collider	$\langle\sigma_{tot}\rangle$ / Å^2
He	29 ± 1
Ar	53 ± 3
N_2	72 ± 4
O_2	51 ± 2

From Table 1.6, the cross-sections for Ar and O_2 are nearly identical, being almost twice that of He, but both are much lower than the cross-section for N_2. These observations may appear surprising, as O_2 presents the possibility of extra loss channels compared to Ar, such as rotation-rotation transfer and electronic and reactive quenching, as discussed earlier. Similar cross-sections may also have been expected for

N_2 and O_2, given their similar nature as first row diatomics. The van der Waals radii for Ar, O_2 and N_2 are 3.42 Å, 3.43 Å and 3.68 Å, respectively, which predict the Ar and O_2 cross-sections to be similar and the N_2 cross-section to be slightly larger, as approximately observed.[198] However, an argument based solely on the van der Waals radii is too simplistic. The differences in measured cross-sections for each partner may reflect differences in their interaction potentials with CN($A^2\Pi$) and in electronic and reactive quenching abilities.

The most recent work on rotationally inelastic collisions of CN($A^2\Pi$) with small molecules was presented by Dagdigian and co-workers.[206, 224] They used the LIF-OODR technique to measure fully state-resolved $jF\varepsilon \rightarrow j'F'\varepsilon'$ RET rate constants of low-j CN($A^2\Pi$, $v = 3$) colliding with N_2, CO_2 and CH_4. For CN($A^2\Pi$)+N_2, *ab initio* PESs for 3 limiting orientations of the CN and N_2 molecules were also calculated. These were then spherically-averaged and approximate V_{sum} and V_{dif} PESs formed. Subsequent QS calculations were then performed using these surfaces.[206] Experimental total removal rate constants from the initial rotational level were measured for collisions of CN($A^2\Pi$) with N_2, and were found to be fairly rapid, at around $(4 – 5) \times 10^{-10}$ cm^3 s^{-1}.[206] This is in good agreement with the QS predictions, although much larger than the electronic quenching rate constant of CN($A^2\Pi$, $v = 3$)+N_2, measured by Halpern and co-workers.[110] Quenching was concluded to comprise only ~4% of the total population removal, suggesting the dominance of rotationally inelastic collisions over other loss channels for N_2. In fact, for all colliders, their spectra showed that removal by electronic quenching or reaction does not dominate the loss of CN($A^2\Pi$) compared to other loss mechanisms, such as radiative decay and physical diffusion.

For CN($A^2\Pi$)+N_2 state-to-state RET, there was a clear disagreement between experiment and theory, in both the relative propensities for scattering into different spin-orbit and Λ-doublet manifolds, and in the relative Δj propensities within specific fine-structure manifolds. Theory predicted distributions consistent with the CN($A^2\Pi$)-Ar system,[15] with propensities centred energetically on the initially prepared level and spin-orbit changing transitions having rate constants around a quarter the size of those for spin-orbit conserving transitions. There was no clear preference for Λ-doublet conserving or changing collisions, although the even-odd alternation, consistent with a preference for rotational parity-conservation, was still present and observed experimentally.[206] While the experimental results for spin-orbit and Λ-doublet

conserving transfer showed good agreement with the QS predictions, both spin-orbit conserving Λ-doublet changing, and all of the spin-orbit changing, transitions were dramatically different. The rate constants for spin-orbit changing collisions were very small, with measureable transfer to only a few levels. The spin-orbit conserving Λ-doublet changing rate constants were also consistently zero or very small. In both cases, the non-zero rate constants occurred at unusual ranges of Δj. Dagdigian and co-workers attributed this remarkable disagreement between experiment and theory as a failure of the theory, suggesting it to be a result of the spherical averaging of the CN($A^2\Pi$)+N_2 PESs and neglecting the rotational inelasticity of the N_2 molecule. The similar predicted behaviours of CN($A^2\Pi$)+N_2 and CN($A^2\Pi$)+Ar suggests similarities in their interaction potentials.[15, 206]

The separate experimental measurements of RET in CN($A^2\Pi$) with CO_2 and CH_4 collision partners saw similarly striking spin-orbit and Λ-doublet propensities, with fine-structure and Λ-doublet conserving collisions displaying the conventional Δj-dependence, whilst fine-structure changing and Λ-doublet changing collisions were both small in overall magnitude, but also displayed extremely unusual j' dependences, with large Δj transfer more probable than small Δj.[224] Unfortunately, *ab initio* PESs for CN($A^2\Pi$)-CO_2 and CN($A^2\Pi$)-CH_4 were not calculated and no QS predictions performed.

The total removal rate constants for CN($A^2\Pi$, v = 3)+N_2 measured by Dagdigian and co-workers[206] were strikingly similar to those for CN($X^2\Sigma^+$, v = 2)+N_2 from Olkhov and Smith, despite the different electronic and vibrational states.[223] Rotationally inelastic collisions within these two electronic states are mediated by the anisotropy of the repulsive parts of the $V_{sum}(\Pi)$ and V_Σ PESs, respectively. The similar magnitude of the rate constants therefore suggests that the strength of the anisotropies for the two systems are similar. The observed propensity for strong conservation of fine-structure label in scattering CN($A^2\Pi$) with N_2, CO_2 and CH_4 could imply that the V_{dif} potentials for these collision pairs are significantly smaller than the V_{sum} potentials. This may be due to the long-range attractive forces present in the molecule-molecule interactions. The relevant dipole and quadrupole moments and polarizabilities of each species are summarized Chapter 4 (Table 4.8). Since the dipole moment of CN($A^2\Pi$) is small (0.3 D) and the molecular collision partners have no net dipole moment, the quadrupole-quadrupole

interaction is thought to be the leading long-range interaction. For Ar, which posseses neither a dipole nor quadrupole moment, the leading long-range interaction is dispersion. The quadrupole-quadrupole interaction has $\lambda = 4$ anisotropy, which enables both fine-structure conserving and changing collisions.[225] Within a given fine-structure manifold, this interaction couples Λ-doublets of the same *e*/*f* symmetry for even-Δ*j* and opposite *e*/*f* symmetry for odd-Δ*j*. This therefore does not provide a satisfactory explanation to the observed dynamics of Dagdigian and co-workers, and so other factors may contribute.

1.9 Summary

Measurements of collisional energy transfer clearly provide a powerful dynamical insight into the fundamental properties of molecular interactions. Even more revealing are the subtle vector attributes that are typically more experimentally challenging to probe. Both scalar and vector quantities also serve as robust tests of high level scattering theory. This thesis aims to contribute to and strengthen this burgeoning field by employing the versatile and highly sensitive FMS technique to monitor rotationally elastic and inelastic collisions of the CN($A^2\Pi$) radical. Specifically, the removal and transfer of polarised rotational angular momentum is followed upon collisions with Ar, before extending the study to small molecular targets, N_2, O_2 and CO_2. This progresses from the preliminary CN($A^2\Pi$)+Ar measurements of Ballingall *et al*.,[199] improving on the experimental conditions and optimising the kinetic analysis. The open-shell nature and non-zero orbital angular momentum of the CN($A^2\Pi$) radical adds intricate complexity to the scattering problem, however collisions with Ar are simple enough to allow for exact QS calculations in *ab initio* PESs to be performed and directly compared to the experiment. The ultimate goal is to fully characterise this benchmark $^2\Pi$+Rg system and reveal how the additional dimensions and other properties available to molecular partners affect the collision dynamics.

Chapter 2

Experimental Methodology

This work monitors the collisional evolution of polarised rotational angular momentum in the CN($A^2\Pi$) radical. Laser photolysis of cyanogen iodide (ICN) was used to create CN($X^2\Sigma^+$), which was then optically pumped to CN($A^2\Pi$) and monitored with continuous-wave FMS. These are the three main requirements of all experiments described in this thesis and are outlined in this chapter. Any changes to the experiment are addressed in the relevant chapters. A schematic and photographs of the experimental set-up are shown in Figure 2.1 to Figure 2.3.

The experimental design was modified from a previously used multi-pass set-up[64, 161, 198, 199] that studied velocity-angular momentum correlations of CN in photodissociation and inelastic collisions. The changes increased the temporal resolution of the experiment and simplified the use of circular laser polarisations. Since the experiments followed collisions of CN radicals with collider gases, it was important that these were the only species present. For this purpose, the experiments were performed in a leak-tight vacuum chamber with high purity collider gases. CN is an unstable transient molecule and as such was produced *in situ via* laser photolysis of a photolabile precursor, ICN.

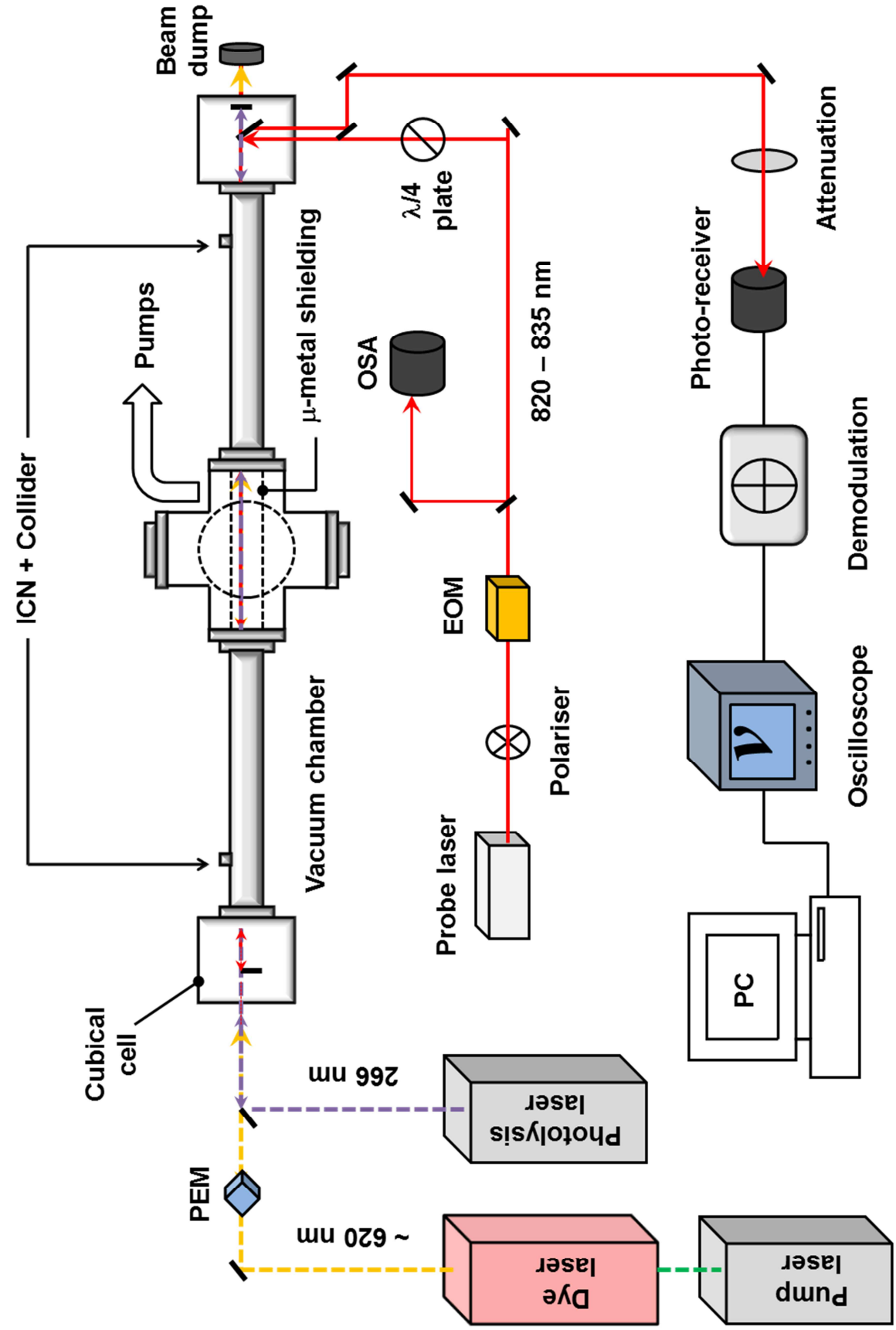

Figure 2.1 – A schematic of the experimental set-up. EOM = Electro-optic (phase) modulator, OSA = optical spectrum analyser, PEM = photo-elastic modulator.

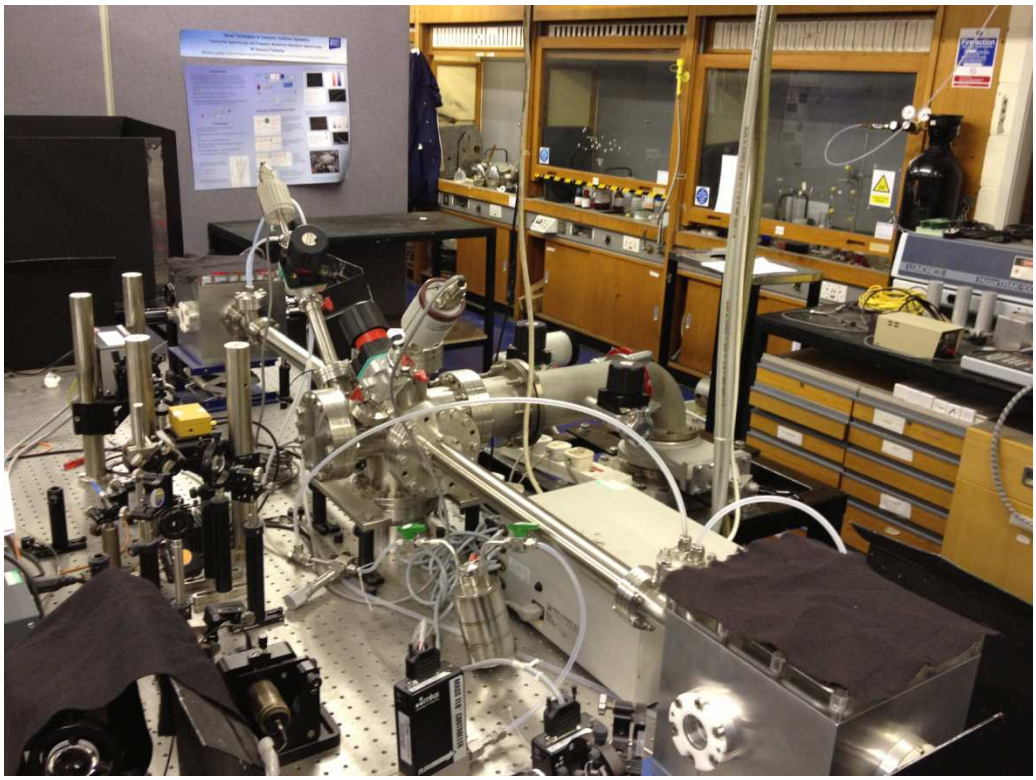

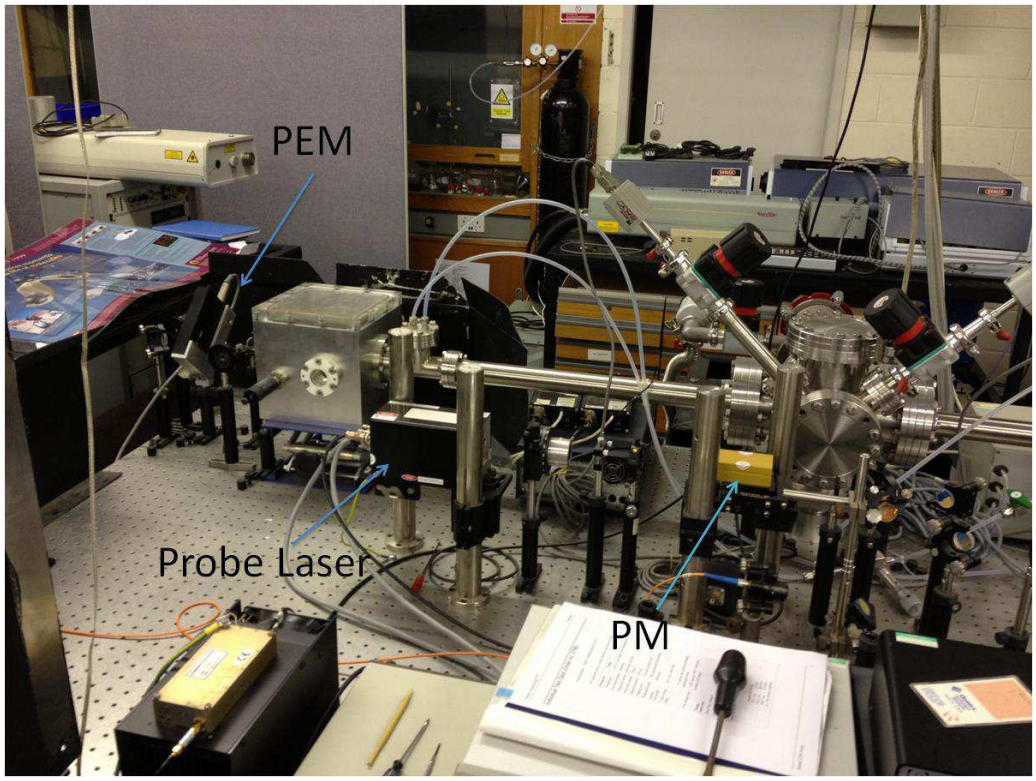

Figure 2.2 – Photographs of the experimental set-up used for the work in this thesis.

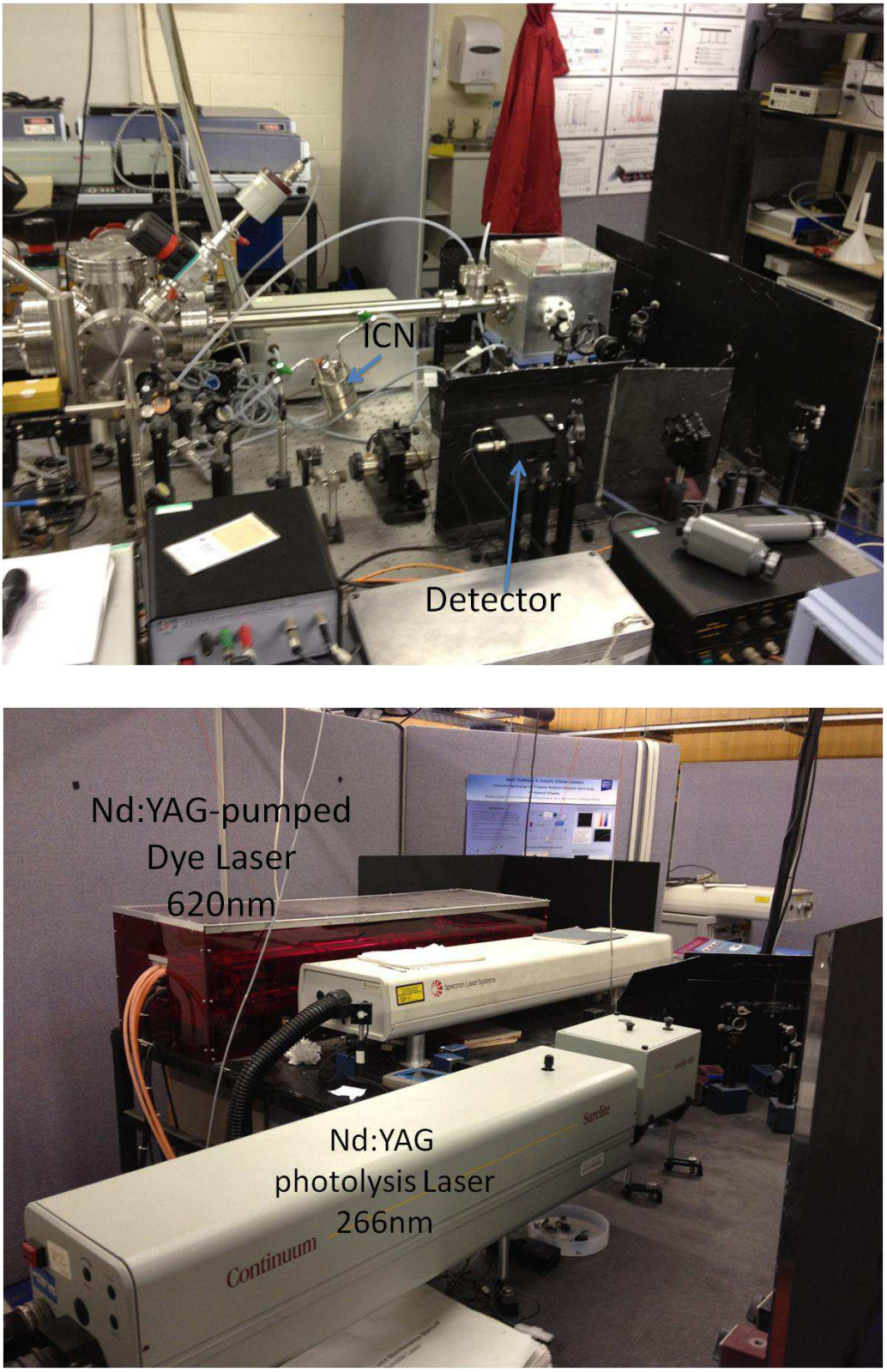

Figure 2.3 – Photographs of the experimental set-up used for the work in this thesis.

2.1 Vacuum Systems and Gas Handling

The experiments were performed in a 2 m long, ~11 – 12 L longitudinal stainless steel high vacuum chamber (Vacuum Components), consisting of a six-way-cross at the centre (6 × 100 mm ports). Extending from this were two arms (1 m × 38 mm), each connected to a cubical mirror housing (15.63 L) with a perspex lid. This defined the main axis of the chamber. The cubical cells both had two orthogonal synthetic fused silica windows (50 mm × 5 mm) to allow for the input and exit of laser beams. The probe laser entrance window was wedged at 1° to reduce etalon effects that could introduce wavelength-dependent background signals.

Incorporated at the end of the arms before the cubical cells were T-junctions to allow for gas inputs to the chamber. A cylinder of μ-metal shielding was placed along the inside of the arms and across the central 6-way cross between the T-junctions, to shield against stray magnetic fields.[127] Another 100 mm port perpendicular to the arms lead to an evacuation stage consisting of a baffled diffusion pump (2000 L s^{-1}, Edwards E06), backed by a foreline filtered mechanical rotary pump (Edwards E2M18). This allowed the vacuum chamber to reach a base pressure of ~10^{-6} Torr. When not in use, the chamber was kept at around 10^{-3} Torr using only the rotary pump. The chamber pressure was monitored using 0 – 1 Torr and 0 – 10 Torr capacitance manometers (MKS Instruments). The unused 100 mm ports were fitted with blank CF flanges.

The CN radicals were produced by a photolytic precursor, ICN (Acros Organics, 98% purity, ~829 mTorr vapour pressure at 296 K), which was stored in a custom-made stainless steel vessel. ICN vapour was picked up by a slow flow (~1 sccm) of collider gas (research grade >99%, BOC) controlled *via* a 10 sccm mass-flow controller (MKS Instruments), and passed to the vacuum chamber *via* ~6 mm diameter swaged teflon tubes. By throttling the diffusion pump gate valve, the partial pressure of the precursor mix was set at ~30 mTorr, around 10% of which was ICN. The desired total pressure of 100 – 1500 mTorr was obtained by addition of a separate flow of collider gas through a 100 sccm mass-flow controller (MKS Instruments). The collider gases were supplied by dedicated pipelines from cylinders located close to the experiment, so as to minimise the possibility of cross-contamination or atmospheric leaks.

2.2 Laser Systems

Three separate laser systems were implemented in the experiment. The first laser was used to generate CN($X^2\Sigma^+$) molecules by photolysis of ICN. The second laser was used to optically pump the molecules to specific ro-vibronic levels of the CN($A^2\Pi$) state and create a rotational anisotropy. The third laser probed the collisional evolution of the prepared or product levels.

2.2.1 Photolysis Laser

The photoloysis laser was a Continuum Surelite SLIII-10 pulsed Nd:YAG laser (10 Hz repetition rate, ~5 ns pulse length). The lasing medium was a Nd:YAG rod pumped by two Xenon-filled gas discharge lamps. This gave a 1064 nm fundamental output, which was *Q*-switched at 238 μs delay to optimise the pulse energy. The *Q*-switching was achieved by a Pockels cell, polariser and quarter wave plate set-up in the cavity.

The fundamental output was frequency doubled to 532 nm using a type-II potassium dideuterium phosphate (KD*P) second harmonic generation (SHG) crystal. The 532 nm output was then doubled again using a β-barium borate (BBO) fourth harmonic generation (FHG) crystal. The quadrupled 266 nm output was horizontally polarised with a typical pulse energy of ~80 – 90 mJ, and a beam diameter of approximately 5 mm. The laser specifications are summarised in Table 2.1.

Table 2.1 – Specifications of the photolysis laser.

Laser type:	Continuum Surelite SLIII-10 (Nd:YAG)
Pulsed or cw:	Pulsed
Repetition rate:	10 Hz
Pulse length:	~5 ns
Flashlamp discharge voltage:	1.40 kV
***Q*-switch delay:**	238 μs
1064 nm energy (fundamental):	~800 mJ
532 nm energy (SHG - KD*P):	~400 mJ
266 nm energy (FHG - BBO):	80 - 90 mJ
Output polarisation:	Horizontal

Wavelength separation was performed in a separator housing unit (Surelite Separation Package SSP-3) directly after the laser output shutter. This consisted of two dichroic mirrors that reflected out 266 nm and transmitted the fundamental (1064 nm) and

doubled (532 nm) outputs to a beam dump. The photolysis beam was steered into the vacuum chamber using three 45^o turning mirrors (25 mm) with high reflectivity (HR) coating at 266 nm. The laser beam entered the chamber through a fused silica window on the cubical cell along the main axis of the chamber. After exiting the chamber it was immediately retro-reflected by a 0^o normal incidence HR 266 nm mirror along the same axis, resulting in a double pass of the chamber (see Figure 2.1). The absorption cross-section of ICN at 266 nm is ~68 L mol^{-1} cm^{-1},[226] therefore under these experimental conditions the multiple laser passes would dissociate approximately ≤ 10% of the ICN present (see reference 226).

2.2.2 Pump Laser

The experiment required populating isolated CN($A^2\Pi$, v = 4, $jF\varepsilon$) rotational levels on the $A^2\Pi \leftarrow X^2\Sigma^+$ (4,0) band and creating a rotational anisotropy. This was achieved by optical excitation using a narrow-bandwidth tuneable dye laser (Spectron SL4000G), pumped by a 10 Hz pulsed (~15 ns pulse width) Nd:YAG laser (Spectron SL803). The SL803 laser consisted of an oscillator and amplifier section, each containing an Nd:YAG rod housed with a Xenon flashlamp. The oscillator section contained a Pockels cell, polariser and quarter wave plate to provide *Q*-switching. The fundamental output of the laser was horizontally polarised 1064 nm light (~800 mJ per pulse), which was frequency doubled to 532 nm using a temperature controlled type-II KD*P SHG crystal, providing ~300 mJ per pulse. This second harmonic was used to pump the dye laser unit.

The dye laser also consisted of an oscillator and amplifier section. An input beam splitter guided ~10% of the pump light to the oscillator section, which contained a transversely pumped dye cell, a prism beam expander, a holographic grating (50 mm, 1800 lines per mm), a tuning mirror and an output coupler. The grating and mirror formed the laser cavity. The tuning mirror was mounted on to a mechanical sine drive, which could be scanned using a scanning controller unit (Spectron SL4000SC) to tune the wavelength to a desired spectroscopic transition. The scanning unit was controlled by the experiment computer *via* an RS-232 interface.

The amplifier section incorporated two dye cells (pre-amplifier and main amplifier), pumped longitudinally by the remainder of the input beam. Addition of the wavelength-

selected oscillator light through the amplifier dye cells enabled amplification of the output power. The output light from the dye laser was horizontally polarized, due to the spatial orientation of the grating. The desired wavelength range of the laser light was ~620 nm. This was achieved using DCM (dicyanomethylene) laser dye dissolved in HPLC grade methanol with the following quantities: oscillator – 400 mg DCM in 1 L methanol, amplifier – 80 mg DCM in 1 L methanol. The DCM output covers the wavelength range 615 – 660 nm, peaking near to 640 nm. The specifications of the pump and dye lasers are detailed in Table 2.2. The temporal waveform of the dye laser is shown in Figure 2.4.

Table 2.2 – Specifications of the pump and dye lasers

(a) Pump laser	
Laser type:	Spectron SL803
Pulsed or cw:	Pulsed
Repetition rate:	10 Hz
Pulse length:	~15 ns
Flashlamp discharge voltage:	~700 - 1200 V
***Q*-switch delay:**	178 μs
1064 nm energies (fundamental):	~275mJ[a], ~235 mJ[b], ~800mJ[c]
532 nm energy (SHG - KD*P):	~300 mJ
Output polarisation:	Horizontal
(b) Dye laser	
Laser type:	Spectron SL4000G (Nd:YAG pumped)
Input light:	532 nm
Output light:	~620 nm
Dye:	DCM in methanol (HPLC grade)
Output energy:	1 - 2 mJ (osc only) 10 - 20 mJ (osc and amp)
Output polarisation:	Horizontal

Energies are typical for 800 V amplifier and 750 V oscillator flashlamp voltages.
[a]Oscillator without *Q*-switch. [b]Oscillator with *Q*-switch.
[c]Amplifier with *Q*-switch.

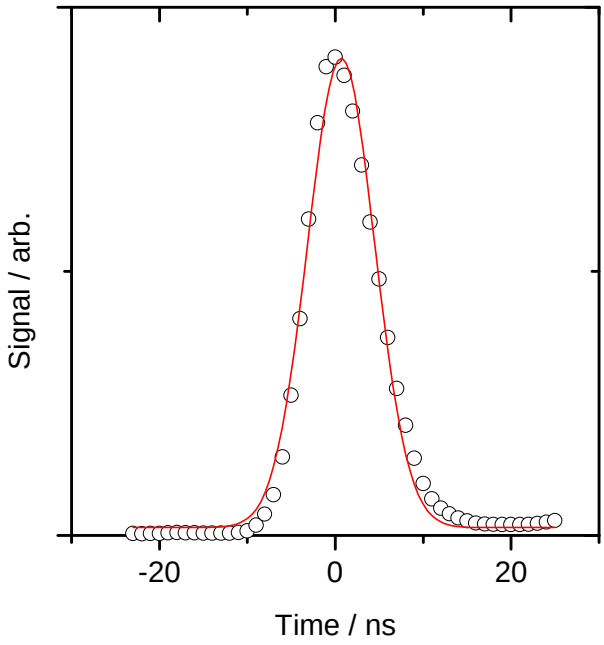

Figure 2.4 – The temporal waveform of the dye laser fitted with a Gaussian lineshape. FWHM ≈ 10 ns. The light was detected by a fast photo-diode (EOT, ET200, risetime: < 200 ps).

The dye laser output (hereafter called the pump beam) was collimated using a long focal converging lens and guided to the chamber with three 45° 400 – 700 nm HR mirrors (25 mm diameter), entering the chamber through the same input window as the photolysis laser and as close (~5 mm) to the final photolysis input mirror as possible. The pump beam made a single pass of the chamber along the same axis as the photolysis laser, with a crossing angle of < 1° and an effective overlap pathlength of ~3 m. Immediately before the chamber entrance the beam went through the centre of a photo-elastic modulator (PEM) crystal to allow for polarisation control (see Section 2.4.3).

2.3 Probe Laser

The collisional evolution of the prepared CN($A^2\Pi$, $v = 4$, $jF\varepsilon$) molecules was probed by FM stimulated emission on the A-X (4,2) vibronic band. The probe laser was a linearly polarised (vertical as mounted) near-infrared (NIR) 820-835 nm continuous-wave (cw) external cavity tuneable diode laser (TEC 500, Sacher Lasertechnik), with a >30 mW power output, ~2 mm beam diameter, a typical operation current of ~ –100 mA and operation temperature of ~20 – 25 °C. The diode laser had a Littman configuration, designed to produce a narrow linewidth with high mechanical stability, and the output facet of the laser diode was anti-reflection (AR) coated (< 10^{-4} reflectivity) to allow a

broad mode-hop free tuning range (manufacturer specification ≈ 100 GHz). Coarse tuning (~15 nm range, ~0.1 cm^{-1} resolution) was performed by manual rotation of the cavity mirror with a tuning screw. Fine tuning, over a range of ~0.2 nm used a piezo element on the tip of the adjustment screw. In practice, the piezo voltage was provided by the -10 V to +10 V DC 16 bit analogue output of a PCI card (NI 6014) in the data acquisition computer. This gave a fine tuning range of ≈ 300 GHz, with a resolution of 5 MHz, similar to typical time-averaged bandwidth of the laser. Minor adjustment of the operation current and temperature allowed for optimisation of the mode-hop free tuning range at the wavelength of a particular spectroscopic transition. The probe laser specifications are summarised in Table 2.3.

Table 2.3 – Specifications of the probe laser.

Laser type:	Sacher Lasertechnik, TEC 500 diode laser (Littman)
Pulsed or cw:	Cw
Wavelength range:	820 - 835 nm
Wavelength power peak:	830 nm
Output power:	>30 mW
Operation current:	-100 mA
Operation Temperature:	20 - 25 ^{o}C
Output polarisation:	Vertical (as mounted)

The probe laser beam was passed through a Glan-Taylor polariser (CVI Melles-Griot) to ensure pure vertical polarisation. It was then collimated and passed through a phase modulator (see Section 2.4.1) . The frequency-modulated probe beam was then guided to the chamber *via* broadband (Melles-Griot, HR 600 nm – 900 nm) 45^{o} turning mirrors, entering the chamber through a window perpendicular to the photolysis and pump laser exit window.

On enterting the chamber, the probe beam was reflected by 90^{o} to counter-propagate the photolysis and pump beams at an acute crossing angle from the input mirror (< 1^{o}). The probe beam was then retro-reflected along a near identical return path, giving an effective overlap pathlength of ~3 m. The probe beam subsequently exited the chamber *via* the entry window and was separated from the in-going beam by a pick-off mirror. Further mirrors directed it onto a photo-receiver for subsequent demodulation and analysis (see Section 2.4.2). All the probe mirrors after the chamber exit were custom dichroic mirrors (HR 830 nm, AR 620 nm, Laser Components GmbH) to separate any scattered pump light from the probe beam. An IR transmitting cut-off colour glass filter

(centre wavelength 750 nm, Laser 2000) was mounted in front of the photo-receiver for the same purpose. A neutral density filter wheel (New Focus) before the photo-receiver allowed for variable attenuation of the probe laser beam to avoid saturation of the detector.

2.4 Data Acquisition and Control

2.4.1 Probe Laser Polarisation and Modulation

The probe laser beam was frequency modulated using a phase modulator (Quantum Techology, TWAP-10) consisting of two 45° mounted AR 600-900 nm coated $LiTaO_3$ crystals. A 400 MHz reference signal from a radio-frequency (RF) generator (TTI TGR1040, range 0-1 GHz) was split in two using a Minicircuits ZFSC-2-1 power splitter, with one path (-3 – -4 dBm) going to a RF power amplifier. This gave a 400 MHz output with +40 dBm gain, which was used to drive the phase modulator. The second path was sent as a local oscillator (LO) reference through a phase shifter and +10 dBm amplifier to an I&Q demodulator. The frequency modulation and demodulation and associated signal analysis is discussed in greater detail in Section 3.2.1.

A small portion of the probe laser light was split off after the phase modulator to give two beams for laser monitoring. One of these beams was guided to a scanning Fabry-Perot interferometer optical spectrum analyser (CVI Technical Optics, FSR = 2 GHz), which was used to monitor the spectral waveform and modulation depth of the probe light. This was also used to check for mode-hops during wavelength scans and provided the information required to subsequently linearise the probe frequency axis during data analysis. An example FM probe waveform from the spectrum analyser is shown in Figure 2.5. The second beam was coupled into a fibre-optic cable and transferred to a wavelength meter (Angstrom WS-6) used to monitor the probe laser frequency during coarse laser-tuning. Similarly, a weak back-reflection of the pump light was coupled through another fibre-optic cable to the wavelength meter to monitor its frequency.

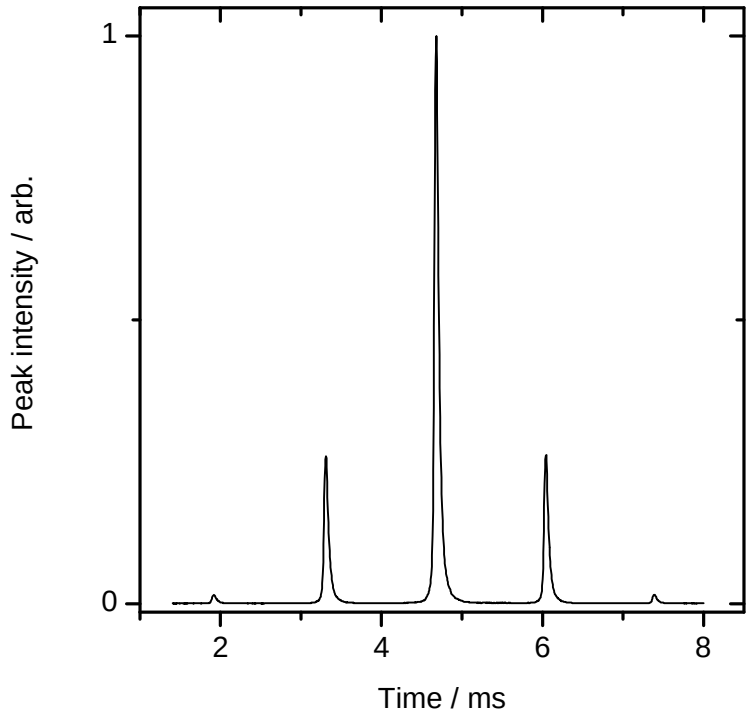

Figure 2.5 – Example carrier and first- and second-order FM sideband peaks from the OSA. Modulation frequency = 400 MHz, modulation index = 0.9. The x-axis is the true experimental acquisition time from the OSA.

For experiments requiring the probe beam to be linearly polarised, the probe laser's vertical polarisation was left unchanged. For experiments requiring the probe beam to be circularly polarised, a Berek's compensator (New Focus) acting as a λ/4-plate was placed directly before the chamber entrance window. A Berek's compensator consists of a single birefringent uniaxial crystalline plate with its extraordinary axis perpendicular to the surface of the crystal. When light is at normal incidence to the plate, it propagates through the device with a velocity independent of polarisation. When the plate is tilted with respect to the direction of the incident light, the plane of incidence becomes the plane of the extraordinary index of refraction. Light polarised in this plane is retarded by an amount that depends on the angle of tilt and on the wavelength. Light polarised perpendicular to the plane of incidence continues to propagate as an ordinary wave with velocity independent of tilt angle. Thus, the light in the two planes of polarisation accumulates a relative phase shift.[58]

To set the probe laser as circularly polarised:

1. The probe beam was firstly picked off by a 45^o mirror before the chamber entrance and guided through a Glan-Taylor polarising prism.
2. The angle of the polariser was adjusted to find the null point and then rotated by 90^o to transmit the full beam.
3. The transmitted beam was sent through a Babinet-Soleil compensator (Optics for Research SB-10) and immediately retro-reflected back through the Babinet-Soleil compensator and the polariser.
4. The return beam was picked off by another 45^o mirror and sent to a photo-diode connected to a digital storage oscilloscope (Lecroy Wave Runner LT264, 350 MHz, 1 Gs S^{-1}).
5. The Babinet-Soleil compensator angle was rotated to 45^o and the retardance adjusted until a transmission null was found. This meant the Babinet-Soleil compensator was acting as a $\lambda/4$-plate, as the input beam polarisation was rotated by 45^o to give a particular handedness of circular polarisation. Normal incidence reflection from the retro-reflecting mirror then changed the return beam polarisation to the opposite handedness. On going back through the Babinet-Soleil compensator, the polarisation was rotated to the opposite linear polarisation from the input beam, hence a null was seen on the oscilloscope.
6. Being confident the Babinet-Soleil compensator was acting as a $\lambda/4$-plate, the probe beam was returned to its normal path through the chamber. The return mirror in the chamber was then adjusted so that the return probe beam exited from the same window as the pump and photolysis laser beams.
7. The Babinet-Soleil compensator was placed in the beam path after the chamber exit window. The polariser, at the angle preset in step 2, was placed after the Babinet Soleil compensator. Behind this was the photo-diode connected to the oscilloscope.
8. The Berek's compensator was placed in the probe input path immediately before the entrance window. The orientation and retardance of the Berek's compensator were then adjusted as necessary to null the transmission through the polariser, and hence balance any retardance introduced by the reflection of the probe beam from the in-chamber mirrors. The meant that the probe beam was circularly polarised. The set-up of these steps is summarised in Figure 2.6.

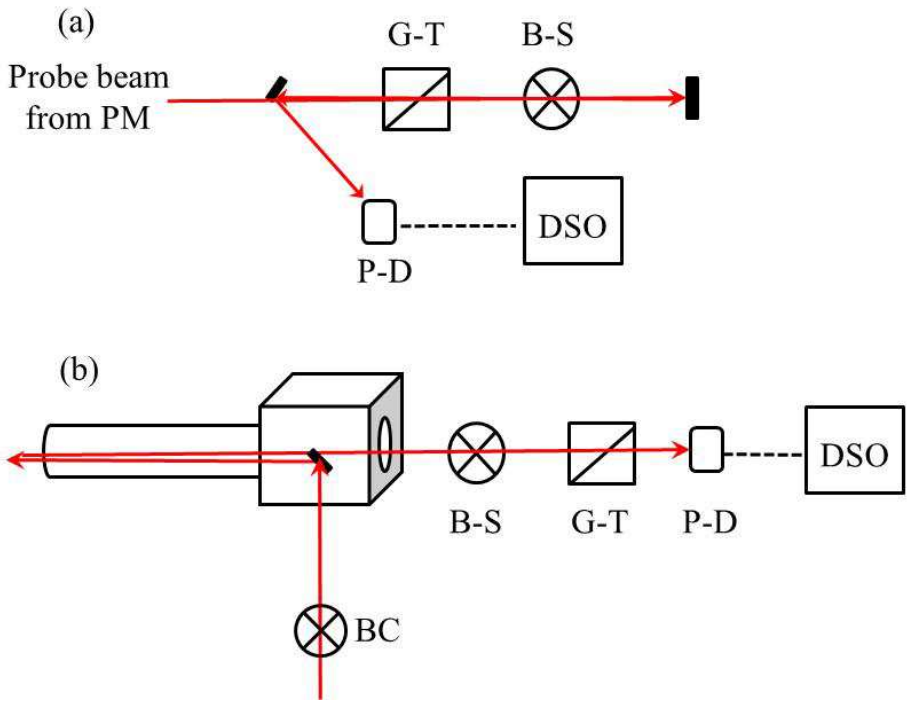

Figure 2.6 – The optical set-up to make the probe laser beam circularly polarised. (a) Steps 1 – 5. (b) Steps 6 – 8. G-T = Glan-Taylor polarising prism. BC = Berek's Compensator. B-S = Babinet-Soleil compensator. DSO = Digital Storage Oscilloscope. P-D = Photo-Diode. PM = Phase Modulator.

A Babinet Soleil compensator is a variable retardance zero-order optical wave plate, consisting of two birefringent magnesium fluoride wedges, one moveable and the other fixed to a compensator plate. The orientation of the major axis of the wedges is perpendicular to the major axis of the compensator plate. When mounted on a precision rotation stage, any arbitrary polarisation state may be set by a combination of adjustment of the retardance and rotation of the major axis relative to the input polarisation axis.

2.4.2 Probe Laser Detection and Demodulation

The frequency modulated probe laser sidebands were equal in magnitude but opposite in phase. With a sample of CN molecules present in the vacuum chamber, the sidebands underwent differential absorption (stimulated emission) and dispersion, causing amplitude and phase modulation of the probe beam, as discussed in more detail in Chapter 3. On exiting the chamber, the probe laser was detected by a 1 GHz photo-receiver (New Focus, 1601FS-AC) and split into AC (fast) and DC (slow) signal components using a fast bias-T. The DC component includes frequencies of up to 20

kHz and samples the amplitude noise from the diode laser. It was also used to normalise the FM signal in subsequent analysis. The 400 MHz FM beat signal (AC component) was amplified with a gain of +24 dBm (Mini-circuits ZFL-500LN). It was then sent to the RF arm of an I&Q demodulator (Pulsar Microwave, ID-10-412, centre 400 MHz, bandwidth 50 MHz) *via* a 300-550 MHz low-high band-pass filter system (Mini-circuits LPF SLP-550 and HPF SHP-300). The I&Q demodulator consists of an RF signal input and a local oscillator (LO) reference input from the RF generator and is formed of 0° (I) and 90° (Q) power splitters and a pair of double-balanced mixers. The RF input power to the demodulator was kept below the saturation limit of -10 dBm using a combination of 1-10 dBm attenuators, as required. The LO component was passed through a DC controlled phase shifter (Pulsar Microwave Corp., ST-10, 400 MHz) before the I&Q demodulator to introduce a variable phase shift of up to 180° between the input and output signals. The variable control voltage was adjusted through the NI6014 PCI card on the data acquisition computer, with a 0.1 V increase corresponding to a typical phase change of 5°. The phase shifted output was passed through an RF amplifier (Mini-circuits ZFL-500HLN, +19 dBm) and connected to the LO arm of the I&Q demodulator through a band-pass filter and attenuated at –9 dBm to get the final LO signal to +10 dBm for optimum operation of the I&Q demodulator.

The I&Q signals were sent as separate inputs to a four-channel digital storage oscilloscope (DSO, Lecroy Wave Runner LT264, 350 MHz, 1 Gs S^{-1}) connected to the data acquisition computer *via* GPIB, using the National Instruments LabVIEW® programming environment. During experimental scans, the signals were averaged over multiple (typically 10-100) photolysis and pump laser shots in the DSO at fixed probe laser frequencies, and then passed to, and stored, on the computer. The probe laser was step-scanned in approximate 100 MHz increments over the spectroscopic line of interest by the programme. A schematic of the RF signal generation and demodulation is shown in Figure 2.7.

The electronic power supplies and RF amplifier were carefully earthed to the laser table to reduce RF ground loops. The demodulation components were housed in a shielded box acting as a Faraday cage and earthed to the laser table. This helped to eliminate RF interference from the amplifier and other sources such as the laser *Q*-switches.

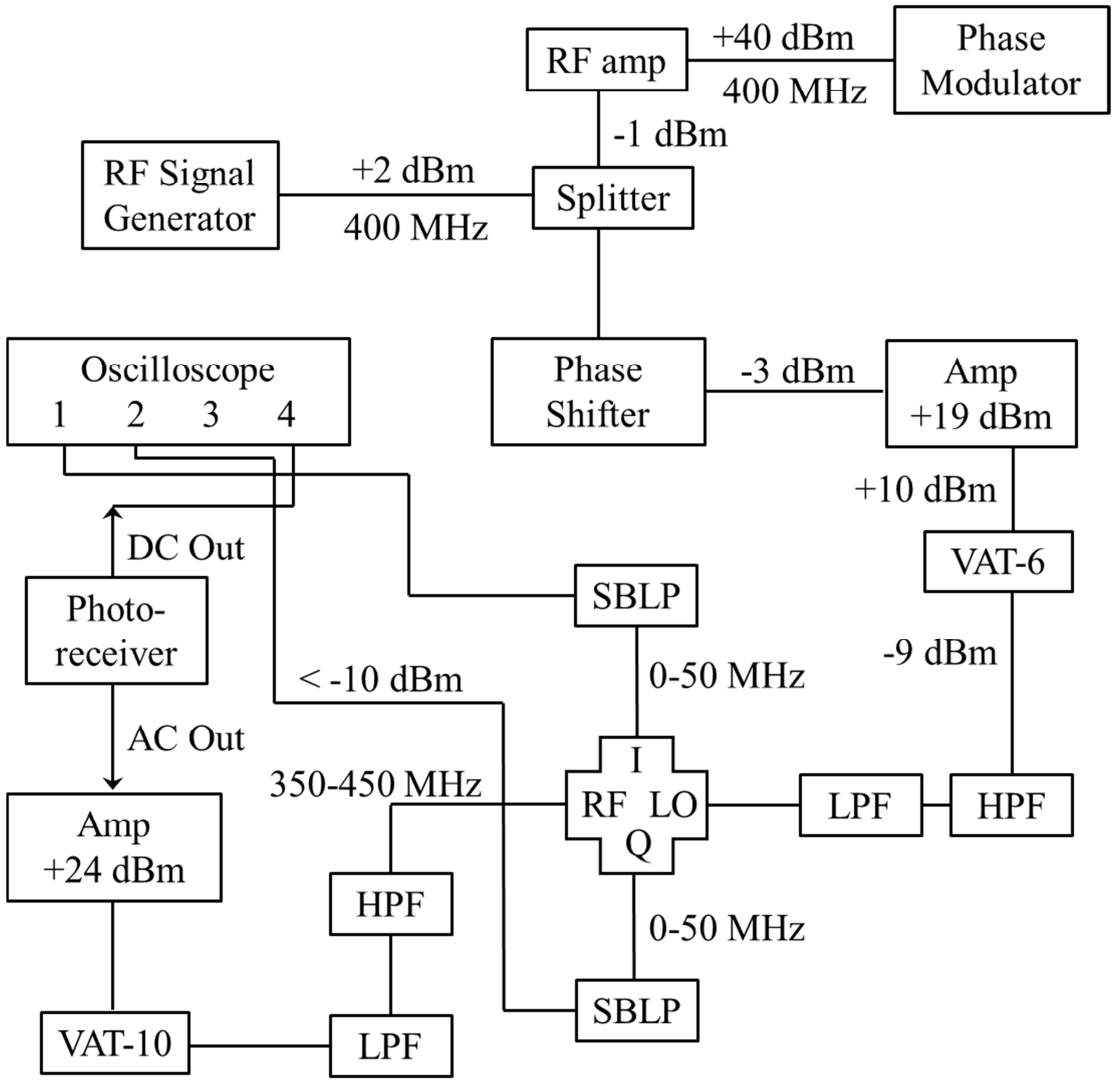

Figure 2.7 – A schematic of the radio frequency (RF) signal generation and demodulation components used in the experiments. HPF = High Pass Filter. LPF = Low Pass Filter. SBLP = Bessel-Thompson filter. VAT = Variable Attenuation.

2.4.3 Photo-Elastic Modulator (PEM)

The experiments outlined in this thesis involved the preparation and probing of rotational angular momentum anisotropy. To do this, the polarisation of the pump laser needed to be periodically rotated throughout a probe laser wavelength scan. This was acheived by passing the pump beam through a photo-elastic modulator (PEM-80, Hinds Inc.) before entering the vacuum chamber. A PEM consists of a fused silica crystal transparent to the wavelength region of the pump laser. The crystal vibrates at its lowest frequency of standing compression soundwaves, creating a time-varying birefringence at the centre of the crystal. A quartz transducer attached to the crystal maintains the

vibration frequency and allows the amplitude of the vibrations and hence the magnitude of birefringence to be controlled.

The crystal periodically compresses or elongates along its major optical axis in a ~50 kHz (~20 μs) cycle between relaxed-compressed-relaxed-elongated (each being 5 μs). The laser beam polarisation along this axis undergoes retardance compared to those along the other axes, producing a net change of polarisation. In the relaxed state, light passes through unchanged; when compressed, one linear component undergoes retardance; when elongated, the orthogonal component undergoes retardance. The PEM cycle is shown in Figure 2.8. The laser light can pass through the crystal at any point of the cycle.

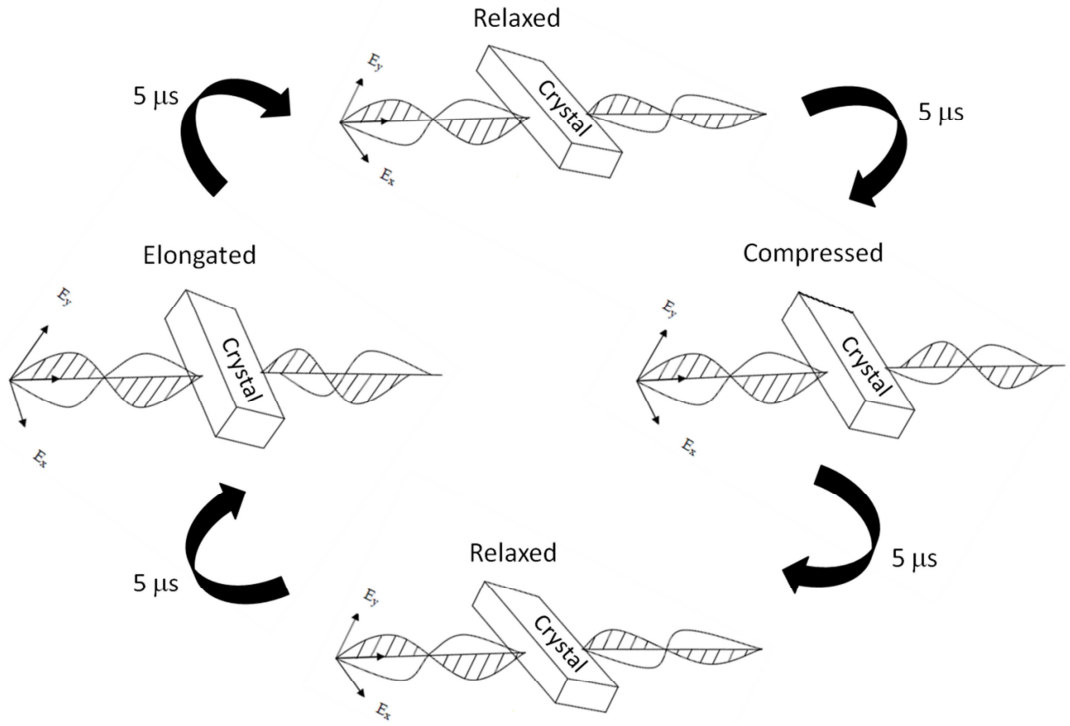

Figure 2.8 – The 20 μs cycle of the photo-elastic modulator (PEM). Relaxed: component waves are in-phase. Compressed: x-component wave leads, y-component wave in-phase. Elongated: x-component wave lags, y-component wave in-phase.

The PEM control unit produced a TTL output signal phase referenced to the cycle, which was sent to a counter-timer on a NI 6014 PCI card controlled by the data

acquisition computer, which down-counted the phase-reference to the 10 Hz repetition rate of the pulsed lasers. This allowed the pump laser to be triggered with respect to the PEM cycle. Therefore, by changing the triggering time of the pump laser and adjusting the retardance on the PEM unit, the PEM was able to act as a variable λ/2- or λ/4-plate, allowing the pump laser to be switched between horizontal or vertical linear polarisations or left- and right-handed circular polarisations during a probe wavelength scan. Figure 2.9 shows the retardance *vs*. time for the PEM cycle with indicators at several time points marking the polarisation states.

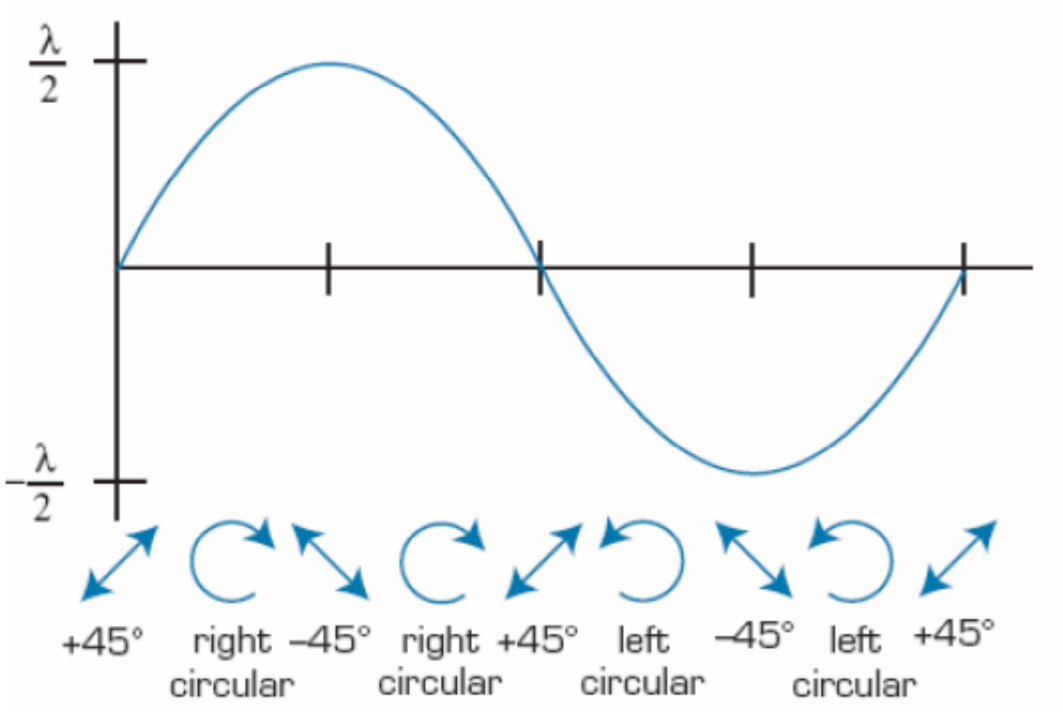

Figure 2.9 – Retardance vs. time for the PEM cycle with indicators marking the polarisation states. Taken from reference 63.

2.4.4 Laser Timings

The photolysis and pump lasers were timed according to the PEM compression cycle using a four channel digital delay generator (SRS DG535) under experimental software control (GPIB under LabVIEW®). The various channels of the delay generator are defined as follows:

***t*₀** – Counter-timer trigger phase-referenced to the PEM cycle (input).

A – Photolysis laser flashlamps (output).

B – Photolysis laser *Q*-switch (output).

C – Pump laser flashlamps (output).

D – Pump laser *Q*-switch (output).

Delay A was timed relative to t_0, delays B and C relative to delay A and delay D relative to delay C, as shown in Figure 2.10. Delay D determined when the pump laser fired through the PEM crystal, and the oscilloscope was triggered from either delay B or D. In a wavelength scan, both signal and background traces were acquired sequentially at each probe laser step (see Chapter 3). For the signal traces, the *Q*-switch timings of the photolysis and pump lasers were optimised and set at 298 μs and 178 μs, respectively. The timings of delays B and D with respect to t_0 were therefore made by adjusting delays A and C (flashlamp times). For the background traces, the pump laser *Q*-switch delay was moved to 98 μs, resulting in no pump laser light output, and all other delays were kept the same as for the signal trace set-up. This ensured that any reproducible RF noise produced by the pump laser *Q*-switch (a significant noise source in this apparatus) was captured in the background scans.

The photolysis-pump laser delay (Δt) was optimised for the Ar, N_2 and CO_2 colliders to ensure translational and rotational thermalisation of the $CN(X^2\Sigma^+)$ molecules before pumping. For the O_2 collider, Δt was varied with O_2 pressure to ensure minimal reactive removal of $CN(X^2\Sigma^+)$. This is outlined in Section 4.3.

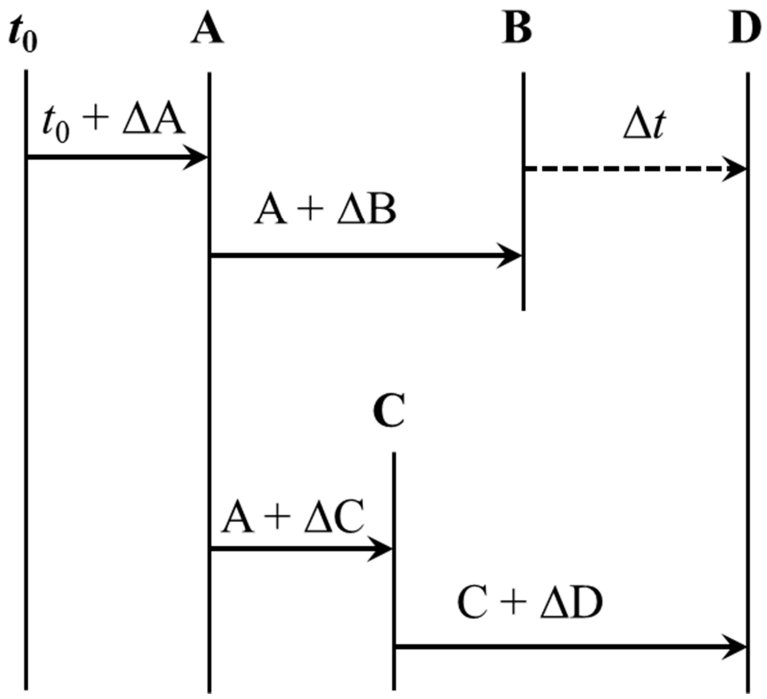

Figure 2.10 – A timing diagram for the photolysis and pump laser delays showing the various channels of the delay generator. For signal traces, the photolysis laser Q-switch delay was fixed at ΔB = 238 μs relative to delay A, and the pump laser Q-switch delay was fixed at ΔD = 178 μs relative to delay C. For background traces, ΔD was set at 98 μs and all other delays were the same as for the signal traces. Δt is the time delay between the the photolysis and pump lasers firing.

2.4.5 Pump (Dye) Laser Polarisations

The pump laser timings to switch between either of the two sets of linear or circular polarisations were set as follows. Only the oscillator output of the dye laser was used and the centre of the beam was irised to a pin hole size.

Linear Polarisations

1. The attenuated dye laser output was firstly passed through a Glan-Taylor polarising prism before the PEM or chamber entrance. A null was found by rotating the polariser and looking at the signal from a photo-diode connected to the digital oscilloscope. Once a null was found, the polariser was rotated by 90^o to transmit the laser's horizontal polarisation.
2. The polariser was then moved behind the chamber pump laser exit window and the attenuated beam monitored using the photo-diode and oscilloscope.

3. With the PEM switched on and the beam going through the centre of the PEM crystal, delay A (Section 2.4.4) was varied using a computer control program. When a null was found, the PEM retardance was adjusted to optimise the null.
4. Step 3 was repeated until the null had been optimised. The meant that the PEM was acting as a variable λ/2-plate and rotating the pump laser polarisation to that opposite of the polariser. The delay settings were saved as 'Delay 1'.
5. The polariser was rotated by 90^{o} and steps 3 and 4 repeated. The delay settings were saved as 'Delay 2'. The two delay sets had opposite linear pump laser polarisations.

Circular Polarisations

1. Steps 1 – 7 of setting the probe laser circular polarisation (Section 2.5.1) were used to set the Babinet-Soleil compensator as a λ/4-plate for the pump laser. This was performed before the PEM and chamber entrance.
2. With the pump laser beam going through the PEM crystal, steps 3 – 5 of setting the linear pump polarisations (this section) were repeated, but with the Babinet Soleil compensator before the polariser. When both nulls had been found, this meant that the PEM was acting as a variable λ/4-plate and that the two delay sets had opposite circular pump laser polarisations.

2.5 Experimental Geometries

Four experimental collinear pump-probe geometries were used in the experiments, two for alignment and two for orientation measurements, respectively. For the first set the pump beam was rotated between vertical and horizontal polarisations using the PEM, and the probe laser was kept vertically polarised. This gave parallel (∥) and perpendicular (⊥) geometries. For the second set the pump beam was rotated between left- and right-handed circularly polarised using the PEM, whilst the probe laser was passed through the Berek's compensator acting as a λ/4-plate. This gave co-rotating (co) and counter-rotating (con) geometries, as summarised in Figure 2.11.

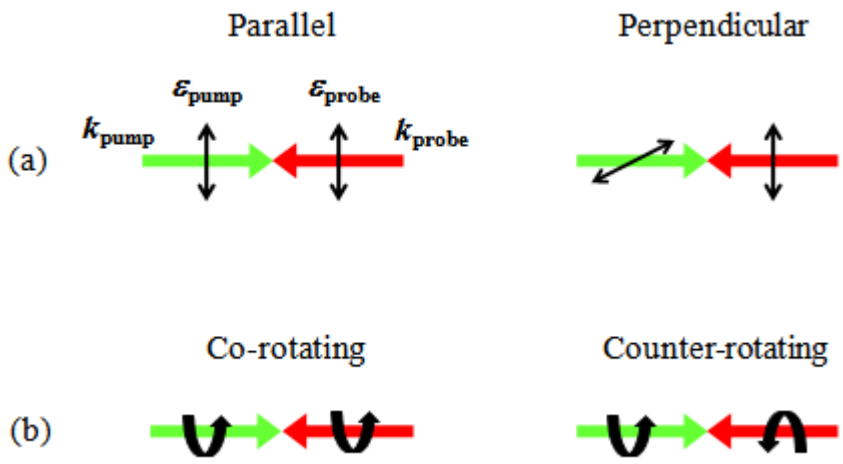

Figure 2.11 – (a) The parallel and perpendicular pump-probe geometries used in the alignment measurements. (b) The co-rotating and counter-rotating geometries used in the orientation measurements. k_{pump} is the pump propagation vector, ε_{pump} is the pump polarisation vector, k_{probe} is the probe propagation vector and ε_{probe} is the probe polarisation vector.

2.6 Spectroscopy of the CN Radical

Spectroscopy utilises the descrete energy levels of a molecule to provide an insight into electronic and nuclear motion. The CN molecule has two main electronic transitions, the violet $B^2\Sigma^+ - X^2\Sigma^+$ system and the red $A^2\Pi - X^2\Sigma^+$ system. These have both been extensively studied, with many vibrational bands and rotational transitions identified.[146] This thesis utilises the red system, which is in the visible and near-infrared regions, in a suitable wavelength range for the diode laser. The electronic ground state of CN has the configuration $(1\sigma)^2(1\sigma*)^2(2\sigma)^2(2\sigma*)^2(2\pi)^4(3\sigma)^1$, as shown in Figure 2.12. All the valence electrons are distributed symmetrically across the internuclear axis and the electronic wavefunction has positive inversion symmetry (parity). The unpaired electron has a spin of S = ½ and a spin multiplicty of $(2S+1)$ = 2. Therefore, the electronic ground state of CN is given the term symbol $X^2\Sigma^+$. The first excited state of CN has the electronic configuration $(1\sigma)^2(1\sigma*)^2(2\sigma)^2(2\sigma*)^2(2\pi)^3(3\sigma)^2$, shown in Figure 2.13. The non-zero orbital angular momentum, Λ = 1, means the term symbol now becomes $A^2\Pi$.

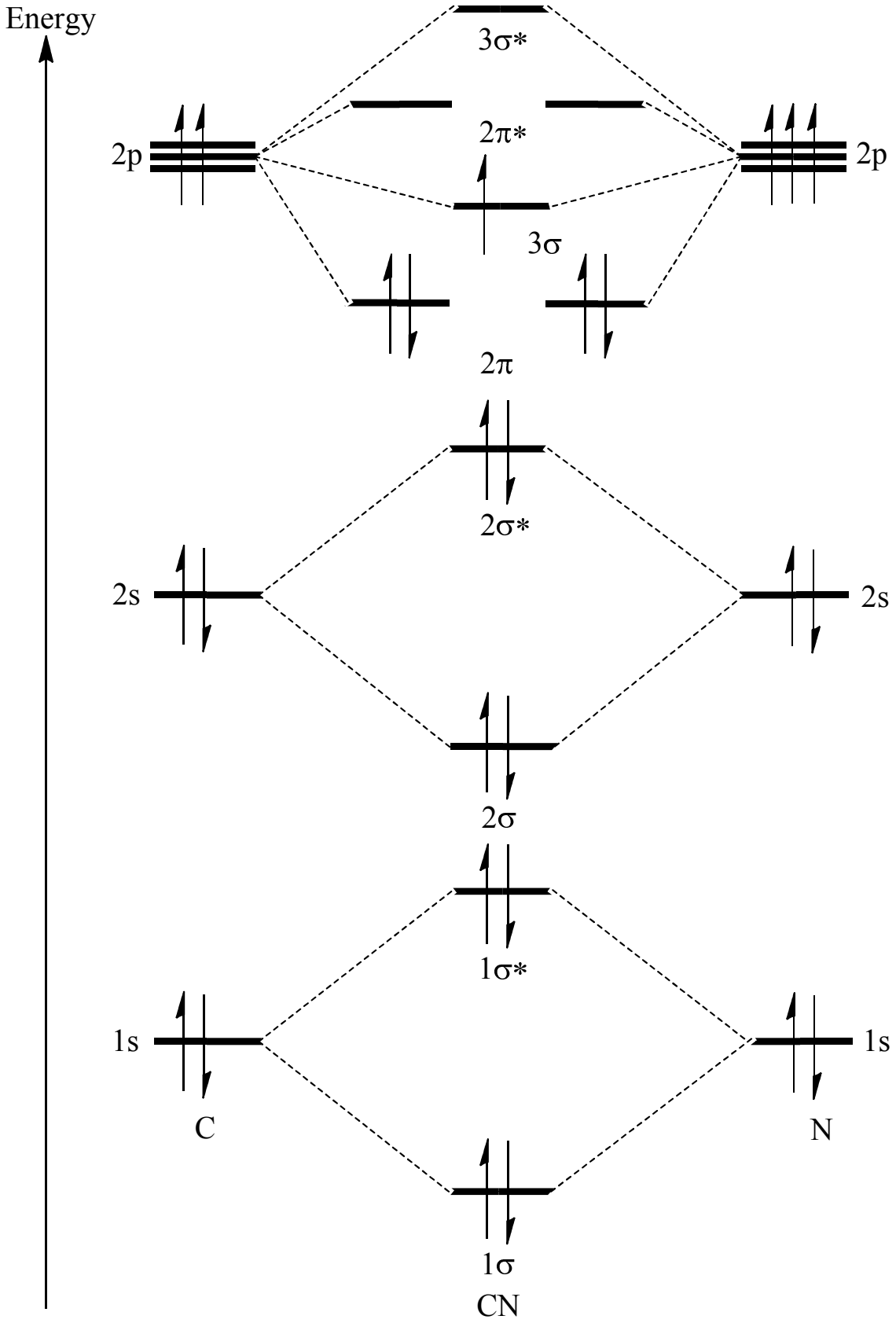

Figure 2.12 – A molecular orbital diagram for the $X^2\Sigma^+$ electronic ground state of CN.

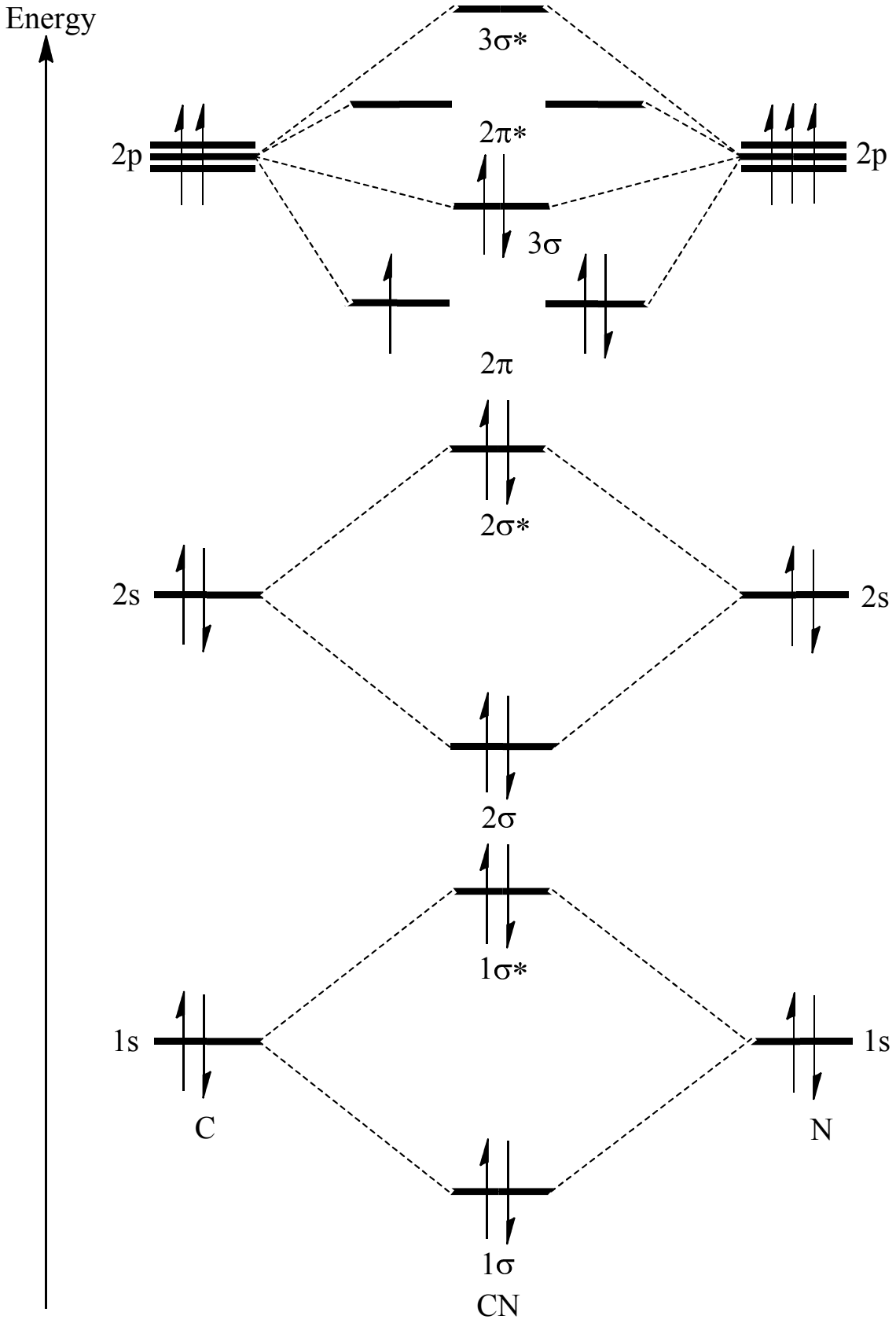

Figure 2.13 – A molecular orbital diagram for the $A^2\Pi$ first electronic excited state of CN.

CN($X^2\Sigma^+$, v = 0) molecules were produced by laser photolysis of ICN at 266 nm. These were then optically pumped to CN($A^2\Pi$, v = 4, $jF\varepsilon$) on the $A^2\Pi \leftarrow X^2\Sigma^+$ (4,0) band at

around 620 nm. The collisional evolution of the prepared or populated product levels was probed using FM spectroscopy in stimulated emission on the $A^2\Pi \rightarrow X^2\Sigma^+$ (4,2) band. These vibronic bands were chosen due to their spectroscopic accessibility, favourable Frank-Condon factors and because the $X^2\Sigma^+$ $v = 2$ ground state is relitively unpopulated from the photodissociation step.[227] The pump and probe steps are shown on the CN potential energy curves in Figure 2.14.

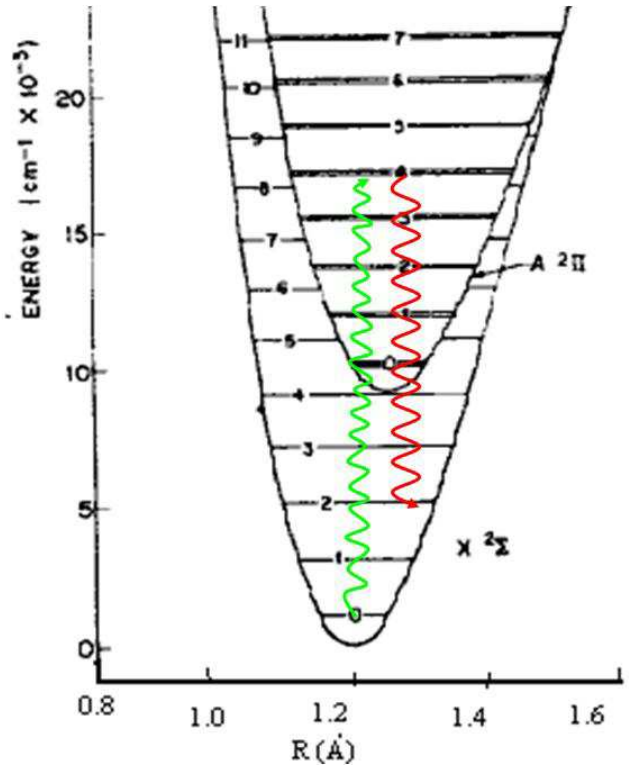

Figure 2.14 – The spectroscopic pump (4,0) (green) and probe (4,2) (red) CN $A^2\Pi$-$X^2\Sigma^+$ vibronic transitions used in the experiments of this thesis. The CN potential energy curves were provided from reference 63.

Being an open-shell diatom, CN possesses electronic orbital (L), spin (S) and nuclear rotation (R) angular momenta, all of which may couple through Hund's cases-(a) and (b), as described below.

2.6.1 Hund's Case-(a)

This case gives the best description for low rotation, where L and S couple strongly to the internuclear axis, r, but only have a weak interaction with R. The projection of these momenta onto r are labelled Λ and S, respectively, and they add together to give the total electronic orbital angular momentum (spin-orbit) projection, $\Omega = |\Lambda + \Sigma|$. The

coupling of Ω with R gives the total rotational angular momentum vector, j, with $j \geq \Omega$, as shown in Figure 2.15.

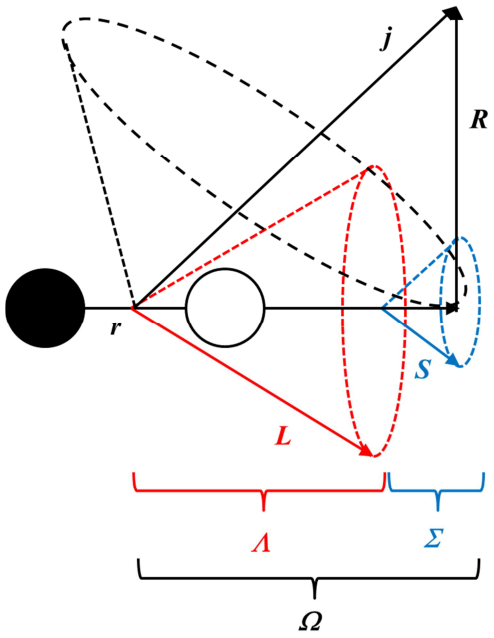

Figure 2.15 – A vector diagram outlining Hund's case-(a) coupling scheme with the notation the explained in the text.

2.6.2 Hund's Case-(b)

As the magnitude of rotation increases, the magnetic field arising from the nuclei rotating perpendicular to r causes S to uncouple from the internuclear axis, as the electrons are increasingly incapable of following the motion of the nuclear framework.[228] This means Ω is no longer well defined and the Λ and R vectors couple to form N, the total angular momentum neglecting electron spin. This then couples with S to give $j = |N + S| \ldots |N - S|$, and since CN has $S = ½$, this produces two spin-rotation manifolds $j = N + ½$ and $j = N - ½$, known as f_1 and f_2, respectively. Hund's case-(b) is summarised in Figure 2.16.

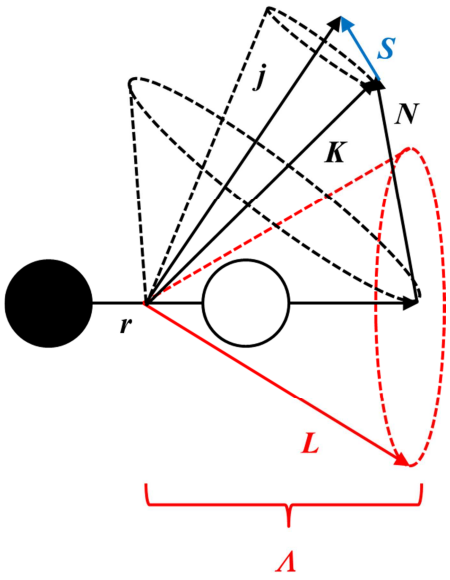

Figure 2.16 – A vector diagram outlining Hund's case-(b) coupling scheme with the notation the explained in the text.

2.6.3 Rotational Energy Structure

The ground electronic state of CN, $X^2\Sigma^+$, has $\Lambda = 0$, and so there is no projection of L along r, meaning $N = R$ and S couples to N to give the total rotational angular momentum, j. This hence follows Hund's case-(b) with f_1 ($j = N + ½$) and f_2 ($j = N - ½$) spin-rotation levels, although only f_1 exists for $N = 0$, as j cannot be negative. The CN($X^2\Sigma^+$) ground state is described with the following spectroscopic terms, where B is the rotational constant, D and H the first- and second-order centrifugal distortion constants and γ is the spin-rotation coupling constant.

$$F_1(N) = BN(N+1) - D[N(N+1)]^2 + H[N(N+1)]^3 + 1/2\gamma N$$

Equation 2.1

$$F_2(N) = BN(N+1) - D[N(N+1)]^2 + H[N(N+1)]^3 + 1/2\gamma(N+1)$$

Equation 2.2

The CN $A^2\Pi$ first excited state has $\Lambda = \pm 1$ and therefore both Hund's cases-(a) and (b) apply. For low j, the coupling is close to the Hund's case-(a) limit, as S interacts with r and the spin-orbit coupling is larger than the rotational energy splitting. This results in

two spin-orbit manifolds, $A^2\Pi_{3/2}$ (F_1) < $A^2\Pi_{1/2}$ (F_2), since Ω = 3/2 and 1/2. The spin-oribit coupling in CN($A^2\Pi$) is termed *irregular* or *inverted*, as Ω = 3/2 is lower in energy, with a negative spin-orbit coupling constant, A_e, (see Table 2.4) although the magnitude of the splitting varies with vibrational levels.[227] For high *j*, *S* uncouples from *r* and so Hund's case-(b) is more applicable.

For a stationary molecule, Λ = ±1 is doubly degenerate, however rotation lifts the degeneracy due to the total electronic angular momentum coupling to the nuclear framework. This results in each *j* level splitting into a closely spaced pair of Λ-doublets, with the splitting increasing with *j*. The Λ-doublets are distinguised by their reflection symmetry with respect to the plane of rotation, corresponding to the orbital of the unpaired electron lying either in the plane (*A′*) or perpendicular to the plane (*A″*) of rotation, as shown in Figure 2.17.[229] Each CN($A^2\Pi$, *v*, *j*) rotational level is therefore split into four fine structure levels, as described below.

1. **Spin-orbit manifold** – $\boldsymbol{F_1}$ (Ω = 3/2) and $\boldsymbol{F_2}$ (Ω = 1/2).
2. **Total parity** – Inversion symmetry of the electronic wavefunction, alternates with *j*. This is represented by symmetry labels (+) or (-). The parity of a rotational state is given by $P = (-1)^{j - \varepsilon/2}$.
3. **Total parity neglecting rotation –** Inversion symmetry of the electronic wavefunction neglecting rotation, alternates with *j*. These are given labels ***e*** and ***f***, which represent symmetry indices ε = 1 and ε = -1.
4. **Symmetry with respect to plane of rotation –** ***A′*** (in-plane) or ***A″*** (out-of-plane).

The CN($X^2\Sigma^+$, *v*, *j*) rotational levels are labelled as following:

1. **Spin-rotation level** – $\boldsymbol{f_1}$ (N + ½) or $\boldsymbol{f_2}$ (N - ½)
2. **Total parity** – even-numbered rotational levels have positive (+) parity and the odd-numbered levels have negative (-) parity.
3. **Total parity neglecting rotation** – ***e*** and ***f***, alternates with *j*.

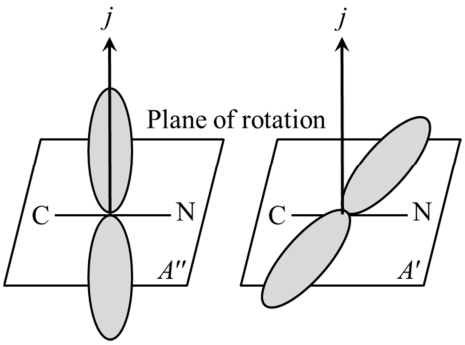

Figure 2.17 – Λ-doublets corresponding to the π–orbital being perpendicular (A″) or parallel (A′) to the plane of rotation.

The spectroscopic constants of CN $X^2\Sigma^+$ and $A^2\Pi$ are shown in Table 2.4. These were taken from reference 230.

Table 2.4 – Spectroscopic constants of CN from reference 230. All units are in cm^{-1} except for r_e, in Å. The numbers in parentheses are 2σ uncertainties.

Constant	$X^2\Sigma^+$	$A^2\Pi$
[a] r_e	1.171806(4)	1.232980(4)
[b] G_v	0.0; 4058.55176(67)	16114.7716(96)
[c] ω_e	2068.67860(59)	1813.419(42)
[d] $\omega_e x_e$	13.11735(37)	12.819(18)
[e] $\omega_e y_e$	$-6.543(64) \times 10^{-3}$	-
[f] B_e	1.89977481(23)	1.7159372(22)
[g] D_e	$6.41(31) \times 10^{-6}$	$6.1434(14) \times 10^{-6}$
[h] H_e	$6.488(44) \times 10^{-12}$	$4.20(28) \times 10^{-12}$
[i] A_e	-	-52.6872(27)
[j] γ_e	$7.463(20) \times 10^{-3}$	-
α_A	-	-0.0743(33)
α_B	0.01737135(45)	0.017237(55)
α_D	-	$1.22(10) \times 10^{-8}$
α_H	$2.64(28) \times 10^{-13}$	-
α_γ	$7.4(11) \times 10^{-4}$	-
α_q	-	$8.3(20) \times 10^{-6}$
β_B	$-2.543(22) \times 10^{-5}$	$-1.54(35) \times 10^{-5}$
γ_B	$-4.59(32) \times 10^{-6}$	$-1.53(67) \times 10^{-6}$
[k] p_e	-	$8.427(35) \times 10^{-3}$
[k] q_e	-	$-3.855(13) \times 10^{-4}$

[a] *Equilibrium internuclear separation.*

[b] *Vibronic term energy ($v = 0$; $v = 2$ for $X^2\Sigma^+$, $v = 4$ for $A^2\Pi$).*
$G_v = \omega_e(v + ½) - \omega_e x_e(v + ½)^2 + \omega_e y_e(v + ½)^3 + \ldots$

[c] *Harmonic oscillator frequency.*

[d] *First order anharmonicity term.*

[e] *Second order anharmonicity term.*

[f] *Equilibrium rotational constant.* $B_v = B_e - \alpha_B(v + ½) + \beta_B(v + ½)^2 + \gamma_B(v + ½)^3 + \ldots$

[g] *First order centrifugal distortion constant.* $D_v = D_e + \alpha_D(v + ½) + \ldots$

[h] *Second order centrifugal distortion constant.* $H_v = H_e - \alpha_H(v + ½)$.

[i] *Spin-orbit coupling constant.* $A_v = A_e - \alpha_A(v + ½) + \ldots$

[j] *Spin-rotation coupling constant.* $\gamma_v = \gamma_e - \alpha_\gamma(v + ½) + \beta_\gamma(v + ½)^2$.

[k] *Λ-doubling constants.* $p_v = p_e - \alpha_p(v + ½) + \ldots$; $q_v = q_e - \alpha_q(v + ½) + \ldots$

2.6.4 Selection Rules

In the pure Hund's case-(b) limit, the CN $A^2\Pi$–$X^2\Sigma^+$ band is strongly parallel (Σ–Σ) in character, and N is therefore a good quantum number. Only main-branch transitions are allowed, which are labelled by $\Delta j_{F_mF_n}$ or $\Delta N_{F_mF_n}$ (N.B. F can be F or f), with $\Delta j = \Delta N =$ –1, 0 and +1 denoted by the letters P, Q and R, respectively, as summarised in Figure 2.18. The main-branch selection rules are as follows:[231, 232]

$$\Delta N = \Delta j = 0, \pm 1$$

$$\Delta S = 0$$

$$\Delta \Lambda = 0, \pm 1;\ \Sigma^+ \leftrightarrow \Sigma^+, \Sigma^- \leftrightarrow \Sigma^-, \Sigma^+ \nleftrightarrow \Sigma^-$$

$$\Delta \Sigma = 0$$

$$F_1 \leftrightarrow F_1, F_2 \leftrightarrow F_2, F_1 \nleftrightarrow F_2 \text{ (N.B. also for } f_m \leftrightarrow f_n \text{ transitions)}$$

$$e \leftrightarrow f$$

$$+ \leftrightarrow -$$

In the Hund's case-(a) regime, the transitions become more perpendicular and both main- and sub-branches are allowed, making N a poorer quantum number. The sub-branch transitions are labelled ${}^{\Delta N}\Delta j_{F_m F_n}$, with the following selection rules (as outlined in Figure 2.19):

$$\Delta j \neq \Delta N$$

$$\Delta N = 0, \pm 1, \pm 2$$

$$\Delta j = 0, \pm 1$$

$$F_1 \leftrightarrow F_2, F_1 \not\leftrightarrow F_1, F_2 \not\leftrightarrow F_2$$ (N.B. F can be F or f)

For states intermediate between Hund's cases-(a) and (b), the sub-branches get gradually stronger as the pure Hund's case-(a) limit is approached.

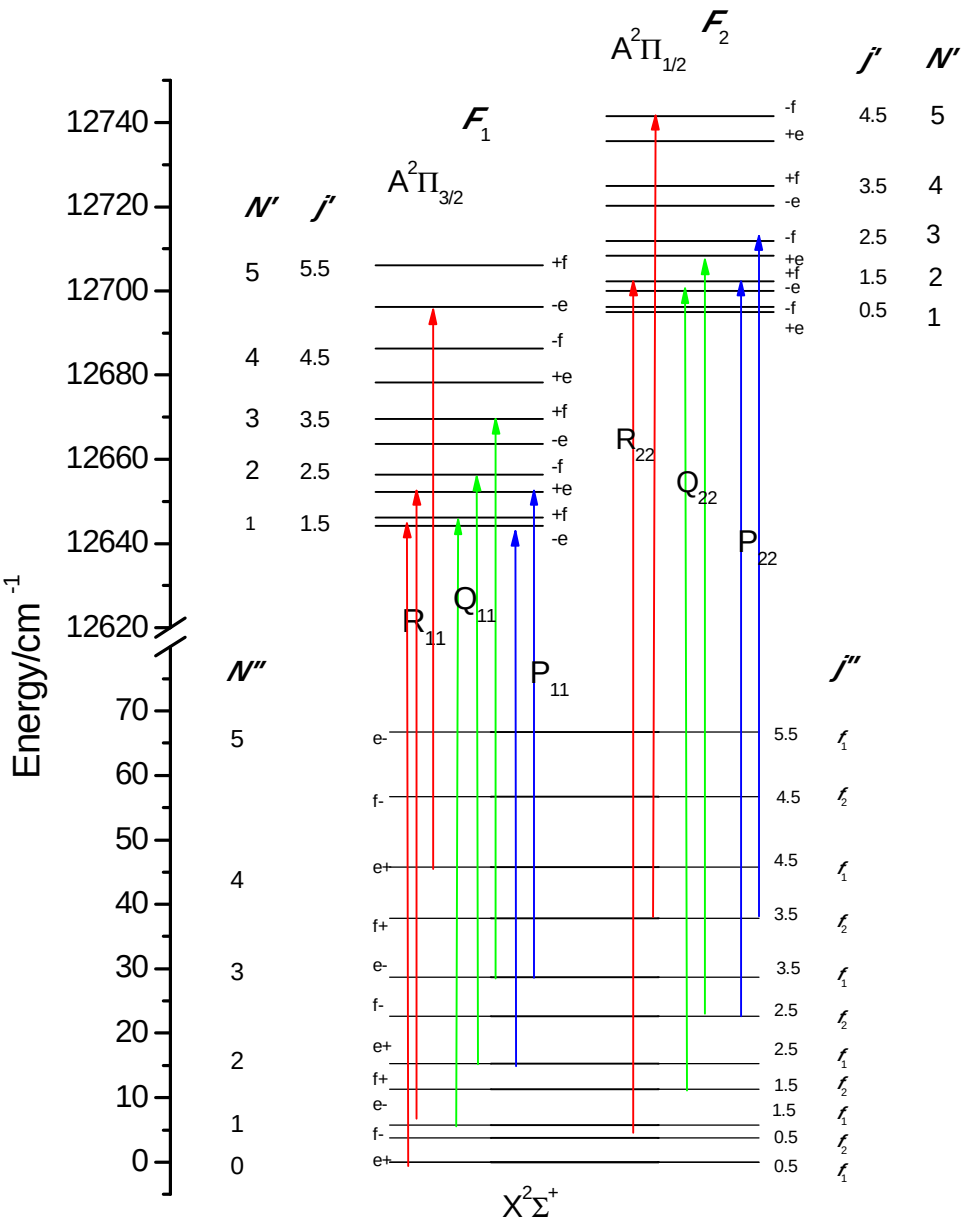

Figure 2.18 – The main-branch rotational transitions of the CN A-X band, labelled $\Delta j_{F_m F_n}$ *. The Λ-doubling in the* $A^2\Pi$ *state has been exaggerated. Adapted from reference 63.*

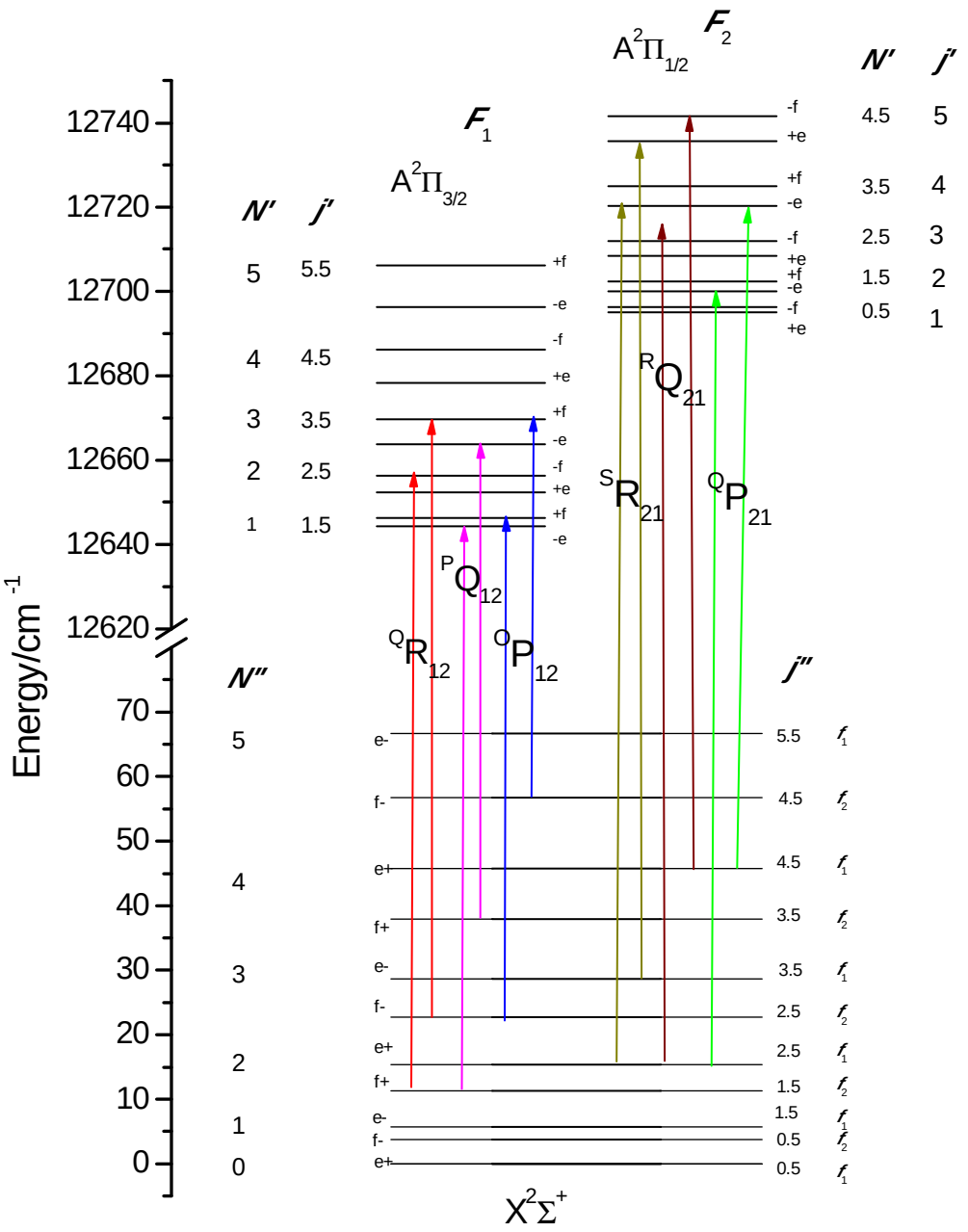

Figure 2.19 – The sub-branch rotational transitions of the CN A-X band, labelled $^{\Delta N}\Delta j_{F_m F_n}$ *. The Λ-doubling in the* $A^2\Pi$ *state has been exaggerated. Adapted from reference 63.*

Chapter 3

Frequency Modulated Spectroscopy and Experimental Data Processing

3.1 Introduction

Pulsed dye lasers and flourescence detection experiments generally have spectral bandwidths that make up a significant portion of the spectral feature. This makes them unsuited for probing weak or overlapped spectroscopic transitions and for high resolution Doppler profile analysis. Continuous-wave (cw) modulation techniques, such as Wavelength Modulation Spectroscopy (WMS) and Frequency Modulation Spectroscopy (FMS), have demonstrated increased spectral and temporal resolution compared to conventional detection methods.[233] In both WMS and FMS, the single-mode output frequency of, typically, a cw diode or Ti:Sapphire laser, known as the carrier, ω_0, is modulated at frequency ω_m to add sideband pairs at integer multiples of $\omega_0 \pm \omega_m$, with amplitudes that are a function of the modulation index, M. Preferential absorption or dispersion of individual sidebands by a spectral feature results in a heterodyne beat signal at ω_m that may be demodulated to yield a signal proportional to the differential absorption or dispersion.

The WMS and FMS techniques are differentiated by the values of M and ω_m used. The WMS method utilises a large modulation index, i.e. $M > 1$, and a modulation frequency that is much smaller than the spectral linewidth, Γ, i.e. $\omega_m << \Gamma$, where ω_m is typically a few KHz. In contrast, FMS usually has a small modulation index, $M < 1$, and a modulation frequency that is much larger than the spectral linewidth, $\omega_m >> \Gamma$,

generally in the MHz radio frequency (RF) range. The modulation in WMS is applied either directly to a mechanical component of the laser cavity, or by modulating the diode current. Although in principle current modulation could also be applied to FMS, use of an external electro-optic modulator (EOM) driven at ω_m is preferred in order to avoid unwanted experimental artifacts, such as residual amplitude modulation (RAM), which become much more significant in this frequency range, as discussed in Section 3.2.1. An EOM phase modulator consists of a non-linear optical crystal, which in this case is $LiTaO_3$, mounted between two electrode plates. An external electric field is passed along the crystal's principal axis, causing a change in the refractive index of the crystal proportional to the magnitude of the applied electric field. Light polarised along the crystal axis therefore experiences a phase shift proportional to the electrical field.[234]

Wavelength modulation spectroscopy was developed in 1964 by Bonfiglioli and Brovetto,[235] and an early example of its use is by Moses and Tang in studying the overtone absorption spectrum of benzene.[236] Frequency modulation spectroscopy was developed in the early 1980s by Bjorklund and co-workers[237-239] as an exension of the WMS technique, and has been noted to provide over a ten-fold increase in signal-to-noise over equivalent direct absorption methods with similar resolution.[240, 241] This is a result of shifting the detection frequency to the RF regime, where the laser noise is low. A notable example of the sensitivity of FMS is its use in single molecule spectroscopy.[242]

FMS employs tuneable single mode cw-lasers rather than ns-pulsed lasers, as the latter have bandwidths larger than the typical modulation frequency and often generate considerable RF *Q*-switch noise. External-cavity tuneable lead-salt diode lasers have narrow linewidths, large tuning ranges and stable outputs that can be modulated using an external phase modulator. This makes them well suited for use in FMS. Tang and co-workers demonstrated the increased spectral resolution and experimental convenience that can be achieved by using tuneable modulated laser sources.[236, 243, 244] RF heterodyne beats have also become a standard method to lock the output frequency of a laser.[245] Brewer utilised heterodyne methods in detection of optical free-induction decay signals in coherent transient spectroscopy.[246] Owyoung, Eesley and co-workers further applied heterodyne beat detection to measure separately the real and imaginary parts of the third order non-linear susceptibility.[247, 248] Continuous-wave FM lasers have also been used in studies of optical media exhibiting group velocity dispersion.[249] Optical FM techniques

have also been central to advanced precision measurements, such as in gravity wave detection,[250, 251] frequency standards[252] and measurement of minute magnetic fields.[253]

The applications of FMS discussed so far have all been time-independent measurements, where the concentration of the sample does not vary significantly on the timescale of the measurement. However, FMS may also be applied to the measurement of transient species, as is the focus of this thesis. Transient FMS has been used to study the spectroscopy and kinetics of reactive species, for example Steimle and co-workers[254] applied this technique to detect transition metal-containing molecules generated in a laser ablation chemical reaction supersonic beam expansion. Chang and co-workers utilised FMS to study the spectroscopy of bromoethylene in a slit expansion.[255] Variations of the FMS technique have also been applied to shock-tube kinetic studies[256, 257] and high resolution spectroscopy of molecular ions in a modulated discharge.[258] Field and co-workers employed laser frequency modulation in a laser guided plasma to locate Na vapour line positions.[259]

The measurement of Doppler-broadened lineshapes by FMS provides a complementary alternative to methods such as LIF, REMPI-TOF and VMI for measuring polarised photofragment correlations. Examples include CN($X^2\Sigma^+$) from ICN photolysis[159, 162, 167, 171] and singlet CH_2 detection following photodissociation of CH_2CO.[260] Most recently in our lab, Costen and co-workers utilised FMS to study the scalar and vector correlations of superthermal collisions of CN($X^2\Sigma^+$) and CN($A^2\Pi$) molecules with a range of atomic and molecular partners, including He, Ar, N_2, O_2 and CO_2.[64, 161, 198] The group further employed FMS to study the collisional evolution of rotational angular momentum in CN($A^2\Pi$)+Ar.[199]

The experiments in this thesis measure the Doppler-broadened spectroscopic lineshapes of translationally thermalised CN($A^2\Pi$, v = 4) rotational transitions, which have linewidths of FWHM ≈ 1.7 GHz.[261] The diode laser used in the experiments has a bandwidth of around 5 MHz, which is negligible compared to the much larger Doppler linewidth, and so gives full spectral resolution without contributing to the measured lineshape. Stepping of the laser wavelength then allows the entire lineshape of the spectral feature to be scanned. During the experiments, the probe laser was stepped across the transition of interest in 100 MHz increments.

Note, throughout this chapter the term *absorption* is used. However, the experiments in this thesis measured *stimulated emission*, together with the associated dispersion signals. Since absorption and stimulated emission are the reverse processes of one another, the two terms are considered interchangeable in this chapter, with stimulated emission corresponding to a positive absorption contribution.

3.2 Principles of FMS

3.2.1 Frequency Modulation and Detection

A single frequency laser beam with carrier frequency, ω_0, has an electric field given by:

$$E_1(t) = E_0 \exp -(i\omega_0 t) + c.c.$$

Equation 3.1

where E_0 is the electric field amplitude and *c.c.* the complex conjugate. The carrier frequency passes through an electro-optic phase modulator (EOM) driven at a modulation frequency ω_m, which in this work is fixed in the radio-frequency range, at 400 MHz. This results in a field that has components that are oscillating at frequencies above ($\omega_0+n\omega_m$) and below ($\omega_0-n\omega_m$) the carrier frequency, at integer (n) multiples of the modulation frequency. These additional components are refered to as 'sidebands'. The electric field of the modulated beam is now described by:

$$E_2(t) = \frac{E_0}{2} \sum_{n=-\infty}^{\infty} J_n(M) \exp\left[i(\omega_0 + n\omega_m)t\right]$$

Equation 3.2

The amplitudes of the n^{th} sidebands are given by the n^{th}-order spherical Bessel function, $J_n(M)$ where M is the modulation index, which determines the relative magnitudes of the carrier frequency and sideband pairs. The even and odd order sidebands are respectively in and out of phase, as the Bessel functions of negative integer order have the symmetry properties:

$$J_{-n}(M) = (-1)^n J_n(M)$$

Equation 3.3

The n^{th}-order sidebands are therefore equal in magnitude but opposite in phase. The interaction of a sideband with an optical sample is described by a complex, frequency-dependent transmission function:

$$T_n(\omega_n) = \exp[-\delta_n(\omega_n) - i\phi_n(\omega_n)]$$

Equation 3.4

Here, δ_n is the amplitude attenuation or gain (absorption or stimulated emission) of the sideband at frequency ω_n and ϕ_n is the phase shift (dispersion), as defined in Equation 3.5 and Equation 3.6, where L is the optical pathlength, $\alpha_n(\omega_n)$ is the absorption coefficient, $\eta_n(\omega_n)$ is the index of refraction and c is the speed of light.[237]

$$\delta_n(\omega_n) = \frac{\alpha_n(\omega_n)L}{2}$$

Equation 3.5

$$\phi_n(\omega_n) = \frac{\eta_n(\omega_n)L(\omega_0 + n\omega_m)}{c}$$

Equation 3.6

In the absence of lifetime and collisional broadening mechanisms, the spectral lineshape is determined by the projection of the velocity distribution onto the propagation axis and the resulting Doppler shift, giving rise to what is often called a "*Doppler profile*". Since the experiments in this thesis were performed under such conditions, the spectral lineshapes will henceforth be referred to as Doppler profiles. The Doppler shift (in units of m s^{-1}), δ', is defined as the fractional detuning from the linecentre times the speed of light:

$$\delta' = \frac{\omega_m c}{\omega_0}$$

Equation 3.7

FM Doppler absorption and dispersion profiles are related to integral Doppler profiles by a weighted sum of the absorption at the different sideband frequencies, shown in Equation 3.8 and Equation 3.9. Note, the term "integral" refers to conventional (non-FM) spectral features.

$$\delta'_{FM} = \sum_{n=0}^{\infty} J_n(M) J_{n+1}(M) \left[\delta_{-n-1} - \delta_{n+1} + \delta_{-n} - \delta_n\right]$$

Equation 3.8

$$\phi'_{FM} = \sum_{n=0}^{\infty} J_n(M) J_{n+1}(M) \left[\phi_{-n-1} - \phi_{n+1} + \phi_{-n} - \phi_n\right]$$

Equation 3.9

The integral dispersion is related to the integral absorption function by the Kramers-Kronig transform, where *P.V* refers to the Cauchy principle value:[160, 262, 263]

$$\phi(\omega) = -\frac{1}{\pi} P.V \int_{-\infty}^{\infty} \frac{\delta(\omega')}{\omega - \omega'} d\omega'$$

Equation 3.10

In this work, the modulation index is set to $M \approx 0.9$, i.e. $M < 1$, which means the carrier and sidebands of order n with the most significant intensities are $n = 0 - 3$, as listed in Table 3.1.

Table 3.1 – Bessel functions $J_n(M)$ of order n and argument M = 0.9.

$J_0(M) = 0.87$
$J_1(M) = 0.28$
$J_2(M) = 0.05$
$J_3(M) = 0.01$

The FM probe light is detected with a square law photodetector that produces a photocurrent proportional to the slowly varying part of the intensity, with frequency components at DC and integer multiples of ω_m, as shown in Equation 3.11.

$$\left|\overline{E}_T(t)\right|^2 = I_T(t) = E_0^2 \exp(-2\delta_0)\left\{\begin{array}{l} 1+2\cos\omega_m t\sum_{n=0}^{\infty} J_n(M)J_{n+1}(M)\left[\delta_{-n-1}-\delta_{n+1}+\delta_{-n}-\delta_n\right] \\ +2\sin\omega_m t\sum_{n=0}^{\infty} J_n(M)J_{n+1}(M)\left[\phi_{-n-1}-\phi_{n+1}+\phi_{-n}-\phi_n\right] \end{array}\right\}$$

Equation 3.11

The signal strength is proportional to the geometric mean of each sideband and the carrier. When no spectroscopic sample is present to interact with the FM probe light, the sidebands at $\pm n\omega_m$ exactly cancel and only a DC output is given. When a sample preferentially absorbs or phase-shifts a sideband of the FM probe light, the sidebands are no longer symmetric and the beam undergoes a differential change in amplitude, $\Delta\delta$, and phase, $\Delta\phi$. This results in a DC output for the slowly varying part of the electric field and an RF beat signal (AC component) at $n\omega_m$, which for n = 1 arises from heterodyning of ω_m with ω_0 and for $n \neq 0$ or 1 arises from heterodyning of the higher order sideband with the neighbouring lower-order sideband, causing amplitude modulation of the beam.

The DC and AC signal components can be separated using a fast bias-T and the AC signal sent to the RF arm of an I&Q demodulator. The I&Q demodulator has two input arms, one for the the RF signal and the other for the local oscillator (LO) reference from the RF generator. Incorporated along the input paths are two signal splitters, one with a 0^o phase shift and the other with a 90^o phase shift, followed by a pair of double balanced mixers. This gives an in-phase (I) and an orthogonal quadrature (Q) signal output. The I&Q demodulator is outlined in Figure 3.1.

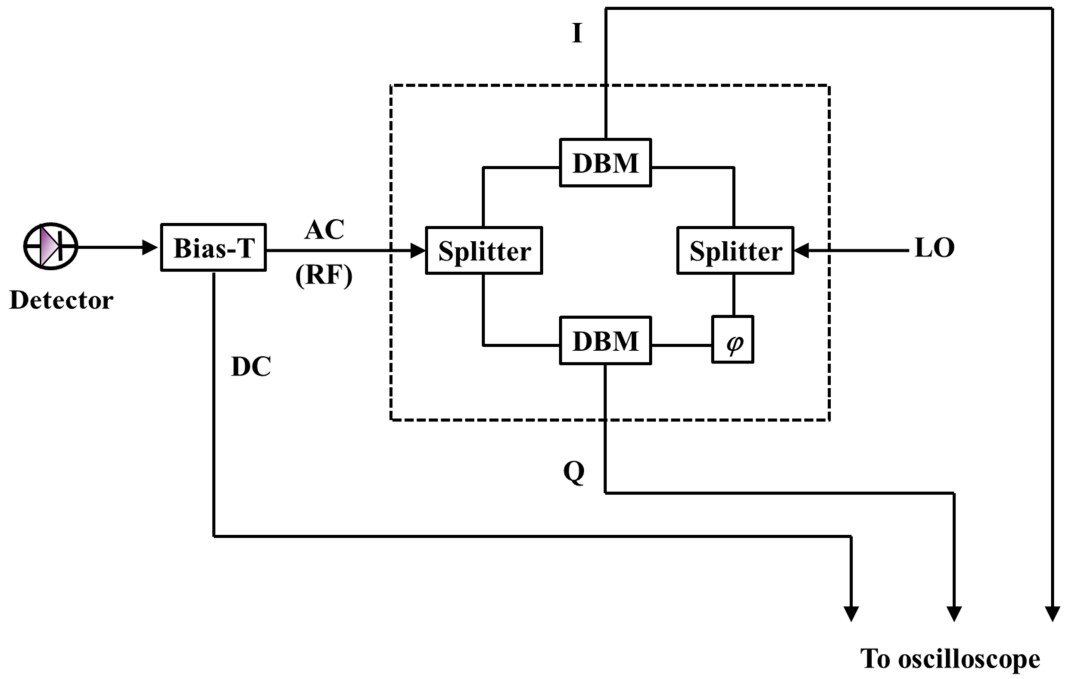

Figure 3.1 – I&Q demodulation of the RF signal (within the dashed box). There is a 90^o phase shift along the LO arm, represented by φ.

Phase-sensitive detection at ω_m produces a signal that depends on the phase difference (designated by the phase angle, θ) between the RF and LO arms of the I&Q demodulator from the RF generator. The phase angle varies with the signal pathlengths of the two input arms i.e. the electrical pathlengths following the splitter as well as the optical pathlength of the probe laser beam from the modulator to the detector. The I&Q outputs, I_{FM} and Q_{FM}, can then be described as a θ-dependent sine and cosine weighted sum of the FM absorption (A_{FM}) and dispersion (D_{FM}) components:

$$I_{FM}(\omega) = \cos\theta A_{FM}(\omega) + \sin\theta D_{FM}(\omega)$$

Equation 3.12

$$Q_{FM}(\omega) = \sin\theta A_{FM}(\omega) - \cos\theta D_{FM}(\omega)$$

Equation 3.13

Therefore, comparing Equation 3.11 to Equation 3.13 gives:

$$A_{FM}(\omega) = E_0^{\,2} \exp(-2\delta_0) \sum_{n=0}^{\infty} J_n(M) J_{n+1}(M) [\delta_{-n-1} - \delta_{n+1} + \delta_{-n} - \delta_n]$$

Equation 3.14

$$D_{FM}(\omega) = E_0^{\,2} \exp(-2\delta_0) \sum_{n=0}^{\infty} J_n(M) J_{n+1}(M) [\phi_{-n-1} - \phi_{n+1} + \phi_{-n} - \phi_n]$$

Equation 3.15

At low modulation index, $M << 1$, only the first order sidebands have significant intensity, i.e. $J_{n>1}(M << 0) \approx 0$, and so Equation 3.12 can then be written as:

$$I_{FM}(\omega) = E_0^{\,2} \exp(-2\delta_0) [M(\delta_{-n-1} - \delta_{n+1} + \delta_{-n} - \delta_n)\cos\theta + M(\phi_{-n-1} - \phi_{n+1} + \phi_{-n} - \phi_n)\sin\theta]$$

Equation 3.16

where the $\cos\theta$ term describes the imbalance between the absorption of the sidebands, and the quadrature, $\sin\theta$, the dispersion. When $M << 1$, $\omega_m << \Gamma$ and $\theta \approx 0^o$, the FM absorption lineshape to a first approximation appears as the first derivative of a normal absorption lineshape, and FM dispersion appears approximately as the first derivative of a normal dispersion lineshape.

To isolate the pure absorption and dispersion components from the I and Q channels, the phase angle, θ, needs to be determined. This is discussed in Section 3.2.2. The frequency modulation and sample interaction are outlined in Figure 3.2. The FM beam generation, detection and demodulation steps are described in more detail in Section 2.4. Figure 3.3 represents the superposition of three uniformly spaced sine waves, where the sidebands have undergone a differential absorption and phase-shift.

Further information about frequency modulated spectroscopy can be found in references 63 and 160.

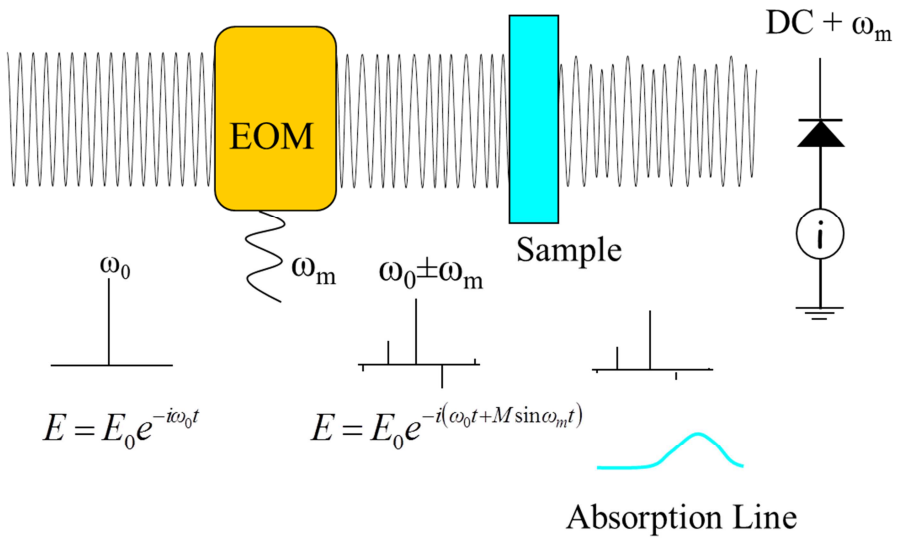

Figure 3.2 – Frequency modulation of a single-mode laser carrier frequency, ω_0, using an external electro-optic phase modulator (EOM) driven at modulation frequency ω_m, followed by differential sideband absorption by a sample, causing amplitude modulation of the composite waveform, and square law detection.

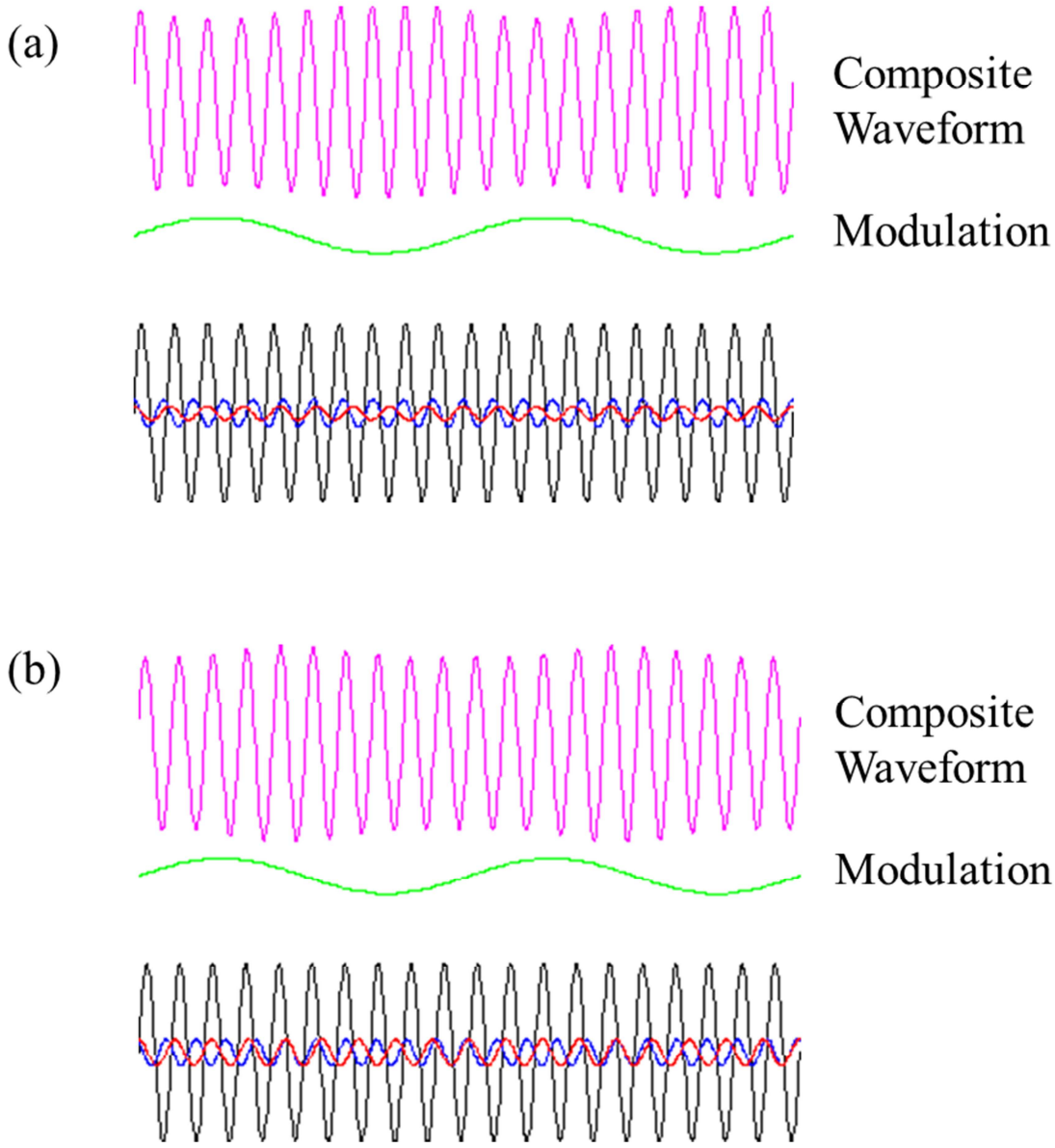

Figure 3.3 – The superposition of three uniformly spaced sinewaves. The purple trace is a composite waveform of the carrier frequency (black), ω_0, and the modulation frequency (green), ω_m. The red and blue waves represent $\omega_0-\omega_m$ and $\omega_0+\omega_m$ with *(a) unbalanced amplitudes of the two sidebands and (b) unbalanced phases of the sidebands. There is a 90^o phase shift between absorption (a) and dipersion (b). Adapted from reference 160.*

It is often difficult in practice to realise the very high theoretical sensitivity of FMS, due to background signals introduced through the experiment. Imperfect phase modulation of the laser beam causes residual amplitude modulation (RAM) at the modulation frequency, which upon phase-sensitive detection appears as a slowly varying non-zero baseline. This can be reduced by careful alignment of the phase modulator, so that the beam travels exactly down the centre of the crystal. RAM also arises due to an impure polarisation input of the laser through the phase modulator.[238] This causes polarisation

modulation of the beam as well as frequency modulation, which is turned into amplitude modulation by any phase-sensitive optic after the phase modulator. This effect is reduced by setting a polariser before the phase modulator input. RAM is also minimised by anti-reflection coating of the phase modulator crystal surface.[264-266] Low-finesse étaloning in the sample cell also causes a non-zero baseline. This may be overcome by use of wedged windows at the chamber. All of these RAM sources are cw, rather than transient, and may therefore be discriminated against in transient experiments such as those in this thesis.

Another source of noise is electromagnetic interference from *Q*-switched lasers used in the experiment, where the probe laser wavelength can end up being modulated by the *Q*-switch pick-up. This would be a problem regardless of experimental technique. This source of noise may be reduced by careful earthing and shielding of the appropriate electrical apparatus. No other noise is picked up from the FM components. Photon (shot) counting noise is minimal, as the experiment is close to the shot noise limit.

Whilst taking the above preventative measures helps to minimise unwanted background sources, any that do appear during an experimental scan are subtracted out during the analysis by the recorded background traces. Instability of the diode laser, such as multi-modal lasing or power fluctuations at certain wavelengths, can also be a problem. This can be overcome by selecting a stable working temperature and current for the diode laser.

3.2.2 Phase Correction

The FM I&Q signals are linear combinations of the absorption and dispersion components dependent upon the phase angle, θ. This means that at an arbitrary phase angle, there will be contributions from both A_{FM} and D_{FM} components to the I and Q channels. Setting θ to integer multiples of 90° (± ~5^{o}) at the start of a wavelength scan allows separation of A_{FM} into one channel and D_{FM} into the other, as seen in Equation 3.12 and Equation 3.13. This also means that the derived A&D outputs are insensitive to small changes in θ or errors in its determination.

The phase angle must be set at integer multiples of 90^{o} before an experiment and remain stable during the experiment. The phase angle is set by application of a control voltage (up to 10 V) to a phase shifter incorporated along the LO input arm before the I&Q

demodulator, allowing the LO signal to be phase-shifted relative to the RF arm. A change in 0.1 V corresponds to a phase change of 5°. With the phase angle set correctly, the absorption (stimulated emission) and dispersion signals may be separated into the I and Q channels. Figure 3.4 shows a "phase angle clock" of the different I and Q Gaussian FM lineshapes at various values of θ.

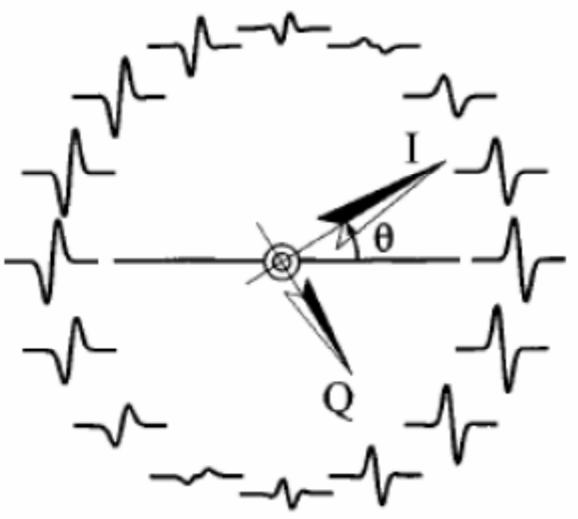

Figure 3.4 – A phase angle clock showing the different I and Q Gaussian FM lineshapes at various values of θ. The arrows indicate the I and Q lineshapes for $\theta = 32^o$. Adapted from reference 267.

The phase angle can be accurately found using a self-consistent iterative procedure,[160] as detailed in Figure 3.5. A recorded $I_{FM}(\omega)$ and $Q_{FM}(\omega)$ data set are numerically rotated by a trial phase angle, θ, to give $A_{FM}(\omega)$ and $D_{FM}(\omega)$ lineshapes:[159, 160, 267]

$$A_{FM}(\omega) = \cos\theta I_{FM}(\omega) + \sin\theta Q_{FM}(\omega)$$

Equation 3.17

$$D_{FM}(\omega) = \sin\theta I_{FM}(\omega) - \cos\theta Q_{FM}(\omega)$$

Equation 3.18

The $A_{FM}(\omega)$ component is transformed to a trial integral absorption, from which a trial dispersion lineshape is calculated using the Kramers-Kronig transform. The finite difference of this trial dispersion according to Equation 3.9 gives a trial FM dispersion, which is compared with the initial rotated FM dispersion lineshape. The best value of θ (within $\pm 0.1^o$) is then found by minimising the χ^2 between the rotated and trial $D_{FM}(\omega)$

lineshapes. This routine is performed using a custom written LabVIEW® program and typically takes only a few seconds of computer time. The phase angle may be optimised by adjusting the phase voltage in subsequent scans and repeating the phase angle finding procedure. Once the phase angle is set at 0^o (or integer multiples of 90^o), the corresponding phase voltage can be used for all subsequent scans, provided that the optical and electrical paths of the RF and LO signals are not significantly altered. The front panel of the phase angle finder routine is shown in Figure 3.6.

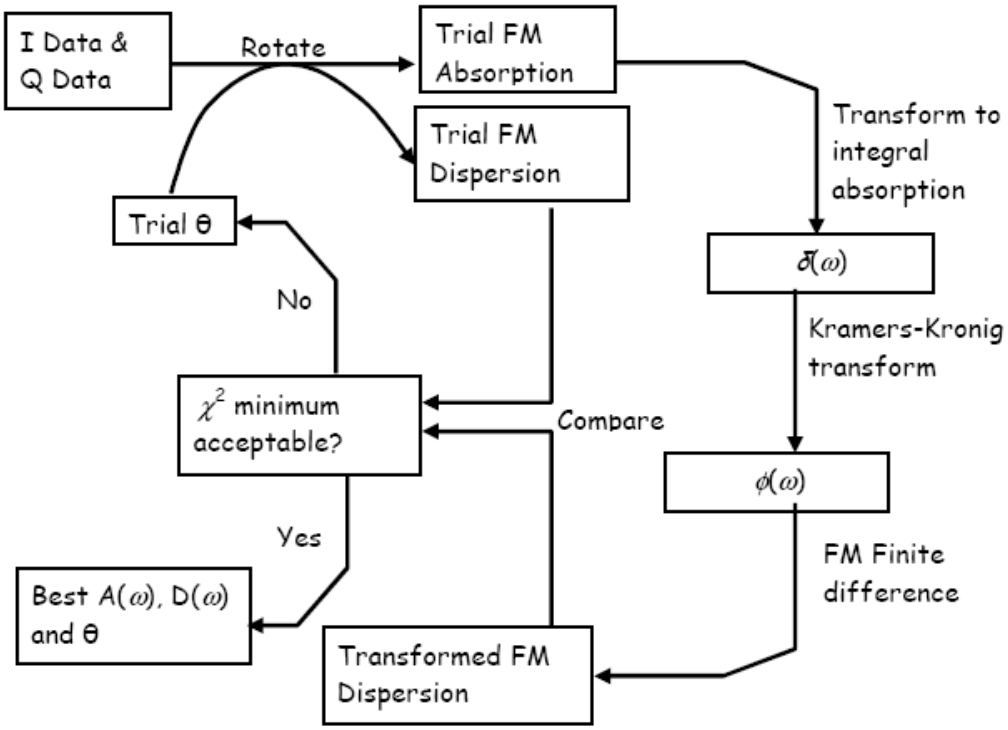

Figure 3.5 – The algorithm used to determine the phase angle, θ, from $I_{FM}(\omega)$ and $Q_{FM}(\omega)$ data. Adapted from references 63 and 160.

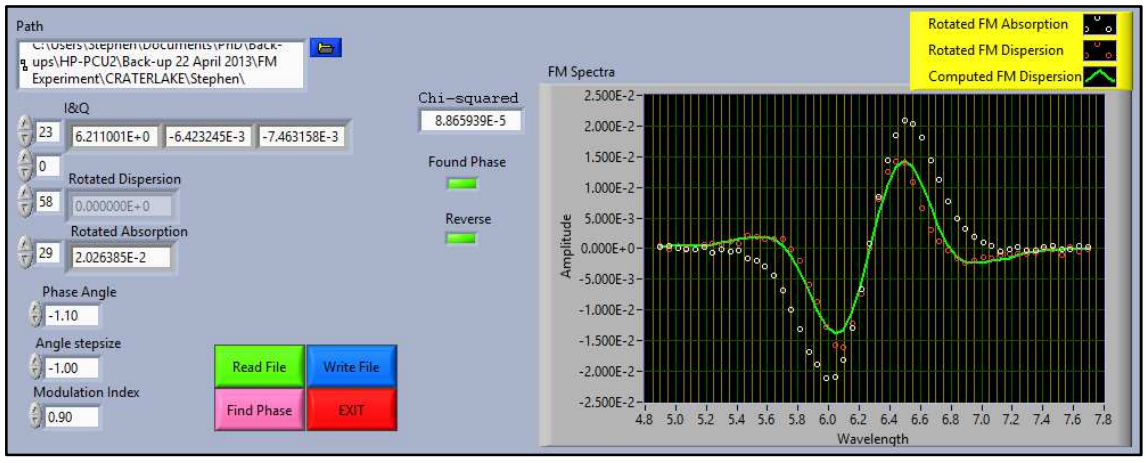

Figure 3.6 – The front panel of the phase angle finder LabVIEW® routine.

3.3 FM Signal Processing

This section outlines the procedures required to process the raw experimental I and Q data into population, orientation and alignment time traces suitable for further kinetic analysis. All data processing and analysis was performed using custom-written LabVIEW® routines developed by Dr. Matthew L. Costen at Heriot-Watt University.

The experiments described in this thesis concern the optical preparation of a rotational population and anisotropy in CN($A^2\Pi$, v = 4) from an initially isotropic sample of CN($X^2\Sigma^+$) in a thermal bath of collider gas. Two sets of experiments were performed, the first probing the total population removal and depolarisation of orientation and alignment from a prepared rotational level and the second probing the collisional RET and polarisation transfer from an initial rotational level to nearby rotational levels within CN($A^2\Pi$, v = 4).

The collisional evolution of the population and anisotropy were probed with an FM cw-diode laser. The probability that a molecule absorbs or emits light is proportional to the (squared) projection of the molecule transition dipole moment, μ, onto the electric vector of the the excitation light, ε (see Section 1.6.2). Since the rotational angular momentum of a molecule is related to μ through the molecular framework, interaction with polarised light can both prepare a rotational population and polarisation and probe the evolution of the polarisation of a prepared or collisionally populated product level. Measurement of the intensity of any single polarisation is not sufficient to separate the population and polarisation moments of interest.[19] For a one-photon interaction process in an isotropic collision environment, used in this work, two pump-probe polarisation geometries are needed. Also to re-state from Chapter 1, to prepare and probe a rotational orientation (tensor rank K = 1), circular laser polarisations are required, and for a rotational alignment (K = 2), linear laser polarisations are required. Two sets of polarisation geometries were therefore used, *parallel* (∥) and *perpendicular* (⊥) for the alignment measurements, and *co-rotating* (*co*) and *counter-rotating* (*con*) for the orientation measurements, as discussed in Chapter 2.

The strongly saturating pump pulse could, in principle, lead to the generation of polarisation moments in the prepared level of rank $K \geq 2$.[268] However, the one-photon linear FM probe used is only sensitive to moments of rank K = 0, 1 and 2,[269] and in an

isotropic collision environment, moments of different rank cannot mix.[17] Optical excitation also imposes cylindrical symmetry upon the prepared distribution. With a linearly polarised pump, the observed signal is dependent on the population, $A_0^{(0)}$ and alignment, $A_0^{(2)}$. With a circular pump polarisation, this becomes population, $A_0^{(0)}$, orientation, $A_0^{(1)}$, and alignment, $A_0^{(2)}$. The $A_0^{(1)}$ and $A_0^{(2)}$ moments have the conventional high-*j* limits of -1 and +1, and -1 and +2, respectively. The probe sensitivity to $A_0^{(0)}$, $A_0^{(1)}$, and $A_0^{(2)}$ depends on both the spectroscopic branch used, and the relative polarisations of the pump and probe lasers. The integral intensities of the observed signals in the different experimental polarisation geometries, $I_{\parallel}$ and $I_{\perp}$, or I_{co} and I_{con} are accordingly given by:

$$I_{\parallel} = \frac{ES}{3(2j+1)} A_0^{(0)} \left[1 + h^{(2)}(j) A_0^{(2)}\right]$$

Equation 3.19

$$I_{\perp} = \frac{ES}{3(2j+1)} A_0^{(0)} \left[1 - \frac{1}{2} h^{(2)}(j) A_0^{(2)}\right]$$

Equation 3.20

$$I_{co} = \frac{ES}{3(2j+1)} A_0^{(0)} \left[1 + \frac{3}{2} h^{(1)}(j) A_0^{(1)} - \frac{1}{2} h^{(2)}(j) A_0^{(2)}\right]$$

Equation 3.21

$$I_{con} = \frac{ES}{3(2j+1)} A_0^{(0)} \left[1 - \frac{3}{2} h^{(1)}(j) A_0^{(1)} - \frac{1}{2} h^{(2)}(j) A_0^{(2)}\right]$$

Equation 3.22

Here, *E* is a constant that contains the experimental sensitivity to parameters such as optical pathlength, absolute number density and detector response; *S* is the rotational linestrength factor; and $h^{(K)}(j)$ is the rotational branch sensitivity to the moment of rank *K*.[167, 270] The $h^{(K)}(j)$ values are listed in Table 3.2, and the rotational linestrengths are listed on page 314 of reference 10.

Table 3.2 – Rotational branch sensitivities to moment of rank K, for the probed rotational level, j. Taken from references 167 and 270.

Branch		$h^{(1)}(j)$	$h^{(2)}(j)$
Abs.	S.E.		
P	*R*	$(j+1)[j(j+1)]^{-1/2}$	$-(j+1)/(2j-1)$
Q	*Q*	$[j(j+1)]^{-1/2}$	1
R	*P*	$-(j+1)[j(j+1)]^{-1/2}$	$-j/(2j+3)$

Photolysis of ICN at 266 nm produces a small fraction of $CN(X^2\Sigma^+)$ in $v = 2$,[169] resulting in an unwanted background absorption signal underneath the $CN(A^2\Pi)$ (4,2) stimulated emission signal. Other undesirable background sources include possible electrical *Q*-switch noise from the pulsed lasers used in the experiment. Therefore, at each probe wavelength step, four experimental time-traces were acquired sequentially: pump-induced signal and then background for the first geometry; followed by pump-induced signal and background for the second geometry. The wavelength scans were stored as data files on the experimental computer for future analysis. The cw-probe method and the typical equilibration timescale at the collider pressures used of < 10 μs meant that the complete time evolution of the signal including a short pretrigger period was acquired for each pump laser pulse by the digital storage oscilloscope, with a time resolution of 1 ns.

The full background-subtracted (signal trace minus background trace) I and Q signals and corresponding time-traces for a single polarisation geometry could be viewed in a custom-written LabVIEW® program for subsequent phase angle finding. This also enabled both the pre-pump baseline and pump-induced signal start and finish gates to be determined, allowing the average baseline in the pretrigger gate to be subtracted from the timetrace for each wavelength point and the time range for subsequent analysis to be defined. These gates should be the same for all experiments that are directly compared to one another, for example total removal at different collider pressures, and of particular importance for the RET and polarisation transfer experiments, where both the initial and product state data sets must have the same starting points (t_0). The front panel of this data interpretation program is shown in Figure 3.7. The wavelength and time signal traces could be written as I and Q output files suitable for loading on to the *phase angle finder* program, discussed in the previous section.

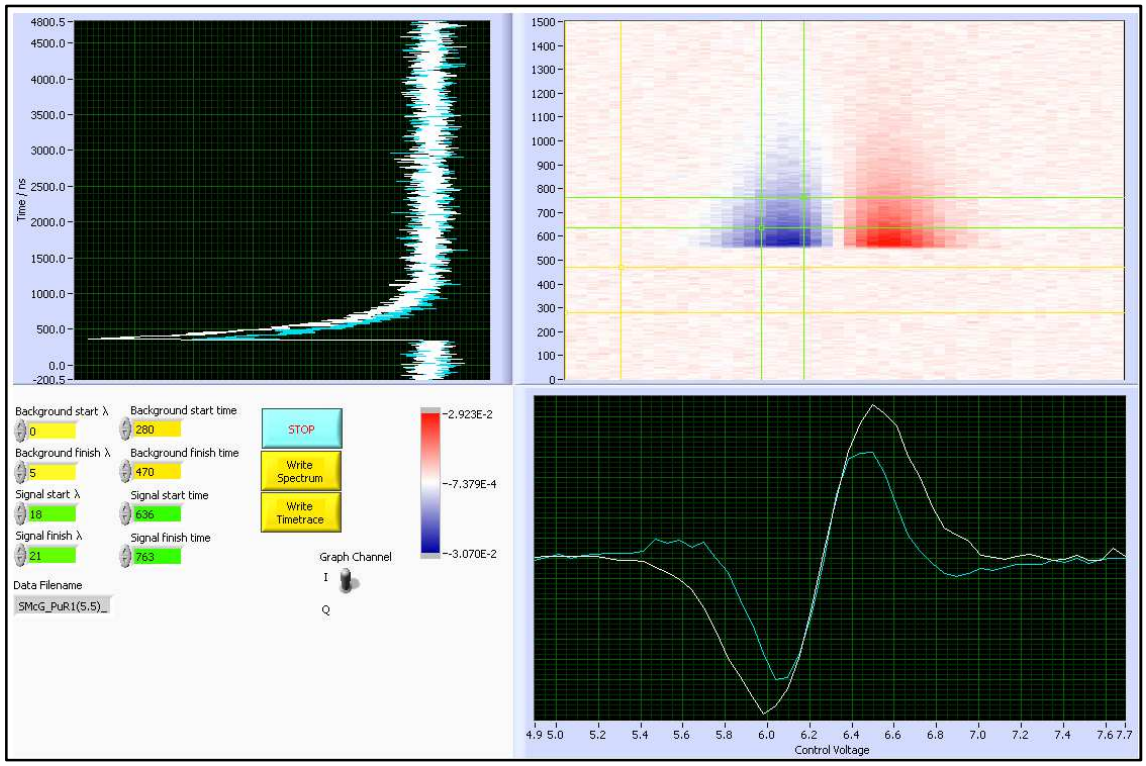

Figure 3.7 – The front panel of the data interpretaion LabVIEW® program used to look at the complete wavelength and time signal traces from the I and Q channels of a FM wavelength scan. This example is of the CN($A^2\Pi$, v = 4, j = 6.5 F_1e) prepared level on the $R_1(5.5)$ spectroscopic transition for a circular polarisation geometry. Top right: The I channel signal (z-axis) as a function of time (y-axis) and diode control voltage (x-axis), which is proportional to the laser wavelength. The yellow lines are the baseline pre-pump start and finish gates, and the green lines are the signal start and finish gates. This panel can be switched between I and Q channels. Top left: the time trace between the green time gates with the yellow baseline gates subtracted. Bottom right: the signal trace between the green signal gates with the yellow baseline gates subtracted. The white time and signal traces are from the I channel and the blue traces are from the Q channel. Bottom left: the baseline and signal gate values and program controls.

After the phase angle had been found, all the data sets for a particular experimental scan were loaded into the *kinetic data processing* program. In total there are eight input files, comprising of the two-dimensional pump-induced signal and background data sets and the monitor étalon traces from the optical spectrum analyser (OSA), for each polarisation geometry. Other inputs needed for the data processing included: The baseline gates (the range of which was determined from the data interpretation program described above); the time-range required for the kinetic analysis; the previously determined phase angle; the transition linecentre frequency (cm^{-1}); the spectroscopic

branch and rotational level of the transition; and the high and low Doppler limits (m s^{-1}) of the processed spectra. The processing routine was capable of fitting both isolated main branch, or mixed main and sub-branch transitions, with the latter requiring the separation frequency of the main to sub-branch linecentres.

The experimental data were analysed as FM Doppler lineshapes. The acquired FM background 2-d arrays were first subtracted from the corresponding signal arrays, for each experimental geometry. The I&Q arrays were normalised by the DC voltage and then rotated by θ to yield pure stimulated emission (SE) and dispersion (D) arrays.[267] The linecentre was found by averaging a slice of data for one geometry and fitting a second-order polynomial ($y = a + bx + cx^2$) through a small selection of data points around the maximum and minimum turning points, then finding x_{max} and x_{min}. FM Doppler lineshapes for sequential user-selected time-averages (slices), usually 10 ns, of the SE and D signals for each of the two geometries were constructed as the difference of the averaged 'slice' signal and the baseline average over the relevant pre-trigger gate for each wavelength point. The 10 ns range for the averages was chosen as a compromise between the time-resolution of the experiment and the desired signal-to-noise of the kinetic traces. The pump laser has approximately Gaussian pulses of full width half maximum ≈ 10 ns, whilst the probe beam path in the chamber is ≈ 4 m (double-pass), giving a temporal overlap of the pump and probe which is also ≈ 12 ns. Consistent with this, the 10% – 90% rise time of the signals was typically found to be ≈ 12 ns. The overall signal is the result of the finite difference of the signal at the sideband positions. The 400 MHz FM sidebands were stepped across a spectral feature in 100 MHz increments. The true wavelength *x*-axis was therefore found using the acquired monitor étalon traces by identifying sets of sideband and carrier peaks, monitoring the stepping of these across the wavelength scan and then spline interpolating the data onto the linearised axis. High and low Doppler limits were set on the linearised wavelength axis in order to truncate the spline interpolated signal onto the data set.

For the linear polarisation measurements, integral Gaussian Doppler lineshapes were constructed for the the || and ⊥ geometries according to Equation 3.23,[267] whose widths depend on the translational temperature, *T*:

$$\delta(\omega) = \exp-\left(\frac{(\omega-\omega_0)}{(\omega_0/c)\sqrt{2kT/m}}\right)^2$$

Equation 3.23

where δ_0 is the amplitude attenuation at ω_0, the linecentre frequency, $\sqrt{2k_BT/m}$ is the most probable speed in a thermal distribution, and m is the mass of CN. The integral areas of the lineshapes, given by Equation 3.19 and Equation 3.20, were then simulated from assumed $A_0^{(0)}$ and $A_0^{(2)}$ moments, together with an assumed translational temperature. The polarisation sensitivities, $h^{(2)}(j)$ and rotational linestrengths, S, were calculated from the initial ground state j and spectroscopic branch probed. The integral Gaussian lineshapes were then transformed into FM SE and D lineshapes by finite difference according to Equation 3.8 and Equation 3.9, and were then simultaneously least-squares fitted to the experimental FM lineshapes, using the Levenberg-Marquardt (LM) method, to optimise the moments and translational temperature. The previous x-axis linearisation gave the experimental and simulated FM spectra a common true x-axis, so that they could be directly compared at each averaged time step and the least-squares reduction performed. This fitting procedure was applied to each averaged slice over the selected time range, and resulted in time-dependent population and alignment kinetic traces, and the time-dependence of the translational temperature, which were stored for further analysis. The FM SE & D Doppler profiles for each slice in each geometry and the resulting fits were also stored for further inspection and presentation.

The circularly polarised geometries have opposite sensitivities to $A_0^{(1)}$, but equal sensitivities to $A_0^{(2)}$, as seen in Equation 3.21 and Equation 3.22. It is therefore not completely possible to isolate the $A_0^{(1)}$ dependence of the signal. As seen in Chapter 4, the initial alignment generated in the linear pump experiments was typically $A_0^{(2)} \leq$ -0.3. However, this is defined in a laboratory frame referenced to the electric vector of the pump light. The correct laboratory frame for $A_0^{(2)}$ is the pump quantisation axis, which for the the circular pump polarisations is either parallel or anti-parallel to the pump propagation direction. As a result, the alignment is multiplied by a factor of -½.[167] Also, for the P- and R-branches probed, $h^{(2)}(j) \approx$ -½. The overall alignment contribution to the orientation measurements is therefore:

$$-\frac{1}{2}h^{(2)}(j)A_0^{(2)} \approx -\frac{1}{2}\left(-\frac{1}{2}\right)\left(-\frac{1}{2}\right)(-0.3) \approx +\frac{3}{80}$$

Equation 3.24

The experimental measurements of the orientation depolarisation, discussed in Chapter 4, involved probing exclusively on the R_1 branch, where all of the transitions are spectrally isolated. In this case, the experimental data were treated in the same fashion as those for linear polarisations, up to the formation of averaged FM SE and D Doppler profiles. Simulated FM SE and D line shapes were again least-squares fitted to the data, but in this case the LM minimisation was applied directly to the intensities of the integral-space Gaussians, I_{co} and I_{con}, as well as the translational temperature. The resulting time-dependent kinetic traces were used to form the quantity C (Equation 3.27), derived using Equation 3.21 and Equation 3.22, and defined as:[271]

$$I_{co} - I_{con} = \frac{ES}{3(2j+1)}A_0^{(0)}\left[1 + 3h^{(1)}(j)A_0^{(1)}\right]$$

Equation 3.25

$$I_{co} + I_{con} = \frac{ES}{3(2j+1)}A_0^{(0)}\left[2 - h^{(2)}(j)A_0^{(2)}\right]$$

Equation 3.26

$$C = \frac{I_{co} - I_{con}}{I_{co} + I_{con}} = \frac{3h^{(1)}(j)A_0^{(1)}}{2 - h^{(2)}(j)A_0^{(2)}}$$

Equation 3.27

In principle, the time-dependence of the alignment, separately determined from the linear polarisation measurements, could then be introduced to determine the time-dependent orientation from C. In practice, however, the small magnitude of the initial alignment, given in Equation 3.24, meant that this correction was insignificant under the typical signal-to-noise observed. Ignoring the small alignment contribution, the parameter C was therefore considered to be directly proportional to the orientation, $A_0^{(1)}$. Similarly, the sum I_{co} + I_{con} (Equation 3.26) was treated as proportional to the population, $A_0^{(0)}$.

This approach could not be used in the orientation transfer experiments described in Chapter 5, as it was necessary to use some main+sub-branch blended transitions to acquire complete *j*-dependent data sets. For these experiments, the data were treated in the same manner as for the linear polarisations, this time using the LM minimisation routine to optimise the $A_0^{(0)}$ and $A_0^{(1)}$ moments, in Equation 3.21 and Equation 3.22, and the translational temperature. As detailed above for the earlier depolarisation analysis, it was assumed that the alignment contribution to the signal intensity was negligible. Figure 3.8 shows an example of the fitting routine from the kinetic data processing program front panel, where in this case the circular polarisation geometries have been fitted to find the $A_0^{(0)}$, $A_0^{(1)}$ and T time traces for the j = 6.5 F_1e prepared level of CN($A^2\Pi$, v = 4) on the $R_1(5.5)$ transition colliding with 200 mTorr CO_2.

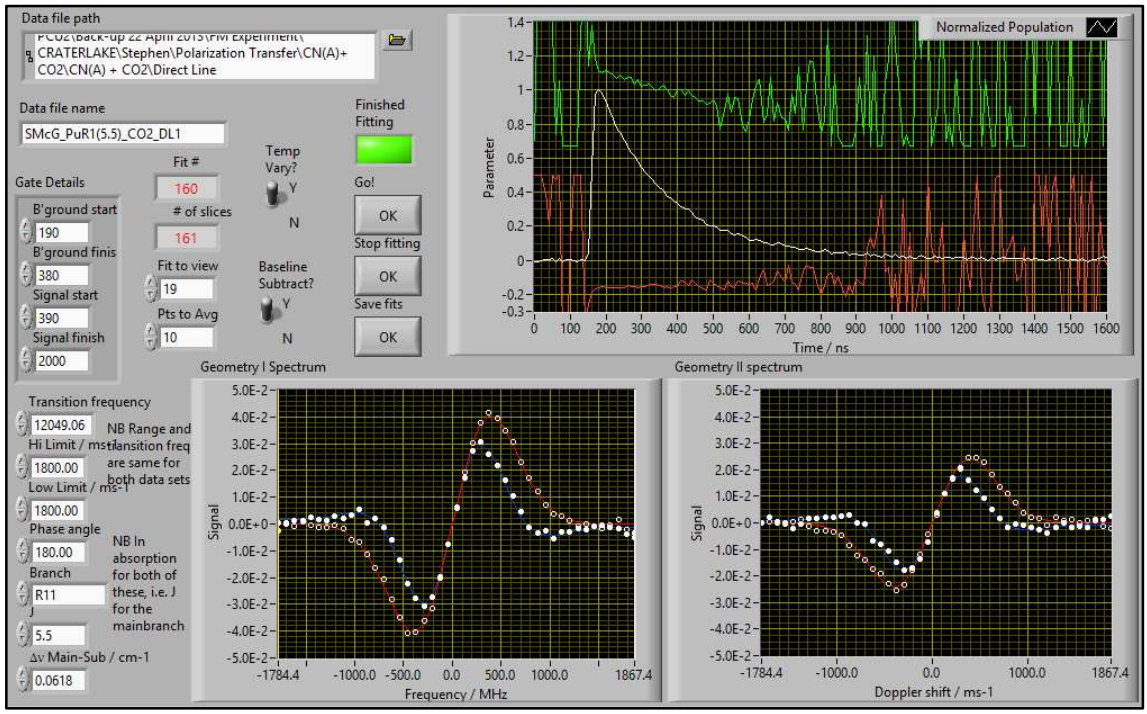

Figure 3.8 – Example kinetic processing of the circular polarisation I and Q arrays for the CN($A^2\Pi$, v = 4, j = 6.5 F_1e) prepared level, using the $R_1(5.5)$ spectroscopic transition, colliding with 200 mTorr CO_2, as explained in the main text. Top right panel: $A_0^{(1)}$ orientation time trace (red), $A_0^{(0)}$ population time trace normalised by the peak population (white) and the temperature time trace normalised by 298 K. The population and temperature traces were normalised for representation in the same panel. Bottom panels: individual counter-rotating and co-rotating FM SE (filled points) and D (open points) Doppler lineshapes with fits (red and blue lines), as

explained in the main text. The lineshapes and fits correspond to individual 10 ns slices of the time traces near the population peak.

3.3.1 Summary

The FMS kinetic processing procedure is summarised below in Figure 3.9.

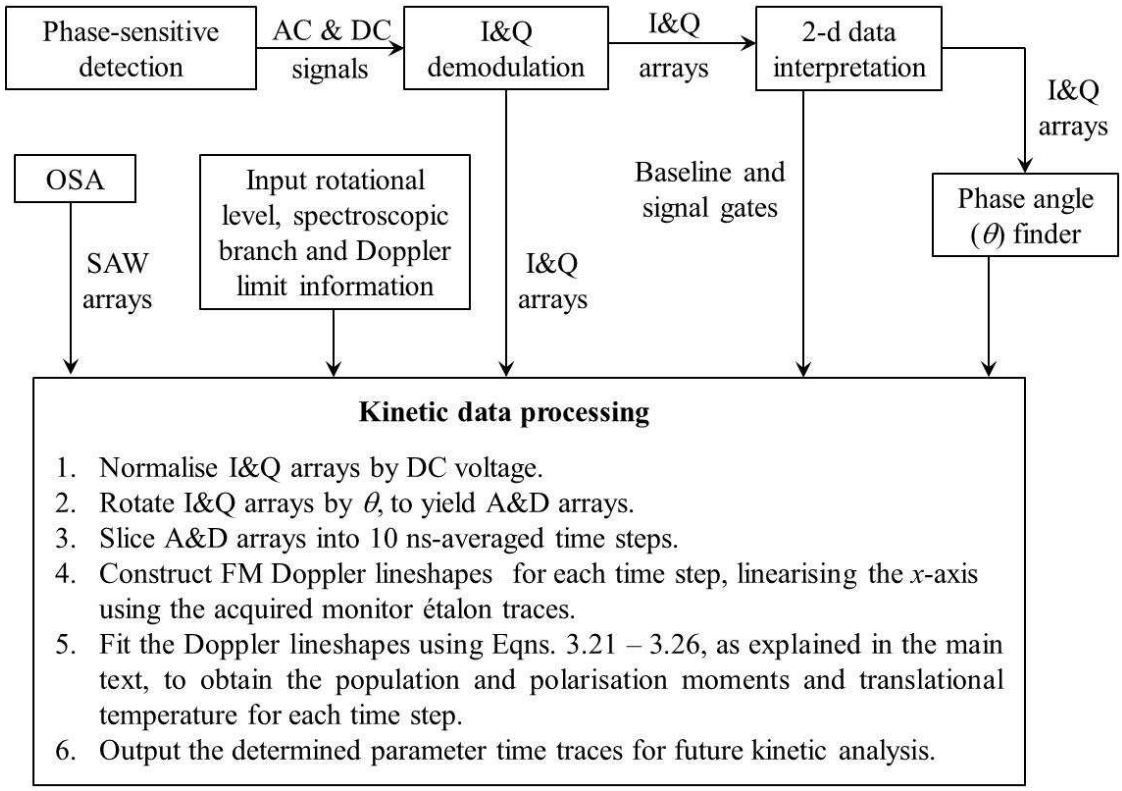

Figure 3.9 – A flow diagram for the kinetic processing of the I&Q arrays from the FMS experiment, as described in Section 3.3. SAW = optical spectrum analyser waveform, i.e. the acquired monitor étalon traces.

Chapter 4

Total Removal and Depolarisation of Rotational Angular Momentum in CN($A^2\Pi$)

4.1 Introduction

In this chapter, the FMS cw-probe technique is employed in a pulsed pump OODR set-up to measure the absolute rate constants and cross-sections for the total removal and elastic depolarisation of rotational angular momentum in CN($A^2\Pi$, v = 4, j, F_1e) upon collisions with Ar, N_2, O_2 and CO_2. Starting with a brief overview of the literature, aims and motivations behind this work, relevent experimental details are then listed and preliminary tests described that demonstrate the correct conditions were met and the desired polarised ensembles generated and probed. The raw and processed results of the CN($A^2\Pi$)+Ar measurements are then presented, followed by optimisation and detailed evaluation of the single exponential and multi-level kinetic models implemented to correctly extract and fit the phenomenological observables. The end results are then compared with complementary exact QS predictions from the best existing previous and brand new sets of *ab initio* CN($A^2\Pi$)+Ar PESs to provide a test of the latest theoretical accuracy. The QS results directly feed into full ME simulations that take into account different contributing RET and depolarisation pathways. Scaling of the experimental data to these simulations then completes the overall physical interpetation of what happens to polarised rotational angular momentum as it is removed from an initially prepared level and further assesses the approximations imposed in the experimental

kinetic fitting routines. In light of this, the study finally extends to measurements of CN($A^2\Pi$) with small molecular partners, namely N_2, O_2 and CO_2, in order to gauge the effects of increased degrees of freedom, low-order electrostatic forces and additional product branching channels. Contributions from colleagues and collaborators have been duely noted where appropriate throughout the following sections.

The collisional phenomena addressed here are ubiquitous to many important gas-phase chemical environments.[5] Small open-shell molecule and rare gas systems serve as benchmarks to develop predictive tools and test the latest in state-of-the-art scattering theory.[6] The previous Berning-Werner CN($A^2\Pi$, v = 3)-Ar potentials from 2000 produced full QS total removal rate constants ranging between $(3.6 – 3.9) \times 10^{-10}$ cm^3 s^{-1} for rotational levels near the peak of the Boltzmann distribution.[15] These were in good agreement with accompanying LIF-OODR measurements, showing only a slight (~8%) over-prediction. Later work in our group by Ballingall *et al*. utilised the FMS technique in a thermalised multi-pass configuration to study the total removal of population and alignment depolarisation in low-j F_1e manifolds of CN($A^2\Pi$, v = 4)+Ar.[199] Fast rate constants for both these processes were observed, each in the order of 10^{-10} cm^3 s^{-1}, as shown in Figure 4.1, which is surprising for a system with a relatively heavy rotor and modest attractive forces evident from the earlier potentials. This is exacerbated by recent calculations and PS experiments on the electronically and kinematically similar NO($X^2\Pi$)+Ar system, which saw much slower elastic depolarisation rate constants, around $(2 – 4) \times 10^{-11}$ cm^3 s^{-1}, across the same range of j.[136]

The experimental conditions of Ballingall *et al*.[199] were less than ideal, as the set-up limited the time resolution (~50 ns) and prevented any sensitivity to rotational orientation. The primary motivation behind the work presented in this chapter is to improve on and extend those measurements by setting up an apparatus specifically designed for polarisation measurements, with fast time resolution and orientation sensitivity. The experimental data fitting method from which the rate constants are obtained is then reevaluated and collaborations brought in to cast the results in a theortical framework.

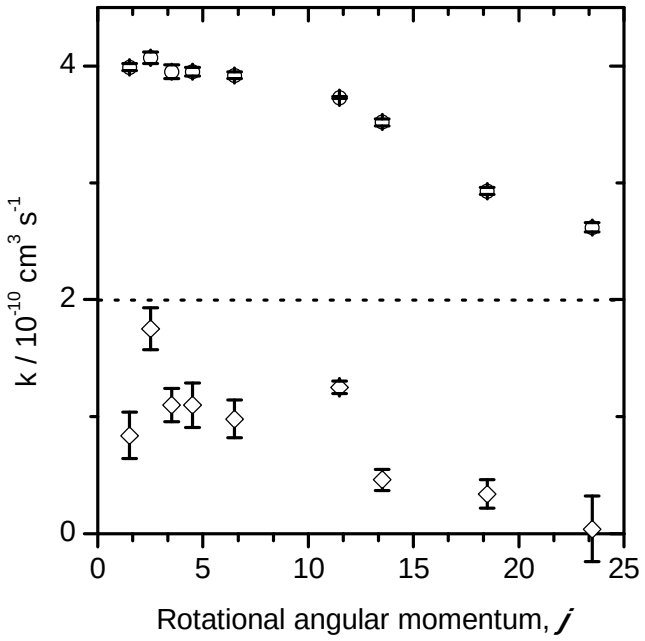

Figure 4.1 – The previously measured rate constants for CN($A^2\Pi$, v = 4, j, F_1e)+Ar total population removal (circles) and alignment depolarisation (diamonds), above and below the dotted line respectively, from Ballingall et al. using the multi-pass FMS set-up in our laboratory.[199]

Molecule-molecule collision systems present added complexity to the construction of full-dimensional interaction potentials and to the treatment of QS calculations. Spherically-averaged *ab initio* CN($A^2\Pi$, v = 3)-N_2 PESs have previously been computed by Dagdigian and co-workers. These are outlined in Chapter 5 but also addressed where relevent in Section 4.6. Molecular partners also offer additional or enhanced energy disposal pathways compared to rare gases, such as VET, EET, reactive quenching, resonant energy exchange or correlated intermolecular motions. The relative sizes of collisional rate constants for molecular partners have often been attributed to low-order electrostatic forces.[134, 135] An interesting prospect is then how these incidences unique to molecular colliders influence the measurements presented in the last parts of this chapter and whether they provide further insight into the ensuing dynamics.

4.2 Experimental Details

The experimental details have been discussed in Chapter 2 and the FMS technique introduced in Chapter 3. Photolysis of ICN at 266 nm produced CN($X^2\Sigma^+$, v = 0). For

Ar, N_2 and CO_2 collision partners, a typical 30 μs photolysis-pump delay ensured complete translational thermalisation and substantial thermalisation of the rotational distribution. The post-photolysis delay was varied with O_2 collider pressure to provide ~5 pre-pump collisions, which serves as a compromise between reactive loss and thermalisation of CN($X^2\Sigma^+$). Section 4.3 provides tests of the isotropy and thermalistion of the experiment.

The generated CN molecules were optically pumped on R_1 spectroscopic branches of the A-X (4,0) band to prepare CN($A^2\Pi$, v = 4, j, F_1e) for j = 2.5, 3.5, 6.5, 11.5, 13.5 and 18.5. The transition frequencies are listed in Table 4.1. The polarisation of the pump laser created the desired rotational anisotropy (orientation or alignment). The collisional evolution of the prepared levels was probed using an FM cw-diode laser on the A-X (4,2) band in stimulated emission. For alignment measurements, the parallel (∥) and perpendicular (⊥) linear polarisation geometries were used. For orientation measurements, the co-rotating (*co*) and counter-rotating (*con*) circular polarisation geometries were used. Tests of the laser polarisations and rotational anisotropy are presented in Section 4.3. Wavelength scans across each spectroscopic transition were repeated for collider pressures between 100 – 1500 mTorr. The phase angle was set at $\theta \approx 0^o$ for all experiments.

Table 4.1 – R_1-branch pump and probe spectroscopic transition frequencies (in cm^{-1}) used in the total removal and depolarisation measurements.

j^a	Transition	Pump freq.^{b}	Probe freq.^{c}
2.5	R_1(1.5)	16095.88	12037.40
3.5	R_1(2.5)	16099.44	12041.10
6.5	R_1(5.5)	16106.56	12049.06
11.5	R_1(10.5)	16106.81	12052.09
13.5	R_1(12.5)	16102.94	12049.83
18.5	R_1(17.5)	16083.65	12035.78

[a] *F_1e.*
[b] *A-X (4,0) band.*
[c] *A-X (4,2) band.*

In the CN($A^2\Pi$)+Ar depolarisation data analysis, the population and alignment parameters, $A_0^{(0)}$ and $A_0^{(2)}$, were formed by fitting to Equation 3.19 and Equation 3.20 (Section 3.3). The orientation parameter, $A_0^{(1)}$, was treated as directly proportional to the

signal ratio, C, of I_{co} and I_{con} in Equation 3.25, and similarly $A_0^{(0)}$ proportional to the denominator of Equation 3.25. For the molecular partners, $A_0^{(0)}$ and $A_0^{(1)}$ were found by fitting directly to Equation 3.21 and Equation 3.22.

4.3 Preliminary Tests

The 266 nm photodissociation of ICN produces CN($X^2\Sigma^+$) molecules with non-statistical and anisotropic rotational and translational distributions, as highlighted in Section 1.8.1. To ensure an isotropic and thermal collision environment, the molecular ensemble must be relaxed to a statistical Maxwell-Boltzmann range of relative velocities and internal energies, importantly with, due to the polarisation-sensitive nature of the experiments, no rotational anisotropy prior to pumping to CN($A^2\Pi$). Since O_2 reacts efficiently with CN($X^2\Sigma^+$), the best compromise between reactive loss and thermalisation needs to be optimised. Checks must also be made prior to commensing a series of experiments that the desired rotational anisotropy (orientation or alignment) is being generated and probed within CN($A^2\Pi$).

The following sub-sections outline preliminary tests that were performed to confirm that the experiment was sufficiently thermalised, the laser polarisations properly set and the desired rotational anisotropy generated and measured. Selected results of these tests are presented.

4.3.1 Thermalisation of CN($X^2\Sigma^+$)

Ar, N_2 and CO_2 Collision Partners

The nascent CN($X^2\Sigma^+$) molecules produced from ICN photolysis are collisionally thermalised in the bath of buffer gas within the experimental cell. The average number of CN-buffer collisions (r) is proportional to the number density [M] of the buffer gas and the time delay (t) between the photolysis laser generating the CN($X^2\Sigma^+$) molecules and optical pumping of the generated molecules to CN($A^2\Pi$), i.e. the photolysis-pump delay, as shown in Equation 4.1. The proportionality constant in this case is the bimolecular collision rate consant, k.

$$r = k \times [M] \times t$$

$$\left(\text{collisions} = \text{collisions} \cdot \text{cm}^3 \cdot \text{s}^{-1} \times \text{cm}^{-3} \times \text{s}\right)$$

Equation 4.1

The reaction of CO_2 with CN($X^2\Sigma^+$) is insignificant at thermal collision energies and Ar and N_2 are unreactive. Therefore, once the minimum number of collisions, and corresponding time delay, required to thermalise the CN($X^2\Sigma^+$) is found for the lowest collider pressure used (100 mTorr), the same delay can then be used for all other collider pressures. To increase the number of collisions at a constant pressure (number density), the photolysis-pump delay must be increased.

As a starting point, the previous delay of 5 μs from the multi-pass FMS configuration of Ballingall *et al*. was chosen,[199] followed by step-wise increments of 5 μs. In the following example, the experiment was set-up for alignment depolarisation measurements using the Ar buffer gas set at ~100 mTorr. A FM probe step-wavelength scan was performed for j = 13.5 F_1e at each photolysis-pump delay and processed as per Section 3.3 to give CN($A^2\Pi$) population, alignment and translational temperature kinetic traces. The CN($X^2\Sigma^+$) velocity distribution remains undistorted upon optical excitation to CN($A^2\Pi$), and so the temperature at 10 ns past the peak population (to avoid pump laser overlap) should be proportional to and hence used as an indicator of the CN($X^2\Sigma^+$) translational temperature. The initial CN($A^2\Pi$) temperature should decrease with collision number as the pumped sample of CN($X^2\Sigma^+$) thermalises, becoming steady when it is fully thermalised.

The average number of collisions and CN($X^2\Sigma^+$) translational temperature for t = 5 – 35 μs at 10 ns post-pump delay are shown in Table 4.2 and Figure 4.2. As a reasonable approximation, the average number of collisions were calculated using Equation 4.1 with k equal to the CN($A^2\Pi$, v = 4, j = 13.5 F_1e)+Ar total population removal rate constant, k_{pop} = 3.52 × 10^{-10} cm^3 s^{-1}, from Ballingall *et al*.[199] In Figure 4.2, there is a large decrease in temperature from 5 μs followed by a gentle decline after 10 μs, indicating substantial to complete thermalisation of the translational energy. For Ar, N_2 and CO_2 collision partners, a 30 μs post-photolysis delay ensured essentially complete

thermalisation of the initial CN($X^2\Sigma^+$) velocity distribution and significant relaxation of the nascent rotational distribution.

Table 4.2 – The photolysis-pump delay, average number of CN($X^2\Sigma^+$) collisions and translational temperature, as derived in the text.

Delay / μs	Ave. No. Collisions	Temperature / K
5	6	451
10	11	354
15	17	352
20	23	339
25	28	340
30	34	336
35	39	325

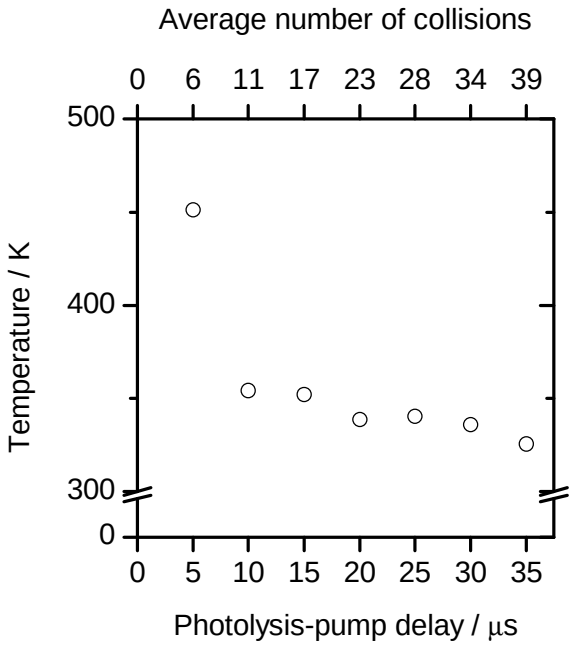

Figure 4.2 – The CN($X^2\Sigma^+$) translational temperature for each photolysis-pump delay and corresponding collision number, as explained in the text.

As well as translational thermalisation, it is important that the initial rotational anistropy of CN($X^2\Sigma^+$) produced in the photolysis of ICN is destroyed before the pump step. This can be tested in the following fashion. The parallel linear polarisation geometry could correspond to both the pump and probe lasers being either vertically polarised (VV), as used in this work, or horizontally polarised (HH). In an isotropic collision environment, these two polarisation sets should have equivalent FM signal sizes. Similarly, the perpendicular linear geometry with the pump laser horizontally polarised and probe

laser vertically polarised (HV), again used in this work, should have an equivalent signal size to the VH linear geometry. Any deviation from this equivalence would be evidence for a preferred alignment in the $X^2\Sigma^+$-state relative to the photolysis laser. For this test, the experiment was set-up for CN($A^2\Pi$)+Ar alignment depolarisation measurements using linear laser polarisations, pumping and probing j = 6.5 F_1e on the R_1(5.5) transition, with 480 mTorr Ar. A probe wavelength scan was performed with the probe laser vertically polarised and switching the pump polarisation between vertical and horizonal. A λ/2-plate was then placed along the probe input path to rotate the probe beam 90° to horizontally polarised and the scan repeated. The first scan resulted in VV parallel and HV perpendicular geometries and the second scan in HH parallel and VH perpendicular pump-probe geometries. For each scan, the output files were transferred to the 2d-data interpetation program and the signal gates set at 10 ns past the peak for a 10 ns-averaged time interval. The saved baseline-subtracted I&Q files were then loaded on to the phase angle finder program to check that $\theta \approx 0^o$, then saved as an A&D file. The resulting FM SE lineshapes are shown in Figure 4.3.

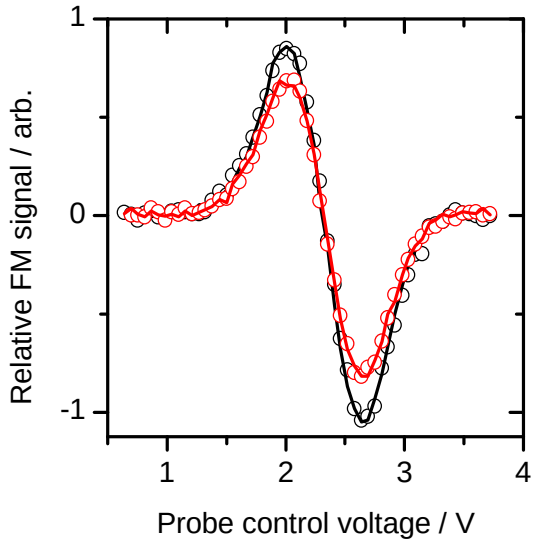

Figure 4.3 – CN($A^2\Pi$)+Ar FM SE signals for VV (open black points), HH (black line), HV (open red points) and VH (red line) parallel and perpendicular linear pump-probe polarisation geometries from two consecutive probe wavelength scans. In the first scan (VV and HV), the probe beam was vertically polarised and in the second scan the probe beam was horizontally polarised using a λ/2-plate. The results from the second scan were multiplied by a common scaling factor of 0.8.

Two separate scans were performed essentially back-to-back, with the optical wave-plate set-up and configured between the scans. The slight change in experimental detail, for example minor differences in beam paths and polarisaiton purities, meant that the results from the second scan (HH and VH) were multiplied by a common scaling factor of 0.8 in order to directly compare with the first scan. As seen in Figure 4.3, the two parallel geometries (VV and HH) overlap, as do the perpendicular HV and VH geometries. This shows that samples have been prepared with the same rotational alignment within the $A^2\Pi$-state. Within the signal-to-noise, there is no evidence for persistence of any photolytic rotational anisotropy within the $A^2\Sigma^+$-state at this collision number.

O_2 Collision Partner

As discussed in Section 1.8.2, O_2 reacts readily with CN($X^2\Sigma^+$) under thermal conditions, with a reaction rate constant of $k_{298} = 5 \times 10^{-11}$ cm^3 s^{-1}.[272] Quenching of CN($X^2\Sigma^+$) leads to a lower yield of CN($A^2\Pi$) and hence depletion of the experimental signal. However, the velocity and rotational distributions still need to be thermalised prior to pumping. Therefore, the best compromise between reactive loss and thermalisation of CN($X^2\Sigma^+$) needs to be optimised by controlling the number of pre-pump collisions. This was performed in the following manner:

1. Connect both N_2 and O_2 buffer gases *via* a T-piece (each separated by a stop-valve) to the vacuum chamber.
2. With the experiment set-up for CN($A^2\Pi$) $j = 6.5$ F_1e orientation depolarisation measurements (circular pump and probe polarisations), find the signal maximum for a particular pressure of N_2.
3. Leaving everything else unchanged, close the N_2 and open the O_2 to the same pressure.
4. After allowing the experiment to equilibrate, record the signal maximum for O_2.
5. Repeat steps 3 and 4 for a range of photolysis-pump delays at the same pressure.
6. Repeat steps 2 – 5 for different pressures of N_2 and O_2.

The various photolysis-pump delays and O_2 pressures were converted to an average number of CN($X^2\Sigma^+$)+O_2 collisions using a bimolecular average collision rate constant of 10^7 collisions Torr^{-1} s^{-1} = 3.13×10^{-10} collisions cm^3 s^{-1}, and the optimal number of pre-pump collisions found. The signal size depended strongly on the collision number

and overall it was concluded that ~5 collisions were needed to retain sufficient signal. Table 4.3 shows the appropriate photolysis-pump delay time required to achieve 5 collisions at a particular pressure of O_2 used in the experiment. The delay times were set by adjusting the photolysis and pump laser flashlamp timings prior to tuning-up and running the experiment.

Table 4.3 – Photolysis-pump delay times for particular pressures of O_2 sufficient for ~5 CN($X^2\Sigma^+$)+O_2 pre-pump collisions.

$[O_2]$ / mTorr	Delay / μs
100	5
200	2.5
300	1.667
400	1.25
500	1
600	0.833
700	0.714
800	0.625
900	0.556
1000	0.5

4.3.2 Polarisation Tests

For one-photon optical excitation with cylindrical symmetry, a circular laser polarisation will generate and probe a rotational population, orientation, and alignment, whereas a linear polarisation will generate and probe only a rotational population and alignment. In each case, the population and anisotropy moments are measured by recording two orthogonal pump-probe laser polarisation geometries (Section 2.5), achieved by periodically rotating the pump laser polarisation according to the PEM retardance and compression cycle. Setting and testing of the probe laser polarisation has been discussed in Section 2.4.1 and pump laser timings according to the PEM cycle in Section 2.4.5. Once the laser polarisations were set and confirmed, test measurements were performed to ensure the correct rotational anisotropy was being created and measured within CN($A^2\Pi$).

The degree of rotational anisotropy created is proportional to the pump laser power. A low pump fluence will prepare fewer CN($A^2\Pi$) molecules, but generate a larger anisotropy for a specific low rotational level, whereas a higher fluence will result in a larger population, but smaller anisotropy as the saturation limit is approached. The

typical pump laser fluence of ~65 mJ cm^{-2}, although strongly saturating, was chosen to optimise the trade-off between excited population and the magnitude of prepared rotational anisotropy. The pump laser fluence was controlled by monitoring the pump laser power and each geometry signal size before an experimental scan and manually adjusting the pump laser amplifier voltage as necessary.

Rotational Alignment

With the experiment configured for linear laser polarisation geometries, there are two tests to confirm that a rotational alignment is being correctly generated and probed. As stated in Section 1.6.2, $j = 0$ cannot be polarised, $j = 0.5$ may only possess an orientation (cannot be aligned), and $j = 1$ is the lowest value of j that can be both oriented and aligned. The first test therefore comprises of pumping and probing $j = 0.5$ F_2f on the $P_2(1.5)$ transition, which is spectroscopically isolated. If the experiment has been correctly set-up, there will be no difference between the parallel and perpendicular geometries. Any differences will be indicative of other polarisation-sensitive artifacts affecting the experiment. Figure 4.4 shows CN($A^2\Pi$)+Ar FM SE lineshapes for the two linear geometries at 10 ns past the signal peak for a 10 ns-averaged baseline-subtracted signal gate at a phase angle of $\theta \approx 0^o$. The overlap of the two geometries in Figure 4.4 reveals that there are no other polarisation effects present and suggests that the experiment has been configured correctly.

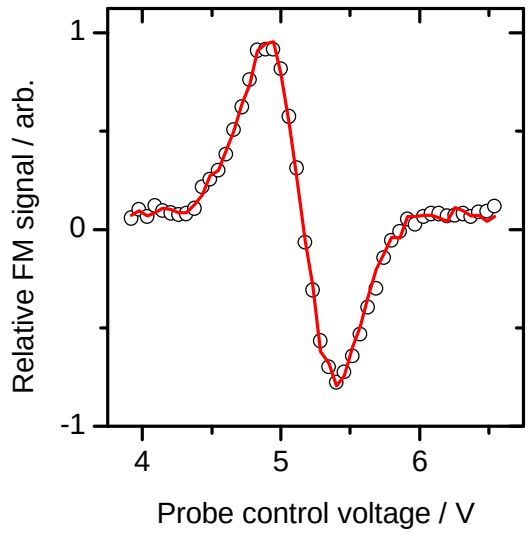

Figure 4.4 – CN($A^2\Pi$)+Ar FM SE signals for parallel (open points) and perpendicular (red line) linear geometries, pumping and probing $j = 0.5$ F_2f. A pressure of 300 mTorr Ar was used.

The second test for rotational alignment involves pumping and probing a rotational state that can be aligned. The results from the isotropy test in Section 4.3.1 (Figure 4.3) were conveniently used for this purpose, preparing and monitoring the j = 6.5 F_1e level on the $R_1(5.5)$ transition. Note, the HH and VH signals are still scaled by a factor of 0.8. There is a marked but equal difference between the size of the parallel and perpendicular signals, indicating the presence of a rotational alignment in an isotropic collision environment.

Rotational Orientation

In order to prepare and measure a rotational orientation, the pump laser polarisation is switched between left and right circular. A probe wavelength scan with the probe laser linearly polarised should then give two identical signal sets, since the rotational anisotropy generated in the circular pump step here is symmetrically distributed about the linear probe polarisation. Figure 4.5 shows the resulting FM SE profiles from such a test for CN($A^2\Pi$)+Ar. Within the experimental signal-to-noise, the signals from the two circular pump polarisations in Figure 4.5 are of the same magnitude, indicating that the pump laser is indeed circularly polarised in each case.

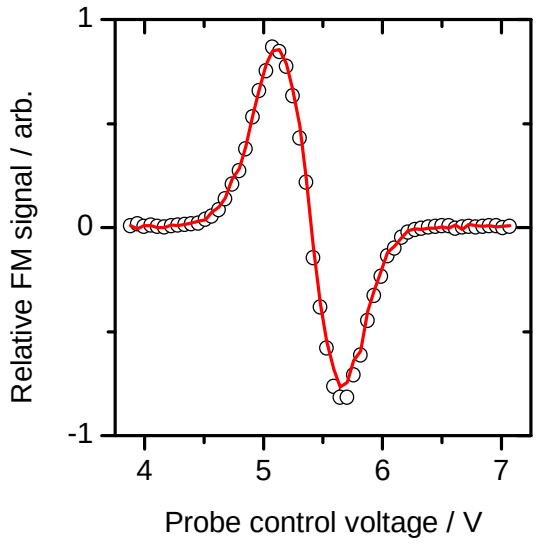

Figure 4.5 – CN($A^2\Pi$)+Ar (~160 mTorr collider gas) 10 ns-averaged FM SE profiles at 10 ns past the signal peak resulting from the pump laser switching between opposite-handed circular polarisations and a linear probe polarisation.

As outlined in Section 1.6.2 and Section 3.3, P- and R- spectroscopic branches have opposite orientation sensitivities, whilst Q-branches are insensitive to rotational

orientation. Therefore, with the probe beam set as circularly polarised, an orientation created on an R-branch and probed on a P-branch will appear to have the opposite sign to an orientation created on an R-branch and probed on an R-branch. When probed on a Q-branch there will appear to be no net orientation. This can be used to test the polarisation setting of the probe laser.

The pump laser was accordingly tuned to the $R_1(12.5)$ transition to populate the j = 13.5 F_1e level and generate a suitable rotational orientation. The probe laser was tuned to the $P_1(14.5)$ main-branch + $^{P}Q_{12}(13.5)$ sub-branch transitions and an experimental scan performed. The scan was then repeated with the probe laser set on the $R_1(12.5)$ transition. This permitted the prepared level to be monitored on all three P-, Q- and R-branch transitions. Resulting CN($A^2\Pi$)+Ar FM SE lineshapes are displayed in Figure 4.6. Apparent when probing on the $P_1(14.5)$ branch, the co-rotating geometry is larger than the counter-rotating geometry, whereas the opposite is true for probing on $R_1(12.5)$. The measured orientation therefore appears to be proportionate in magnitude, but opposite in sign. There is no difference in the signal sizes for the $^{P}Q_{12}(13.5)$ sub-branch. This is consistent with the expected behaviour from the rotational branch sensitivities and demonstrates that both the pump and probe laser polarisations have been set correctly, and that a rotational orientation is being successfully generated and probed.

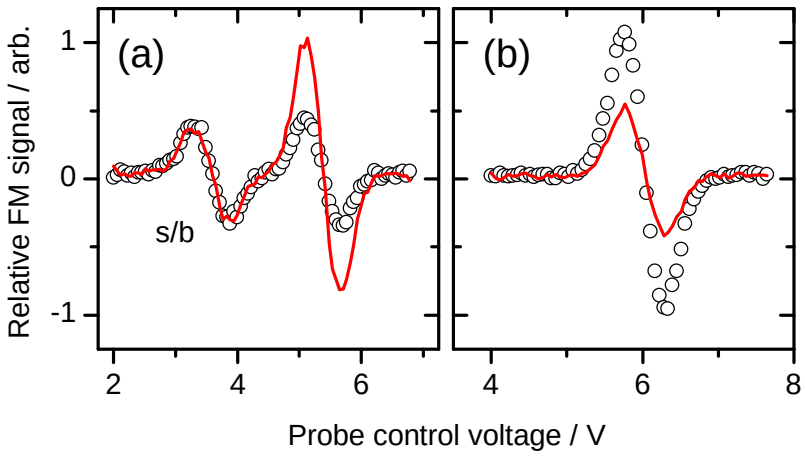

Figure 4.6 – CN($A^2\Pi$)+Ar counter-rotating (open points) and co-rotating (red line) 10 ns-averaged FM SE lineshapes at 10 ns past the signal maximum for j = 13.5 F_1e, with ~100 mTorr Ar, pumped on $R_1(12.5)$ and probed on (a) $P_1(14.5)$ main-branch + $^{P}Q_{12}(13.5)$ sub-branch (indicated by s/b) transitions, and (b) $R_1(12.5)$ transition.

4.4 Nuclear Hyperfine Quantum Beats

Nuclei in a molecule that possess non-zero nuclear spins will couple to the molecular rotation through the electronic framework. The nuclear spin of ^{14}N is $\boldsymbol{I} = 1$, which couples to $\boldsymbol{j}$ to give the total (hyperfine) angular momentum, $\boldsymbol{F} = j, j \pm I$, as shown in Figure 4.7 and Figure 4.8. Polarised optical excitation orients or aligns the populated j-level in the LAB-frame. However, I is initially randomly oriented and remains unpolarised after the optical excitation, due to the sudden nature of the pump process compared to the timescale associated with the hyperfine splittings. The oriented or aligned j will then recouple to the isotropically distributed I, resulting in a space-fixed F, around which j and I precess (Figure 4.7). As the projection of j along the initial quantisation axis varies with the precession, so too must the apparent polarisation of j.

From a quantum mechanical view, if the energy separation of the hyperfine levels is smaller than the frequency bandwidth of the pump laser, then these levels will be excited coherently. The resulting coherent superposition in the prepared state evolves in time, causing the measured polarisation to oscillate with beat frequencies that depend on the F, F' energy splitting. The depth of the the oscillations depends on the relative magnitudes of j and I, becoming negligible as $j >> I$. The effect is therefore more pronounced at low j, and for alignment rather than orientation, reflecting the quadrupolar *versus* dipolar nature of these moments.

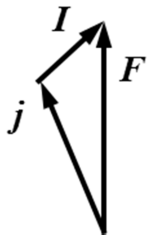

*Figure 4.7 – Coupling of the rotational angular momentum, **j**, and nuclear spin, **I**, vectors to form the total (hyperfine) angular momentum, **F**.*

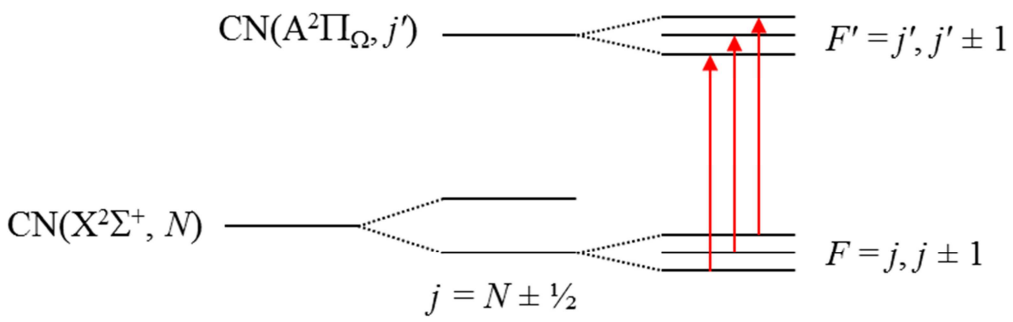

Figure 4.8 – Splitting of the CN($X^2\Sigma^+$) and CN($A^2\Pi$) rotational levels, j, into F = j, j ±I nuclear hyperfine levels, where I = 1 is the ^{14}N nuclear spin. The F′ ← F transitions are shown in red. The hyperfine splittings are ~20-100 MHz.

The oscillations of the prepared polarisation over time are termed nuclear hyperfine quantum beats (NHQBs). This is a well known phenomenon that has been widely reported in the literature.[10] Examples include depolarisation of orientation and alignment in OH($X^2\Pi$),[126, 128-133] CN($X^2\Sigma^+$) from photodissociation of ICN,[171] optical pumping of HCl,[273] and collisional depolarisation of NO($A^2\Sigma^+$).[46, 274]

The time-dependent oscillation of the polarised *j* is represented by the following equations:[10]

$$A_0^{(K)}(j,t) = G^{(K)}(j,t)A_0^{(K)}(j,t=0)$$

Equation 4.2

$$G^{(K)}(j,t) = \sum_{F,F'} \frac{(2F+1)(2F'+1)}{(2I+1)} \begin{Bmatrix} F' & F & K \\ j & j & I \end{Bmatrix}^2 \cos\left[\frac{(E_F - E_{F'})t}{\hbar}\right]$$

Equation 4.3

where {:::} is a 6-*j* symbol, *K* is the rank of the angular momentum tensor moment and E_F is the energy of the *F* eigenstate. Equation 4.3 holds if the hyperfine oscillation frequency is slow compared to the temporal evolution of the pump and probe lasers. However, if the relative oscillation is fast, i.e. the hyperfine splittings are small, then an average is measured:

$$\left\langle G^{(K)}(j,t)\right\rangle_{Average} = \frac{1}{2I+1}\sum_{F}(2F+1)^2\begin{Bmatrix} F & F & K \\ j & j & I \end{Bmatrix}^2$$

Equation 4.4

Hyperfine quantum beats are expected and indeed visible in the low-j CN($A^2\Pi$) depolarisation data, as displayed in Figure 4.9 for j = 2.5 F_1e and j = 3.5 F_1e alignment decays at ~100 mTorr Ar collider pressure. The data are 1 ns intervals from the kinetic processing routine. A small early time window (0 – 500 ns) is shown, so as to best view the quantum beats. To demonstrate that these are the result of hyperfine structure, the beats were simulated using Equation 4.3 with the $\Delta E_{F\text{-}F'}$ hyperfine splittings given in the caption of Figure 4.9.

The simulations were performed in a custom-written LabVIEW® routine by Dr. Matthew L. Costen at Heriot-Watt University. The resulting output files from the LM kinetic processing of the data were Fourier transformed in Origin® to give Fourier amplitude spectra with peaks corresponding to the beat frequencies of the hyperfine splittings. These frequencies were input to the LabVIEW® code that implemented Equation 4.3 for the time-dependence of the hyperfine structure. The code calculated this as a function of the pump-probe delay using two assumed splittings (the third frequency being the sum of the other two), and an assumed initial alignment. The result was convoluted with a Gaussian to represent the time response of the system (trial adjustment gave 12 ns FWHM as the best compromise). The code then compared the initial Gaussian-convoluted simulation to the data and employed LM minimisation to optimise the splittings and the initial alignment. The data range was adjusted to exclude significant noise and the zero-time was manually set to provide the best fit.

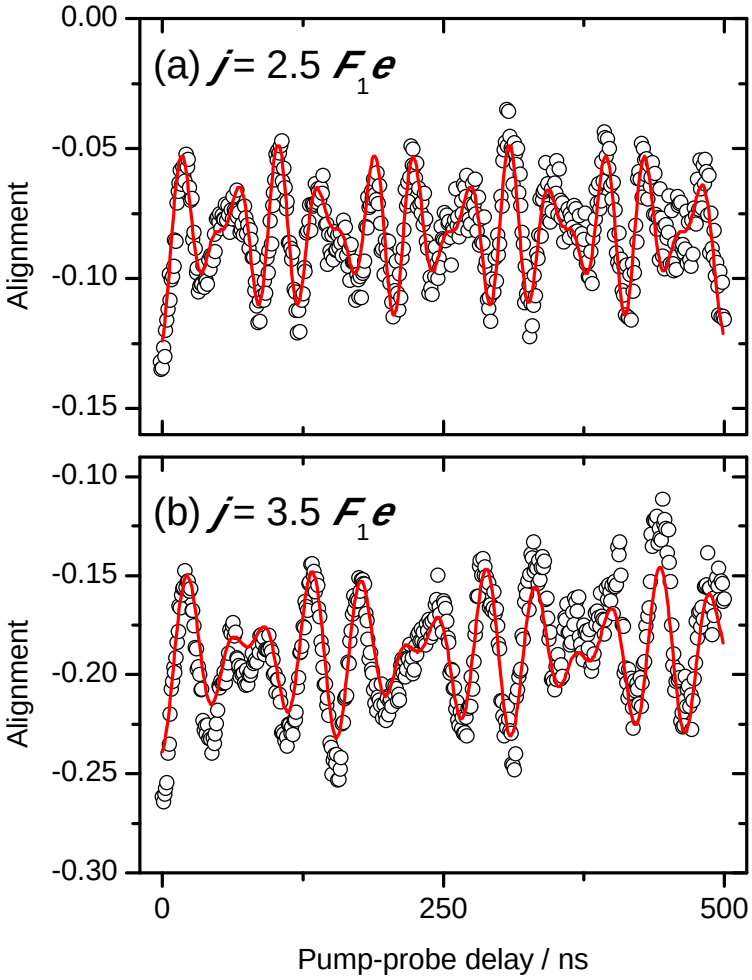

Figure 4.9 – CN($A^2\Pi$) alignment decays with ~100 mTorr Ar for (a) j = 2.5 F_1e, with hyperfine splittings $\Delta E_{F\text{-}F'}$ (2.5-1.5) = 34.1 MHz and $\Delta E_{F\text{-}F'}$ (3.5-2.5) = 24.5 MHz, and (b) j = 3.5 F_1e, with hyperfine splittings $\Delta E_{F\text{-}F'}$ (3.5-2.5) = 19.2 MHz and $\Delta E_{F\text{-}F'}$ (4.5-3.5) = 25.9 MHz. Open circles = 1 ns-averaged alignment data from the experimental measurements, red lines = simulations.

The data and simulations in Figure 4.9 are in good agreement and clearly exhibit the NHQBs. In principle, the NHQBs could have been included in subsequent kinetic fitting of the orientation and alignment. However, it was decided that including these into all of the kinetic analysis routines would be counter-productive. The implementation would significantly complicate and slow the fitting procedure and introduce a number of new uncertanties, such as the beat frequencies, laser pulse shape parameters and true zero-time adjustment. The hyperfine beats are only of significant magnitude and observable for the lowest two rotational levels probed (j = 2.5 F_1e and j = 3.5 F_1e). The NHQB timescales are considerably shorter than those involved in the collisional polarisation effects studied in this thesis. The NHQBs have therefore been ignored in the rest of this

thesis. Instead, the data has been averaged in 10 ns intervals, which smooths out much of the oscillation observed in Figure 4.9 above. Any remaining beats then appear as fluctuations on the overall smoothly varying polarisation and do not influence the fitting results.

4.5 CN($A^2\Pi$)+Ar Population Removal and Depolarisation

4.5.1 Experimental Results

The kinetic processing has been described in detail in Chapter 3. Figure 4.10 shows typical FM SE Doppler profiles immediately (10 ns) after the pump pulse for (i) co- and counter-rotating geometries and (ii) parallel and perpendicular geometries, together with their fits, for j = 2.5, 6.5 and 11.5 F_1e at pressures of ~100 mTorr. The simulated curves fit very well to the FM lineshapes, and a strong dependence of the signal size on the experimental geometries is also apparent. The difference between the alternate-polarisation lineshapes shows that a rotational anisotropy has been created by the pump pulse. The orientation in the circular geometries appears to be much larger in magnitude than the alignment in the linear geometries. This is because the one-photon probe technique used is more sensitive to orientation than alignment, as discussed in Section 3.3 and reference 167. The experimental dispersion curves were simultaneously fitted with the FM SE profiles as described in Chapter 3 and with a similar level of agreement, but are not shown in Figure 4.10 for reasons of visual clarity.

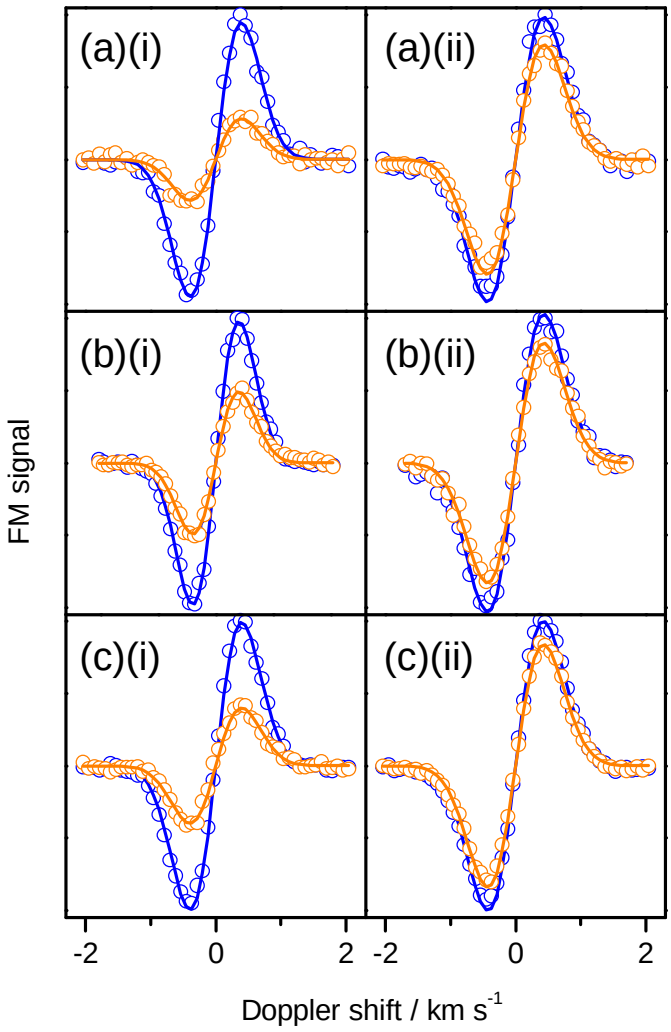

Figure 4.10 – FM SE Doppler profiles and fits for the first 10 ns after the pump laser pulse for (a) j = 2.5 F_1e on the $R_1(1.5)$ transition, (b) j = 6.5 F_1e on the $R_1(5.5)$ transition and (c) j = 11.5 F_1e on the $R_1(10.5)$ at total pressures of ~100 mTorr. (i) Circular polarisation orientation experiments and (ii) linear polarisation alignment experiments.

Figure 4.11 shows the kinetic traces for I_{co} and I_{con}, and $I_{\parallel}$ and $I_{\perp}$, resulting from the sequential Doppler profile analysis, for j = 6.5 F_1e at total pressures of ~100, ~500 and ~1000 mTorr. The difference between the intensities is evident at t = 0, showing in all cases that a rotational anisotropy has been created. The traces then decay with time as population is collisionally removed from the initial level, but they *clearly converge*, indicating even by eye that collisional removal of the initial polarisation is partially competetive with the loss of population. Comparison of the observed decays also shows clearly that they depend strongly on the collider pressure.

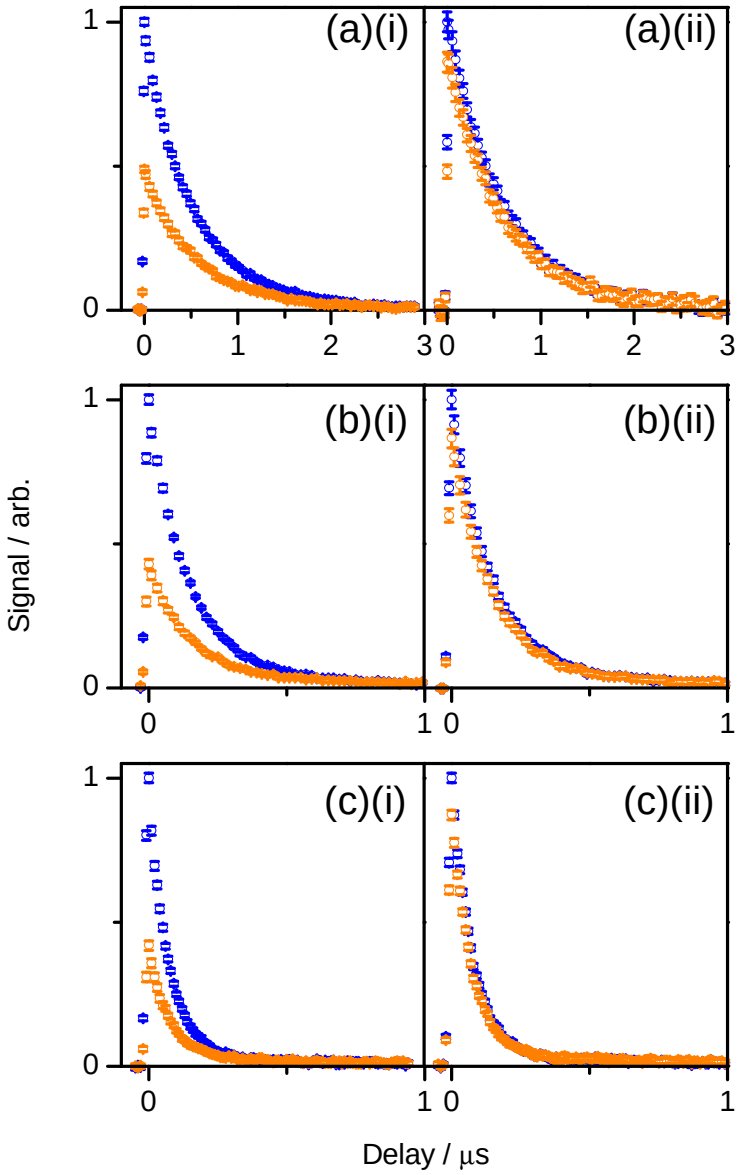

Figure 4.11 – Signal decays for j = 6.5 F_1e at (a) ~100 mTorr (every 4th data point shown), (b) ~500 mTorr (every 2nd data point shown), and (c) ~1000 mTorr total pressure. (i) Co-rotating and counter-rotating geometries from the circular polarisation experiments and (ii) parallel and perpendicular geometries from the linear polarisartion experiments. Error bars are 2σ statistical uncertainties.

Presented in Figure 4.12 are the time-dependences of the translational temperature from the circular polarisation Doppler fits for j = 2.5, 6.5 and 11.5 F_1e at ~100 mTorr. As with the linear polarisation data in Section 4.3.1, the temperature immediately after the pump pulse was typically found to be ~330 ± 8 K, independent of the collider pressure. This slightly higher temperature may be an optical pump saturation effect combined with possible influences from the unresolved hyperfine structure and a small contribution from instrumental broadening.[275] The observed temperature then declines,

typically reaching a minimum around 300 K. This behaviour has previously been observed in similar experiments, and has a straightforward physical explanation.[276] Those CN radicals within the Maxwell-Boltzmann distribution that have a higher velocity necessarily collide at a higher frequency. Provided that the population removal cross-section does not have strong collision energy dependence, then the faster moving CN radicals will be preferentially removed, resulting in the observed decrease in translational temperature. At later times, the population evolves back to a fully thermalised Maxwell-Boltzmann distribution. As the observed variations in temperature are relatively small, it is expected that any effect on the measured rate constants will be negligible in comparison with the other experimental uncertainties.

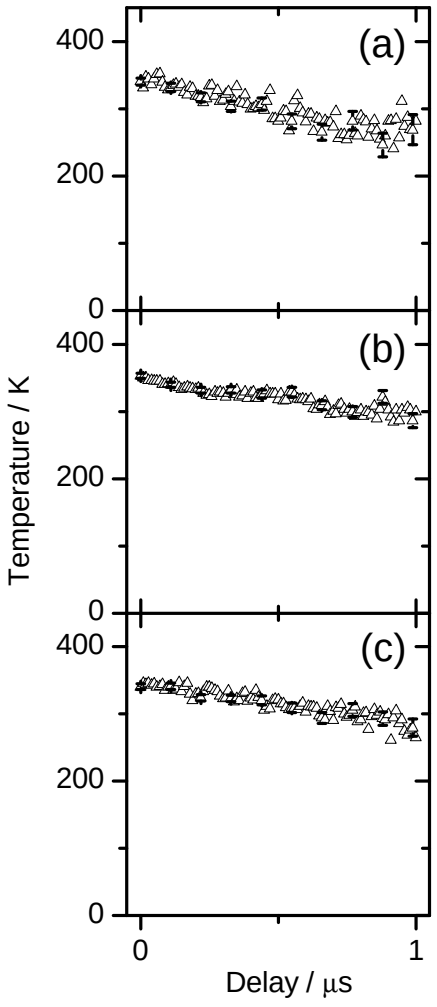

Figure 4.12 – Kinetic traces of the translational temperatures determined from the processing routine from circular laser polarisations for (a) j = 2.5 F_1e (b) j = 6.5 F_1e and (c) j = 11.5 F_1e at total pressures of ~100 mTorr. Representative 2σ error bars are displayed on selected data points. Individual error bars for each data point have been omitted for visual clarity.

The time-dependence of the population moment, $A_0^{(0)}$, alignment moment, $A_0^{(2)}$, and orientation parameter, *C*, derived from the linear and circular polarisation experiments are shown in Figure 4.13 and Figure 4.14 for j = 2.5, 6.5 and 11.5 F_1e, at ~100 mTorr, ~500 mTorr and ~1000 mTorr total pressures, suitable for further analysis. The populations decay in an exponential or near-exponential fashion, with a visible pressure dependence. At long post-pump delay times there is a non-zero baseline, evidence of the thermalisation of the initial population across the Boltzmann distribution within $A^2\Pi$ (v = 4). The population traces from both sets of experiments at similar pressures appear to be indistinguishable, showing that they are measurements of the same parameter and highlighting the consistency of the experiments.

The orientation and alignment decays suggest that collisional depolarisation is a significant process occuring on the timescale of population removal. Both decay much more slowly than the population, and also depend strongly on the collider pressure. At long times, the anisotropies are scattered around zero, as there cannot be any anisotropy at thermal equilibrium, and at low population the orientation and alignment are necessarily ill-determined. The polarisation decay traces for the same rotational level appear similar, suggesting that depolarisation of the orientation and alignment occur with similar rates. There is also a mild j-dependence of the depolarisation for both data sets.

Kinetic fitting to the population and polarisation decays to extract the total population removal and elastic depolarisation rates is presented and discussed in the following sections.

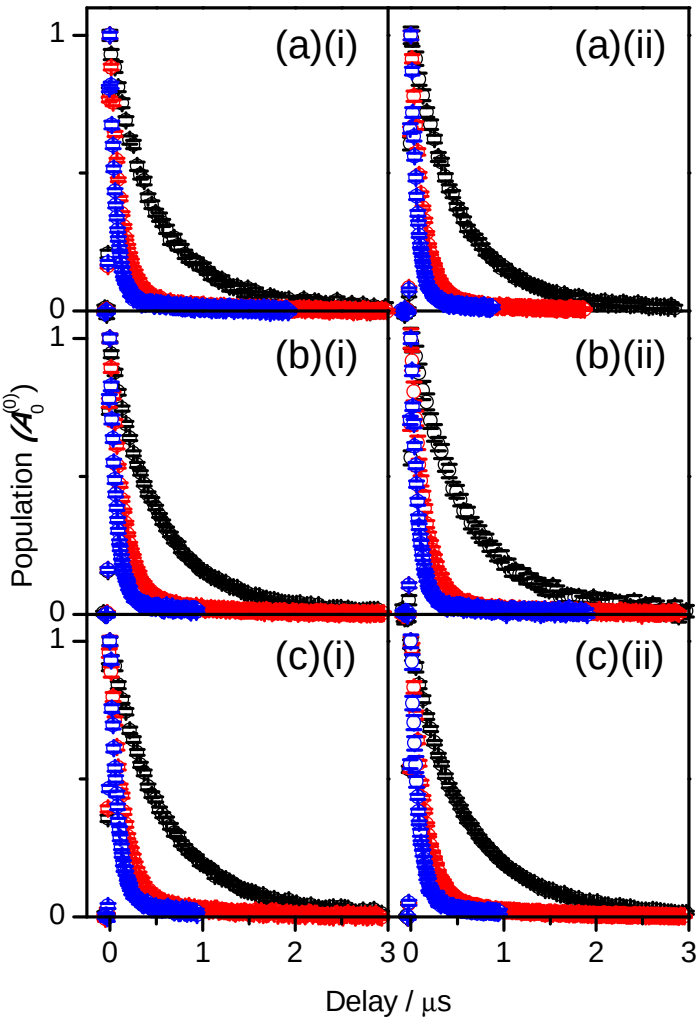

Figure 4.13 – The time-dependence of the population moment, $A_0^{(0)}$, derived from (i) circular and (ii) linear polarisation experiments for (a) j = 2.5 F_1e, (b) j = 6.5 F_1e and (c) j = 11.5 F_1e, at ~100 mTorr (black, every 4th data point shown), ~500 mTorr (red, every 2nd data point shown) and ~1000 mTorr (blue) total pressures. Error bars are 2σ statistical uncertainties.

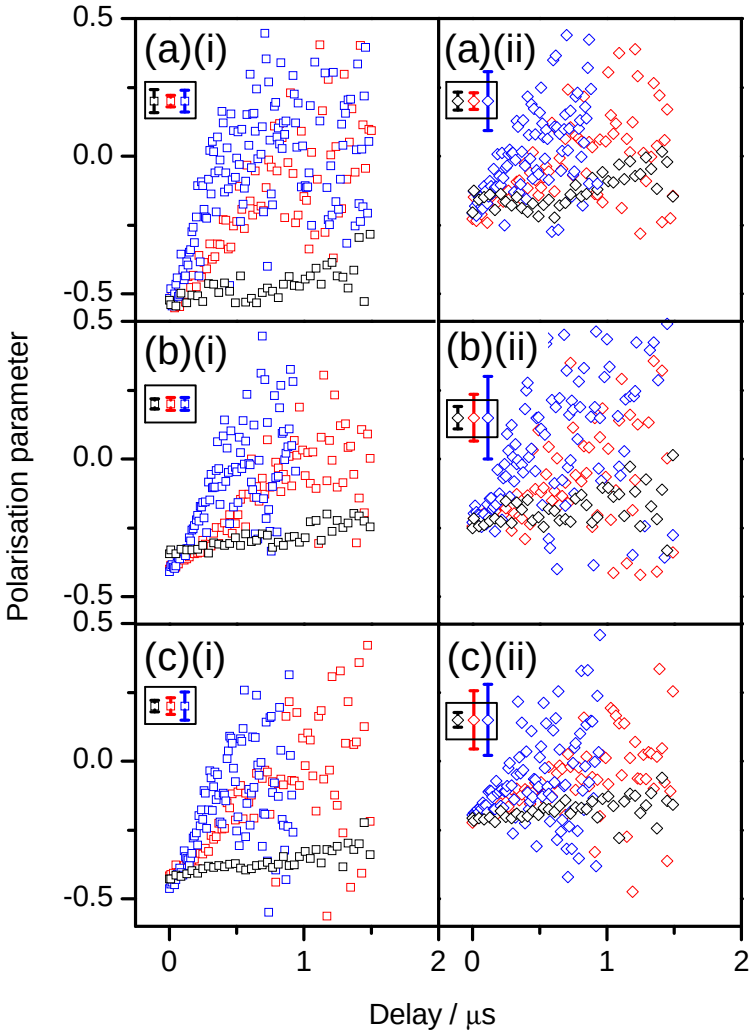

Figure 4.14 – The time-dependence of the orientation parameter, C, and the alignment moment, $A_0^{(2)}$*, derived from (i) circular and (ii) linear polarisation experiments for (a) j = 2.5* F_1e*, (b) j = 6.5* F_1e *and (c) j = 11.5* F_1e*, at ~100 mTorr (black, every 4th data point shown), ~500 (red, every 2nd data point shown) and ~1000 mTorr (blue) total pressures. Representative average 2σ error bars are displayed within the inset of each panel. Error bars for individual data points have been omitted for visual clarity.*

4.5.2 Single Exponential Kinetic Model

A useful review of the kinetic treatment of collisional population removal and depolarisation of rotational angular momentum is found in reference 19. The simplest kinetic model to consider the collisional evolution of the prepared level is that of a single exponential decay. This model assumes that back-transfer (re-population) into the initial level is not possible and that the sample is in a thermal bath of gas with a Maxwell-Boltzmann distribution of relative velocities.

The prepared population and polarisation have, to a good approximation, two possible outcomes during a collision. These include: irreversible transfer to product levels, j_p, with rate $\Gamma^{(K)}_{i\to p}$, that incorporate nearby rotational levels and unobserved far away levels (in energy, angular momentum or fluorescence), or elastic depolarisation within the subset of populated *m* levels, with rate $\Gamma^{(K)}_{dep,j_i}$. These processes are shown in the kinetic scheme in Figure 4.15.

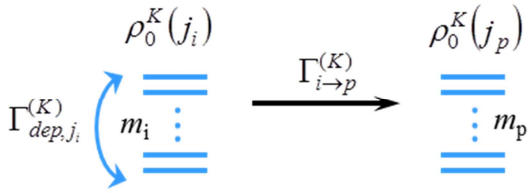

Figure 4.15 – The kinetic scheme to describe the transfer of prepared rotational population (K = 0), orientation (K = 1) or alignment (K = 2) upon collision with a partner for the single exponential model. The prepared population and rotational anisotropy in an initial level, j_i, may be irreversibly transferred to product levels, j_p, that include nearby rotational levels or far away levels, with rate $\Gamma^{(K)}_{i\to p}$. Additionally, the prepared orientation or alignment may be depolarised in the initial level with rate $\Gamma^{(K)}_{dep,j}$. The $\rho_0^K(j)$ is a tensor moment of rank K and level j, as described in Section 1.5.2.

The tensor rate for transfer of population (K = 0) or polarisation (K = 1, 2) from an initial state j_i to a product state j_p, $\Gamma^{(K)}_{i\to p}$, is defined as the sum of the microscopic transfer rates, $\Gamma^{(K)}_{j_i m_i\to j_p m_p}$, between states $|j_i m_i\rangle$ and $|j_p m_p\rangle$:

$$\Gamma^{(K)}_{i\to p} = \sum_{m_i,m_p}(-1)^{j_i-m_i-j_p-m_p}[K]\begin{pmatrix} j_p & j_p & K \\ m_p & -m_p & 0\end{pmatrix}\begin{pmatrix} j_i & j_i & K \\ m_i & -m_i & 0\end{pmatrix}\Gamma^{(K)}_{j_i m_i\to j_p m_p}$$

Equation 4.5

where as usual, $[K] = 2K + 1$ and (:::) are 3-*j* symbols. This collisional transfer tensor rate is directly comparable to that defined by Rowe and McCaffery[55] and the tensor cross-section, $\sigma^{(K)}_{j_i\to j_p}$, defined by Alexander and Davis.[56]

The elastic depolarisation rate of the tensor moment $\rho_0^K(j)$, given by $\Gamma_{dep,j}^{(K)}$, is defined as the sum of the reversible microscopic transfer rates between $m \leftrightarrow m'$, $\Gamma_{jm\to jm'}$ and $\Gamma_{jm'\to jm}$, as shown in Equation 4.6. The m' includes all m and hence includes the '*super-elastic*' $m \to m$ process.

$$\Gamma_{dep,j}^{(K)} = \left[\sum_m [K] \begin{pmatrix} j & j & K \\ m & -m & 0 \end{pmatrix}^2 \sum_{m'} \Gamma_{jm\to jm'} - \sum_{m,m'} (-1)^{2j-m-m'} [K] \begin{pmatrix} j & j & K \\ m & -m & 0 \end{pmatrix} \times \begin{pmatrix} j & j & K \\ m' & -m' & 0 \end{pmatrix} \Gamma_{jm'\to jm} \right]$$

Equation 4.6

where

$$(-1)^{2j-2m} = (-1)^{2(j-m)} = 1$$

Equation 4.7

and due to the othogonality of the 3-*j* symbols:[10]

$$\sum_m \begin{pmatrix} j & j & K \\ m & -m & 0 \end{pmatrix}^2 = \frac{1}{[K]}$$

Equation 4.8

In an isotropic collision environment, the 'super-elastic' rate must be independent of *m*. Using this rule, and the orthogonality of the 3-*j* symbols, the first term in Equation 4.6 can be replaced by a *total* elastic scattering rate, $\Gamma_{j\to j}^{(0)}$. The second term can be replaced with an equivalent tensor rate, $\Gamma_{j\to j}^{(K)}$, that describes the preservation of the polarisation of ranks $K = 1$ and $K = 2$ during an elastic $j \to j$ process. Therefore, Equation 4.6 now simplifies to:

$$\Gamma_{dep,j}^{(K)} = \Gamma_{j\to j}^{(0)} - \Gamma_{j\to j}^{(K)}$$

Equation 4.9

Neglecting any re-population of the initial level, the rate of change of $\rho_0^K(j_i)$ is given by:

$$\frac{d\rho_0^{(K)}(j_i)}{dt} = -\rho_0^{(K)}(j_i)\Gamma_{tot,j_i}^{(K)}$$

Equation 4.10

where $\Gamma_{tot,j_i}^{(K)}$ is the total tensor removal rate out of j_i, which is the sum of the first-order elastic depolarisation rate, $\Gamma_{dep,j_i}^{(K)}$, and the first-order total population removal rate out of j_i, Γ_{pop,j_i}:

$$\Gamma_{tot,j_i}^{(K)} = \Gamma_{dep,j_i}^{(K)} + \Gamma_{pop,j_i}$$

Equation 4.11

The time-dependence of $\rho_0^K(j_i)$ takes the single exponential form of Equation 4.10:

$$\rho_0^{(K)}(j_i;t) = \rho_0^{(K)}(j_i;t=0)e^{-\Gamma_{tot,j_i}^{(K)}t}$$

Equation 4.12

The experiments in this work are sensitive to the normalised orientation and alignment moments, $A_0^{(1)}$ and $A_0^{(2)}$. The observables in these experiments are therefore separately the population removal and depolarisation rates, $\Gamma_{pop,j}$ and $\Gamma_{dep,j}^{(K)}$. The time-dependence of the prepared population is simply Equation 4.12 expressed with respect to the population:

$$A_0^{(0)}(j;t) = A_0^{(0)}(j;t=0)e^{-\Gamma_{pop,j}t}$$

Equation 4.13

The measured time-dependent polarisation moments, $A_0^{(K)}(j;t)$, are renormalised from the respective tensor moments by a *j*-dependent factor, $V^{(K)}(j)$,[167, 277] and by the $K = 0$ tensor moment:

$$A_0^{(K)}(j;t) = V^{(K)}(j)\frac{\rho_0^K(j;t)}{\rho_0^0(j;t)}$$

Equation 4.14

where

$$V^{(1)}(j) = 1$$

Equation 4.15

$$V^{(2)}(j) = \left[\frac{j(2j+1)}{(2j-1)(2j+3)}\right]^{1/2}$$

Equation 4.16

In the same manner as Equation 4.13, the time-dependence of the prepared polarisation is then Equation 4.12 expressed with respect to the normalised $A_0^{(K)}(j;t)$ moments and $\Gamma_{dep,j}^{(K)}$:

$$A_0^{(K)}(j;t) = A_0^{(K)}(j;t=0)e^{-\Gamma_{dep,j}^{(K)}t}$$

Equation 4.17

Therefore, the prepared rotational population and polarisation moments in level *j* will, according to this model, undergo single exponential decays with rates $\Gamma_{pop,j}$ and $\Gamma_{dep,j}^{(K)}$. The population and tensor removal rates are related to the desired bimolecular rate constants, $k_{pop,j}$ and $k_{dep,j}^{(K)}$, by the following linear relationships:

$$\Gamma_{pop,j}^{(0)} = k_{pop}[M] + \Gamma_{pop,\mathrm{int},j}^{(0)}$$

Equation 4.18

$$\Gamma_{dep,j}^{(K)} = k_{dep,j}^{(K)}[M] + \Gamma_{dep,\mathrm{int},j}^{(K)}$$

Equation 4.19

where [*M*] is the collider number density and $\Gamma^{(0)}_{pop,\mathrm{int},j}$ and $\Gamma^{(K)}_{dep,\mathrm{int},j}$ are the population- and tensor-dependent zero-pressure intercept rates, resulting from collisions with the ICN precursor and from non-collisional loss processes, such as 'fly-out' from the probed region and radiative loss of CN($A^2\Pi$).

The population and polarisation decays were fitted to Equation 4.13 and Equation 4.17 using Origin®. The population kinetic fitting had an additional offset to account for non-zero population at long times, whereas the polarisation moments by necessity decay to zero, as there cannot be any polarisation at thermal equilibrium. Fits of Equation 4.13 and Equation 4.17 to the population and polarisation decays, along with the corresponding residuals, are shown in Figure 4.16 – Figure 4.19.

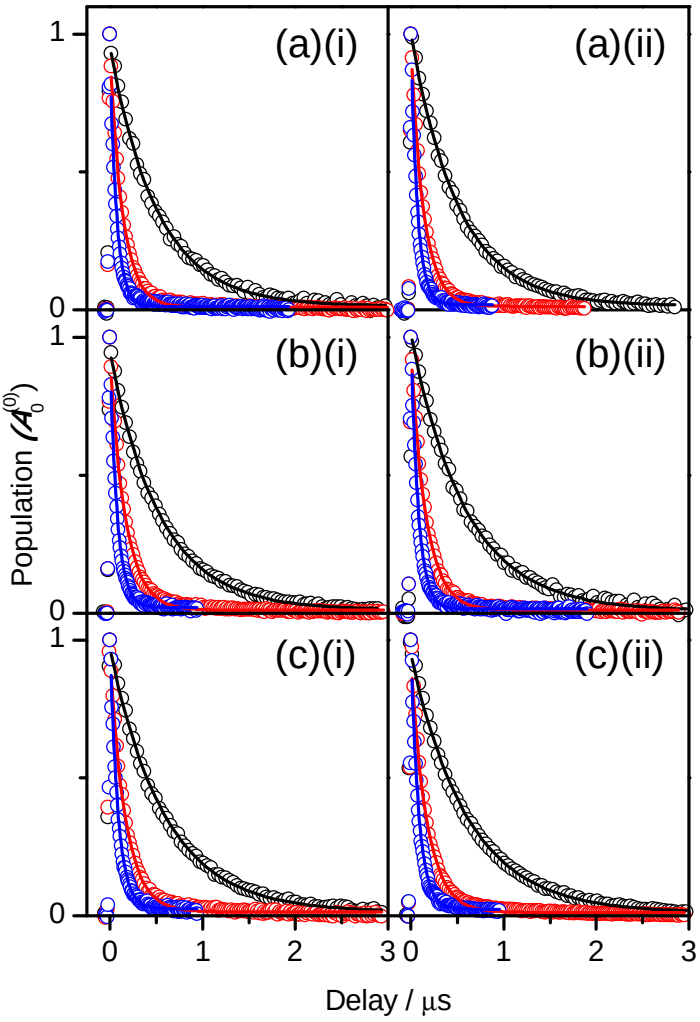

Figure 4.16 – The time-dependence of the population moment, $A_0^{(0)}$, derived from (i) circular and (ii) linear polarisation experiments for (a) j = 2.5 F_1e, (b) j = 6.5 F_1e and (c) j = 11.5 F_1e, at ~100 mTorr (black), ~500 mTorr (red) and ~1000 mTorr (blue) total pressures. Solid lines

are single exponential fits to the data. Error bars are the same as for Figure 4.13 and have been omitted here for visual clarity.

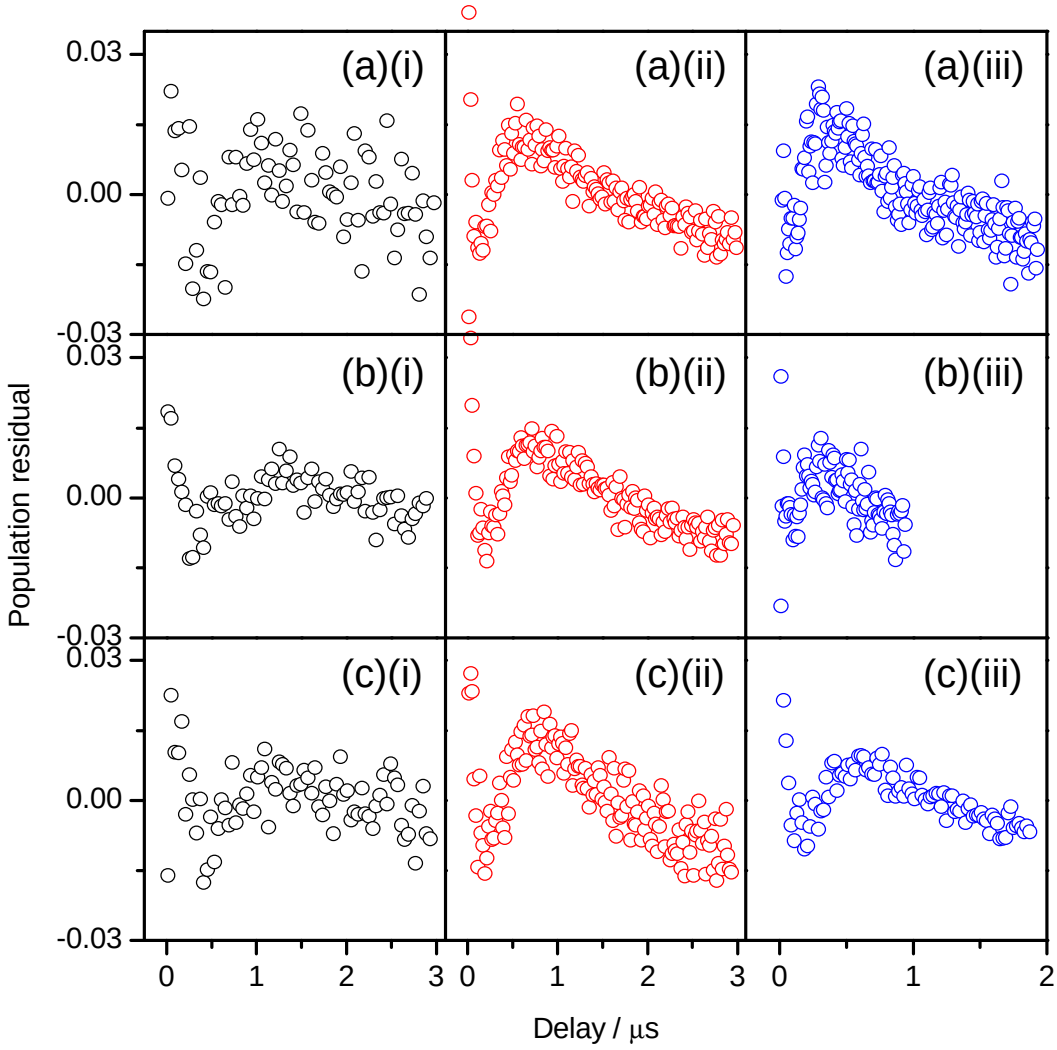

Figure 4.17 – Residuals of the data and fits from Figure 4.16 for the time-dependence of the population moment, $A_0^{(0)}$, derived from (i) circular and (ii) linear polarisation experiments for (a) j = 2.5 F_1e, (b) j = 6.5 F_1e and (c) j = 11.5 F_1e, at (i) ~100 mTorr (black), (ii) ~500 mTorr (red) and (iii) ~1000 mTorr (blue) total pressures.

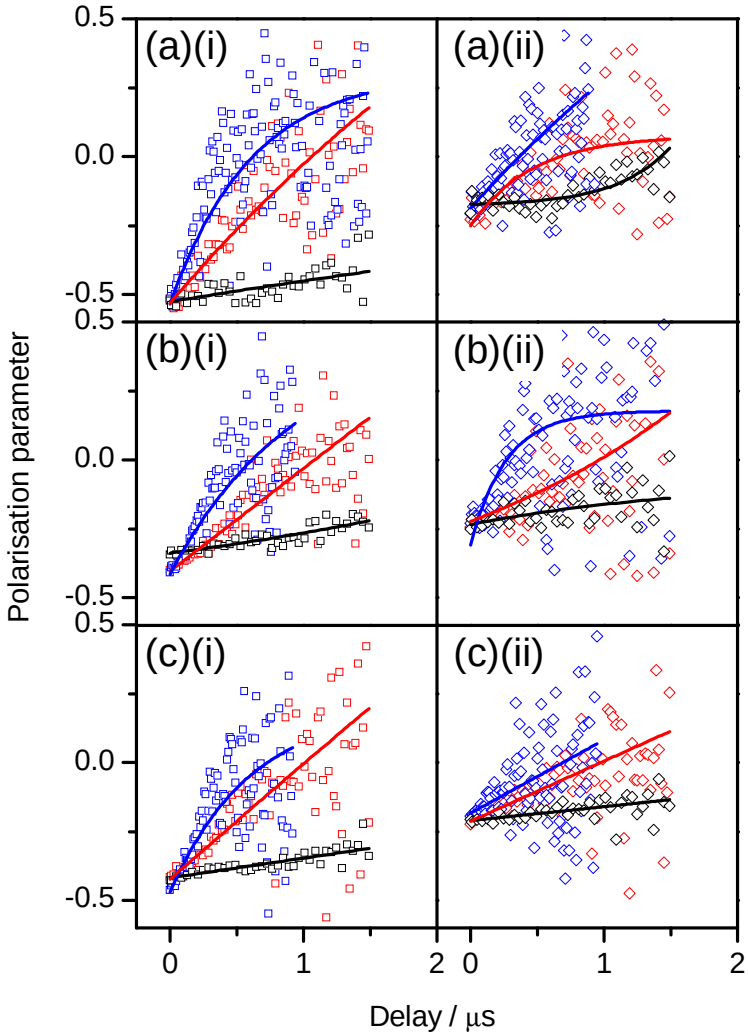

Figure 4.18 – The time-dependence of (i) the orientation parameter, C, from the circular polarisation experiments and (ii) the alignment moment, $A_0^{(2)}$, from the linear polarisation experiments for (a) j = 2.5 F_1e, (b) j = 6.5 F_1e and (c) j = 11.5 F_1e, at ~100 mTorr (black), ~500 (red) and ~1000 mTorr (blue) total pressures. The solid lines are single exponential fits to the data. Error bars are the same as for Figure 4.14 and have been omitted here for visual clarity.

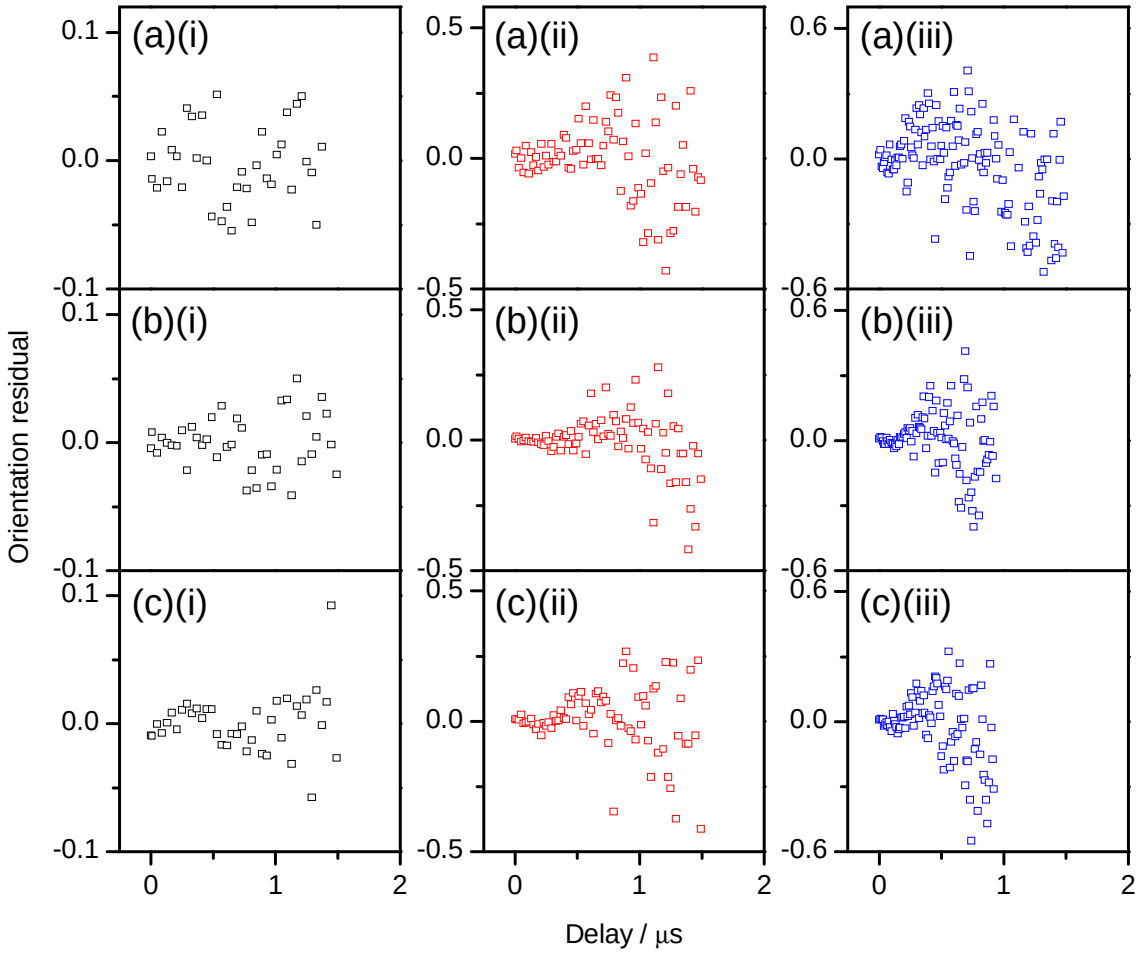

Figure 4.19 – Residuals of the data and fits from Figure 4.18 for the time-dependence of the orientation parameter, C, from the circular polarisation experiments for (a) j = 2.5 F_1e, (b) j = 6.5 F_1e and (c) j = 11.5 F_1e, at (i) ~100 mTorr (black), (ii) ~500 mTorr (red) and (iii) ~1000 mTorr (blue) total pressures.

The polarisation fits were optimised to exclude points during the pump pulse and where the population has fallen to less than ~10% of the peak, where the polarisation is poorly determined. The first observation from the single exponential fits is that $\Gamma_{pop,j}$ is larger than $\Gamma_{dep,j}^{(K)}$ for all *j*-levels shown, reaffirming that the removal of population from the prepared level is a faster process than depolarisation. The single exponential function appears upon casual inspection to fit the data well. However, inspection of the residuals shows systematic differences between the data and fits in Figure 4.17 and Figure 4.19, more noticeably as the collider pressure increases. This deviation from the single exponential character suggests that multiple collisions are producing multimodal decays, particularly apparent at higher pressures where multiple collisions are more

significant within the observed time frame. This can be clearly seen in a semi-logarithm plot of the population removal, shown in Figure 4.20. Taking the natural logarithm of Equation 4.13 gives the linear Equation 4.20. Therefore, if the population decay is truly a single exponential, then plotting $\ln\left[A_0^{(0)}(j;t)\right]$ againt the time delay, *t*, should give a straight line with rate Γ_{pop}.

$$\ln\left[A_0^{(0)}(j;t)\right] = \ln\left[A_0^{(0)}(j;t=0)\right] - \Gamma_{pop}t$$

Equation 4.20

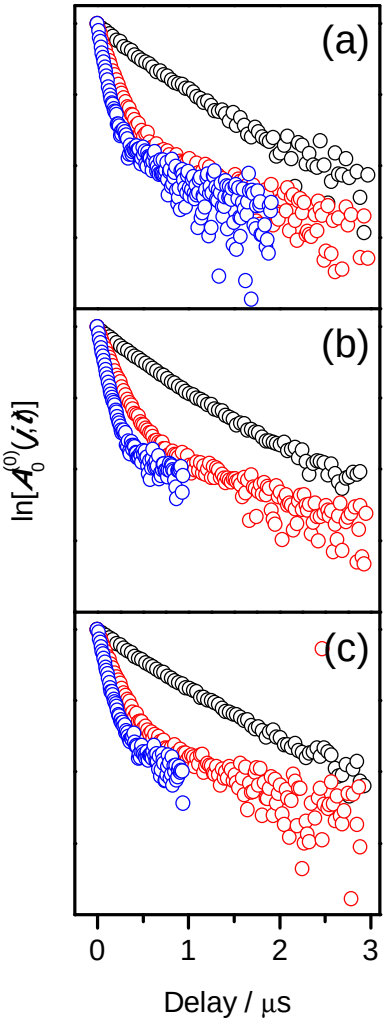

Figure 4.20 – A semi-logarithm plot of the time-dependence of the population for (a) j = 2.5 F_1e, (b) j = 6.5 F_1e and (c) j = 11.5 F_1e at ~100 mTorr (black), ~500 mTorr (red) and ~1000 mTorr (blue) total pressures.

The number of collisions is proportional to both the the time delay and the collider pressure (number density). For each rotational level shown in Figure 4.20, at low

collision numbers the plots are relatively linear, implying that the single exponential model is reasonable. However, at higher collision numbers, especially apparent at larger pressures, the line deviates to a positive direction, exhibiting multimodal character, and hence the single exponential model breaks down. The fact that the lines deviate to the positive side is consistent with the population removal slowing down, which is suggestive of multiple collisions returning the population to the initial level.

Ignoring, for the moment, the implied breakdown of the model at high collision number, bimolecular plots of the rates $\Gamma_{pop,j}$ and $\Gamma_{dep,j}^{(K)}$ against the Ar collider number density can be constructed to yield the bimolecular rate constants $k_{pop,j}$ and $k_{dep,j}^{(K)}$. Figure 4.21 shows these as an example for j = 2.5, 6.5 and 11.5 F_1e. The measured $k_{pop,j}$ and $k_{dep,j}^{(K)}$ rate constants from the single exponential model for all j-levels studied are presented in Table 4.4 and Figure 4.22. These are compared with the previous measurements from reference 199.

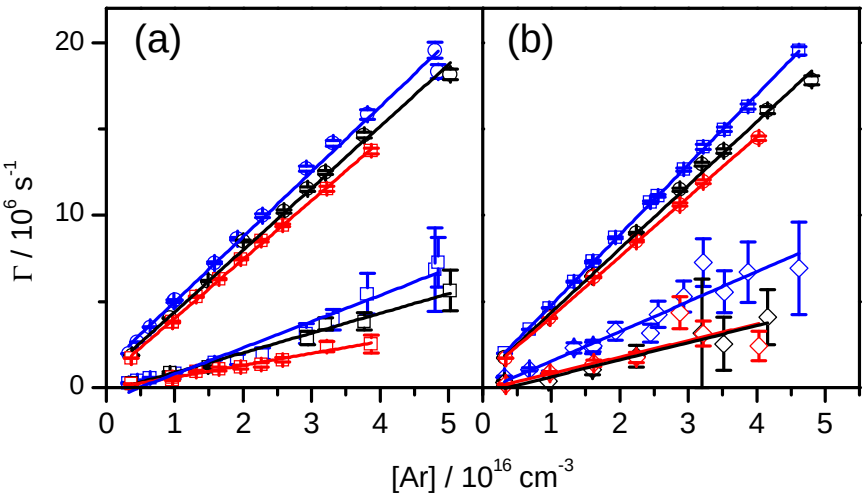

Figure 4.21 – Plots of the total population removal rates (circles), $\Gamma_{pop,j}$, orientation elastic depolarisation rates (squares), $\Gamma_{dep,j}^{(1)}$, and alignment depolarisation rates (diamonds), $\Gamma_{dep,j}^{(2)}$, for j = 2.5 F_1e (blue), j = 6.5 F_1e (black) and j = 11.5 F_1e (red). Solid lines are linear fits to the data. Error bars are 2σ statistical uncertainties.

Table 4.4 – Rate constants determined from the single exponential kinetic fitting for the total removal of population $k_{pop,j}$*, and elastic depolarisation of orientation,* $k^{(1)}_{dep,j}$*, and alignment,* $k^{(2)}_{dep,j}$*, in units of* 10^{-10} cm^3 s^{-1}*, with* 2σ *statistical uncertainties.*

j	$k_{pop,j}$ [a]	$k_{pop,j}$ [b]	$k^{(1)}_{dep,j}$ [a]	$k^{(2)}_{dep,j}$ [b]
2.5	4.18 ± 0.20	4.09 ± 0.05	1.52 ± 0.19	1.73 ± 0.31
3.5	3.91 ± 0.07	4.16 ± 0.07	1.24 ± 0.25	0.96 ± 0.25
6.5	3.60 ± 0.15	3.68 ± 0.14	1.15 ± 0.10	0.96 ± 0.24
11.5	3.24 ± 0.12	3.59 ± 0.07	0.69 ± 0.08	1.00 ± 0.14
13.5	3.45 ± 0.05	3.30 ± 0.06	0.46 ± 0.14	0.68 ± 0.18
18.5	3.08 ± 0.16	3.20 ± 0.09	0.43 ± 0.11	-

[a] *Determined from circular polarisation experiments.*

[b] *Determined from linear polarisation experiments.*

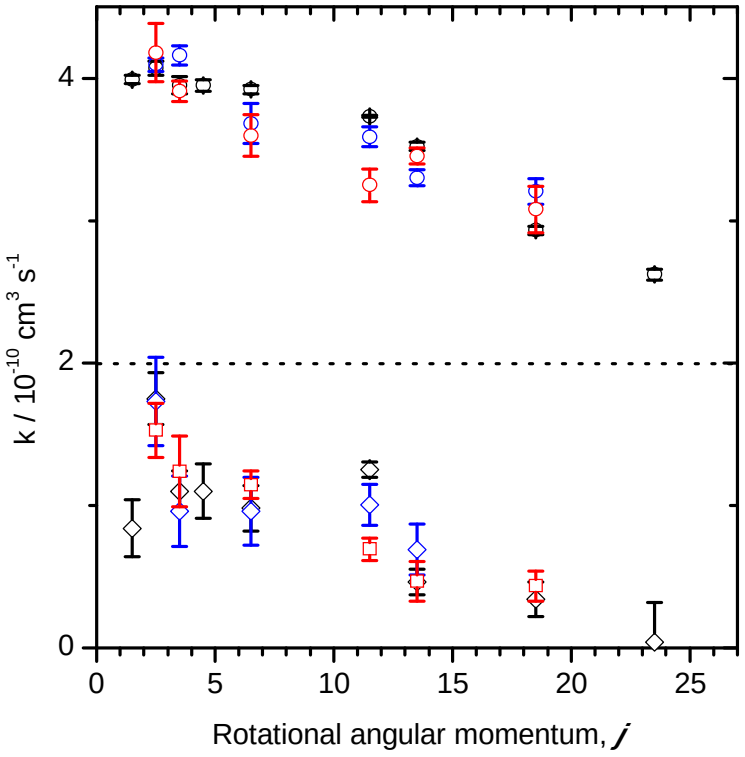

Figure 4.22 – Population removal (circles), orientation depolarisation (squares) and alignment depolarisation (diamonds) bimolecular rate constants from the circular polarisation (red) and linear polarisation (blue) experiments fitted according to the single exponential model. Black data points are the previously measured rate contants from Figure 4.1. Error bars are 2σ *statistical uncertainties. A dotted line shows more clearly the separation between the population removal and depolarisation rate constants.*

In Figure 4.21, both gradients $k_{pop,j}$ and $k_{dep,j}^{(K)}$ increase with *j*, indicating that lower rotational levels undergo faster RET and depolarisation. The decrease in population removal rate constants with increasing *j* is commonly observed, and can be explained by the increasing energy gaps between adjacent rotational levels. Similarly, conservation of angular momentum implies that the faster an object is rotating, the harder it will be to tilt, consistent with the observed decrease in depolarisation rate constant with increasing *j*. These general trends are again apparent in Figure 4.22. The rate constants from reference 199 are in close agreement with those measured in this work, which is encouraging, as they are measurements of the same quantity from different experimental set-ups at different time periods. This shows the reproducibility of the FM technique and supports the decision to ignore the small alignment contribution to the population traces derived from the circular polarised measurements.

The population removal is seen to be a rapid process in the presence of slower polarisation removal. The phenomenological (elastic in this model) depolarisation is still significant on the time scale of population loss, with rate constants for both orientation and alignment of the order of 10^{-10} cm^3 s^{-1}, but with no obvious *K*-dependence. Similar behaviour was seen in stimulated Raman pumping experiments by Halpern and co-workers on ground state C_2H_2 self-collisions.[80-82, 108] Those authors also noted elastic depolarisation of the prepared orientation or alignment to be an efficient process, with both associated tensor rate constants approximately equal in magnitude and declining with increasing *j*. Although a closed-shell species, this can approximately be treated as diatomic C_2, which is kinematically equivalent to CN, with a rotational constant $B_{C_2H_2(X)} = 1.18$ cm^{-1}.[278, 279]

Such behaviour suggests an unrestricted change in *m* during a collision, resulting in complete randomisation of the initial *m* distribution. The rapid depolarisation seen here is more akin to the OH($X^2\Pi$)+Ar system,[126, 129-131] rather than the kinematically and energetically similar NO($X^2\Pi$)+Ar system,[136] where much slower depolarisation is seen. A heavy-light kinematic rotor, such as OH, has large rotational spacings that hinder RET, while the re-orientation of the light atom towards the collider is relatively facile. In contrast, heavy-heavy kinematic rotors, such as CN and NO, are classically harder to reorient, and the smaller rotational energy spacings result in a bias towards RET. This is consistent with McCaffery and co-workers' studies of kinematically similar alkali dimer-rare gas collisions, where elastic depolarisation is seen to be very

inefficient.[280, 281] It is therefore surprising that fast depolarisation is observed for CN($A^2\Pi$)+Ar.

A potential explanation for the large measured depolarisation rate constants could be return of population to the initial level through multiple collisions. This is a reasonable premise, due to the large density of states (j, F_1/F_2, e/f) available near the peak of the Boltzmann distribution. Previous FMS measurements from Costen and co-workers reported state-to-state alignment muiltipole transfer efficiencies of $E^{(2)}(j,j') \leq \sim 0.5$ from $j = 6.5$ F_1e.[199] This shows that there is considerable depolarisation during RET and hence suggests that population returning to the original level will have been substantially depolarised in the product levels, thus making the assumed *elastic* depolarisation rates appear faster. This concept of *inelastic* depolarisation is supported by the apparent multimodal characters of the population and polarisation decays. The single exponential model may therefore be too simplistic to describe the observed dynamics, and further kinetic analysis needs to be applied. The subsequent sections investigate the effect of multiple collisions on the measurements.

4.5.3 Three-Level Kinetic Model

The main conclusion from the previous sub-section was that multiple collisions could be influencing the apparent size of the population removal and elastic depolarisation rate constants, causing a breakdown of the single exponential kinetic model. The model therefore needs to be extended to include the effects of multiple collisions, namely the transfer of depolarised population back into the initial level. The simplest model to account for back-transfer involves three distinct levels, as shown in Figure 4.23. This is similar in form to the "Basin-Bath" model used to analyse collisions of formaldehyde by Field and co-workers.[282] The kinetics of population transfer in such a three-level system have been previously published by Randall *et al.*[283] and are generalised here for the time evolution of both the population and orientation and alignment tensor moments of the initial level.

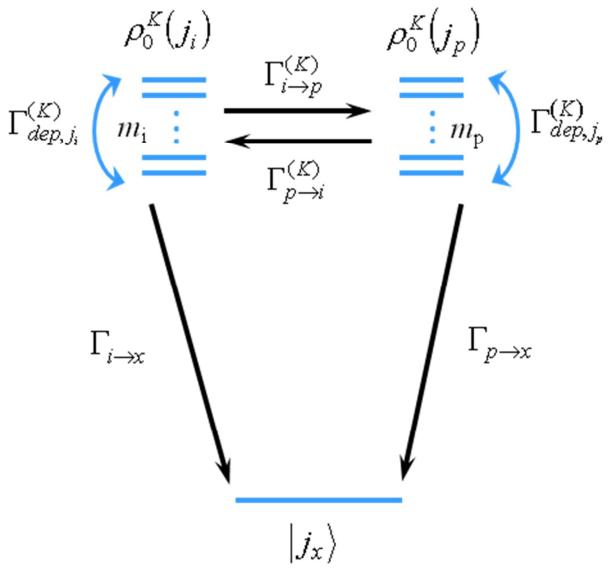

Figure 4.23 – The multi-level kinetic model to describe the transfer of prepared rotational population (K = 0), orientation (K = 1) or alignment (K = 2) upon collision with a partner. The prepared population and rotational anisotropy in an initial level j_i may be reversibly transferred to nearby product rotational levels, j_p,with rates $\Gamma_{i\to p}^{(K)}$ and $\Gamma_{p\to i}^{(K)}$, or irreversibly lost to far-away levels from both j_i and j_p, with rates $\Gamma_{i\to x}$ and $\Gamma_{p\to x}$. The anisotropy may also undergo elastic depolarisation in both j_i and j_p, with rates $\Gamma_{dep,j_i}^{(K)}$ and $\Gamma_{dep,j_p}^{(K)}$.

The first level is the observed spectroscopic level, j_i. The second level, j_p, represents close-lying rotational levels from which back-transfer to j_i is possible. Finally, j_x, represents those levels that are either far enough away (e.g. in energy, angular momentum, or even vibrational or electronic state), that back-transfer is effectively impossible. The rates for the transfer processes between j_i and j_p depend on the tensor rank and are given as $\Gamma_{i\to p}^{(K)}$ and $\Gamma_{p\to i}^{(K)}$, while those for total removal to j_x are independent of rank, $\Gamma_{i\to x}$, and $\Gamma_{p\to x}$. The other significant process is elastic depolarisation, which may occur within either j_i or j_p, with the rate $\Gamma_{dep,j}^{(K)}$. The time-dependence of a tensor moment of rank K of the initial level, j_i, is:[12, 19, 283]

$$\rho_0^K(j_i;t)=\frac{\rho_0^K(j_i;t=0)}{\left(\lambda_1^{(K)}-\lambda_2^{(K)}\right)}\left[\left(\Gamma_{i,tot}^{(K)}+\lambda_1^{(K)}\right)e^{\lambda_2^{(K)}t}-\left(\Gamma_{i,tot}^{(K)}+\lambda_2^{(K)}\right)e^{\lambda_1^{(K)}t}\right]$$

Equation 4.21

Since the K = 0 tensor moment is directly proportional to the population, $A_0^{(0)}$, the time-

dependence of the population can be expressed as:

$$A_0^{(0)}(j_i;t) = \frac{A_0^{(0)}(j_i;t=0)}{\left(\lambda_1^{(0)} - \lambda_2^{(0)}\right)}\left[\left(\Gamma_{i,tot}^{(0)} + \lambda_1^{(0)}\right)e^{\lambda_2^{(0)}t} - \left(\Gamma_{i,tot}^{(0)} + \lambda_2^{(0)}\right)e^{\lambda_1^{(0)}t}\right]$$

Equation 4.22

where $\Gamma_{i,tot}^{(0)}$ and $\Gamma_{p,tot}^{(0)}$, are the total population removal rates, which are the sums of the individual population transfer rates:

$$\Gamma_{i,tot}^{(0)} = \Gamma_{i\to p}^{(0)} + \Gamma_{i\to x}$$

Equation 4.23

$$\Gamma_{p,tot}^{(0)} = \Gamma_{p\to i}^{(0)} + \Gamma_{p\to x}$$

Equation 4.24

The parameters $\lambda_1^{(0)}$ and $\lambda_2^{(0)}$ have the forms:

$$\lambda_1^{(0)} = -\frac{1}{2}\left[\Gamma_{i,tot}^{(0)} + \Gamma_{p,tot}^{(0)}\right] - \sqrt{\left(\Gamma_{i,tot}^{(0)} - \Gamma_{p,tot}^{(0)}\right)^2 + 4\Gamma_{i\to p}^{(0)}\Gamma_{p\to i}^{(0)}}$$

Equation 4.25

$$\lambda_2^{(0)} = -\frac{1}{2}\left[\Gamma_{i,tot}^{(0)} + \Gamma_{p,tot}^{(0)}\right] + \sqrt{\left(\Gamma_{i,tot}^{(0)} - \Gamma_{p,tot}^{(0)}\right)^2 + 4\Gamma_{i\to p}^{(0)}\Gamma_{p\to i}^{(0)}}$$

Equation 4.26

The polarisation moments are proportional to the relevant K = 1 or 2 tensor moment normalised by the K = 0 tensor moment.[16] The time-dependence of the polarisation of the initial state, $A_0^{(K)}(j_i)$, is therefore:

$$A_0^{(K)}(j_i;t) = A_0^{(K)}(j_i;t=0)\left[\frac{\left(\lambda_1^{(0)} - \lambda_2^{(0)}\right)}{\left(\lambda_1^{(K)} - \lambda_2^{(K)}\right)}\right]\frac{\left[\left(\Gamma_{i,tot}^{(K)} + \lambda_1^{(K)}\right)e^{\lambda_2^{(K)}t} - \left(\Gamma_{i,tot}^{(K)} + \lambda_2^{(K)}\right)e^{\lambda_1^{(K)}t}\right]}{\left[\left(\Gamma_{i,tot}^{(0)} + \lambda_1^{(0)}\right)e^{\lambda_2^{(0)}t} - \left(\Gamma_{i,tot}^{(0)} + \lambda_2^{(0)}\right)e^{\lambda_1^{(0)}t}\right]}$$

Equation 4.27

where $\Gamma_{i,tot}^{(0)}$ and $\Gamma_{p,tot}^{(0)}$, $\lambda_1^{(0)}$ and $\lambda_2^{(0)}$, are as defined in Equation 4.23 – Equation 4.26 above. For tensors of rank $K \geq 1$ the elastic depolarisation must be included as an additional loss process in the total removal rates:

$$\Gamma_{i,tot}^{(K)} = \Gamma_{i\to p}^{(0)} + \Gamma_{i\to x} + \Gamma_{dep,j_i}^{(K)}$$

Equation 4.28

$$\Gamma_{p,tot}^{(K)} = \Gamma_{p\to i}^{(0)} + \Gamma_{p\to x} + \Gamma_{dep,j_p}^{(K)}$$

Equation 4.29

Similarly, polarisation may be lost in the transfer between j_i and j_p. It is convenient to include this by expressing the tensor transfer rates, $\Gamma_{i\to p}^{(K)}$ and $\Gamma_{p\to i}^{(K)}$, in terms of multipole transfer efficiencies, $E^{(K)}(j, j')$.

$$\Gamma_{i\to p}^{(K)} = \Gamma_{i\to p}^{(0)} E^{(K)}\left(j_i, j_p\right)$$

Equation 4.30

$$\Gamma_{p\to i}^{(K)} = \Gamma_{p\to i}^{(0)} E^{(K)}\left(j_p, j_i\right)$$

Equation 4.31

The coefficients $\lambda_1^{(K)}$ and $\lambda_2^{(K)}$ are then given by:

$$\lambda_1^{(K)} = -\frac{1}{2}\left[\Gamma_{i,tot}^{(K)} + \Gamma_{p,tot}^{(K)}\right] - \sqrt{\left(\Gamma_{i,tot}^{(K)} - \Gamma_{p,tot}^{(K)}\right)^2 + 4\Gamma_{i\to p}^{(0)} E^{(K)}\left(j_i, j_p\right)\Gamma_{p\to i}^{(0)} E^{(K)}\left(j_p, j_i\right)}$$

Equation 4.32

$$\lambda_2^{(K)} = -\frac{1}{2}\left[\Gamma_{i,tot}^{(K)} + \Gamma_{p,tot}^{(K)}\right] + \sqrt{\left(\Gamma_{i,tot}^{(K)} - \Gamma_{p,tot}^{(K)}\right)^2 + 4\Gamma_{i\to p}^{(0)} E^{(K)}\left(j_i, j_p\right)\Gamma_{p\to i}^{(0)} E^{(K)}\left(j_p, j_i\right)}$$

Equation 4.33

Expressions for the time-dependence of the population, and orientation or alignment now exist, which can be fitted to the experimental data. Additional constraints have also

been applied on the rates in the above expressions. The removal rate to the final level, j_x, should not depend sensitively on the identity of j_i or j_p, giving the constraint:

$$\Gamma_{i\to x} = \Gamma_{p\to x}$$

Equation 4.34

The elastic depolarisation rate should not vary rapidly with j enough to strongly influence the values of the other fitted parameters, and since j_p is not a unique level, the following constraint is therefore applied:

$$\Gamma^{(K)}_{dep,\,j_i} = \Gamma^{(K)}_{dep,\,j_p} = \left\langle \Gamma^{(K)}_{dep} \right\rangle$$

Equation 4.35

Also, in the absence of any *a priori* information on the MTEs, an average value of the MTE for transfer in both directions was chosen, as shown in Equation 4.36. This decision is supported by the success of the model in trial fitting to the experimental data with this restricted set of parameters.

$$E^{(K)}\left(j_i, j_p\right) = E^{(K)}\left(j_p, j_i\right) = \left\langle E^{(K)}\left(j, j'\right)\right\rangle$$

Equation 4.36

Fits to the experimental data were performed using this model in the following fashion. First, the population kinetic trace was fitted to Equation 4.22, varying the initial population, $A_0^{(0)}\left(j_i; t=0\right)$, and the three rates $\Gamma_{i\to x} = \Gamma_{p\to x}$, $\Gamma^{(0)}_{i\to p}$ and $\Gamma^{(0)}_{p\to i}$. This yielded the total population removal rate for the initial level, $\Gamma^{(0)}_{i,tot}$ as defined in Equation 4.23. These population rates were then fixed in the fitting of the orientation or alignment kinetic trace to Equation 4.27, varying the initial orientation or alignment, $A_0^{(K)}\left(j_i; t=0\right)$, and the elastic depolarisation rate $\left\langle \Gamma^{(K)}_{dep} \right\rangle$. Trial fitting showed strong correlations between the elastic depolarisation and MTE for any single kinetic trace, and the average MTE was therefore held at a pre-selected constant value in the fits reported below. The fitting was performed using a LM minimisation by custom-written LabVIEW® routines (developed by Dr. Matthew L. Costen, Heriot-Watt University), with the kinetic data traces weighted by the errors previously determined by the data

analysis code. The fits were started 10 ns after the peak population, to avoid overlap with the pump pulse. The full range of acquisition times was used when fitting the population; for the orientation or alignment the fit was truncated to exclude times where the polarisation was ill-defined, around < 1% of the initial population. Figure 4.24 and Figure 4.25 show the result of this fitting procedure applied to the population and orientation data for j = 2.5, 6.5 and 11.5 F_1e at pressures of~100 mTorr, ~500 mTorr and ~1000 mTorr with three different assumed values of the average MTE. The excellent fits to the data yield only statistical residual errors.

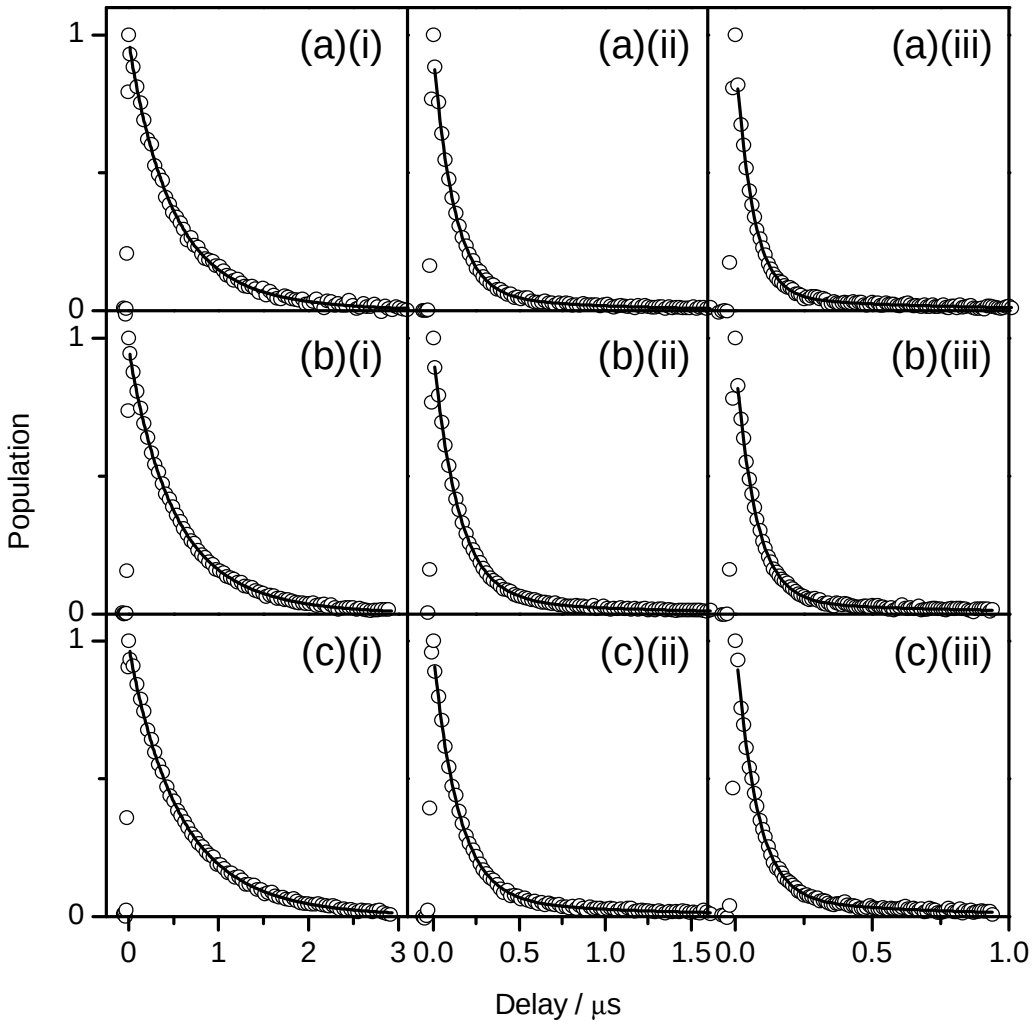

Figure 4.24 – Fits of three-level model to the population kinetic traces for (a) j = 2.5 F_1e, (b) j = 6.5 F_1e and (c) j = 11.5 F_1e at (i) ~100 mTorr, (ii) ~500 mTorr and (iii) ~1000 mTorr total pressures. Error bars are the same as for Figure 4.13 and have been omitted here for visual clarity.

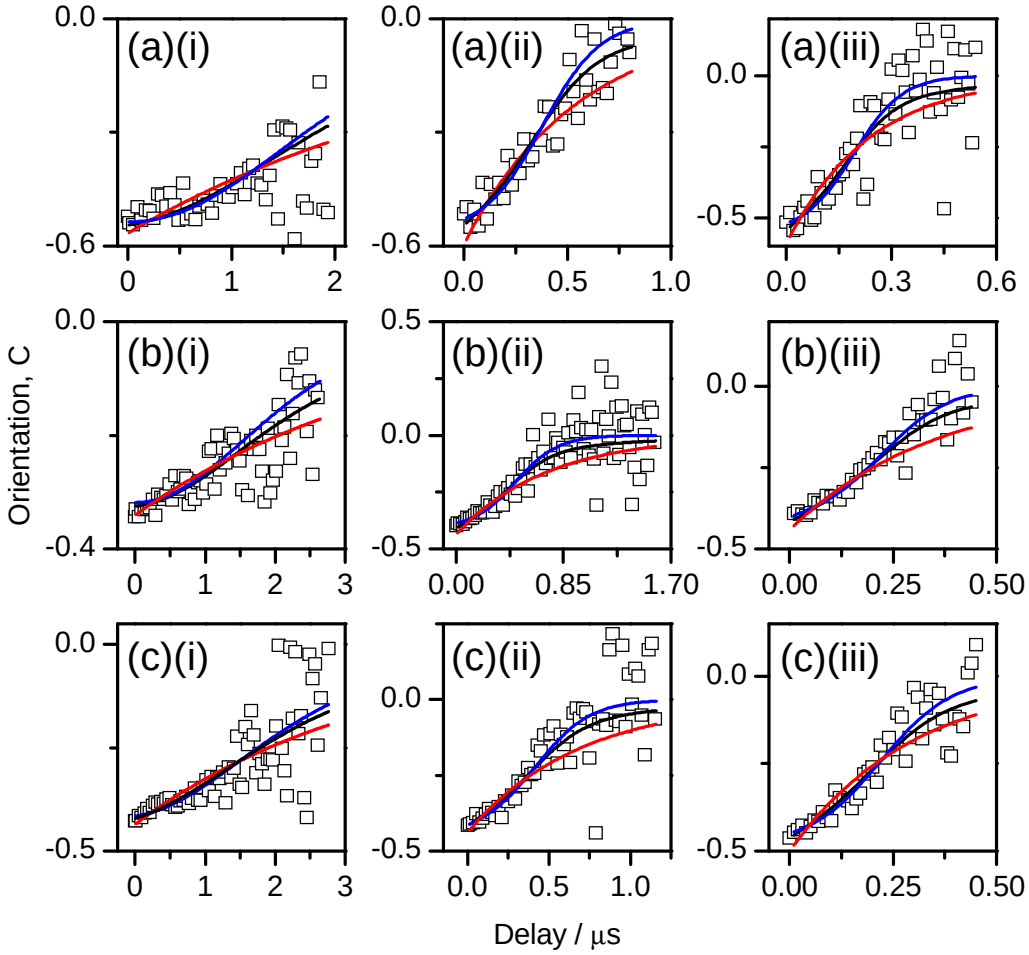

Figure 4.25 – Fits of the three-level model to the orientation kinetic traces for (a) j = 2.5 F_1e, (b) j = 6.5 F_1e and (c) j = 11.5 F_1e at (i) ~100 mTorr, (ii) ~500 mTorr and (iii) ~1000 mTorr total pressures. The population rates from the previous figure were fixed in the analysis, as explained in the text. Three different fits to the orientation data are shown, where $\langle E^{(1)}(j, j')\rangle$ *= 0 (blue), 0.5 (black) and 1 (red). Error bars are the same as for Figure 4.14 and have been omitted here for visual clarity.*

There are three different fits to the orientation data in Figure 4.25, using the same population rates, where the MTEs, $\langle E^{(1)}(j, j')\rangle$, were fixed at values of 0, 0.5 and 1, to show the effect of full, half and no inelastic depolarisation, respectively. Inspection of Equation 4.21 – Equation 4.36 shows that constraining $\langle E^{(1)}(j, j')\rangle = 1$ results in a single exponential decay of the orientation, consistent with the general shape of the red curves in Figure 4.25. This is equivalent to the single exponential model applied in the previous section. The red curves are clearly considerably poorer fits to the data, failing to reproduce the observed multiple curvature. Conversely, the blue curves with no depolarisation are better fits and reproduce the the multimodal character, although are

slightly slower than the observed polarisation decays. The best fits to the data are the black curves, where $\langle E^{(1)}(j, j')\rangle = 0.5$, showing that there is substantial inelastic depolarisation. This MTE value was optimised in trial fits to the orientation data, and is in accord with the alignment MTEs from reference 199, which range between 0.3 – 0.55. Similar effects are observed for both the orientation and alignment decays in this work.

The total population removal rates, $\Gamma^{(0)}_{i,tot}$, and the elastic depolarisation rates, $\Gamma^{(K)}_{dep}$, for orientation and alignment for all rotational levels and collider pressures studied were determined from these fits, constraining the average MTEs to $\langle E^{(K)}(j, j')\rangle = 0.5$. Figure 4.26 shows example plots of the population and orientation removal rates for three rotational levels as a function of Ar number density, together with weighted linear least-squares fits to extract the bimolecular rate constants, k_{pop,j_i} and $k^{(K)}_{dep,j_i}$. The measured rate constants derived from the three-level kinetic fits are listed in Table 4.5 and Figure 4.27 compares them to the single exponential rate constants from Section 4.5.2.

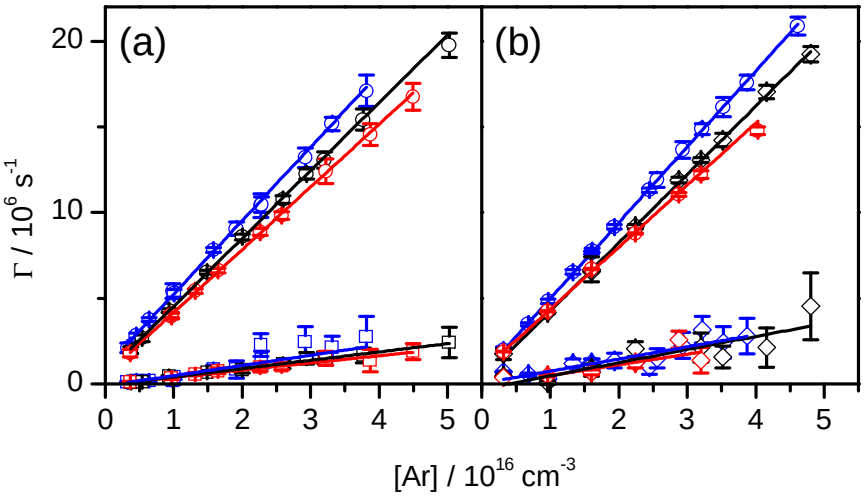

Figure 4.26 – Plots of the population removal rates, $\Gamma^{(0)}_{i,tot}$, (circles), orientation depolarisation rates, $\Gamma^{(1)}_{dep}$, (squares) and alignment depolarisation rates, $\Gamma^{(2)}_{dep}$, (diamonds), determined from the three-level kinetic model for j = 2.5 F_1e (blue), j = 6.5 F_1e (black) and j = 11.5 F_1e (red). The straight lines are linear least-squares weighted fits to the data points to determine the bimolecular rate constants k_{pop,j_i}, $k^{(1)}_{dep,j_i}$ and $k^{(2)}_{dep,j_i}$. Error bars are 2σ statistical uncertainties.

Table 4.5 – Rate constants determined from the three-level kinetic model for the total removal of population $k_{pop,j}$, and elastic depolarisation of orientation, $k^{(1)}_{dep,j}$, and alignment, $k^{(2)}_{dep,j}$, with 2σ statistical uncertainties. Units are 10^{-10} cm^3 s^{-1}.

j	$k_{pop,j}$ [a]	$k_{pop,j}$ [b]	$k^{(1)}_{dep,j}$ [a]	$k^{(2)}_{dep,j}$ [b]
2.5	4.23 ± 0.12	4.43 ± 0.06	0.59 ± 0.14	0.35 ± 0.30
3.5	4.35 ± 0.09	4.46 ± 0.13	0.54 ± 0.07	0.40 ± 0.18
6.5	3.90 ± 0.10	3.98 ± 0.08	0.56 ± 0.12	0.32 ± 0.38
11.5	3.64 ± 0.09	3.62 ± 0.10	0.45 ± 0.06	0.62 ± 0.38
13.5	3.55 ± 0.08	3.50 ± 0.04	0.47 ± 0.09	0.54 ± 0.25
18.5	3.52 ± 0.20	3.52 ± 0.06	0.15 ± 0.28	0.36 ± 0.42

[a] *Determined from circular polarisation experiments.*

[b] *Determined from linear polarisation experiments.*

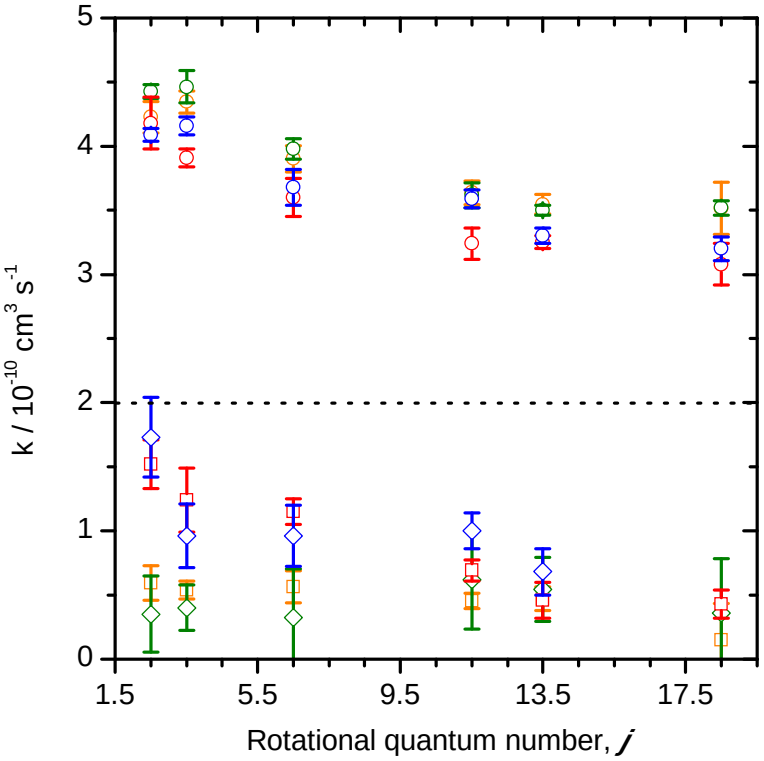

Figure 4.27 – Population removal (circles), orientation depolarisation (squares) and alignment depolarisation (diamonds) bimolecular rate constants from the single exponential fits (red = cirular pump-probe geometries, blue = linear pump-probe geometries), and from fits to the three-level kinetic model (orange = circular pump-probe geometries, green = linear pump-probe geometries). Error bars are 2σ statistical uncertainties. The dotted line shows more clearly the separation between the population removal and elastic depolarisation rate constants.

The population removal rate constants determined from the three-level fits are typically 10% – 15% larger than those derived from single exponential fits. This is consistent with a slight underestimation of the previously determined rate constants, due to neglect of back-transfer into the initial level. The orientation and alignment experiments provide independent measurements of the population removal rate constants, and are found to agree quantitatively with each other for all *j* within experimental error. This supports the assumption to ignore the small alignment contribution to the orientation measurements. The three-level orientation and alignment elastic depolarisation rate constants lie in the range $(0 – 5) \times 10^{-11}$ cm^3 s^{-1}, with no obvious correlation with *K* or *j*. The uncertainties in these measurements are considerably larger than for the corresponding populations, reflecting both the difficulty in measuring such slow processes in the presence of much faster population removal, and the additional complication of inelastic depolarisation. However, they are noticeably smaller than the depolarisation rate constants derived from fits to the (now clearly too simplistic) single exponential model in Section 4.5.2.

To support the experimental measurements and help synergistically gauge the underlying collision dynamics, full *cc*-QS calculations were performed on previous[15] and new *ab initio* CN($A^2\Pi$)-Ar PESs. The QS predictions were then used in master equation (ME) modeling of the population removal and depolarisation kinetics, the results of which are compared to the experimental measurements. This information is presented in the next two sections.

4.5.4 PESs and QS calculations

The CN($A^2\Pi$)-Ar interaction potentials and QS rate constants were calculated by our collaborators, Prof. Paul J. Dagdigian, Prof. Millard H. Alexander and co-workers at the Johns Hopkins University and the University of Maryland, USA. The earlier Berning-Werner (B-W) PESs, new Bennett-Kłos (B-K) PESs and the QS calculations are outlined here.

As introduced in Chapter 1, the approach of a spherical collider towards a $^2\Pi$ molecule results in two separate adiabatic potential energy surfaces (PESs), of A' and A'' symmetry. In QS calculations, it is more convenient to use the diabatic average sum and difference of these surfaces, V_{sum} and V_{dif}. The coupling of the ground state (V_Σ) and excited state PESs may be described by a separate coupling potential, V_1. The PESs are

functions of the Jacobi coordinates describing the triatomic system: ***r*** (the C-N bond distance), ***R*** (the distance between the Ar atom and the CN centre-of-mass) and θ (the angle between ***r*** and ***R***, where θ = 0^o corresponds to a linear Ar-N-C geometry). Calculations of both the B-W and B-K PESs were carried out with the MOLPRO® suite of *ab initio* programs.[8]

Berning-Werner PESs

The augmented correlation-consistent valence triple-zeta (avtz) basis set of Dunning and co-workers was used[284, 285] with a complete-active-space self-consistent field (CASSCF).[286-288] Calculations were performed using the multireference, internally contracted configuration-interaction (MRCI) method.[289, 290] The contribution of higher-order excitations was estimated using the internally contracted multireference version of the Davidson correction[291, 292] with standard counterpoise and size-consistency corrections.[13, 200, 293, 294] The average v_A = 3 C-N bond distance, *r*, was fixed at 2.396 bohr and the PESs calculated at 13 values of *R* (between 4 – 7 bohr) and 7 angles (θ = 0^o, 30^o, 60^o, 90^o, 120^o, 150^o and 180^o). The B-W V_{sum} and V_{dif} potentials are shown in Figure 4.28. Angular expansions of the *R* dependence are shown in Figure 4.29. In the proceeding figures, the terms 'V_{dif}' and 'V_{diff}' are considered interchaneable for referring to the difference potentials.

The V_{sum} well-depth is 75 cm^{-1} with a T-shaped minimum. The CN($A^2\Pi$)-Ar dissociation energy was computed to be D_0 = 65.5 cm^{-1} through a variational calculation using the distributed Gaussian method of Hamilton and Light.[295] QS predictions from the B-W PESs have previously been compared to experimental measurements of CN($A^2\Pi$, v = 3)+Ar state-to-state population transfer rate constants for highly excited rotational levels (N = 60) and levels near the peak of the Boltzmann distribution (around j = 6.5 F_1e).[15, 190, 194] Qualitatively, there was generally good agreement, suggesting the repulsive core of the PESs to be accurate. Separate CN($X^2\Sigma^+$, $A^2\Pi$)-Ar van der Waals predissociation spectroscopy confirmed that the general form of the PESs is correct, but suggested a larger CN($A^2\Pi$, v = 3)-Ar dissociation energy of D_0 = 125 ± 2 cm^{-1}.[196] Subsequent empirical re-scaling of the B-W PESs to reproduce the observed spectrosopy gave a modified well-depth of 138 cm^{-1}. The new Bennett-Kłos *ab initio* CN($A^2\Pi$, v = 4)-Ar PESs were later calculated for this work and are presented in the next sub-section.

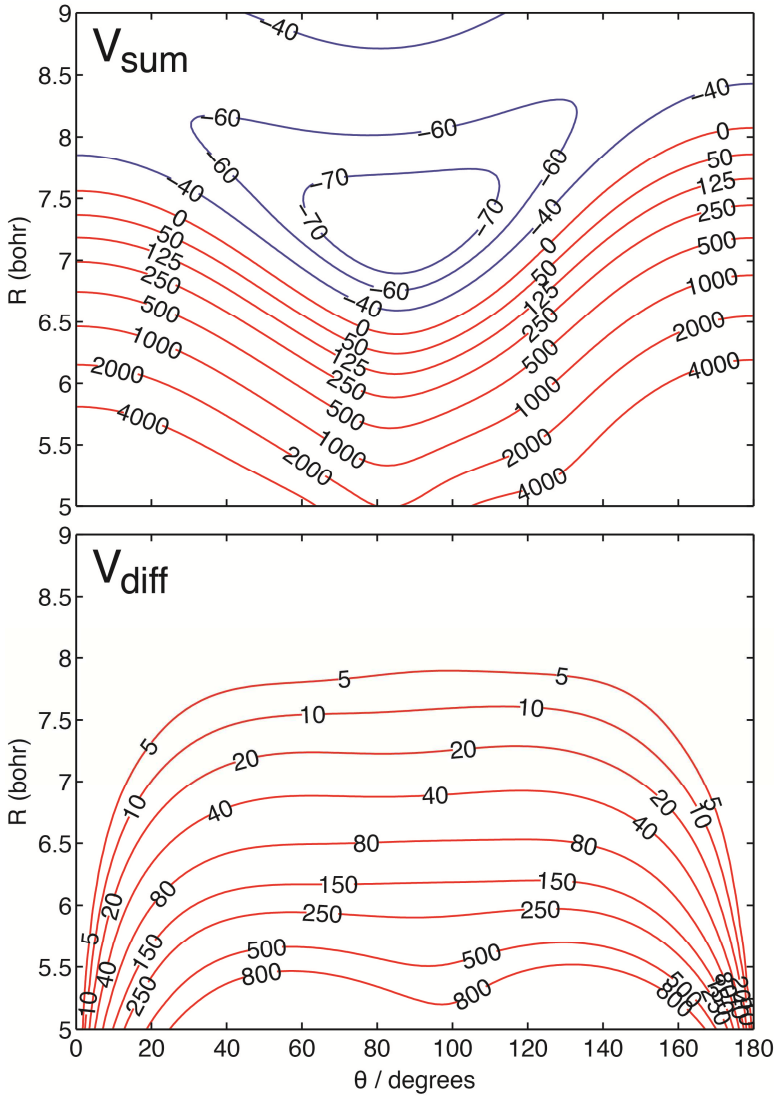

Figure 4.28 – Contour plots of the B-W CN($A^2\Pi$, v = 3)-Ar V_{sum} and V_{dif} potentials from reference 15. The contours are labelled in units of cm^{-1}.

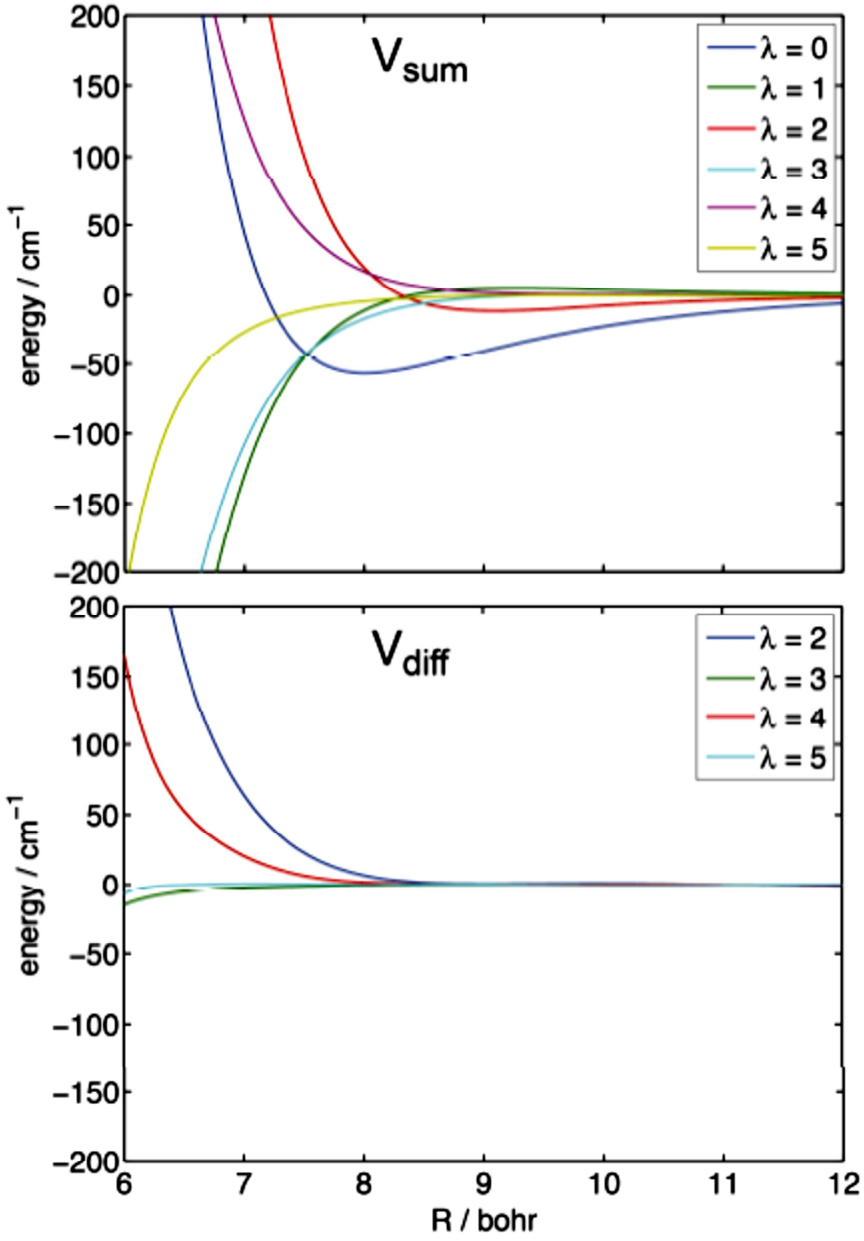

Figure 4.29 – Plots of the R dependence of the leading angular expansion coefficients $V_{\lambda 0}(R)$ (top panel) and $V_{\lambda 2}(R)$ (bottom panel) of the B-W V_{sum} and V_{dif} PESs, respectively, for the interaction of CN($A^2\Pi$, v=3) with Ar, reproduced from the supplimentary material in reference 296.

Bennett-Kłos PESs

The new B-K potentials pertain to CN($A^2\Pi$, v = 4), for which the average CN interatomic distance of r = 2.43 bohr was used. Such a small change from the B-W v_A = 3 value of r = 2.396 bohr is unlikely to have a significant effect on the overall PES. The B-K PESs were calculated at 66 values of R between 4.9 to 23 bohr with a denser grid

around the van der Waals minima. A 30^o grid of θ was used, spanning 0^o – 180^o. An atom-centred avqz atomic-orbital basis was implemented[291, 292] with additional 3s3p2d2f1g basis functions with exponents sp 0.9, 0.3, 0.1; df, 0.6, 0.2; and g, 0.3 placed in the middle of the Jacobi vector, ***R***, and standard counterpoise correction.[293] The restricted Hartree-Fock (RHF) method was used to generate reference wavefunctions for the CN($X^2\Sigma^+$)-Ar and CN($A^2\Pi$)-Ar states. The reference wavefunction for the CN($A^2\Pi$)-Ar A' adiabatic state was obtained by rotation of the HOMO orbital of the CN($X^2\Sigma^+$)-Ar state to obtain the proper occupation pattern corresponding to the A-state. The reference wavefunctions were used as starting points for spin-unrestricted coupled-cluster calculations with single, double and non-iterative triple excitations [UCCSD(T)].[297] The reproducing kernel Hilbert space method[298, 299] was used to construct an analytic representation of the V_{sum} *and* V_{dif} potentials. The 3D kernel spans both the radial and angular coordinates. Contour plots of the B-K V_{sum} *and* V_{dif} potentials are shown in Figure 4.30. Angular expansions of the *R* dependence are shown in Figure 4.31.

A T-shaped V_{sum} minimum of -115 cm^{-1} was calculated, corresponding to a computed dissociation energy of D_0 = 110.0 cm^{-1} (using the same distributed Gaussian method as the B-W PESs). This is considerably deeper than the previous B-W potentials and compares favourably with the experimentally determined value of D_0 = 125 ± 2 cm^{-1} from reference 196. Evident in both the B-W and B-K PESs is a near-head-tail symmetry and subsequent dominance of the even-λ terms in the angular expansions, which results from the near-homonuclearity of the CN molecule.

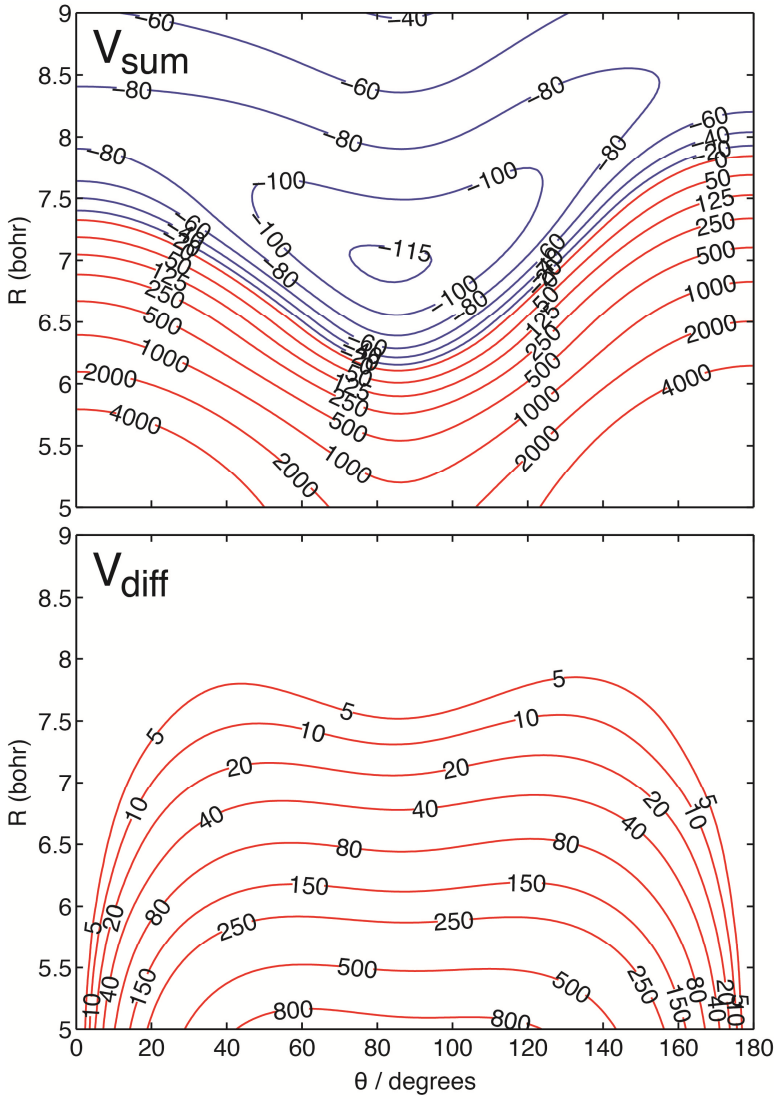

Figure 4.30 – Contour plots of the B-K CN($A^2\Pi$, v = 4)-Ar V_{sum} and V_{dif} potentials from reference 296. The contours are labelled in units of cm^{-1}.

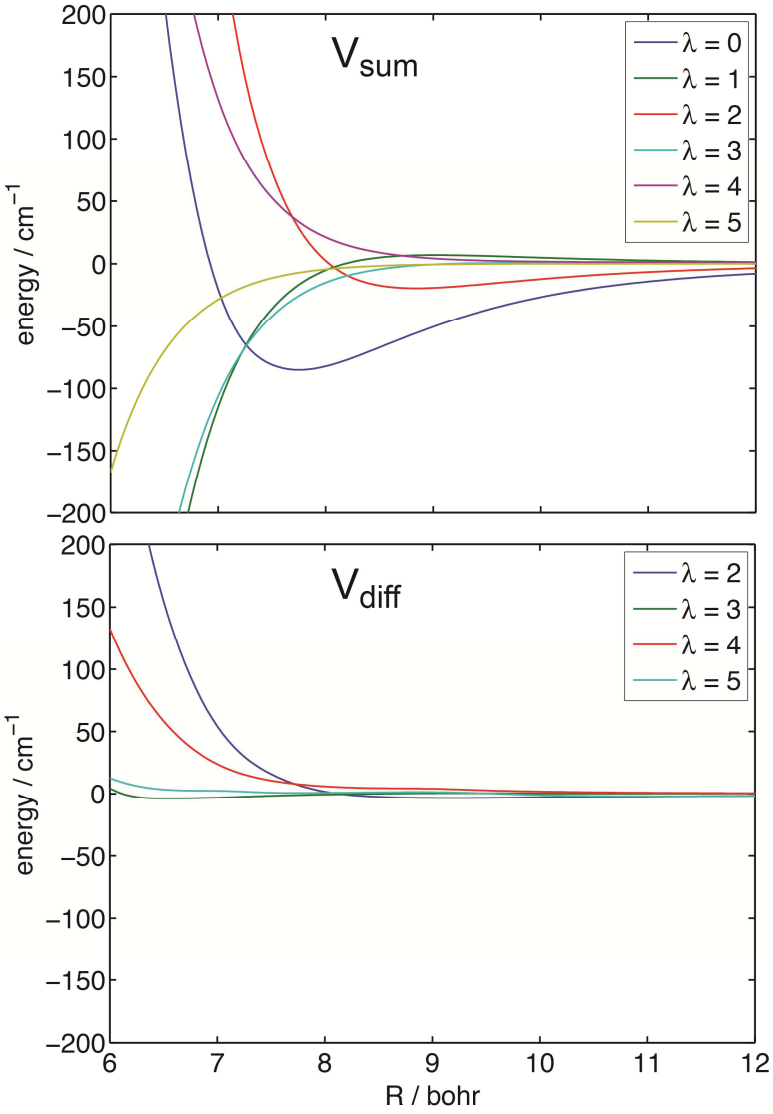

Figure 4.31 – Plots of the R dependence of the leading angular expansion coefficients $V_{\lambda 0}(R)$ (top panel) and $V_{\lambda 2}(R)$ (bottom panel) of the B-K V_{sum} and V_{dif} PESs, respectively, for the interaction of CN($A^2\Pi$, v = 4) with Ar. Reproduced from the supplementary material in reference 296.

QS calculations

The QS calculations at a particular collision energy give the $\sigma^{(K)}_{jF\varepsilon \to j'F'\varepsilon'}$ tensor cross-sections, as defined in terms of the scatterting matrix elements by Equation 1.55 of Section 1.6.1. The elastic depolarisation cross-section of rank K is then given by the difference between the totally-elastic K = 0 cross-section and the elastic tensor cross-sections of rank K, as defined in Equation 1.58.[53] The total population removal cross-section from a given rotational level is determined by the sum of the state-to-state integral cross-sections for K = 0 out of the relevant level.[300]

Energy-dependent integral and tensor cross-sections for collisions of CN($A^2\Pi$)+Ar were computed in a quantum mechanical treatment of the collision dynamics. Close-coupling calculations were performed with the HIBRIDON suite of programs.[301] Tests for the convergence of the cross-sections were carried out to ensure inclusion of a sufficient number of energetically open and closed channels and partial waves. The convergence requirements for elastic cross-sections are greater than for inelastic cross-sections. To compute the thermal rate constants, the cross-sections were calculated over a grid of collision energies up to 2000 cm^{-1} and averaged over a room temperature (T = 298 K) Maxwell-Boltzmann distribution of relative velocities.[302] At the highest energies considered (2000 cm^{-1}), the rotational basis included all levels with $j \leq 25.5$, and the scattering calculations included all angular momenta $J \leq 400.5$.

Elastic tensor cross-sections for ranks K = 0, 1 and 2, and hence depolarisation cross-sections for ranks K = 1 and 2, were calculated for collisions of CN($A^2\Pi$, v = 4, j = 1.5 – 10.5, F_1e). Integral cross-sections for rotationally inelastic transitions out of these levels were computed and summed to obtain the total population transfer cross-sections. Figure 4.32 shows the energy-dependent orientation and alignment elastic depolarisation cross-sections, $\sigma_{dep,j}^{(K)}\left(E_{coll}\right)$, for selected CN($A^2\Pi$) F_1e rotational levels as a function of the incident relative collision energy in collisions with Ar computed from the B-K PESs. As is expected from simple mechanical reorientation arguments and seen in previous QS predictions for collisions of OH($X^2\Pi$) and NO($X^2\Pi$) with Ar,[53, 54, 136, 303] the K = 2 cross-sections are larger than the K = 1 cross-sections. The elastic depolarisation cross-sections in Figure 4.32 appear to be very large at low collision energies and generally decrease with increasing collision energy, as was also found by Dagdigian and co-workers for NO($X^2\Pi$)+Ar collisions.[136] They also decrease in magnitude with increasing j, expected from energy gap and angular momentum restrictions as observed in other systems.[53, 57, 136]

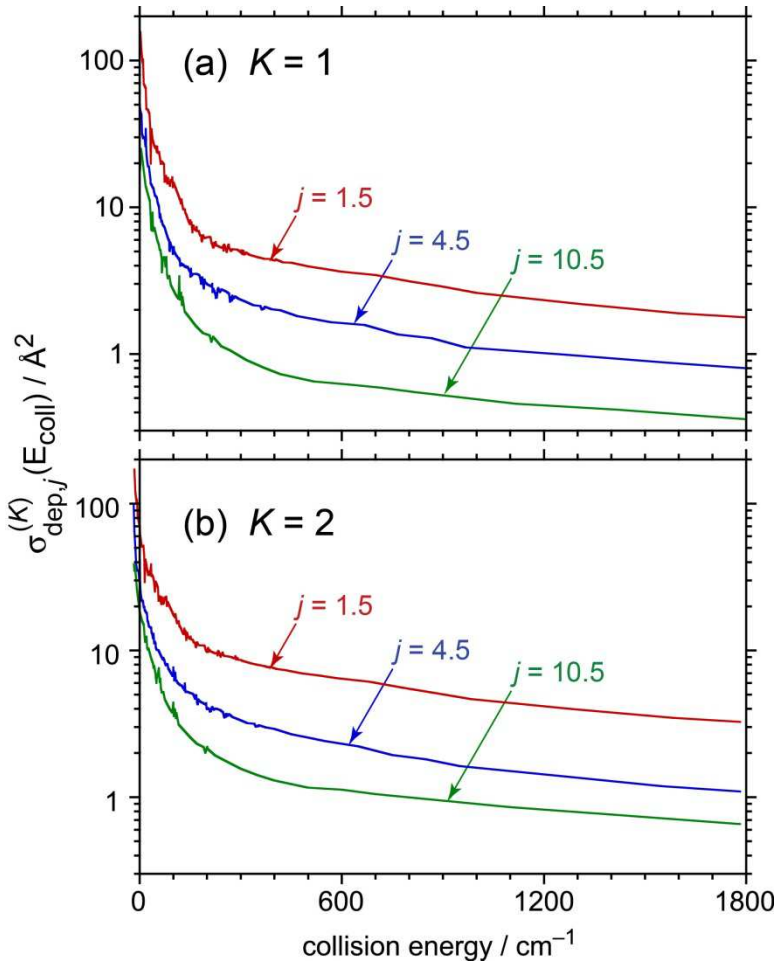

Figure 4.32 – Computed elastic depolarisation cross-sections for loss of (a) orientation [K = 1] and (b) alignment [K = 2] for the CN($A^2\Pi$, v = 4) j = 1.5, 4.5, and 10.5 F_1e rotational levels as a function of the incident relative translational energy in collisions with Ar.These cross-sections were calculated using the B-K PESs.

The energy-dependent total population removal cross-sections, $\sigma_{pop,j}$, from the B-K PESs are shown in Figure 4.33. The individual state-to-state cross-sections which comprise these are presented and discussed in references [15, 184, 199, 304]. The population cross-sections show similar behaviour to the elastic depolarisation cross-sections in Figure 4.32, generally decreasing monotonically with increasing collision energy. Comparing Figure 4.32 and Figure 4.33, population removal by RET is much more efficient than elastic depolarisation. The total removal cross-sections are also seen to decrease in magnitude with increasing *j*, however the *j*-dependence is much weaker than for elastic depolarisation.

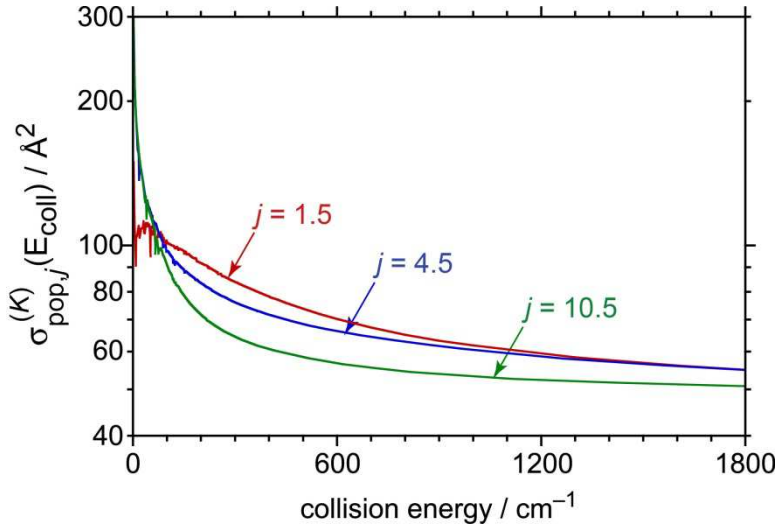

Figure 4.33 – Computed total population removal cross-sections for the CN($A^2\Pi$, v = 4) j = 1.5, 4.5, and 10.5 F_1e rotational/fine-structure levels as a function of the incident relative translational energy in collisions with Ar. These cross-sections were calculated using the B-K PESs.

Energy-dependent cross-sections such as those displayed in Figure 4.32 and Figure 4.33 were used to determine the corresponding thermal rate constants $k_{pop,j}$ and $k^{(K)}_{dep,j}$. The rate constants computed with the B-W and B-K PESs are shown in Table 4.6 and compared with the experimental measurents from the three-level kinetic model in Figure 4.34. The *j*-dependence of the calculated rate constants is similar to that observed for the energy-dependent cross-sections. The elastic depolarisation is considerably slower than the total population removal, with $k^{(2)}_{dep,j}$ being slightly faster than $k^{(1)}_{dep,j}$. Comparing the two sets of PESs, the B-K total population removal rate constants are 11% – 17% larger than those computed on the B-W potentials. Except for the *j* = 1.5 F_1e rate constants, which are significantly larger for the B-K PESs by ~25%, the elastic depolarisation rate constants are similar in magnitude for the two sets of PESs. The main differences between the two potentials therefore seem to manifest in the population removal kinetics.

While the predicted B-W $k_{pop,j}$ rate constants appear to be in close agreement with the measured $k_{pop,j}$ values determined from the three-level kinetic model, the B-K potentials systematically over-predict the measured population removal rate constants by approximately 15%, which is well outside the 2σ experimental uncertainties. Both

the B-W and B-K predicted $k_{dep,j}^{(K)}$ depolarisation rate constants are in good agreement with the lowest observed rotational levels, j = 2.5 and 3.5 F_1e, while at higher j the predicted values decline more rapidly than the measurements.

Table 4.6 – Computed room-temperature rate constants for elastic depolarisation, $k_{dep,j}^{(K)}$, and inelastic population removal, $k_{pop,j}$, for CN($A^2\Pi$, v = 4, j = 1.5 – 10.5 F_1e) + Ar. The rate constants are in units of 10^{-10} cm^3 s^{-1}.

j	Berning-Werner PESs[a]			Bennett-Kłos PESs		
	$k_{\mathrm{pop},j}$	$k_{\mathrm{dep},i}^{(1)}$	$k_{\mathrm{dep},i}^{(2)}$	$k_{\mathrm{pop},j}$	$k_{\mathrm{dep},i}^{(1)}$	$k_{\mathrm{dep},i}^{(2)}$
1.5	4.44	0.327	0.583	5.19	0.422	0.724
2.5	4.50	0.308	0.429	5.24	0.274	0.391
3.5	4.39	0.254	0.347	5.07	0.226	0.335
4.5	4.28	0.183	0.278	4.90	0.189	0.288
5.5	4.17	0.152	0.245	4.73	0.157	0.251
6.5	4.10	0.128	0.22	4.60	0.132	0.22
7.5	4.04	0.113	0.201	4.51	0.113	0.194
8.5	3.98	0.101	0.183	4.43	0.101	0.175
9.5	3.92	0.096	0.173	4.36	0.095	0.164
10.5	3.87	0.093	0.164	4.29	0.093	0.158

[a]*Reference 15.*

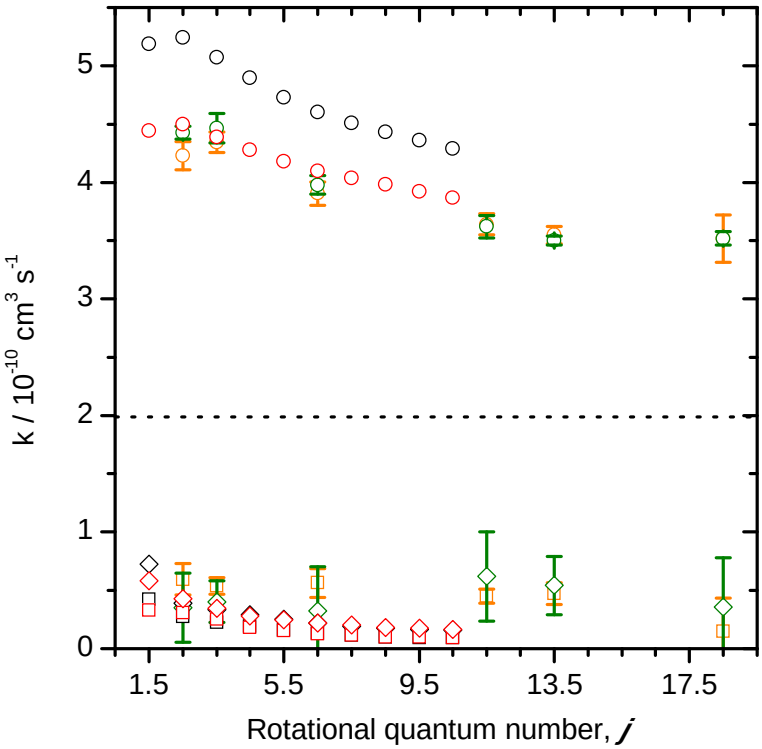

Figure 4.34 – CN($A^2\Pi$, v, j, F_1e)+Ar thermal rate constants for total removal of population (circles), $k_{pop,j}$ and elastic depolarization of orientation (squares), $k^{(1)}_{dep,j}$, and alignment (diamonds), $k^{(2)}_{dep,j}$, above and below the dotted line, respectively, from the three-level kinetic fits to the experimental measurements (orange and green) and predicted from QS calculations on the B-W PESs (red) and B-K PESs (black). The measured and B-K rate constants are for v = 4, while the B-W rate constants are for v = 3. Error bars are 2σ statistical uncertainties from the experiment.

4.5.5 Master Equation Simulations

In order to investigate the effects of multiple collisions and inelastic depolarisation, complete kinetic simulations of the population and polarisation removal out of the initally prepared level j = 6.5 F_1e were performed by Prof. Paul J. Dagdigian at The Johns Hopkins University. The simulations were then compared to the measured kinetic traces by the present author.

As previously noted, state multipoles evolve independently of each other in an isotropic collision environment. The time evolution and flow of population of the K^{th} state multipole in and out of the i^{th} level, $\rho_0^K(i)$, is expressed by:

$$\frac{d}{dt}\rho_0^K(i) = -[M]k_{pop,i}\rho_0^K(i) - [M]k_{dep,i}^{(K)}\rho_0^K(i) + [M]\sum_f k_{f\to i}^{(K)}\rho_{0,f\to i}^K$$

Equation 4.37

where [*M*] is the (Ar) collider number density, $k_{i\to f}^{(K)}$ is the rate constant for collisional transfer of the K^{th} state multipole from level *i* to level *f*, and $k_{pop,i}$ and $k_{dep,i}^{(K)}$ are the population removal and depolarisation rate constants for level *i*, as already defined. The first term on the right-hand side of Equation 4.37 represents the collisional transfer of population (and hence polarisation) to other levels, the second term represents elastic depolarisation of level *i*; and the final term represents collisional back-transfer of the K^{th} state multipole into level *i* from other levels. For the $K = 0$ multipole (proportional to the population), Equation 4.37 reduces to

$$\frac{d}{dt}\rho_0^{K=0}(i) = -[M]k_{pop,i}\rho_0^{K=0}(i) + [M]\sum_f k_{f\to i}^{(0)}\rho_{0,f\to i}^{K=0}$$

Equation 4.38

The $K = 0$ multipole has a different normalisation to the population. The state-to-state $K = 0$ tensor rate constants are related to the state-to-state population transfer rate constants by:[18, 53, 305]

$$k_{i\to f}^{(0)} = \left([j_i]/[j_f]\right)^{1/2} k_{i\to f}$$

Equation 4.39

The CN($A^2\Pi$, $v = 4$, *j*, F_1e)+Ar depolarisation rate constants, $k_{dep,i}^{(K)}$, were taken from the B-K QS predicted values in Table 4.6. Full thermal averaging of the state-to-state integral and tensor cross-sections requires computing many cross-section]#s over a large grid of energies. Therefore, to save computational expense, the state-to-state cross-sections for endothermic transitions were computed at a collisional energy of 300 cm^{-1} and assumed to represent the thermal average in order to determine the thermal rate constants. The rate constants for the reverse exothermic transitions were computed by detailed balance. The population removal rate constants, $k_{pop,i}$, were calculated from the appropriate sums of the individual state-to-state rate constants.

The set of independent differential equations describing the time evolution of the state multipoles, Equation 4.37 and Equation 4.38, were solved through an analytic solution method described by Alexander and co-workers in reference 300. An Ar collider partial pressure of 200 mTorr was used in the calculations, but since all rates scale with the Ar number density, the kinetic simulations can be scaled to any Ar pressure. Figure 4.35 compares the time-dependent population and orientation of the j = 6.5 F_1e level measured at three different Ar pressures with the corresponding master equation simulations. The x-axes have been scaled to collision number using the experimentally determined three-level population removal rate constant of $k_{pop,j} = 3.9 \times 10^{-10}$ cm^3 s^{-1} for j = 6.5 F_1e from Section 4.5.3. Orientation was chosen for the comparison since the experimental sensitivity is higher than for alignment, although similar effects are observed for both.

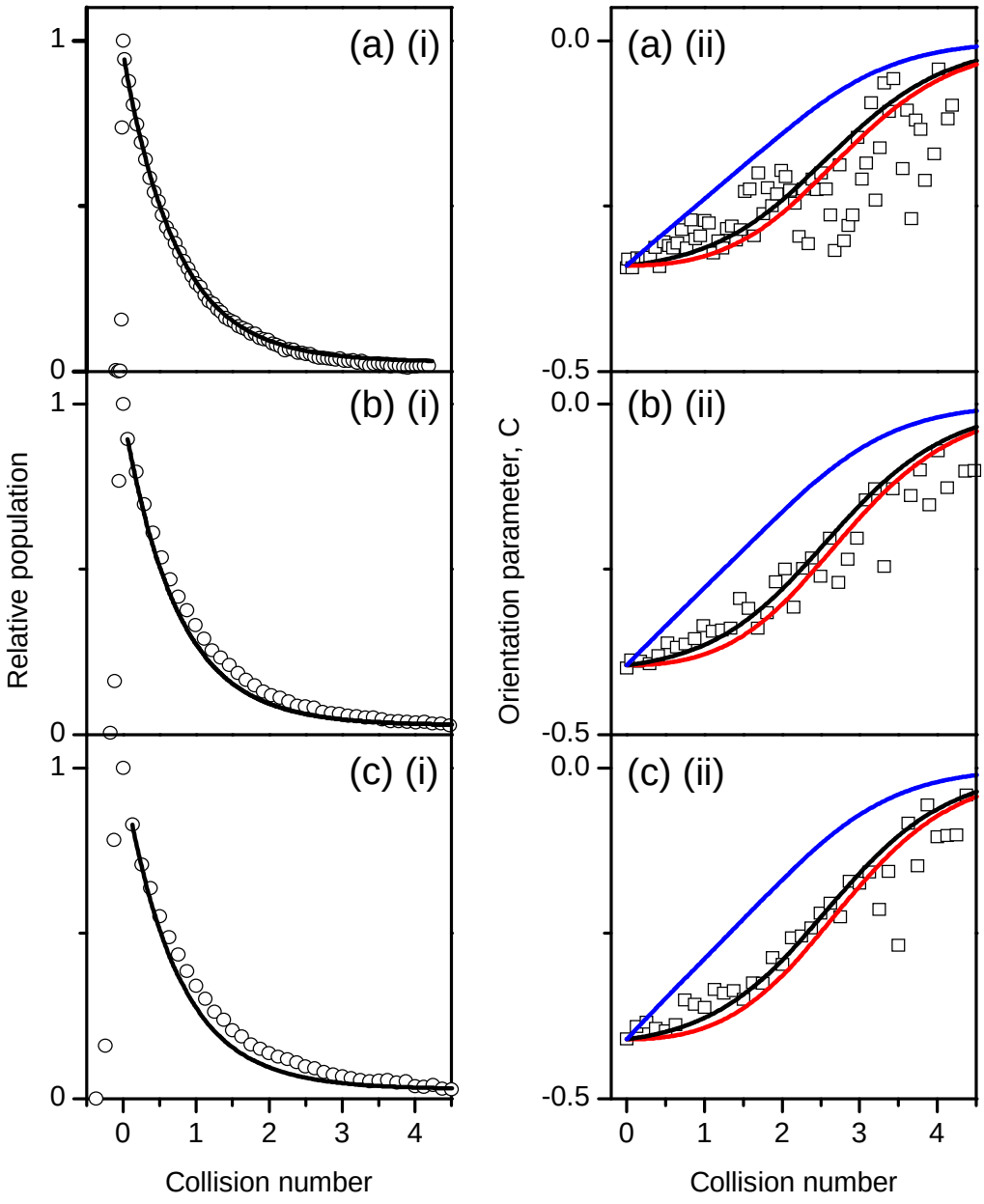

Figure 4.35 – Comparison of the (i) measured population (open circles) and (ii) orientation ratio, C, traces (open squares) for CN($A^2\Pi$, v = 4, j = 6.5 F_1e)+Ar to the master equation simulations (solid lines) for (a) 116 mTorr, (b) 465 mTorr, and (c) 1000 mTorr total pressures, as a function of collision number, calculated assuming k = $k_{pop,j}$ = 3.9 × 10^{-10} cm^3 s^{-1}, as explained in the main text. The black lines are the result of a simulation using the full B-K QS rate constants, the red lines assume no elastic depolarisation, and the blue lines assume all elastic depolarisation rate constants have the value $k_{dep,j}^{(K)}$ = 1 × 10^{-10} cm^3 s^{-1}. In (a) only every 4^{th} data point is shown, in (b) only every 2^{nd} data point and in (c) all data points are shown. Experimental errors are the same as for the relevant traces in Figure 4.13 and Figure 4.14 and have been omitted here for visual clarity.

Figure 4.35 shows that the time-dependence of the population decay is reasonably well described by the kinetic simulation, although in each case the the simulation decays slightly faster than that observed experimentally. As there is no removal process from the $A^2\Pi$ $v = 4$ level in the simulation, the simulated population decays to a thermalised Maxwell-Boltzmann distribution of populations rather than to zero. The measured population experiences slow removal of this thermalised distribution, presumably resulting from a combination of "fly-out" from the probe region, fluorescence and quenching.[110, 304]

Simulations of the orientation were made with the following assumptions of the elastic depolarisation rate constant, $k^{(1)}_{dep,j}$:

1. Using the rate constants obtained from the B-K full QS calculations in Table 4.6.
2. Assuming all $k^{(1)}_{dep,j} = 0$ cm^3 s^{-1}, i.e. no elastic depolarisation.
3. Assuming all $k^{(1)}_{dep,j} = 1 \times 10^{-10}$ cm^3 s^{-1}, approximately the value determined for the $j = 6.5$ F_1e orientation depolarisation rate constant from the single exponential fits in Section 4.5.2.

For all cases in Figure 4.35(ii), the experimental data are not very well fit by the assumption that $k^{(1)}_{dep,j} = 1 \times 10^{-10}$ cm^3 s^{-1}, which yields much faster decays than those observed. The simulated curves are decidedly non-exponential – a straight line at low collision number followed by a curve to zero. This model is clearly inadequate. Conversely, the assumption of no elastic depolarisation ($k^{(1)}_{dep,j} = 0$ cm^3 s^{-1}) predicts a slightly slower orientation decay than is observed experimentally, but does reproduce well the general non-exponential form of the data. The rate constants determined from the QS calculations provide the best description of the measured orientation decay, although overall the observed decay is slightly faster than this full QS simulation at early times.

The polarisation is proportional to the ratio of the $K \neq 0$ to $K = 0$ multipoles, which evolve independently. Figure 4.36 compares the simulated removal of the $K = 0$ and $K = 1$ tensor moments along with the corresponding normalised $(K = 1)/(K = 0)$ orientation moment, $A^{(1)}_0$. The simulated $K = 0$ decay is substantially more non-exponential than that for the $K = 1$ tensor moment. This occurs for two reasons: first, the population

decays to a non-zero Maxwell-Boltzmann value, while the orientation decays to zero at long time, since there can be no orientation at thermal equilibrium. Second, the back-transfer rates are faster for $K = 0$ than $K = 1$, as the polarisation is not perfectly preserved in each collision. That is, the orientation is undergoing *inelastic depolarisation* as a result of the transfer. The observed multimodal decay is therefore a result of the experiment being sensitive to the *normalised polarisation moments* rather than simply the *tensor moments*.

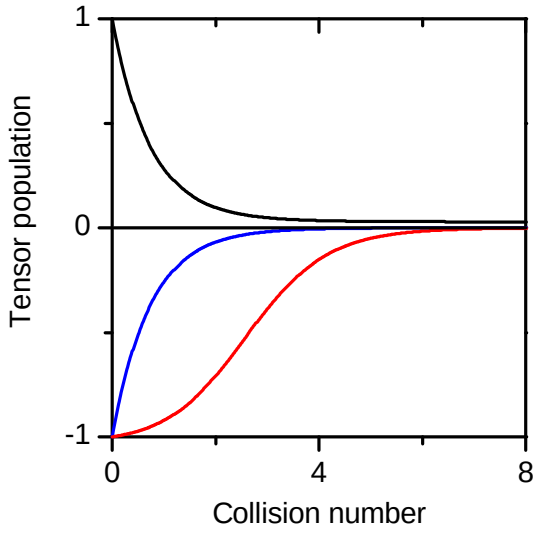

Figure 4.36 – The simulated time traces of the $K = 0$ (black) and $K = 1$ (blue) tensor populations and corresponding normalised $(K = 1)/(K = 0)$ orientation, $A_0^{(1)}$, (red) for CN($A^2\Pi$, $v = 4$, $j = 6.5$ F_1e) colliding with 200 mTorr Ar. The time was converted to collision number using $k = 3.9 \times 10^{-10}$ cm^3 s^{-1}.

4.5.6 Discussion

The FMS technique has been employed to investigate the population removal and depolarisation of rotational orientation and alignment in CN($A^2\Pi$, $v = 4$, j, F_1e)+Ar for j = 2.5, 3.5, 6.5, 11.5, 13.5 and 18.5, respectively. The experimental data is not served well by a single exponential model, which proves insufficient to account for the reversible transfer of population and rotational anisotropy from the prepared state. A three-level kinetic model instead supplies the minimum complexity required to repopulate the initial level.

The total population removal rate constants for the independent orientation and alignment measurements determined from the three-level kinetic model lie within

experimental precision of each other. They are typically 5% – 15% larger than those determined from the single exponential fits, consistent with the neglect of back transfer in the those fits. In Figure 4.34 there appears to be excellent agreement between the three-level population removal rate constants and the QS predictions from the B-W PESs, however the newer B-K predictions consistently exceed the experiment by ~10% – 15%. Comparison of the ME simulations using the B-K QS results in Figure 4.35 confirms that this modest over-prediction is independent of any implicit assumptions in the three-level fitting. Despite these differences, the level of agreement between experiment and theory is much better than compared to other systems, such as NO($X^2\Pi$)+Ar.[136]

The main difference between the B-W and B-K PESs is the considerably deeper attractive well-depth in the latter. As seen in Figure 4.35, the total population removal cross-sections display a negative collision energy dependence, which is consistent with the attractive well playing an important role. Making an unphysical limiting assumption that the transition probability is unity out to some finite value of *R*, and zero thereafter, allows an appreciation of the lower limit on the effective collision radius that contributes to the population removal. Converting the measured three-level $j = 6.5$ F_1e rate constant of $k_{pop,j} = 3.90 \times 10^{-10}$ cm^3 s^{-1} into a thermally averaged cross-section gives a radius of $R = 8.5$ bohr, extending significantly into the attractive region of the PES. When considering a more realistic *R*-dependence to the transition probability, this implies that collisions at even larger values of *R* contribute to the total removal cross-section. This may seem surprising for RET, which is usually more sensitive to the repsulsive core, however such weak long-range interactions have previously been proven to cause efficient pure Λ-doublet transfer in OH($X^2\Pi$)+Ar.[53] The earlier measurements of Alexander *et al.*[15] for low *j* CN($A^2\Pi$, $v = 3$)+Ar produced a mean thermally averaged total removal cross-section of ~55 Å^2. Likewise, previous multi-pass FMS measurements resulted in a superthermal CN($A^2\Pi$, $v = 4$)+Ar total removal cross-section of 53 ± 3 Å^2 and thermal cross-sections ranging from 62 Å^2 for low *j* to ~41 Å^2 for $j = 23.5$.[64, 198, 199] These correspond to a collision radius of around 4 Å, or 7.6 bohr, for lower rotational levels, again supporting the suggestion that attractive forces contribute significantly for CN($A^2\Pi$)+Ar. Predissociation of the CN($A^2\Pi$, $v = 3$)-Ar van der Waals complex strongly supports the deeper attractive well in the B-K PESs.[195, 196] The very good agreement between the QS calculations on the B-W PESs and the results

from the three-level kinetic model may therefore be fortuitous, while the slight over-prediction of the population removal on the B-K PESs reveals that even this highly averaged quantity is extremely sensitive to the form of the PES.

With regards to collisional depolarisation, the primary experimental observation is that the initially prepared orientation and alignment decay non-exponentially, which is inconsistent with the assumption of the single exponential model that elastic depolarisation is the only contributing collisional mechanism. This points to multiple-collisional inelastic depolarisation removing the initial orientation or alignment, as confirmed by comparison of the experimental decays to the ME simulations in Figure 4.35. When the simulations assume rapid elastic depolarisation, akin to the single exponential model, the curves are strikingly different to the observed experimental decays. By contrast, the general shape of the decays is reasonably well reproduced when only inelastic depolarisation is considered, indicating that the majority of the observed depolarisation in these experiments is a result of inelastic depolarisation. This is a consequence of being sensitive to all molecules, polarised and unpolarised, in the prepared rotational state. There is good agreement with both the B-W and B-K QS depolarisation rate constants for the lowest observed levels, j = 2.5 and 3.5 F_1e, while the predictions decine more rapidly than the measurements at higher j. Could this be a result of assuming the average MTE = 0.5 for all fits to the experimental data? Known from the state-to-state RET information in Chapter 5, $\left\langle E^{(1)}(j, j')\right\rangle \approx 0.5$ from the initial level j = 6.5 F_1e to nearby probed j', whereas for transitions starting from j = 10.5 F_2f, on average the orientation is well preserved (MTE → 1). Looking at the orientation time traces in Figure 4.25, the fits with an assumed MTE = 1 are faster than those with MTE = 0.5, and so increasing the average MTE in fits of the higher rotational levels would in fact give a greater difference to the QS rate constants. This shows that the disagreement for the higher j is not an artifact of the kinetic fitting, but is real and must result from slight imperfections in the PESs, specifically in the anisotropy of the attractive region, for which in this system the leading term is the λ = 2 component, as discussed later.

The best agreement between the ME simulations and the experiment is using the B-K QS elastic depolarisation rate constants, a clear indication that the calculations well-represent collisional depolarisation in the system, both elastic and inelastic. There are discrepensies between the data and simulations at low collision number (early times), where elastic depolarisation may be expected to be the dominant process. Here, the

experimental polarisation decay is consistently slightly faster than the simulation. This is in accord with comparison of the elastic depolarisation rate constants in Figure 4.34, albeit with some scatter in the measured values, refering back to the ability of the QS calculations to estimate the elastic depolarisation at higher *j* and reflecting the difficulty in both measuring and extracting from the multi-level fit the rate constant for such a slow process in the presence of much faster population removal. Despite these minor differences, there is overall good agreeement between experiment and theory, importantly confirming that, contrary to previous work,[199] elastic depolarisation is a relatively minor channel in CN($A^2\Pi$)+Ar collisions.

The elastic depolarisation rate constants are very similar for the B-W and B-K PESs. The two potentials may be compared by inspection of the V_{sum} and V_{dif} contour plots and angular expansion coefficients in Figure 4.28 – Figure 4.31. The anisotropy and range of the V_{sum} repulsive wall are reasonably similar for the two potentials. The largest difference, as previously noted, is in the attractive region of the V_{sum} PESs, with the B-K potential exhibiting a substantially deeper attractive well. The most noticable difference between the angular expansion ceofficients is in the isotropic V_{00} term, with a shallower attractive well in the B-W potential. This purely isotropic component of the PES alone is insufficient to induce a torque necessary for RET or elastic depolarisation, however it does influence which parts of the PES are sampled at a particular collision energy, and so may affect more subtly the overall scattering amplitudes and product branching.

The mild elastic depolarisation observed here resembles the kinematically and electronically similar NO($X^2\Pi$)+Ar system,[136] but is noticeably dissimilar to the more rapid depolarisation seen in OH($X^2\Pi$)+Ar,[53, 130] and is very much slower than the strongly attractive OH($A^2\Sigma^+$)+Ar system.[48, 274] As stated in Section 4.5.2, light rotors, such as OH, have large rotational energy spacings that hinder RET, yet the H-atom can be easily reoriented on approach of the collider, as examplified in QCT calculations of OH($A^2\Sigma^+$)+Ar.[274] In contrast, relatively heavy rotors, such as NO and CN, are classically harder to reorient, but have smaller rotational energy spacings, favouring RET over elastic depolarisation.

Both CN($A^2\Pi$) and NO($X^2\Pi$) are near-homonuclear and approach the Hund's case-(a) limit, implying that the majority of elastic depolarisation at thermal energies should arise from the even-λ components of the V_{sum} potential, with only minor contributions

from the odd-λ terms. This was successfully proven by Dagdigian and Alexander, who switched-off the V_{dif} potential in QS calculations of the NO($X^2\Pi$)-Ar system, confirming the near-negligible role of the V_{dif} in that particular case.[303] From inspection of Figure 4.31, the dominant term capable of causing elastic depolarisation in the thermal collision energy range for the CN($X^2\Pi$)+Ar system is V_{20} (where $\lambda = 2$), which is only weakly attractive at longer range. The computed elastic depolarisation cross-sections in Figure 4.32 display a negative collision energy dependence, with a rapid decline until ~300 cm^{-1} and are insignificant thereafter. This is consistent with elastic depolarisation mediated by weak attractive forces that are less able to cause substantial tilting of the CN rotor.[12]

The degree of Hund's cases (a)-(b) uncoupling for the $\lambda = 2$ component is shown in Figure 4.37 for OH($X^2\Pi$), CN($A^2\Pi$) and NO($X^2\Pi$).[12] This gives an indication of the contributions from the V_{sum} and V_{dif} potentials as these systems depart the Hund's case-(a) limit as a function of rotational energy. Dagdigian and Alexander demonstrated that V_{dif} to makes a large contribution to OH($X^2\Pi$)+Ar at low-to-mid *j*, but little or no contribution to NO($X^2\Pi$)+Ar.[199, 303] This is expected when looking at Figure 4.37. Accordingly in Figure 4.37, it is apparent for this range of *j* that although CN($A^2\Pi$) is strongly Hund's case-(a), the role of the V_{dif} potential must still be considered. Inspection of Figure 4.30 reveals the V_{dif} to have appreciable magnitude in the range of the V_{sum} attractive minimum. It is therefore speculated that the attractive well of the V_{sum} PES plays the most significance in RET and elastic depolarisation of CN($A^2\Pi$)+Ar, with minor but important contributions from the V_{dif} PES. As such, most RET collisions out of the prepared level are spin-orbit conserving, accompanied by a small fraction of spin-orbit changing collisions. The observed behaviour in CN($A^2\Pi$)+Ar can therefore be explained in terms of a simple balance between kinematic and potential effects.

In order to further investigate the findings from this section and provide a more rigorous test of the underlying scattering theory, measurements and accompanying QS calculations on the B-K PESs are presented in the next chapter for state-to-state RET and polarisation transfer in CN($A^2\Pi$, $v = 4$)+Ar. The study of population removal and depolarisation in CN($A^2\Pi$) is extended in the next part of the current chapter for collisions with molecular partners, namely N_2, O_2, and CO_2.

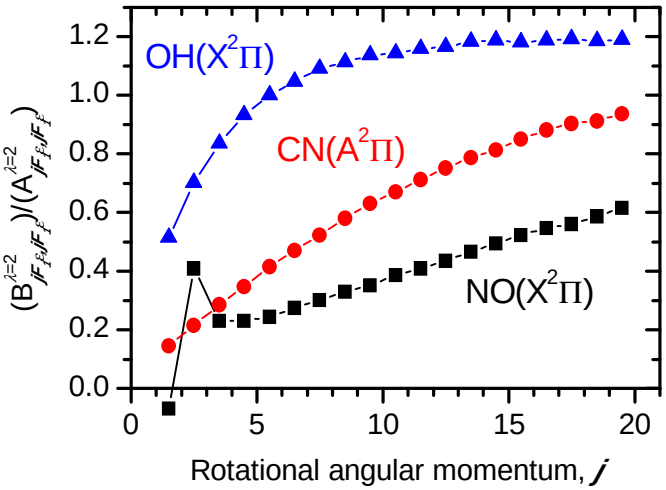

Figure 4.37 – The ratio of coefficients quantifying the contributions from the $\lambda = 2$ components of the V_{sum} and V_{dif} PESs to the potential matrix of elements due to the degree of Hund's cases (a)-(b) uncoupling in OH($X^2\Pi$) (blue), CN($A^2\Pi$) (red) and NO($X^2\Pi$) (black), according to Section 1.6.1. Adapted from reference 12.

4.5.7 Summary

The key conclusions from this section are listed below.

i. The FMS cw-probe technique has been employed in a pulsed pump OODR set-up to investigate the total removal and depolarisation of rotational angular momentum in CN($A^2\Pi$, v = 4, j, F_1e)+Ar for j = 2.5, 3.5, 6.5, 11.5 and 13.5, and 18.5, respectively.

ii. Collisional depolarisation of orientation and alignment appears to be a significant process on the timescale of fast population removal.

iii. The prepared population decays in a near-exponential fashion, whilst the loss of polarisation is clearly non-exponential, exhibiting a multimodal character. This is suggested to be an effect of multiple collisions returning depolarised rotational angular momentum to the initial level, termed *inelastic depolarisation*.

iv. A single exponential kinetic model, which does not account for repopulation of the initial level, fails to fully reproduce the experimental observations. Fits to this model produce rapid population removal and elastic depolarisation rate constants, with k_{pop} and $k_{dep}^{(K)}$ both in the order of 10^{-10}

cm^3 s^{-1}, consistent with previous findings of Ballingall *et al.*,[199] but surprising when compared to similar systems, such as NO($X^2\Pi$)+Ar.[136]

v. A three-level kinetic model produces much better fits, representing the data well. This model includes reversible loss of population and inelastic depolarisation, with an average MTE of $\left\langle E^{(1)}(j, j')\right\rangle$ = 0.5. The determined k_{pop} are 5% – 15% larger than from the single exponential model, both exhibiting a monotonic decrease with increasing j. The $k_{dep}^{(K)}$ lie in the range (0 – 5) × 10^{-11} cm^3 s^{-1}, with no obvious correlation in K or j.

vi. The larger population removal and smaller elastic depolarisation rate constants from the three-level kinetic model are consistent with neglect of back-transfer in the previous model.

vii. The three-level experimental results are compared to complementary full QS calculations on the previous B-W and new B-K CN($A^2\Pi$)-Ar *ab initio* PESs. The main difference between the two sets of PESs is the substantially deeper well-depth in the latter.

viii. The QS B-K k_{pop} values are typically 11% – 17% larger than the B-W predictions. There is fortuitous agreement between the measured and B-W k_{pop} values, whereas the B-K PESs systematically over-predict by 10% – 15%.

ix. The $k_{dep}^{(K)}$ are similar for the two PESs, seeing reasonable agreement to experiment at low j, but declining more rapidly at higher j. This suggests slight imperfections in the PESs, specifically with the anisotropic λ = 2 component.

x. Despite minor differences, there is generally good agreement between experiment and theory, confirming elastic depolarisation to be a relatively minor channel mediated by weak long-range attractive forces.

xi. The experimental data were scaled against complete ME kinetic simulations of the population and polarisation removal out of j = 6.5 F_1e using the B-K QS rate constants and also assuming $k_{dep}^{(K)}$ = 1 × 10^{-10} cm^3 s^{-1} (akin to the single exponential model) and no elastic depolarisation. The fast simulations do not reproduce the data well, while those using the QS predictions have the best agreement, reaffirming the calculations to be a good representation of the data and the prominence of inelastic depolarisation.

xii. Overall, the observed behaviour in CN($A^2\Pi$)+Ar is proposed to stem from a simple balance between kinematic and potential effects. The results highlight the importance of multiple collisions when sensitive to both polarised and unpolarised molecules.

4.6 CN($A^2\Pi$)+N_2, O_2 and CO_2 Population Removal and Depolarisation

This section provides new measurements of the total population removal and elastic depolarisation of rotational angular momentum for a range of CN($A^2\Pi$, v = 4, j, F_1e) rotational levels with kinematically similar molecular collision partners N_2, O_2 and CO_2. These bring with them additional degrees of freedom, low-order electrostatic forces and product branching channels. There is also further complication to the construction of full-dimensional interaction potentials and to the treatment of QS calculations. As discussed in Section 1.8.2, CN($X^2\Sigma^+$) readily reacts with O_2 at thermal energies, however only reacts with CO_2 above ~1000 K and is unreactive with N_2.[210-215] There may therefore be a possibility for exothermic reactive pathways in collisions with CN($A^2\Pi$). Previous electronic quenching measurements of CN($A^2\Pi$, v), summarised in Table 1.4, show that Ar and N_2 are relatively inefficient at quenching CN($A^2\Pi$, v = 4), with rate constants of (2.63 ± 0.2) × 10^{-11} cm^3 s^{-1} and (3.83 ± 0.3) × 10^{-11} cm^3 s^{-1}, respectively. Conversely, CO_2 quenches around four times faster, with k_Q = (13.1 ± 1.0) × 10^{-11} cm^3 s^{-1}, which has been proposed to result from the near-resonance of the CO_2 v_3 anti-symmetric stretch with the CN($A^2\Pi$, v = 4)–CN($X^2\Sigma^+$, v = 7) energy gap.

The experimental approach in this part is analogous to that of the previous sections for the Ar collision partner, with the FMS technique employed in a thermal bath set-up. The same rotational levels (j = 2.5, 3.5, 6.5, 11.5, 13.5 and 18.5 F_1e) are also studied to allow direct comparison between each system. The pump and probe lasers were circularly polarised and switched between the co-rotating and counter-rotating geometries to allow acquisition of the population and orientation time-traces. The rotational alignment was not interrogated for the molecular colliders. Subsequent three-level kinetic fits to the processed data, as per Section 4.5.3, determined the population removal and elastic depolarisation rates and thermally averaged collision cross-sections. The results are discussed with respect to competing RET and quenching channels for

each collider, the form of the interaction potentials and the possible role of long-range intermolecular interactions. Spherically-averaged *ab initio* CN($A^2\Pi$, v = 3)-N_2 PESs have previously been calculated by Dagdigian and co-workers, as outlined in Chapter 5. QS RET predictions from these surfaces were consistent with the CN($A^2\Pi$)+Ar system, however the rate constants compared unfavourably with fully state-resolved RET measurements.[206] Comparisons with between these two sets of work will be made in this section.

4.6.1 Results

Figure 4.38 displays typical co-rotating and counter-rotating FM SE Doppler profiles immediately (10 ns) after the pump pulse together with their fits, for j = 2.5, 6.5 and 11.5 F_1e at pressures of ~100 mTorr for the N_2, O_2 and CO_2 collsion partners. As with Ar, the simulated curves fit very well to the FM lineshapes, and a strong dependence of the signal size on the experimental geometries is also apparent. The difference between the alternate-polarisation lineshapes shows that a rotational orientation has been created and probed in the prepared level. The initial orientation is independent of collider, with variation only in rotational level and statistical deviations of exact pump laser fluence and polarisation between the different sets of experiments.

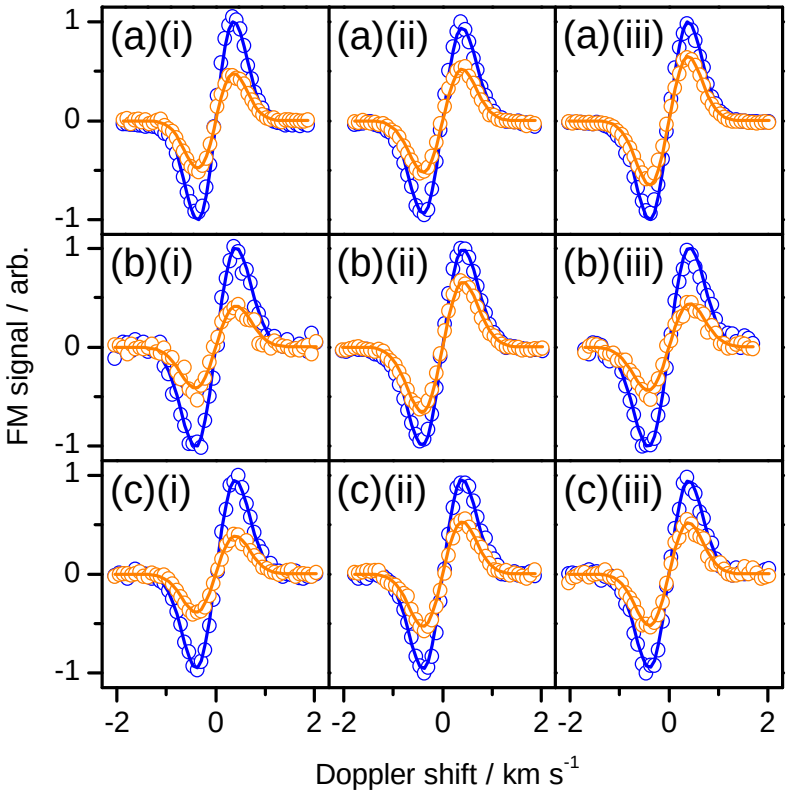

Figure 4.38 – Co-rotating (orange) and counter-rotating (blue) FM SE Doppler profiles and fits (solid lines) for the first 10 ns after the pump laser pulse for (i) j = 2.5 F_1e, j = 6.5 F_1e and j = 11.5 F_1e at total pressures of ~100 mTorr for (a) N_2, (b) O_2 and (c) CO_2 collision partners.

Figure 4.39 shows the time-traces of the co-rotating and counter-rotating integral intensities (I_{co} and I_{con}) in 10 ns-averaged steps before, during and after the pump laser firing, for each collider resulting from the sequential Doppler profile analysis for j = 6.5 F_1e at total pressures of ~100 mTorr, ~500 mTorr and ~1000 mTorr. The difference between the two geometries is evident at t = 0, showing in all cases that a rotational orientation has been generated. The traces then decay with time as population is collisionally removed from the initial level, but converge before complete removal, indicating that collisional depolarisation occurs on a timescale competitive with the loss of population. Comparison of the observed decays shows a marked dependence on both the pressure and identity of the collision partner. As expected, the population decay is proportional to the collider pressure. The most efficient species at removing the prepared population appears to be CO_2, followed by N_2 and lastly O_2. No discernable differences between the depolarisation kinetics for different colliders are apparent from the signal decays.

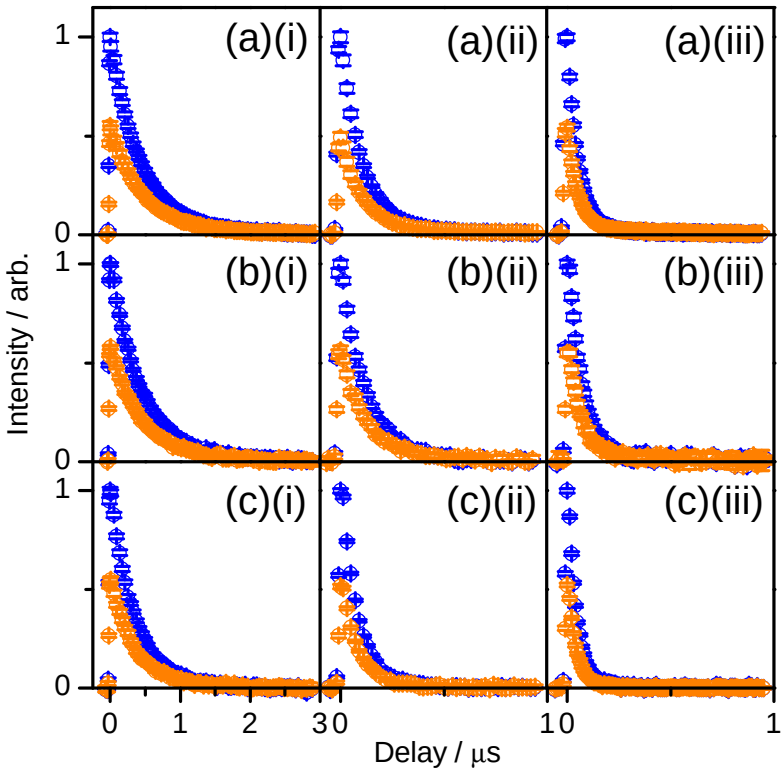

Figure 4.39 – Co-rotating and counter-rotating integral signal traces for j = 6.5 F_1e at (i) ~100 mTorr (every 4th data point shown), (ii) ~500 mTorr (every 2nd data point shown) and (ii) ~1000 mTorr total pressures for (a) N_2, (b) O_2 and (c) CO_2 collision partners. Errors are 2σ statistical uncertainties.

The time-dependence of the population and orientation parameters, $A_0^{(0)}$ and $A_0^{(1)}$, for each collision pair, determined from the processing of the experimental data, are shown in Figure 4.40 and Figure 4.41, along with the LM minimisation fits from the three-level kinetic model for j = 2.5, 6.5 and 11.5 F_1e, at ~100 mTorr, ~500 mTorr and ~1000 mTorr total pressures. An average orientation MTE of $\left\langle E^{(1)}(j,j')\right\rangle = 0.5$ was used in the fits, which was previously optimised in Section 4.5.3. As with CN($A^2\Pi$)+Ar, the populations decay in a near-exponential fashion for each collider, with a visible pressure and collider dependence. At long delay times there is a non-zero baseline for the N_2 partner, indicative of rotational re-equilibration across the Boltzmann distribution. This baseline eventually decays to zero, presumably due to processes such as radiative loss and fly-out. The signals for O_2 and CO_2 reach zero sooner than for N_2, suggesting other loss channels, such as electronic quenching or reaction, could be contributing to the population removal. This is more apparent at longer times and higher pressures. The orientation decays akin to that for CN($A^2\Pi$)+Ar, much slower than the population

removal and in a multimodal fashion towards zero, where no orientation can persist at thermal equilibrium. The decays clearly still depend on collider pressure, however there appears to be little or no variation between the colliders. The fits represent the data well and yield only statistical residual errors. The non-single exponential behaviour of both the population removal and depolarisation suggests the prevalence of inelastic depolarisation for the molecular collision partners and supports the use of the three-level kinetic model.

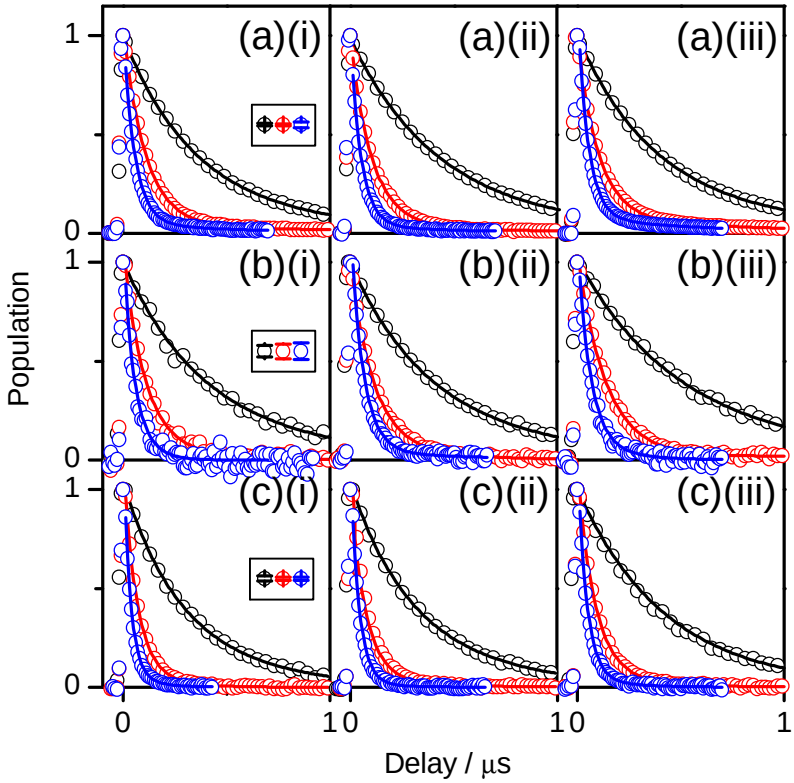

Figure 4.40 – The time-dependence of the population, $A_0^{(0)}$, derived from I_{co} and I_{con} for (i) j = 2.5 F_1e (ii) j = 6.5 F_1e and (iii) j = 11.5 F_1e at ~100 mTorr (black, every 4th data point shown), ~500 mTorr (red, every 2nd data point shown) and ~1000 mTorr (blue) total pressures for (a) N_2, (b) O_2 and (c) CO_2 collision partners. Solid lines are LM fits of the three-level kinetic model to the population traces. The x-axes have been truncated to 1 μs for clarity of presentation. Representative average 2σ error bars are displayed within the inset of (i). Error bars for individual data points have been omitted for visual clarity.

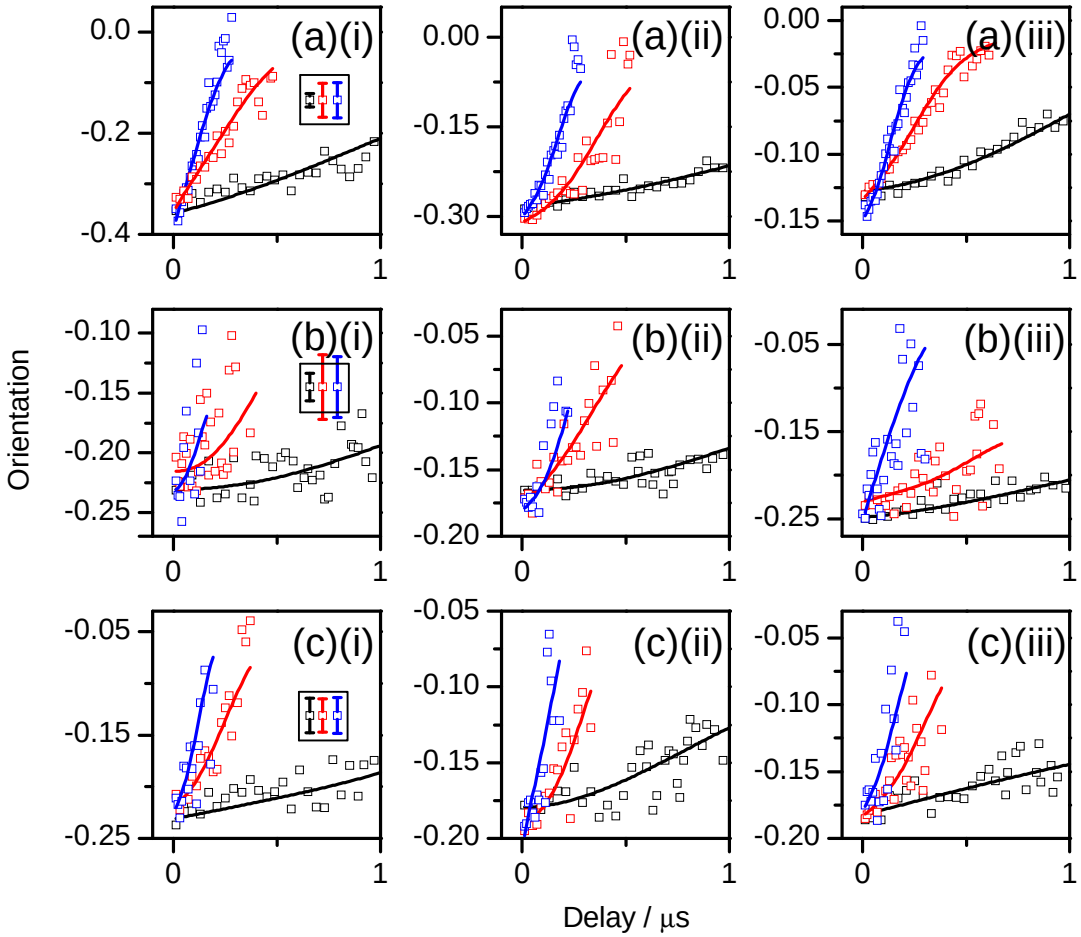

Figure 4.41 – The time-dependence of the orientation parameter, $A_0^{(1)}$, derived from I_{co} and I_{con} for (i) j = 2.5 F_1e (ii) j = 6.5 F_1e and (iii) j = 11.5 F_1e at ~100 mTorr (black, every 4th data point shown), ~500 mTorr (red, every 2nd data point shown) and ~1000 mTorr (blue) total pressures for (a) N_2, (b) O_2 and (c) CO_2 collision partners. Solid lines are LM fits of the three-level kinetic model to the orientation traces. The x-axes have been truncated to 1 μs for clarity of presentation. Representative average 2σ error bars are displayed within the inset of (i). Error bars for individual data points have been omitted for visual clarity.

Figure 4.42 presents plots of the individual total population removal and depolarisation rates $\Gamma_{pop,j}$ and $\Gamma_{dep,j}^{(1)}$ determined from the three-level LM kinetic fits as a function of respective N_2, O_2 or CO_2 collider number density for j = 2.5 F_1e, j = 6.5 F_1e and j = 11.5 F_1e. Weighted least-squares linear fits to the data points according to Equation 4.18 and Equation 4.19 yield the bimolecular population removal and depolarisation rate constants $k_{pop,j}$ and $k_{dep,j}^{(1)}$. The figure clearly shows that the population removal rate constants are well-determined, lying in the order $CO_2 > N_2 > O_2$. This indicates that CO_2 is the most efficient partner at removing the prepared population, be it *via* RET,

electronic quenching or other routes, followed by N_2 and lastly O_2. This trend remains for each rotational level probed, with some variation in the difference between N_2 and O_2, however CO_2 is always noticeably faster. As with Ar, the population gradients decrease with increasing *j*, although more pronounced for CO_2 than N_2 or O_2, showing that population is removed faster for lower *j*. In all cases, the intercept rates resulting from collisions with the ICN precursor and non-collisional processes, such as radiative loss and fly-out, are small, typically 5×10^5 s^{-1}, consistent with the CN($A^2\Pi$, $v = 4$) radiative loss rate (2.6×10^5 s^{-1})[110] and a modest contribution from fly-out. The depolarisation in Figure 4.42 appears to be very weak and insignificant in the presence of much faster population removal, exactly as observed for Ar. The individual depolarisation rates that comprise the plot are scattered, with no apparent dependence on *j* or collider. The rate constants determined from the linear fits were converted to thermally-averaged collision cross-sections according to Equation 1.32 – Equation 1.34 in Chapter 1, to allow for collider comparisons independent of collision frequency. The average relative velocity of each collision pair is listed in Table 1.1. The thermally-averaged population removal and elastic depolarisation cross-sections are summarised in Table 4.7 and displayed in Figure 4.43. The depolarisation cross-sections are represented as bar charts in Figure 4.44 to provide a clearer view of any *j*- or collider-dependence.

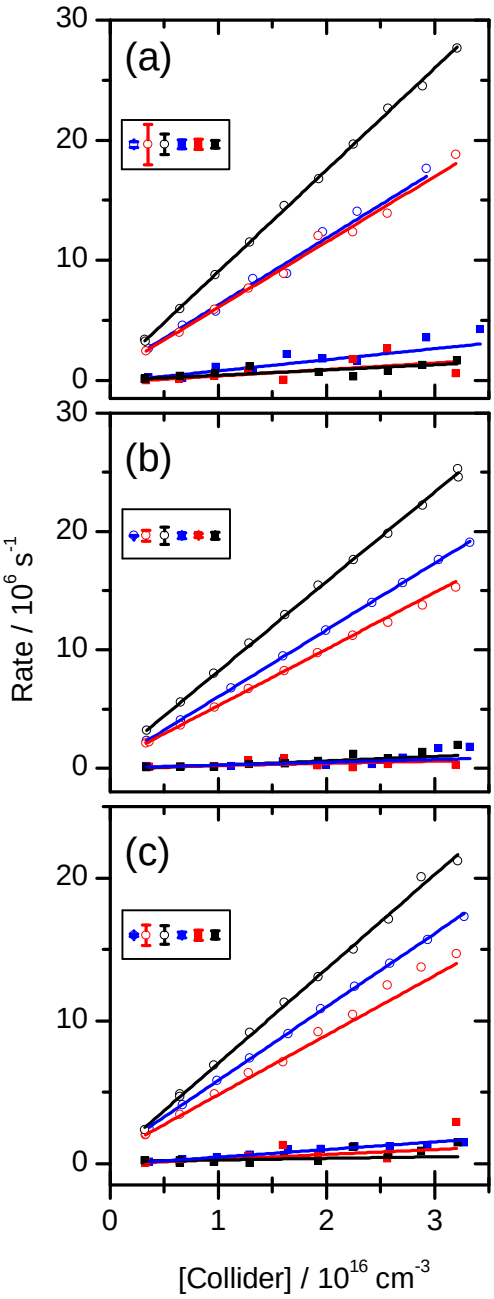

Figure 4.42 – Plots of the population removal rates, $\Gamma_{pop,j}$, (open circles) and orientation depolarisation rates, $\Gamma^{(1)}_{dep}$, (filled squares) determined from the three-level kinetic model for N_2 (blue), O_2 (red) and CO_2 (black) collision partners, where (a) j = 2.5 F_1e,(b) j = 6.5 F_1e and (c) j = 11.5 F_1e. The straight lines are linear least-squares weighted fits to the data points to determine the population removal and depolarisation bimolecular rate constants k_{pop,j_i} and $k^{(1)}_{dep,j_i}$. Representative average 2σ error bars are displayed within the inset of each panel. Error bars for individual data points have been omitted for visual clarity.

Table 4.7 – Thermally averaged CN($A^2\Pi$, v = 4, j, F_1e) total population removal, σ_{pop}, and orientation depolarisation, $\sigma_{dep}^{(1)}$, cross-sections with 2σ statistical uncertainties derived from three-level LM kinetic fits to the experimental data for each collision partner studied. The Ar results from Section 4.5.3 are also included.

Collider	j	σ_{pop} / Å^2	$\sigma_{dep}^{(1)}$ / Å^2
Ar	2.5	66.8 ± 1.9	9.4 ± 2.1
	3.5	68.7 ± 1.4	8.5 ± 1.1
	6.5	61.7 ± 1.6	8.9 ± 1.9
	11.5	57.5 ± 1.4	7.1 ± 0.9
	13.5	56.1 ± 1.2	7.4 ± 1.4
	18.5	55.6 ± 3.2	2.3 ± 4.5
N_2	2.5	81.2 ± 8.6	13.5 ± 6.3
	3.5	84.1 ± 0.7	6.3 ± 2.4
	6.5	82.3 ± 0.6	3.5 ± 2.4
	11.5	75.1 ± 1.1	7.8 ± 0.7
	13.5	76.1 ± 0.7	5.5 ± 1.4
	18.5	70.5 ± 0.7	3.1 ± 5.3
O_2	2.5	82.1 ± 3.9	8.2 ± 5.2
	3.5	79.8 ± 2.5	4.3 ± 1.8
	6.5	71.9 ± 1.1	1.0 ± 0.6
	11.5	62.9 ± 2.7	3.7 ± 2.9
	13.5	67.9 ± 2.1	3.8 ± 0.9
	18.5	63.1 ± 1.0	2.6 ± 1.7
CO_2	2.5	139.1 ± 2.1	6.4 ± 1.5
	3.5	131.6 ± 1.5	11.0 ± 4.1
	6.5	121.6 ± 1.4	6.0 ± 2.0
	11.5	106.3 ± 3.0	1.8 ± 3.2
	13.5	107.2 ± 3.8	4.5 ± 2.4
	18.5	95.5 ± 3.3	4.3 ± 5.9

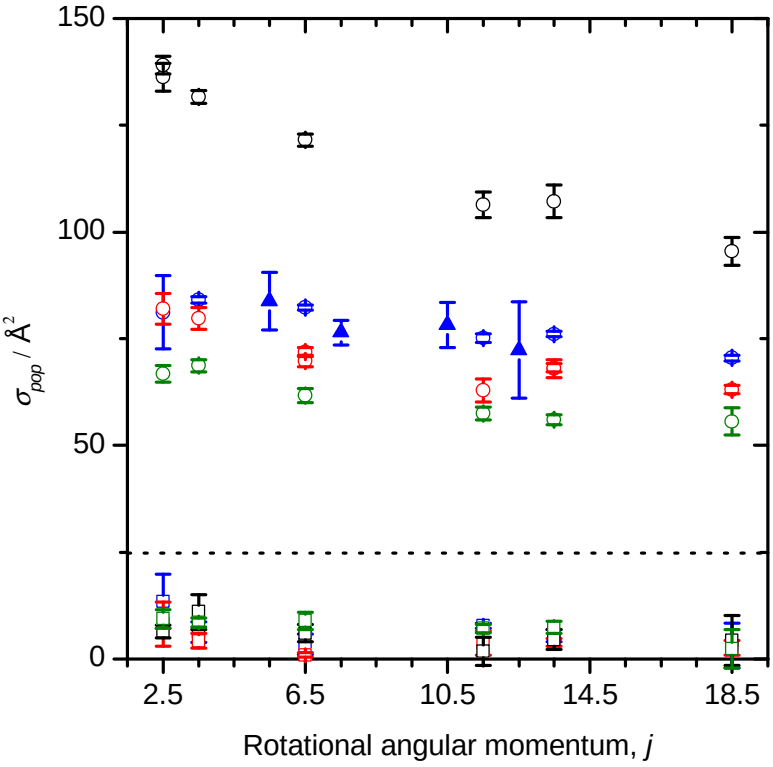

Figure 4.43 – Total population removal (open circles) and orientation depolarisation (open squares) thermally averaged cross-sections, σ_{pop} and $\sigma^{(1)}_{dep}$ (above and below the dotted line, respectively), for different CN($A^2\Pi$, v = 4, j, F_1e) levels determined from the three-level kinetic fits for N_2 (blue), O_2 (red) and CO_2 (black) collision partners. The cross-sections are compared to the previous Ar measurements from Section 4.5.3 (olive points) and σ_{pop} for CN($A^2\Pi$, v = 3, j, F_1f)+N_2 from reference 206 (filled triangles). Error bars are 2σ statistical uncertainties.

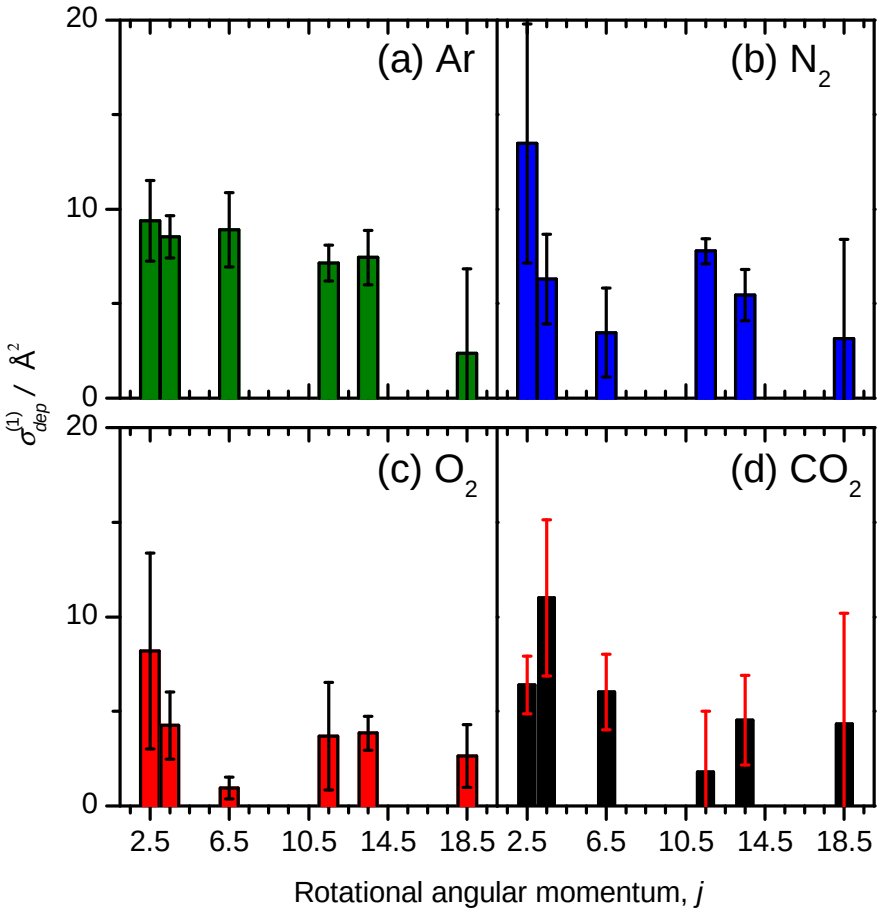

Figure 4.44 – Bar charts of the CN($A^2\Pi$, v = 4, j, F_1e)+Ar, N_2, O_2 and CO_2 orientation elastic depolarisation cross-sections, $\sigma_{dep}^{(1)}$ derived from straight line fits to $\Gamma_{dep}^{(1)}$, as per Figure 4.42. Error bars are 2σ statistical uncertainties from the fits. The results for the Ar collision partner are from Section 4.5.3.

The total population removal cross-sections in Figure 4.43, including the previous data for Ar from Section 4.5.3 and the CN($A^2\Pi$, v = 3, j, F_1f)+N_2 removal cross-sections of Dagdigian and co-workers from reference 206, are found to lie in the order CO_2 > N_2 > O_2 > Ar, irrespective of j. There is quantitative agreement with the previously reported N_2 cross-sections.[206] For all colliders, the expected general decline of σ_{pop} with increasing j is evident, in accord with the increasing energy gaps between successive rotational levels. This trend is somewhat stronger for CO_2. In all instances, the population removal is much faster than the accompanying elastic depolarisation shown in Figure 4.43 and Figure 4.44, which is again very weak, with cross-sections scattered between ~1 – 13 $Å^2$, almost all within 2σ of each other and no obvious or strong correlation in either j or collider. However, some relationships can still be ascertained: depolarisation for Ar is consistent across all levels until j = 18.5 F_1e, N_2 is faster at

depolarising than O_2, and the cross-sections for CO_2 generally lie somewhere between N_2 and O_2. Within margins of error, Ar appears to be the more efficient collider at elastic depolarisation, followed by N_2, CO_2, and finally O_2. The depolarisation uncertainties are generally larger than for the population removal cross-sections, reflecting both the uncertainty of measuring such a slow process in the presence of much faster population removal, and the additional possibility of inelastic depolarisation.

The total removal cross-sections are the sum of all population extinction channels out of the initial level, and alone do not distinguish between reversible or irreversible loss, such as RET or electronic quenching. Because the kinetic traces for the different colliders in Figure 4.39 and Figure 4.40 show different long-time behaviours, and due to the available literature inferring different collider quenching rates, bimolecular fits were also performed to the individual removal rates $\Gamma^{(0)}_{j\to j'}$ and $\Gamma^{(0)}_{j\to x}$ that make up $\Gamma_{pop,j}$, to determine the corresponding thermal rate constants and cross-sections. Figure 4.45 presents these bimolecular plots for the initial states j = 2.5 F_1e, j = 6.5 F_1e and j = 11.5 F_1e for the three molecular colliders and the Ar data from Section 4.5.3. Shown in Figure 4.45, the total population removal rates resulting from collisions with Ar and N_2 are dominated by reversible transfer, $\Gamma^{(0)}_{j\to j'}$. This consists of RET to nearby rotational levels that are close in energy and angular momentum to the initial level. Conversely, O_2 and CO_2 see a substantial contribution from irreversible transfer, $\Gamma^{(0)}_{j\to x}$, to $\Gamma_{pop,j}$, which includes transfer to rotational levels far away in energy and angular momentum, as well as all other irreversible loss channels, such as EET to the CN($X^2\Sigma^+$) ground state, VET or reaction of CN($A^2\Pi$) with the collision partner. It must be stressed that $\Gamma^{(0)}_{j\to j'}$ and $\Gamma^{(0)}_{j\to x}$ were not determined here from measurements of the product states, but instead assumed and optimised from the three-level LM kinetic fits to the total population removal measurements of the initial states.

Figure 4.46 shows the breakdown of σ_{pop} into contributions from the best-fit removal components $\sigma^{(0)}_{j\to j'}$ and $\sigma^{(0)}_{j\to x}$, determined according to Figure 4.45, for each rotational level studied, and each collider, including the results for Ar derived from Section 4.5.3. The return cross-sections $\sigma^{(0)}_{j'\to j}$ for population transfer back into the initial levels (not shown) were determined to be small, scattered between 1 – 5 Å^2 in essentially all cases. Consistent with the observed differences in the long-time kinetic traces for the different

colliders in Figure 4.39 and Figure 4.40 and the second-order plots of the individual $\Gamma^{(0)}_{j\to j'}$ and $\Gamma^{(0)}_{j\to x}$ rates in Figure 4.44, the total population removal cross-sections for Ar and N_2 in Figure 4.46 are completely dominated by reversible RET, $\sigma^{(0)}_{j\to j'}$, whereas O_2 and CO_2 have a substantial contribution from irreversible loss, $\sigma^{(0)}_{j\to x}$. The total bar heights, $\sigma^{(0)}_{j\to j'}+\sigma^{(0)}_{j\to x}$, for Ar and N_2 in Figure 4.46 agree quantitatively with the measured σ_{pop} in Figure 4.43, however those for O_2 and CO_2 are in much poorer agreement. When the individual removal rates $\Gamma^{(0)}_{j\to j'}$ and $\Gamma^{(0)}_{j\to x}$ are both of significant magnitude, the uncertainties in each are found to be large and quite strongly correlated, as visible in Figure 4.45 (c) and (d) for O_2 and CO_2, which lead to the substantial error bars in Figure 4.46 (c) and (d). In contrast, the total population removal rates $\Gamma_{pop,j}$ are typically well-determined, reflected in the fits to the data points in Figure 4.40 and the bimolecular rate plots in Figure 4.42 and Figure 4.45, leading to the generally small statistical uncertainties in Figure 4.43.

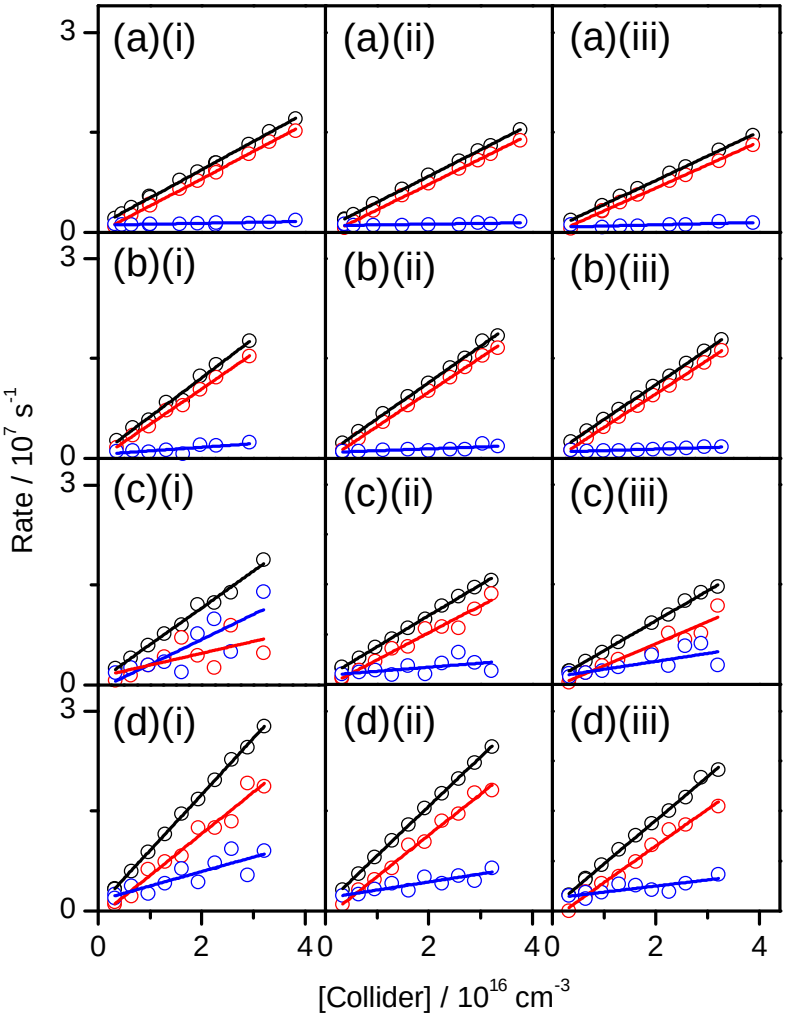

Figure 4.45 – Population removal rates (open circles) as a function of collider number density with linear fits (solid lines). The total removal rate $\Gamma_{pop,j}$ *(black) is broken down into the constituent reversible removal* $\Gamma^{(0)}_{j\to j'}$ *(red) and irreversible removal* $\Gamma^{(0)}_{j\to x}$ *(blue) rates for (a) Ar (from Section 4.5.3), (b)* N_2*, (c)* O_2 *and (d)* CO_2 *collision partners for (i) j = 2.5* F_1e*, (ii) j = 6.5* F_1e *and (iii) j = 11.5* F_1e*. Error bars for the black data points are the same as for the relevant* $\Gamma_{pop,j}$ *uncertainties in Figure 4.42. Error bars for individual data points have been omitted for visual clarity.*

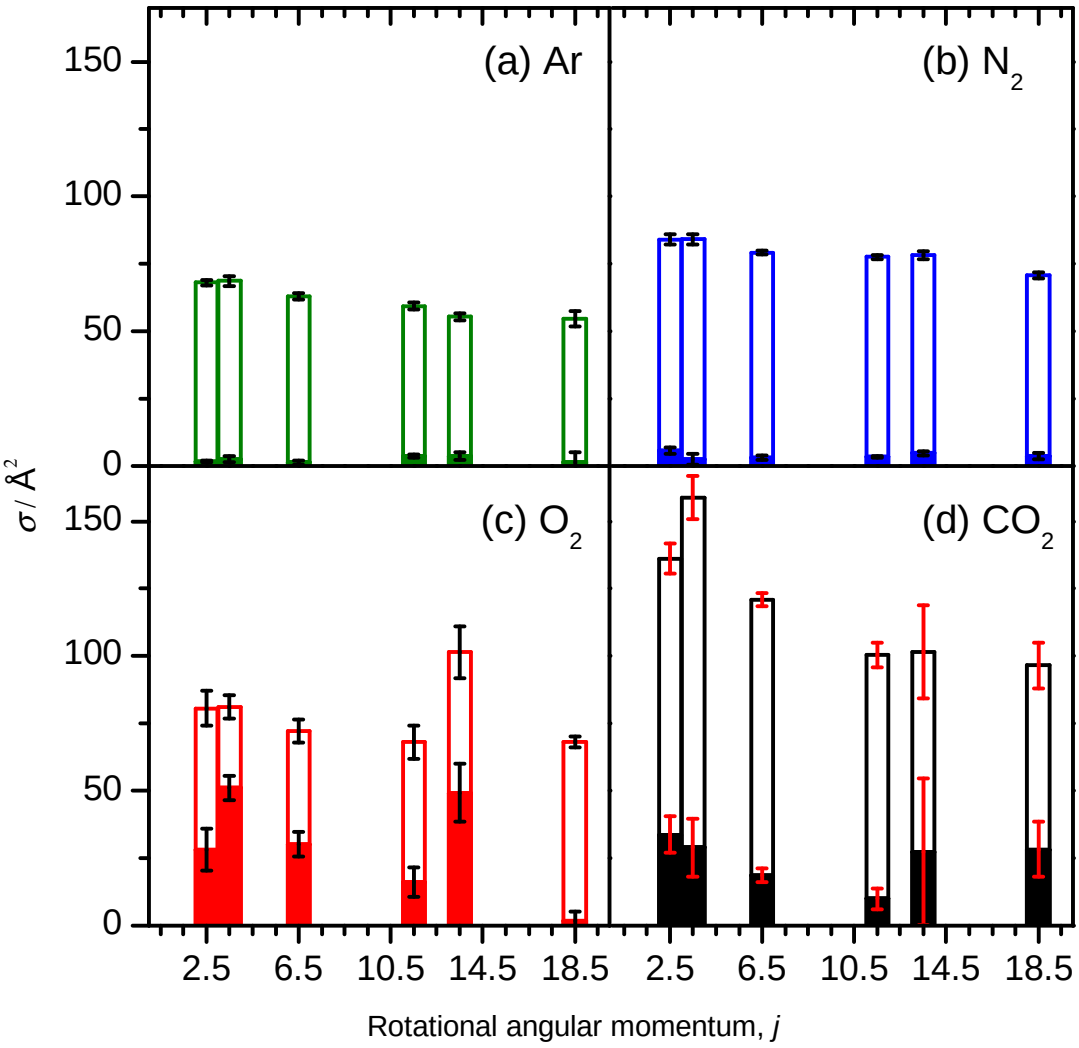

Figure 4.46 – Stacked bar charts of the CN($A^2\Pi$, v = 4, j, F_1e)+Ar, N_2, O_2 and CO_2 total population removal cross-sections, σ_{pop}, as a sum of the reversible removal cross-section $\sigma^{(0)}_{j\to j'}$ (open bars) and irreversible removal cross-section $\sigma^{(0)}_{j\to x}$ (filled bars) derived from the straight line fits of $\Gamma^{(0)}_{j,\mathrm{tot}}$, $\Gamma^{(0)}_{j\to j'}$ and $\Gamma^{(0)}_{j\to x}$, as per Figure 4.45. Error bars are 1σ statistical uncertainties from the independent fits. The results for the Ar collision partner are from Section 4.5.3.

4.6.2 Discussion

Population Removal

As shown in Figure 4.43, the order of σ_{pop} for the different collision partners is CO_2 > N_2 > O_2 > Ar. Previous FMS measurements in our group by Alagappan *et al*. of state-

and velocity-changing efficiencies in superthermal collisions of CN($A^2\Pi$, j = 0.5, F_2f) with He, Ar, N_2 and O_2 observed nearly identical total removal cross-sections for Ar and O_2, but both lower than for N_2.[198] Those results were explained with respect to similar van der Waals radii for Ar and O_2 compared to N_2, and also speculated similarities and differences of the CN($A^2\Pi$) interaction potentials, with the PESs for Ar and O_2 in particular contended to be comparable. There is a visible difference in the total removal cross-sections for collisions with Ar and O_2 in this work, however both are again smaller than the cross-sections for N_2. The order of colliders in this present study appears to be loosely correlated with the long-range attractive dispersion and lowest-order electrostatic forces determined by the polarisabilities and dipole and quadrupole moments of each collision species (where appropriate), as listed in Table 4.8. It has commonly been proposed that the larger absolute magnitude of the N_2 quadrupole moment over that of O_2 is responsible for the larger cross-sections in a variety of related phenomena. For example, Lee and co-workers observed an increased efficiency of N_2 over O_2 to cause RET in NO($A^2\Sigma^+$).[306] Kliner and Farrow saw the same trend for rotational relaxation of OH($X^2\Pi$) following photodissociation of H_2O_2,[88] and several other authors have also noted this behaviour in inelastic spectroscopic line broadening experiments in OH($X^2\Pi$).[134, 307-309] This straightforward argument based on long-range attractive intermolecular forces could also be invoked to rationalise the results for CN($A^2\Pi$) in this work.

Table 4.8 – Dipole moments (μ), quadrupole moments (Θ) and polarisabilities (α) of the collision species relevent to this work.

Species	μ / D	Θ / D·Å	α / Å^3
CN($A^2\Pi$)	0.3[a]	[b]	-
Ar	-	-	1.66[e]
N_2	-	-1.40[c]	1.71[e]
O_2	-	-0.46[d]	1.56[e]
CO_2	-	-4.28[c]	2.51[e]

[a] *Ref. 178.*

[b] *No literature value available.*

[c] *Ref. 310.*

[d] *Ref. 311*

[e] *Ref. 312.*

As noted in Table 4.8, the dipole moment of CN($A^2\Pi$) is small, although there are no measurements or calculations of the CN($A^2\Pi$) quadrupole moment, which prevents any direct quantitative analysis of the balance between dipole-quadrupole or quadrupole-quadrupole interactions. The influence of long-range attractive forces on the population removal cross-sections can be approximated through a Parmenter-Seaver plot, defined in Equation 4.40.[313, 314]

$$\ln(\sigma_Q) = \ln(C) + \left(\frac{\varepsilon_{MQ}}{k_B T}\right)$$

Equation 4.40

Here, σ_Q is the total removal, or quenching, cross-section and ε_{MQ} is the attractive well-depth between the probed molecule (*M*) and the quencher (*Q*). A linear relationship should therefore show that long-range attraction is important in the collision process. Since ε_{MQ} is not known for all collision pairs in this study, Equation 4.40 can be represented with respect to the attractive well-depth of the quencher-quencher interaction, ε_{QQ}, for which literature values are available.[313, 314] Equation 4.40 now becomes:

$$\ln(\sigma_Q) = \ln(C) + \beta\left(\frac{\varepsilon_{QQ}}{k_B}\right)^{1/2}$$

Equation 4.41

where

$$\beta = \left(\frac{\varepsilon_{MM}}{k_B T^2}\right)^{1/2}$$

Equation 4.42

assuming that

$$\varepsilon_{MQ} = \left(\varepsilon_{MM}\varepsilon_{QQ}\right)^{1/2}$$

Equation 4.43

The relevant terms of Equation 4.41 are listed in Table 4.9 and plotted in Figure 4.47, where σ_Q is equal to the population removal cross-section, σ_{pop}. For Ar, the well-depth arises purely from the dispersion interaction. The molecular colliders include the additional quadrupole-quadrupole interaction.

Table 4.9 – Parmenter-Seaver attractive well-depth terms from references 313 and 314 and rotationally averaged population removal cross-sections from this work.

Quencher	$(\varepsilon_{QQ}/k_B)^{1/2}$ / $K^{1/2}$	$\langle \ln(\sigma_{pop}) \rangle$
Ar	11	4.109 ± 0.091
N_2	9.7	4.358 ± 0.067
O_2	10.8	4.261 ± 0.114
CO_2	14	4.749 ± 0.138

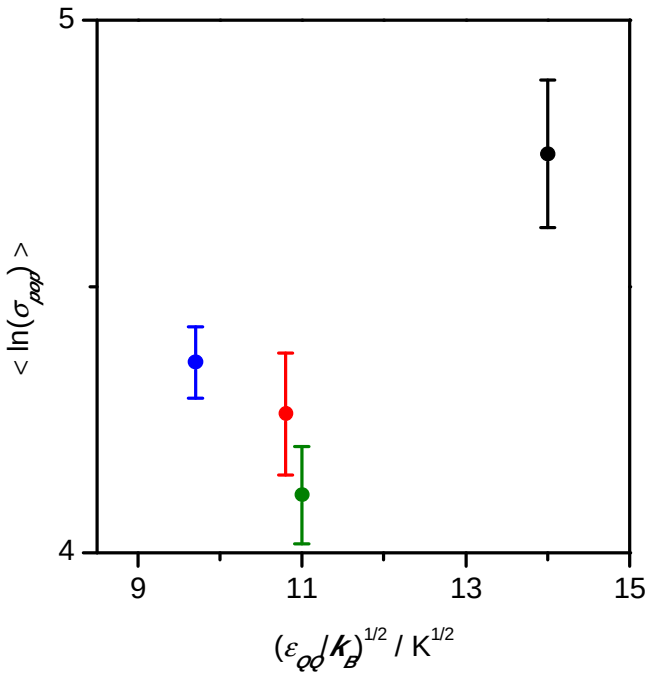

Figure 4.47 – A Parmenter-Seaver correlation plot of the rotationally-averaged population removal cross-sections, σ_{pop}, from this work, and the *collider-collder (quencher self-interaction) attractive well-depth terms, $(\varepsilon_{QQ}/k_B)^{1/2}$, from references 313 and 314. Olive = Ar, blue = N_2, red = O_2, black = CO_2. Error bars are 2σ statistical uncertainties.*

From Figure 4.47, no definitive linear relationship exists between the quencher self-interaction attractive well-depths and the CN($A^2\Pi$, v = 4, j) average population removal cross-sections. The smallest well-depth is that of N_2, but this has a larger total removal cross-section compared to Ar and O_2. Similarly, Ar has the largest well-depth out of

these three, but the smallest cross-section. The CO_2 collider has both the largest self-interaction well-depth and largest average cross-section, which may point to the role of attractive forces on the interaction with CN($A^2\Pi$). The fact that O_2 and Ar have similar self-interaction well-depths and cross-sections supports the proposal by Alagappan *et al.* that the two have similar CN($A^2\Pi$) potential well-depths.[161]

The basis of an analysis that correlates attractive forces with the collision cross-section has been questioned in systems such as OH($X^2\Pi$) with N_2 and O_2, where rigorous calculations have suggested a significantly deeper interaction with O_2.[128] Furthermore, the breakdown of the total removal cross-sections in Figure 4.43 into the reversible and irreversible components shown in Figure 4.46 also dissuades an overly simplistic interpretation based on a common RET mechanism for the CN($A^2\Pi$) collision systems studied here. There is strong evidence for a substantial fraction of σ_{pop} for O_2 and CO_2 to comprise EET or reaction, consistent with the literature CN($A^2\Pi$, v = 4) total quenching rate constants, k_Q, given in Table 4.10 (these have been taken from Table 1.4 of Section 1.8.2). Comparison of σ_{pop} to Table 4.10 suggests that on average, quenching makes up only ~7% of the total value for collisions with Ar and N_2, whereas for CO_2 this approaches ~20%. This is in agreement with the results of Dagdigian and co-workers, who concluded that quenching comprises only ~4% of the total removal of the initially prepared level for CN($A^2\Pi$, v = 3)+N_2.[206] There is no previous measurement of k_Q for O_2 with which to compare. Also displayed in Table 4.10 are the Boltzmann-weighted averages of the individual $k_{j\to x}^{(0)}$ rate constants derived from the breakdown of the total removal measurements, given in Figure 4.45 and Figure 4.46, to yield an approximate k_Q for each collider.

Table 4.10 – CN($A^2\Pi$, v = 4) quenching rate constants, k_Q, from reference 110 and those from this work derived from Boltzmann-weighted averages of the individual $k_{j\to x}^{(0)}$ rate constants for each collider. The errors from this work are 2σ.

Collider	k_Q / 10^{-11} cm^3 s^{-1}	
	This work	Literature
Ar	1.6 ± 0.3	2.36 ± 0.2
N_2	2.6 ± 0.3	3.83 ± 0.3
O_2	21 ± 5	-
CO_2	14 ± 2	13.1 ± 1.0

There is good agreement between the approximate k_Q rate constants determined from this work and the literature k_Q for collisions with Ar, N_2 and CO_2, which is perhaps surprising given that the experiment was not optimised for this type of measurement. Again, there is no literature value for O_2 to compare with, however the rate constant observed in this work (although with large uncertainies) is much faster than the previously reported value of $(3.1 \pm 0.1) \times 10^{-11}$ cm^3 s^{-1} for CN($A^2\Pi$, v = 1) reported in Table 1.4.[208] The differences in the long-time removal kinetics in Figure 4.39 and Figure 4.40 observed for collisions with N_2 and O_2, combined with the good agreement between the N_2 k_Q from this work and the literature, instils confidence, regardless of the large statistical uncertainties, that the total quenching of CN($A^2\Pi$, v = 4) by O_2 is a rapid process.

The inferred total quenching from the analysis of the FMS data cannot directly distinguish between loss due to reaction or EET. The reaction of CN($X^2\Sigma^+$) with both O_2 and CO_2 is exothermic[210-215] and reaction is therefore energetically accessible for CN($A^2\Pi$, v =4), with an additional ~190 kJ mol^{-1} (~15900 cm^{-1}) of energy available. If $k_Q = (21 \pm 5) \times 10^{-11}$ cm^3 s^{-1} for O_2 does include loss due to reaction, then CN($A^2\Pi$, v = 4) is around an order of magnitude more reactive towards O_2 than CN($X^2\Sigma^+$) at room temperature ($k_{reaction,298} = 5 \times 10^{-11}$ cm^3 s^{-1} for CN($X^2\Sigma^+$)+O_2),[272] implying strong electronic and vibrational dependences.[208, 214] The reaction of CN($X^2\Sigma^+$) with CO_2 proceeds over a substantial barrier,[213, 214] making it negligible at thermal temperatures. The large quenching rate constant for CN($A^2\Pi$, v = 4)+CO_2 has previously been explained in terms of the near-resonance of the CO_2 ν_3 anti-symmetric stretch with the energy gap between CN($A^2\Pi$, v = 4) and CN($X^2\Sigma^+$, v = 7) (ΔE = 2373 cm^{-1}),[110] suggesting that quenching by CO_2 is primarily a result of rapid EET. Halpern and co-workers demonstrated that electronic quenching of the CN($A^2\Pi$, v') molecule takes place *via* a cross-relaxation energy transfer mechanism to neighbouring CN($X^2\Sigma^+$, $v = v' + 4$) vibrational levels, due to the near-degeneracy of the two vibronic manifolds.[110] For example, CN($A^2\Pi$, v' = 3) populates CN($X^2\Sigma^+$, v = 7) that lies immediately below. However, EET from CN($A^2\Pi$, v' = 4) was observed to populate both CN($X^2\Sigma^+$, v = 8 and v = 7) levels, supporting the proposal of the near-resonance with CO_2 and the prominence of EET over reaction.

The total population removal cross-sections decline as a function of *j* for all colliders, which is a common observation and usually explained in terms of increasing energy gaps between successive rotational levels and linear-to-angular momentum transfer restrictions.[32] The decrease is considerably faster for CO_2 and O_2 compared to Ar and N_2, with the ratios of the lowest to highest *j*, σ_{pop} (j = 2.5 F_1e)/(j = 18.5 F_1e), in the order N_2 (1:0.86) > Ar (1:0.83) > O_2 (1:0.77) > CO_2 (1:0.69). This may be evidence for a preferred quenching geometry for O_2 and CO_2, which is then washed out as the rotational angular momentum of the CN partner increases.[315, 316] This premise draws from recent experimental and theoretical advances by Brouard and co-workers on the OH($A^2\Sigma^+$)+Kr system,[316, 317] who identified a significant quenching mechanism controlled by a strong attractive interaction at a preferred OH-Kr geometry. The quenching cross-sections were found to decrease sharply with increasing *N* in OH($A^2\Sigma^+$), with the OH($X^2\Pi$) quenching products exhibiting a considerable degree of rotational excitation, but minimal vibrational excitation. Corresponding quantum beat spectroscopy (QBS) measurements of the OH($A^2\Sigma^+$) collisional depolarisation saw cross-sections that were small at low *N* and persistently large at high *N*, consistent with a significant quenching channel competing at low *N*.[317] Computation of the OH($X^2\Pi$, $A^2\Sigma^+$)-Kr PESs together with the non-adiabatic coupling between them, showed that in the near-collinear HO-Kr geometry, there is a conical intersection where the deep $V_\Sigma(A')$ attractive well (0.76 eV ≈ 6130 cm^{-1}) crosses the repulsive wall of the $V_\Pi(A')$ PES, through which EET between the two electronic states is greatly facilitated, mediated by the V_1 coupling term. Single surface QCT calculations failed to reproduce the observed results, especially at low *N*. Improved agreement was seen with multiple trajectory surface-hopping calculations that included non-adiabatic coupling between the two *A′* surfaces, supporting the proposal of collisional transfer through the conical intersection. Experimental data for the analogous NO($A^2\Sigma^+$)+Kr system, which has no significant quenching channel, revealed much slower elastic depolarisation and excellent agreement with the single surface calculations.[317]

It is clear from the discussion so far that O_2 and CO_2 possess appreciable quenching channels for collisions with CN($A^2\Pi$), whereas Ar and N_2 do not. This, in part, accounts for the relative magnitude of σ_{pop} for each collider. Looking at the $\sigma^{(0)}_{j\to j'}$ components from the breakdown of σ_{pop} in Figure 4.46, the order of RET efficiencies is CO_2 > N_2 > Ar > O_2. The RET and quenching pathways are a direct reflection of the respective

PESs. The similar qualitative trends of σ_{pop} and $\sigma^{(0)}_{j\to j'}$ for the molecular colliders to those for Ar suggest that the PESs have similar topologies. The only molecular system for which PESs have been previously constructed and available for comparison are the spherically-averaged CN($A^2\Pi$, v = 3)-N_2 potentials from Dagdigian and co-workers in reference 206. There, reasonable agreement was seen between the experimentally determined total removal rate constants and QS predictions from the PESs, meaning that in this respect, despite the significant differences in their state-to-state RET data, the PESs appear to represent the system well. The excellent reproducibility of their experimental total removal rate constants in this work, as evident in Figure 4.43, reaffirms this statement and upholds the reliability of both sets of population removal measurements and solidifies the integrity of even approximate QS calculations. The CN($A^2\Pi$)-N_2 PESs are presented and examined in Chapter 5. Concurrent with the findings of this chapter, the V_{sum} and V_{dif} potentials resemble the general form of the analogous CN($A^2\Pi$)-Ar PESs shown in Section 4.5.4. Since the results for O_2 and CO_2 follow those of Ar and N_2, albeit with different quenching abilities and associated anisotropies, it may be speculated that these colliders also have PESs somewhat similar to Ar, although there are no available PESs with which to compare. This is addressed further in the next sub-section and in Chapter 5.

Depolarisation

Returning to Figure 4.41 to Figure 4.44, the orientation decays non-exponentially with a multimodal character, consistent with contributions from inelastic removal. Overall, the depolarisation is very weak, with cross-sections between ~1 – 13 $Å^2$ for all of the molecular colliders. These are much smaller than the loss of population, and are therefore akin to those observed for CN($A^2\Pi$)+Ar in Section 4.5.3. Hence all of the collider studied are much better at RET than elastic depolarisation. The $\sigma^{(1)}_{dep}$ cross-sections typically lie within 2σ statistical uncertainties of each other, with no obvious correlations in j and only a weak correlation with collider, in an approximate order of Ar > N_2 > CO_2 > O_2 across the range of j probed. Such weak depolarisation has previously been observed in kinematically similar molecule-molecule systems. For example, Sitz and Farrow measured N_2+N_2 depolarisation to be comparitively slower than population removal, with substantial alignment conservation during state-to-state RET.[111, 112] Likewise, Troe and co-workers concluded the NO_2+NO_2 system to undergo fast RET,

but with minimal depolarisation, suggestive of complex formation.[103] Again, for CH_2O+CH_2O, Field and co-workers found elastic depolarisation to be far less efficient than any other collision pathway, accompanied by strong conservation of polarisation during inelastic transfer.[138] In a separate set of experiments, Field and co-workers measured very inefficient collisional depolarisation in BaO+CO_2, comparable to the analogous Ar system.[105, 106] Investigations of alkali earth metal dimer self-collisions and encounters with other molecules, such as O_2, CO_2 and CHF_3, by McCaffery and co-workers revealed invariably small depolarisation cross-sections, around two orders of magnitude slower than total RET.[139, 140] These particular examples were explained in terms of a general $\Delta m = 0$ propensity with a restricted change in m.

Elastic depolarisation is typically mediated by the attracive regions of the interaction potentials. The fact that the molecular colliders in this work produce values of $\sigma_{dep}^{(1)}$ similar to one another and to Ar from Section 4.5.3 supports the suggestion that the molecule-molecule systems have similar PES to CN($A^2\Pi$)-Ar. This is especially evident when looking at Dagdigian and co-workers' CN($A^2\Pi$)-N_2 V_{sum} and V_{dif} potentials in Chapter 5 and encourages the approximation to treat N_2 as a spherical target by averaging over different relative limiting orientations. The comparable behaviour of O_2 and CO_2 further suggests that this can be applied as a general approximation to any small centrosymmetric molecule colliding with CN($A^2\Pi$). Section 4.5.6 showed that the leading dominant term in the angular expansions of the CN($A^2\Pi$)+Ar PESs capable of causing elastic depolarisation is V_{20} (where $\lambda = 2$), which is only weakly attractive at longer range for that system. The proposal of similar PESs for the molecular colliders then indicates that weak attractive forces are also responsible for the mild elastic depolarisation seen in these systems. The observed variation of $\sigma_{dep}^{(1)}$ for the different colliders could be a result of subtle differences in the interaction potentials and the difficulty of measuring such a slow process in the the presence of more prominent competing channels.

The population removal results in Section 4.6.1 pointed to an enhanced quenching pathway for the CO_2 and O_2 colliders, hinting moreover at a preferred quenching geometry. An important question is whether the elastic depolarisation cross-sections provide further evidence of this. Brouard and co-workers' QBS measurements of OH($A^2\Sigma^+$)+Kr produced elastic depolarisation cross-sections that were small at low N

and persistently large at high *N*, consistent with a significant competing quenching channel through a preferred near-collinear HO-Kr geometry.[317] This effect is mirrored to some degree in previous FMS work from our group on superthermal collisions of CN($X^2\Sigma^+$) with N_2, O_2 and CO_2,[161] In that case, the ***z.j*** (LAB-frame alignment) composite signal component was scrambled to a larger extent for O_2 and CO_2 than for N_2, consistent with more anisotropic potentials for O_2 and CO_2. In other work, ter Meulen and co-workers also came to the conclusion from crossed-beam experiments that collisions of OH($X^2\Pi$) with N_2 should have more symmetric PESs than for collisions with CO_2.[77, 95] There is no clear signature of a preferred quenching geometry for O_2 or CO_2 in the elastic depolarisation results here, with $\sigma_{dep}^{(1)}$ showing no discernible dependence on rotational level. This may simply mean one or either of the following: (i) quenching is not a drastic enough competing prosess to impinge on the elastic depolarisation in this system, (ii) the potentials are much more isotropic than those of OH($A^2\Sigma^+$)-Kr, (iii) the anisotropy is sampled at different ranges. As has previously been discussed in Section 4.5.3, the large rotational energy spacings of a light rotor, such as OH, inhibit RET, whilst the light H-atom may be easily dragged around the PES and reoriented, favouring depolarisation. In contrast, heavy rotors, such as CN, are more difficult to reorient, and the smaller rotational energy spacings favour a bias towards RET, as has been made clear from the results of this chapter. In this regard, the quenching effect would be more pronounced in the population removal cross-sections than the depolarisation cross-sections for CN($A^2\Pi$), as is apparently observed.

Some further insight into the role of attractive long-range electrostatic forces may also be obtained by comparing $\sigma_{dep}^{(1)}$ for N_2 and O_2. Using the TCPS technique in our laboratory, Paterson *et al.*[128] previously measured larger elastic depolarisation cross-sections for collisions of OH($X^2\Pi$) with N_2 than O_2, which was partly linked to the larger quadrupole moment of N_2 and hence stronger long-range interactions for N_2 over O_2, consistent with inelastic line broadening experiments by other authors.[134, 135] Close inspection of Figure 4.44 reveals that the $\sigma_{dep}^{(1)}$ cross-sections for N_2 are consistently larger than for O_2 across all *j*, supporting the argument of long-range attractive forces. However, as previously stated in the discussion of population removal, this premise alone must be used cautiously. The weak elastic depolarisation and large statistical uncertainties observed here also discourage any sensitive comparison between the two colliders and deter a definitive conclusion. The collider dependence here is reminiscent

of the OH($X^2\Pi$)+He, Ar and Xe systems,[126, 129, 130, 132] where the stronger, longer-range forces in Xe did not turn up in elastic depolarisation, but instead in Λ-doublet propensities, i.e. different processes are in competition for the cross-section. Perhaps then collisions that would be expected to significantly enhance depolarisation for N_2 instead turn up in population transfer. Similar behaviour was again seen in the PS measurements of OH($X^2\Pi$)+N_2 with comparatively small rate constants for both orientation and alignment elastic depolarisation, suggesting that they contribute very little to the overall generally fast signal removal.[128]

4.6.3 Summary

The key conclusions from this section are listed below.

i. FMS studies into the total population removal and depolarisation of orientation have been extended to CN($A^2\Pi$, v = 4, j = 2.5, 3.5, 6.5, 11.5, 13.5 and 18.5, F_1e) colliding with N_2, O_2 and CO_2.

ii. As with the previous sections, the population decays in a near-exponential fashion and the orientation with a clear multimodal character, showing the prevalence of inelastic depolarisation in these systems, encouraging the use of the three-level kinetic model in deriving the measured cross-sections and suggesting that these collision partners behave similar to Ar.

iii. The thermally averaged population removal cross-sections, σ_{pop}, for the molecular colliders are all faster than for Ar, lying in the order CO_2 > N_2 > O_2 > Ar. The σ_{pop} for N_2 are in good agreement with previous measurements from Dagdigian and co-workers.[206]

iv. The order of σ_{pop} appears to be loosely correlated with long-range attractive dispersion and low-order electrostatic forces determined by the polarisabilities and dipole and quadrupole moments of each species. A common argument in related systems is that larger collision cross-sections for N_2 over O_2 are related to the larger quadrupole moment of N_2.

v. The influence of long-range attractive forces has been explored using a Parmenter-Seaver correlation, but this proved inconclusive.

vi. A breakdown of σ_{pop} into reversible and irreversible loss components reveals additional rapid removal channels for O_2 and CO_2, likely to be electronic

quenching, whereas Ar and N_2 are dominated by RET to nearby rotational levels.

vii. The σ_{pop} decline as a function of increasing *j*, expected from energy gap laws and angular momentum restrictions. However, the decrease is considerably faster for CO_2 and O_2 compared to N_2 and Ar, which could indicate a preferred quenching geometry for CO_2 and O_2, which then washes out more efficiently than N_2 and Ar as the CN molecule rotates faster. This is in accordance with recent findings from Brouard and co-workers on the OH($A^2\Sigma^+$)+Ar system.[316, 317]

viii. As with Ar, elastic depolarisation is very slow for the molecular partners, with cross-sections, $\sigma_{dep}^{(1)}$, scattered between 1 – 13 Å^2, typically within 2σ of each other. There is no obvious correlation in *j* and only a vague collider dependence, approximately in the order of Ar > N_2 > O_2 > CO_2 across the range of *j* probed.

ix. Previous studies of kinematically similar molecule-molecule systems also found RET pathways to be far more efficient than elastic depolarisation.

x. The role of long-range attractive forces is supported by the $\sigma_{dep}^{(1)}$ for N_2 being persistently larger than for O_2.

xi. The $\sigma_{dep}^{(1)}$ show no signature of a preferred quenching geometry, although this could be masked by the very weak elastic depolarisation.

xii. The similarities of the molecular colliders to Ar for the total removal and depolarisation of rotational angular momentum in CN($A^2\Pi$) suggests that these systems all have similar interaction potentials. This is supported by recent spherically-averaged CN($A^2\Pi$)-N_2 PESs of Dagdigian and co-workers and associated QS rate constants.

xiii. It is therefore proposed from the work so far that small centrosymmetric molecules, such as N_2, O_2 and CO_2, approximately act as spherical targets. This is investigated further in Chapter 5.

Chapter 5

State-to-State RET and Polarisation Transfer in CN($A^2\Pi$)

5.1 Introduction

Similar to the previous chapter, this part of the thesis is split into two main headings. The initial focus is on the systematic experimental and theoretical study of the state-to-state transfer of polarised rotational angular momentum in a $^2\Pi$-rare gas system. Specifically, photolysis of ICN followed by pulsed optical pumping is implemented to generate a known rotational population and LAB-frame orientation in CN($A^2\Pi$, v = 4) for the initial levels j = 6.5 F_1e or j = 10.5 F_2f. The cw-FMS probe technique is then re-employed to monitor the prepared and collisionally populated j' F_1e and j' F_2f product levels upon scattering with Ar to reveal the state, fine-structure and Λ-doublet resolved time-dependence of the initial population and orientation. Subsequent kinetic analysis is used to extract the state-to-state RET rate constants and MTEs, measuring how much orientation is conserved upon inelastic transfer to adjacent levels.

This work is motivated by the main conclusion from the previous chapter, that whilst elastic depolarisation is a relatively minor process in CN($A^2\Pi$)+Ar, depolarisation resulting from multiple inelastic collisions is in fact the dominant polarisation removal pathway. As accounted for by the three-level kinetic model introduced in Section 4.5.3, population from an initially prepared level may be reversibly transferred to nearby product levels without perfect retention of polarisation, termed *inelastic depolarisation*. Measurement of the individual state-to-state RET rate constants and MTEs should then

give further insight to this process. Fully state-specific data provides a more robust test of the underlying PESs, reflecting more delicately the topology. The measurements are accordingly compared to exact QS predictions from the newest set of CN($A^2\Pi$)+Ar interaction potentials, the B-K PESs, which were outlined in Section 4.5.4, to provide a more detailed probe of their theoretical accuracy.

An almost universal trend in RET studies is a strongly decreasing magnitude of the state-to-state RET rate constants with increasing Δj, resulting from the energy gap law and linear-to-angular momentum transfer restrictions. Often superimposed on this so-called *volcano* plot are Δj-dependent oscillations in the product rotational distributions. Examples include rare gas systems containing CaF($A^2\Pi$),[318] CO($X^1\Sigma^+$),[24, 25, 141, 142, 144, 145, 319] CN($X^2\Sigma^+$),[191, 192] CN($A^2\Pi$),[15, 184, 189, 199, 320] NO($X^2\Pi$),[143, 321, 322] and NO($A^2\Sigma^+$).[322] These oscillations are usually attributed to quantum interferences from the near-symmetry of the interaction potentials, more commonly termed the *near-homonuclear effect*. The oscillations depend on whether the rotational parity of the final level is the same as that of the initial level. As explained in Section 1.4, for a $^2\Pi$+Rg system represented in a diabatic basis by V_{sum} and V_{dif} potentials, the angular dependences of these PESs may be conveniently expanded in terms of reduced rotation matrix elements, $d^{\lambda}_{mm'}(\theta)$, and the radial expansion coefficients $V_{\lambda 0}(R)$ and $V_{\lambda 2}(R)$, respectively, facilitating the inspection of the relevant symmetry properties.[49, 50, 52]

As an important reiteration from Chapters 1 and 2, a $^2\Pi$ electronic state contains two spin-orbit manifolds with a body-frame projection of Ω = 1/2 or 3/2, labelled as F_1 or F_2, with F_1 lower in energy. In each spin-orbit manifold, the rotational levels are split into near-degenerate Λ-doublets of symmetry index ε = +1 (labelled as *e*) and ε = -1 (labelled as *f*). The parity *p* of these Λ-doublets depends on the rotational level and symmetry index, with $p = \varepsilon(-1)^{j-½}$. Following the formalism of Alexander and co-workers,[323, 324] it is found that the scattering amplitudes for rotational parity-*conserving* transitions are enabled only by the *even-*λ terms of the expansions, whilst the parity-*changing* transitions arise from the *odd-*λ terms.[49, 52] For a homonuclear molecule, the symmetry of the PES means there are only even-λ terms, and so only parity-conserving collisions occur. For a heteronuclear molecule, both the even and odd terms of the angular expansions mediate the dynamics. Near-homonuclear molecules, such as CN, are described as predominently even in character, and so the even-λ and odd-λ terms

often have very different radial dependences that lead to the parity-dependent alternations of the state-to-state RET rate constants.

A significant number of polarisation transfer studies using OODR techniques have already been performed since the initial inelastic polarisation transfer experiments by McCaffery and co-workers in the 1970s.[55, 325-327] Many of these have been singlet electronic states, for example $N_2(X^1\Sigma_g^+)$,[111] $Li_2(A^1\Sigma_u^+)$,[55] $BaO(A^1\Sigma^+)$,[106] $NaK(A^1\Sigma^+)$,[137] $C_2H_2(X^1\Sigma_g^+)$,[81] and $H_2CO(\tilde{A}\,^1A_2)$.[138, 282] Overall, for collisions of linear singlet molecules with rare gases, it is found that the polarisation is conserved along the kinematic apse, $\hat{a}_k$, defined in Equation 1.39 of Section 1.6.1, consistent with a rigid or hard-shell collision.[28] For small Δj transfer, where scattering is likely to be strongly in the forward direction, this corresponds to strong LAB-frame conservation. For larger Δj, with more sideways and backwards scattering, the conservation of LAB-frame polarisation is much weaker as a result of the larger angle required to rotate the apse-frame into the LAB-frame. Only when the interaction potential is strongly attractive, for example with a reactive system such as $NaK(A^1\Sigma^+)$+K, is essentially complete depolarisation observed.[137]

Symmetry selection rules and polarisation effects in rotationally inelastic collisions of open-shell diatomic molecules were first considered in a theoretical basis by Alexander and Davis in the early 1980s,[56] then generalised by Alexander and Orlikowski for a protoypical $^2\Pi$+Rg system, $NO(X^2\Pi)$+Ar.[20] In the latter of these seminal papers, the MTE was introduced as a measure of inelastic polarisation transfer. For a rotational orientation, the MTE has the limits $-1 \leq E^{(1)}(j,j') \leq +1$, with the positive limit corresponding to complete conservation of initial orientation in the collision and the negative limit corresponding to conservation of the magnitude, but change in the *sign* of orientation. A strong parity dependence to the orientation MTE was predicted, involving either conservation or change in the sign of the LAB-frame orientation.

The only prior experimental measurements of MTEs for collisions in a $^2\Pi$ system, other than from our laboratory,[199] as discussed below, are Norman and Field's circularly polarised OODR experiments on $CaF(A^2\Pi_{1/2}, j = 0.5\ f, m_j = +0.5)$+Ar,[105] probing $j' = 1/2\ e$, $3/2\ f$, and $3/2\ e$ states. A strong final state dependence on the product orientation was observed, with the parity-conserving transfer resulting in products with the same sign of orientation as the initial state, whilst the parity-changing transfer resulted in the

opposite sign of orientation. This corresponds to a positive MTE for the parity-conserving transitions and a negative MTE for the parity-changing transitions, just as predicted earlier by Alexander and Davis and clearly following the behaviour observed in the NO($X^2\Pi$)+Ar system by Alexander and Orlikowski.[20, 56] Dagdigian, Alexander and Yang recently performed experiments (LIF-OODR) and calculations measuring fully state-resolved RET ($jF\varepsilon \rightarrow j'F'\varepsilon'$) in CN($A^2\Pi$, v = 3)+Ar for rotational levels both near the peak of the Boltzmann distribution (j = 6.5) and for very high levels (N = 60).[15, 190, 194] The PESs utilised were the B-W potentials outlined in Section 4.5.4. The results displayed generally good agreement with the QS calculations and reproduced the volcano plot with predicted inelastic parity-dependent oscillations, along with a preference for spin-orbit conservation accounted for by the thermally accessible range of the even-λ terms over odd-λ terms in the PESs. Limited measurements of state-to-state RET and alignment transfer in CN($A^2\Pi$, v = 4)+Ar were later made in our group by Ballingall *et al*. using the FMS technique in a multi-pass set up,[199] alongside the previously reported total removal and depolarisation rate constants presented in Section 4.1. Alignment MTEs of $E^{(2)}(j,j')$ ≈ ~0.3 – 0.5 were reported, however the small selection of product levels probed prevented any examination of parity dependence.

This chapter aims to strengthen these previous investigations by exploring the effects of rotational parity on inelastic polarisation transfer in CN($A^2\Pi$)+Ar. A general survey of thermally accessible product state distributions ($\Delta j = j' - j \leq |5|$) for spin-orbit and Λ-doublet ($F\varepsilon$)-conserving and $F\varepsilon$-changing transitions from two different initial states of opposite spin-orbit, Λ-doublet and parity labels (j = 6.5 F_1e+ and j = 10.5 F_2f-) also highlights additional propensities that may arise from being a near-homonuclear system close to the Hund's case-(a) coupling limit. During state-to-state RET, only a small percentage of the initial population is expected to scatter into any single product level as Δj increases, which is evident in references 15 and 199. This will result in very small detectable signal sizes for the alternate polarisation geometries. Since the one-photon FM probe technique is more sensitive to orientation than alignment, as discussed in Section 3.3 and reference 167, throughout this chapter the circular pump-probe geometries are utilised in order to create and monitor a rotational population and orientation. Unfortunately, this restricts the F_1f and F_2e final levels from being probed, as they are only accessible *via* Q-main branch transitions, which have no sensitivity to orientation away from very low j. In principle these levels could be probed *via* the

associated P & R-sub branches, but these have weak line strengths, resulting in unacceptably poor signal-to-noise ratios.

In the second part of this chapter, the study of state-to-state RET and orientation transfer is extended to collisions of CN($A^2\Pi$, v = 4) with the molecular partners, N_2, O_2 and CO_2, starting from j = 6.5 F_1e to a range of j' F_1e and j' F_2f product states. This is again motivated by conclusions from the previous chapter, where population removal for O_2 and CO_2 was seen to comprise largely of electronic quenching, whereas N_2 and Ar were dominated by reversible RET. Moreover, the σ_{pop} cross-sections hinted at a preferred interaction geometry for CO_2 and O_2. Elastic depolarisation was consistently very weak, with very little collider dependence. The state-specific results in this chapter may provide further insight to these observations and to the possible role of long-range intermolecular interactions. Overall, it was speculated that the CN($A^2\Pi$) PESs for the molecular partners are similar in form to those for Ar. Being more sensitive to the form of the PESs, the state-to-state measurements should shed more light on this. The only existing CN($A^2\Pi$)-N_2 PESs, from Dagdigian and co-workers[206] are introduced here and compared to the CN($A^2\Pi$)-Ar PESs from Section 4.5.4.

CN($A^2\Pi$)+molecule state-to-state RET studies have been limited to encounters with H_2, N_2, CO_2 and CH_4.[203, 204, 206, 224] Heaven and co-workers performed experiments on the predissociation dynamics of CN($A^2\Pi$)-H_2 complexes with product state-resolution and on state-to-state rotationally inelastic collisions of CN($A^2\Pi$)+H_2 at low temperatures (7 K). Strong parity-dependent oscillations were observed in the inelastic scattering, with a preference for conservation of total rotational parity, consistent with that observed in CN($A^2\Pi$)+Rg collisions. Conversly, no parity dependence was observed in the products of predissociation, which was attributed to the lack of parity definition in the excited state complex prior to dissociation. Most relevant to the work in this chapter is the combined experimental and theoretical investigation of CN($A^2\Pi$)+N_2 RET by Dagdigian, Alexander and co-workers, and the experimental study of CN($A^2\Pi$)+CO_2/CH_4 by Khachatrian and Dagdigian.[206, 224] The LIF-OODR technique was employed to measure fully state-resolved $jF\varepsilon \rightarrow j'F'\varepsilon'$ RET rate constants of low j CN($A^2\Pi$, v = 3). Spherically-averaged *ab initio* PESs for CN($A^2\Pi$)+N_2 were computed for three limiting orientations of N_2, and subsequent QS calculations performed. There was a remarkable disagreement between experiment and theory in both the relative propensities for scattering into different spin-orbit and Λ-doublet manifolds, and in the

relative Δj propensities within specific fine-structure manifolds, as discussed in Section 1.8.2. Theory predicted distributions consistent with CN($A^2\Pi$)+Ar, with propensities centered energetically on the initially prepared level, while the experiment measured rate constants with unusual ranges of Δj that did not follow the predicted behaviour. This astonishing disagreement between experiment and theory was attributed to a failure of the theory, suggested to be a result of the spherical averaging of the CN($A^2\Pi$)+N_2 PESs and neglect of the rotational inelasticity of the N_2 molecule. The separate experimental measurements of CN($A^2\Pi$) colliding with CO_2 and CH_4 saw strikingly similar unusual behaviour to the CN($A^2\Pi$)+N_2 observations.[224] The results in this chapter will be directly compared to the measurements and approximate QS rate constants from references [206] and [224] to re-examine the success or failures of the previous work.

5.2 Experimental Details

The experiments in this chapter involve the photolytic generation of CN($X^2\Sigma^+$) from ICN, followed by optical preparation of selected CN($A^2\Pi$, v = 4, $jF\varepsilon$) levels with a rotational orientation, then monitoring the collisional evolution of the prepared and RET product levels with a cw-FM probe laser. The experimental methodology and FM probe technique have been discussed in detail im Chapters 2 and 3. As in Section 4.3, preliminary tests were performed to check that the experiments were set-up correctly. Below is a summary of the experimental details relevent to this chapter.

A mixture of ICN (≤ 5 mTorr) and high purity collider gas (Ar, N_2, O_2 or CO_2) was slowly flowed through the chamber, with the total pressure maintained at 400 ± 5 mTorr for experiments with Ar, N_2 and O_2, and 200 ± 5 mTorr for CO_2. These pressures were based on the measured total removal rate constants from Chapter 4, so that the average time between collisions was of the order of 200 ns. Since the experimental time resolution is about 10 ns, this enabled measurement of the kinetics down into single collision conditions. The ICN was photolysed at 266 nm using an Nd:YAG laser to produce CN($X^2\Sigma^+$, v = 0). For the Ar, N_2 and CO_2 measurements, a post-photolysis delay of 30 μs ensured complete thermalisation of the nascent translational distributions and substantial thermalisation of the rotational distributions, also ensuring that the strong rotational anisotropy of CN($X^2\Sigma^+$) produced in the photolysis was destroyed.[159,

[161] For measurements with O_2, the photolysis-pump delay was set at 1.25 μs to give a compromise between translational and rotational thermalisation whilst minimising reactive loss of CN($X^2\Sigma^+$).

The circularly polarised ~620 nm Nd:YAG pumped dye laser was tuned to either the $R_1(5.5)$ [16106.56 cm^{-1}] or $P_2(11.5)$ [16049.53 cm^{-1}] spectroscopic transitions of the CN $A^2\Pi - X^2\Sigma^+$ (4,0) band, to prepare an oriented sample of CN($A^2\Pi$, $v = 4$, $jF\varepsilon$) for either $j = 6.5$ F_1e or $j = 10.5$ F_2f, respectively. For the molecular colliders only experiments with initial level $j = 6.5$ F_1e were performed. The pump beam polarisation was switched between left- and right-handed circular using the PEM to give co-rotating and counter-rotating pump-probe geometries. The CN($A^2\Pi$, $v = 4$, $jF\varepsilon \rightarrow j'F'\varepsilon'$) initially prepared and RET final levels were probed by the circularly polarised FM cw-diode laser in stimulated emission on selected R_1, P_2 and $R_2+^PQ_{21}$ transitions of the $A^2\Pi - X^2\Sigma^+$ (4,2) band, with line frequencies given in Table 5.1 and Table 5.2. Note, for consistency with the spectroscopy of the pump step, the absorption nomenclature has been retained for the probe step. The phase angle was set at $\theta = 0^o$ for all experiments. To minimise systematic errors arising from slow drifts in the pump laser wavelength, spectra were acquired sequentially for the *prepared* and the *product* states.

Table 5.1 – Spectroscopic probe transitions and frequencies (in cm^{-1}) for the state-to-state RET and polarisation transfer product levels, with the initial level $j = 6.5$ F_1e prepared on the $R_1(5.5)$ transition at 16106.56 cm^{-1}.

Δj	j'	$F\varepsilon$-conserving[a]		$F\varepsilon$-changing[b]	
		Transition	Freq.	Transition	Freq.
-4	2.5	$R_1(1.5)$	12037.40	$P_2(3.5)$	12060.44
-3	3.5	$R_1(2.5)$	12041.10	$P_2(4.5)$	12053.68
-2	4.5	$R_1(3.5)$	12044.28	$P_2(5.5)$	12046.57
-1	5.5	$R_1(4.5)$	12046.93	$P_2(6.5)$	12039.12
0	6.5	$R_1(5.5)$[c]	12049.06[c]	$R_2(5.5)+^RQ_{21}(6.5)$	12086.96+.91
+1	7.5	$R_1(6.5)$	12050.68	$P_2(8.5)$	12023.14
+2	8.5	$R_1(7.5)$	12051.78	$R_2(7.5)+^RQ_{21}(8.5)$	12085.08+.03
+3	9.5	$R_1(8.5)$	12052.39	-	-

[a] *j' F_1e.*

[b] *j' F_2f.*

[c] *Prepared level (direct line).*

Table 5.2 – Spectroscopic probe transitions and frequencies (in cm^{-1}) for the state-to-state RET and polarisation transfer product levels, with the initial level j = 10.5 F_2f prepared on the $P_2(11.5)$ transition at 16049.53 cm^{-1}.

Δj	j'	$F\varepsilon$-conserving[a]		$F\varepsilon$-changing[b]	
		Transition	Freq.	Transition	Freq.
-5	5.5	$P_2(6.5)$	12039.12	-	-
-4	6.5	$R_2(5.5)+{}^RQ_{21}(6.5)$	12086.96+.91	$R_1(5.5)$	12049.06
-3	7.5	$P_2(8.5)$	12023.14	$R_1(6.5)$	12050.68
-2	8.5	$R_2(7.5)+{}^RQ_{21}(8.5)$	12085.08+.03	$R_1(7.5)$	12051.78
-1	9.5	$P_2(10.5)$	12005.70	$R_1(8.5)$	12052.39
0	10.5	$P_2(11.5)$[c]	11996.42[c]	$R_1(9.5)$	12052.48
+1	11.5	$P_2(12.5)$	11986.76	$R_1(10.5)$	12052.09
+2	12.5	$R_2(11.5)+{}^RQ_{21}(12.5)$	12076.82+.73	$R_1(11.5)$	12051.21
+3	13.5	$P_2(14.5)$	11966.30	$R_1(12.5)$	12049.83
+4	14.5	$P_2(15.5)$	11955.48	$R_1(13.5)$	12047.98
+5	15.5	-	-	$R_1(14.5)$	12045.64

[a] *j' F_2f.*

[b] *j' F_1e.*

[c] *Prepared level (direct line).*

5.3 Experimental Kinetic Analysis

The co- and counter-rotating polarisation geometries were utilised to prepare a rotational population, $A_0^{(0)}$ and LAB-frame orientation, $A_0^{(1)}$, then probe their evolution in the initial and collisionally populated adjacent levels. The experimental data were analysed as FM SE&D Doppler lineshapes, as described in the kinetic processing procedure of Chapter 3. The time evolution of the $A_0^{(0)}$ and $A_0^{(1)}$ moments for the prepared and product levels were determined by fitting directly to Equation 3.21 and Equation 3.22 for each 10 ns-averaged time step using the LM minimisation method. For the initial states, the translational temperature was also optimised, however for the transfer states the temperature was fixed at 298 K, since the latter have poorer signal-to-noise. During trial processing of the product states, floating the temperature did not significantly vary from 298 K at any time, and so this parameter was fixed in order to improve the determination of the population and orientation. This resulted in complete

time traces of the population and orientation for both initial and product levels, suitable for further kinetic analysis.

In Section 4.5.3, the time evolution of the population, orientation and alignment of the initial level were well-described by a simple three-level kinetic model. This multiple collision model includes reversible transfer of population and polarisation of rank *K* from an initial level, *j*, to nearby rotational levels, *j′*, with rates $\Gamma^{(0)}_{j\to j'}$ $\Gamma^{(K)}_{j\to j'}$ $\Gamma^{(0)}_{j'\to j}$ and $\Gamma^{(K)}_{j'\to j}$, respectively, and irreversible loss from both the initial and product levels to distant levels, for example in energy, angular momentum, or vibrational or electronic state, j_x, described by the rates $\Gamma^{(0)}_{j\to j_x} = \Gamma^{(0)}_{j'\to j_x}$. The (well-determined) total removal rate out of the initial level, $\Gamma^{(0)}_{j,\mathrm{tot}}$, is then the sum of $\Gamma^{(0)}_{j\to j'}$ and $\Gamma^{(0)}_{j\to j_x}$. This model could in principle be straightforwardly extended to describe the time-dependence of the population and orientation of the product levels. However, the observed signal-to-noise ratio of the product levels is not high enough to support such a model and the large number of associated parameters. Fitting to the product levels is therefore restricted to early delay times where the CN will have undergone one to a few collisions, which simplifies the kinetic modelling. For a single collision that transfers molecules from an initial rotational level, *j*, to a product level, *j′*, the population of the product level at time, *t*, is given by:

$$A_0^{(0)}(j';t) = A_0^{(0)}(j;t=0)\left[\frac{\Gamma^{(0)}_{j\to j'}}{\Gamma^{(0)}_{j,\mathrm{tot}}}\right]\left(1-e^{-\Gamma^{(0)}_{j,\mathrm{tot}}t}\right)$$

Equation 5.1

where $A_0^{(0)}(j;t=0)$ is the population of the initial level at t = 0, proportional to the overall signal size, and $\Gamma^{(0)}_{j,\mathrm{tot}}$ is the total population removal rate from the initial level, both of which are found from fitting the initial level population kinetic trace to the three-level kinetic model. Since the initial and product experimental scans were performed back-to-back under stable conditions, and the rotational line strengths were included in the data analysis to generate the kinetic traces, these proportionality constants are the same for the initial and final levels. Finally, $\Gamma^{(0)}_{j\to j'}$ is the rate of population transfer from the initial level to the product level that is sought. Fitting of the product state population kinetic traces was restricted to the first 200 – 300 ns, which as

noted above, at the pressures used is the approximate average collision time, based on the observed total removal rates, $\Gamma_{j,\mathrm{tot}}^{(0)}$.

The MTE derived from the experimental measurements is defined as:

$$E^{(1)}(j, j') = \frac{A_0^{(1)}(j';t=0)}{A_0^{(1)}(j;t=0)}$$

Equation 5.2

which is simply the ratio of the product state to initial state orientation at time $t = 0$.[19, 20, 45, 57] The orientation of the initial state at $t = 0$, $A_0^{(1)}(j;t=0)$, is found by fitting the orientation kinetic trace for level j to the three-level kinetic model. The orientation of the product level is ill-defined at $t = 0$, as at this time no population has been transferred from the initial level. At early times, for example the first 100 ns, the majority of the CN molecules have still only undergone either zero or one collision, meaning the orientation is still poorly determined. As more population is transferred into the product level and the orientation becomes better determined, it is simultaneously being reduced in magnitude as a result of removal by multiple collisions. It is therefore better to extrapolate the measured orientation at later times back to $t = 0$. The simplest model to successfully fit the product orientation kinetic traces is found to be a single exponential decay. The measured time-dependent transferred orientation is hence fitted to the following form:

$$A_0^{(1)}(j';t) = A_0^{(1)}(j';t=0)e^{-\left\langle \Gamma_{\mathrm{dep}}^{(1)} \right\rangle t}$$

Equation 5.3

by varying the average phenomonological orientation depolarisation rate, $\left\langle \Gamma_{\mathrm{dep}}^{(1)} \right\rangle$, and initial product orientation, $A_0^{(1)}(j';t=0)$. The range of orientation data fitted was varied depending on the signal-to-noise between typically 100 ns $\leq t \leq$ 500 ns. No significance is placed on the value of $\left\langle \Gamma_{\mathrm{dep}}^{(1)} \right\rangle$ in this chapter and it will not be discussed further.

The fitting procedures were performed using a single custom-written LabVIEW® routine, developed by Dr. Matthew. L. Costen at Heriot-Watt University. The population and orientation kinetic traces for an initial and product level that had been recorded sequentially without change to the experimental conditions were analysed

together, with the initial state population and orientation traces fitted to the three-level model as outlined above. The obtained initial level parameters, $\Gamma_{j,\mathrm{tot}}^{(0)}$; $A_0^{(0)}(j;t=0)$; and $A_0^{(1)}(j;t=0)$ were passed to subsequent algorithms that fitted the transferred population and orientation to find $\Gamma_{j\to j'}^{(0)}$, $A_0^{(1)}(j';t=0)$, and hence $E^{(1)}(j,j')$. In each case a LM minimisation routine was used to perform the fitting, with weighting by statistical deviation of the data.

For each product rotational state, multiple independent measurements taken on different days were fitted separately. The resulting rates, $\Gamma_{j\to j'}^{(0)}$, were converted to state-to-state rate constants, $k_{j\to j'}^{(0)}$, by dividing by the collider number density, [*M*], assuming that the pressure of ICN was negligible:

$$k_{j\to j'}^{(0)} = \frac{\Gamma_{j\to j'}^{(0)}}{[M]}$$

Equation 5.4

These multiple independent measurements of $k_{j\to j'}^{(0)}$ and $E^{(1)}(j,j')$ for each RET product level were then averaged. To allow direct comparison of the state-to-state population transfer kinetics for the different collision partners in Section 5.5, independent of trivial differences in the total rate of collisions, the population transfer rate constants were converted to thermally averaged cross-sections, $\sigma_{j\to j'}^{(0)}$, as outlined in Section 1.6.1.

5.4 CN($A^2\Pi$)+Ar State-to-State RET and Polarisation Transfer

5.4.1 Experimental Results

Representative data and fits for the SE FM Doppler lineshapes are shown in Figure 5.1 for the two initial states, j = 6.5 F_1e and j = 10.5 F_2f, prepared and probed on the $R_1(5.5)$ and $P_2(11.5)$ transitions, respectively, and for example product states (Δj = 0 and -1, $F\varepsilon$-changing), where for the purposes of presentation the first 100 ns post-pump signal has

been averaged. In all cases the fits represent the data well. The large difference between the two experimental geometries (co-rotating and counter-rotating) in the prepared levels indicates that a significant rotational orientation has been created. The R- and P-branches used to prepare and probe the initial levels have opposite sensitivities to orientation (see Chapter 3), and so opposite signs for each geometry are seen in the two initial levels. The overall signal sizes for the product levels are considerably smaller than those for the initial levels, indicating that only a small fraction of the initial population is transferred to any single product level. The smaller transferred signal size for the larger Δj product levels is consistent with the 'volcano' effect commonly observed in RET studies, as discussed in Section 5.1. There is a small difference in the polarisations for each product level, indicating that some of the initial orientation is preserved during RET, however there is not complete retention. This is consistent with the need for an inelastic depolarisation channel in the fits to the time-dependence of the initial level in Chapter 4, as included in the three-level kinetic model. Closer inspection of Figure 5.1 reveals that different product states have different relative differences, implying that the MTE changes as a function of final state. This is not a subtle effect, as even the *sign* of the product orientation is seen to change in neighbouring product states. Aside from the sensitivity to the rotational level and spectroscopic branch probed, this shows that the amount of the initial orientation transferred depends on the the final product rotational level and hence rotational parity.

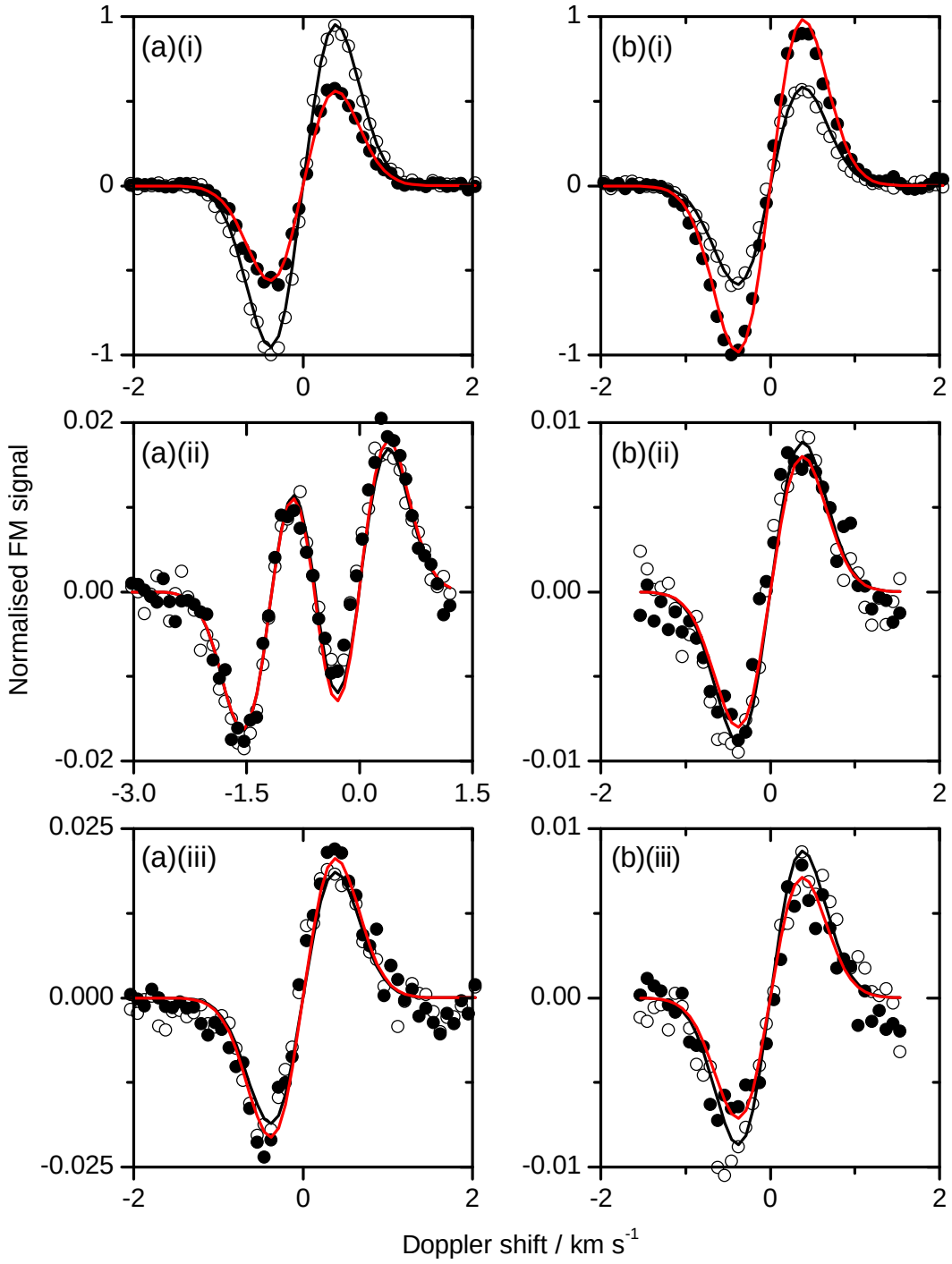

Figure 5.1 – CN($A^2\Pi$)+Ar stimulated emission FM Doppler profiles for preparing (a) the j= 6.5 F_1e initial level on the $R_1(5.5)$ transition and (b) the j = 10.5 F_2f initial level on the $P_2(11.5)$ transition. For the j= 6.5 F_1e initial level, the probed final levels are (a)(i) the initial level probed on the $R_1(5.5)$ transition, (a)(ii) the j = 6.5 F_2f level (Δj = 0) probed on the $R_2(5.5)$ + $^RQ_{21}(6.5)$ transition, (a)(iii) the j = 5.5 F_2f level (Δj = -1) probed on the $P_2(6.5)$ transition. For the j = 10.5 F_2f initial level, the probed final levels are (b)(i) the initial level probed on the $P_2(11.5)$ transition, (b)(ii) the j = 10.5 F_1e level (Δj = 0) probed on the $R_1(9.5)$ line, and (b)(iii) the j = 9.5 F_1e level (Δj = -1) probed on the $R_1(8.5)$ transition. The final levels shown involve

spin-orbit and Λ-doublet changing transitions. Each profile is a 100 ns average slice at early times (for representaiton). Open points are co-rotating, filled points counter-rotating and the solid lines are fits to the data, as outlined in Section 5.3.

Figure 5.2 shows representative data and fits to Equation 4.23 and Equation 4.28 for both initial levels and to Equation 5.1 and Equation 5.3 for a pair of product levels; these are the kinetic traces processed from the spectra in Figure 5.5 for a single set of experimental measurements (j = 6.5 F_1e and j =10.5 F_2f; Δj = 0 and -1, $F\varepsilon$-changing). The initial population decays rapidly and to non-zero values at long times, with a shorter decay time for the lower rotational level, consistent with the behaviour in Chapter 4. As population is removed from the initial level, it transfers to the product levels, with rising edges typically between t = 0 – 300 ns that are well-represented by the single exponential function in Equation 5.1. The particular product population traces shown in Figure 5.2 are similar in magnitude and growth rate, indicating similar state-to-state population transfer rates. As time proceeds, the transferred population is removed from the product levels by subsequent collisions. The product level population decay is not incorporated into the kinetic analysis (see Section 5.3), and so for visual clarity has been omitted from Figure 5.2.

The lower panels of Figure 5.2 show the initial and product level orientation kinetic traces and fits to Equation 3.28 and Equation 5.3. The initial level depolarisation has been discussed in detail in Chapter 4 and is accurately reproduced by the three-level kinetic model. The initial orientation at t = 0 is well-defined and as time progresses it is removed by both elastic and inelastic collisions. Figure 5.2 clearly shows that some of the initial orientation is collisionally transferred during RET to the probed product levels, and is then removed *via* subsequent collisions. To determine the amount of orientation transferred in a single collision, the product orientation traces are fitted to a single exponential decay (Equation 5.3) at early times, where approximately one to three RET collisions have occurred. The fit is then extrapolated back to t = 0, as explained in Section 5.3. The transferred orientation exhibits a striking product state (Δj) dependence, both in magnitude and sign. For example, more orientation has been transferred to the Δj = -1 product level than the Δj = 0 level in Figure 5.2(b). Moreover, in Figure 5.2(a), as well as a difference in magnitude, the Δj = 0 transferred orientation has clearly changed *sign*, meaning that the product orientation has the opposite handedness to that of the original level. This is the same manifestation seen in Figure

5.1 for a single average time of 0 – 100 ns, now shown as a function of delay time.

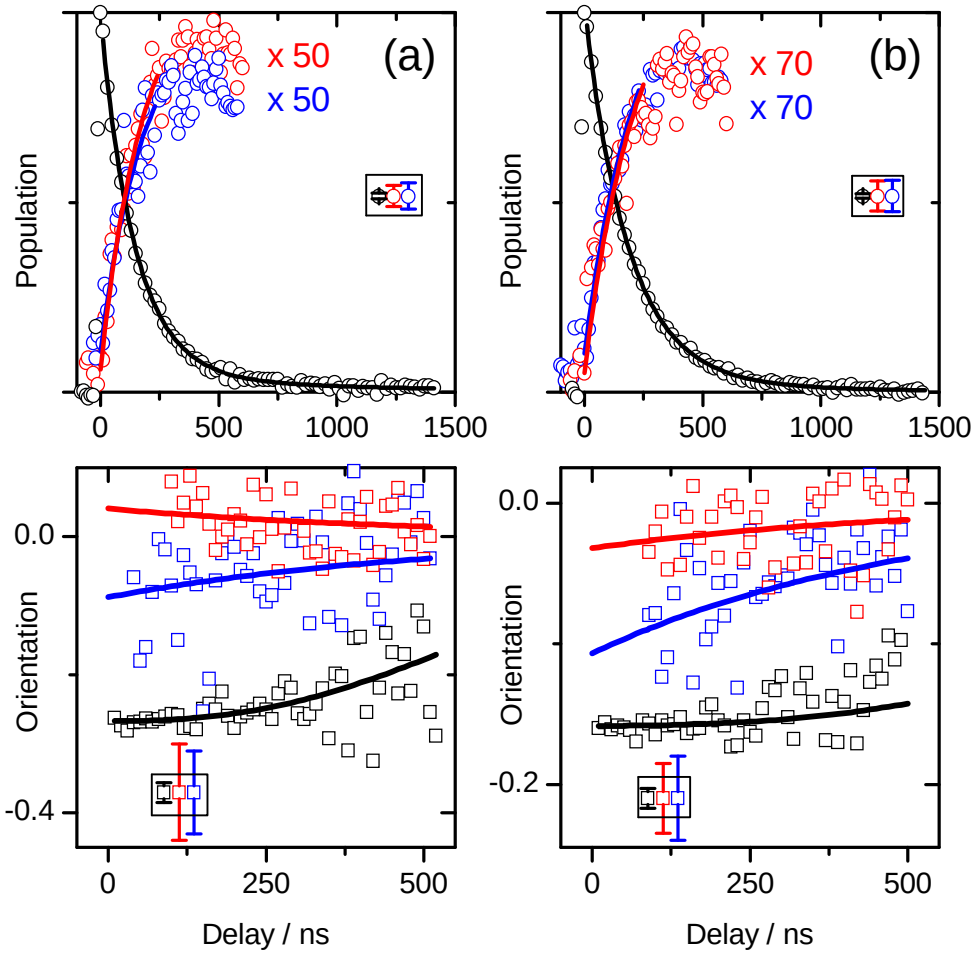

Figure 5.2 – Kinetic traces of the population (top panels), scaled as shown for the transfer levels, and orientation (lower panels) for preparing the (a) j = 6.5 F_1e and (b) j = 10.5 F_2f initial levels. The data points are 10 ns averages of the direct line (black), Δj = 0 Fε-changing (red) and Δj = -1 Fε-changing (blue) transitions, which are parity-changing and parity-conserving, respectively. The solid lines are fits to the data according to the kinetic scheme outlined in the text, extrapolated to t = 0 ns for the transfer level orientation. These traces are for a single set of experimental measurements, i.e. not an average of multiple scans. Representative average 2σ error bars are displayed within the inset of each panel. Error bars for individual data points have been omitted for visual clarity.

As outlined in Section 5.3 above, the individual rate constants for RET and MTEs were found from each measurement, then averaged to yield $k^{(0)}_{j\to j'}$ and $E^{(1)}(j,j')$, along with with the standard errors of the mean. These are shown in Table 5.3, Figure 5.3 and Figure 5.4 for the initial states j = 6.5 F_1e and j = 10.5 F_2f.

Table 5.3 – Measured average state-to-state population transfer rate constants, $k^{(0)}_{j\to j'}$, and multipole transfer efficiencies, $E^{(1)}(j,j')$, for CN($A^2\Pi$, v = 4)+Ar, j = 6.5 F_1e and j = 10.5 F_2f to j' = j + Δj, for Fε-conserving and Fε-changing transitions. Uncertainties are the standard error of the mean.

Δj	$k^{(0)}_{j\to j'}$ / 10^{-11} cm^3 s^{-1}		$E^{(1)}(j,j')$	
	Conserving	Changing	Conserving	Changing
j = 6.5 F_1e				
-4	1.39 ± 0.05	0.50 ± 0.06	0.27 ± 0.03	-0.30 ± 0.06
-3	1.73 ± 0.11	0.80 ± 0.07	0.09 ± 0.01	0.24 ± 0.04
-2	3.35 ± 0.34	0.69 ± 0.06	0.43 ± 0.03	-0.23 ± 0.05
-1	2.55 ± 0.13	0.93 ± 0.06	0.21 ± 0.02	0.33 ± 0.02
0	-	0.76 ± 0.07	-	-0.23 ± 0.02
+1	3.07 ± 0.19	0.89 ± 0.10	0.28 ± 0.02	0.40 ± 0.05
+2	3.23 ± 0.13	0.77 ± 0.07	0.37 ± 0.04	-0.15 ± 0.01
+3	2.74 ± 0.15	-	0.29 ± 0.03	-
j = 10.5 F_2f				
-4	0.50 ± 0.09	0.27 ± 0.03	0.63 ± 0.18	-0.03 ± 0.05
-3	0.68 ± 0.09	0.33 ± 0.04	0.47 ± 0.11	0.19 ± 0.06
-2	1.82 ± 0.15	0.40 ± 0.03	0.94 ± 0.11	-0.05 ± 0.07
-1	1.95 ± 0.21	0.47 ± 0.02	0.88 ± 0.7	0.39 ± 0.07
0	-	0.53 ± 0.03	-	0.13 ± 0.06
+1	1.94 ± 0.14	1.15 ± 0.05	0.85 ± 0.07	0.59 ± 0.07
+2	-[a]	0.75 ± 0.07	-[a]	-0.06 ± 0.08
+3	0.92 ± 0.05	0.39 ± 0.04	0.73 ± 0.13	0.21 ± 0.14
+4	0.29 ± 0.04	0.29 ± 0.04	0.23 ± 0.15	0.16 ± 0.05
+5	-	0.24 ± 0.03	-	-0.17 ± 0.07

[a]*The values for Δj = +2 from j = 10.5 F_2f are not included, as they are from a bad data set.*

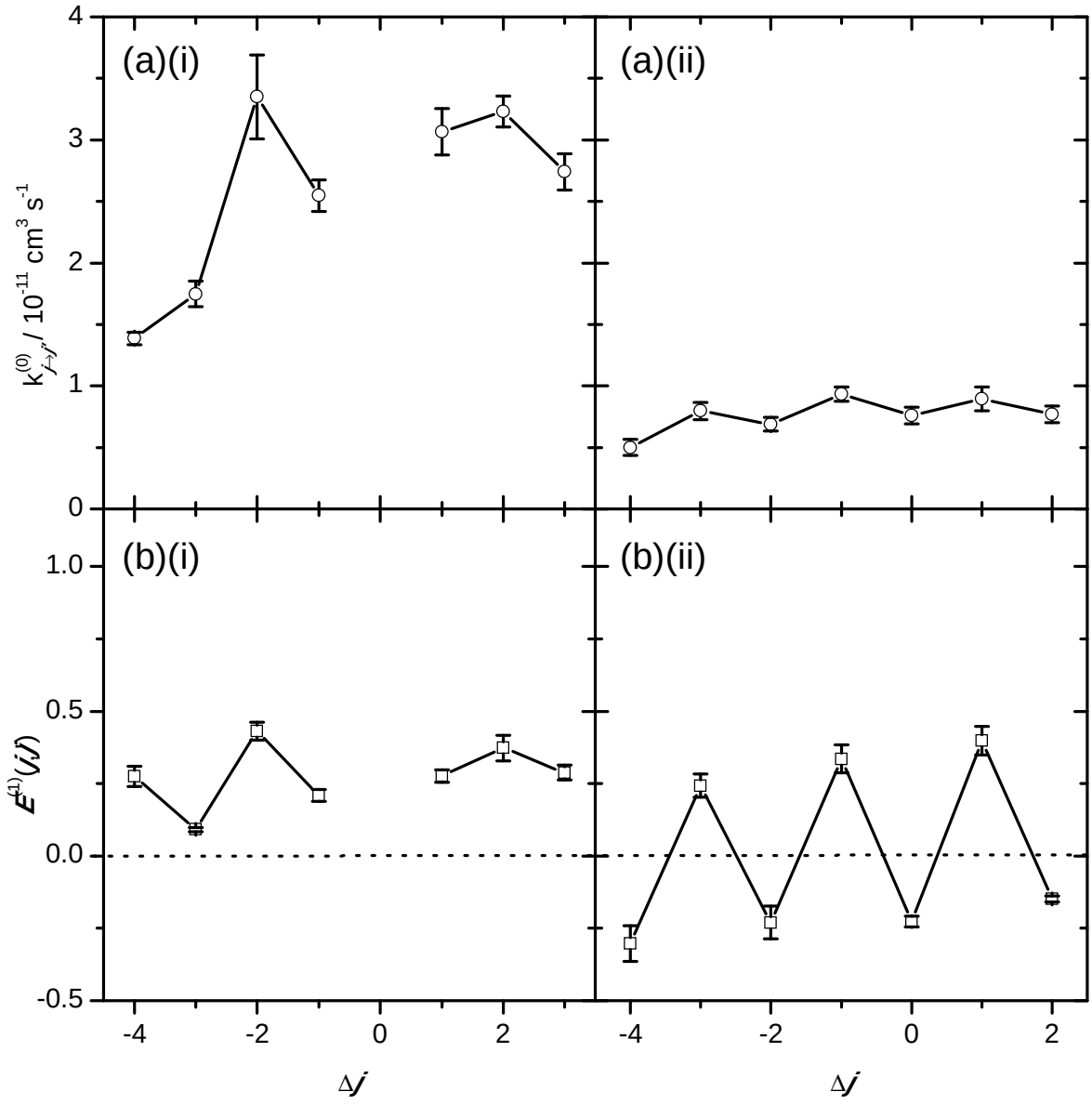

Figure 5.3 – (a) Bimolecular rate constants, $k^{(0)}_{j\to j'}$, for the transfer of population from the j = 6.5 F_1e level. (i) Fε-conserving collisions to j´F_1e levels and (ii) Fε-changing collisions to j´F_2f levels, as a function of Δj = j´- j. (b)(i) and (b)(ii) The orientation MTE, $E^{(1)}(j,j')$, for the same transitions. Data points are averages of 4 – 5 experimental measurements together with the standard error of the mean. A dotted line marks where $E^{(1)}(j,j') = 0$.

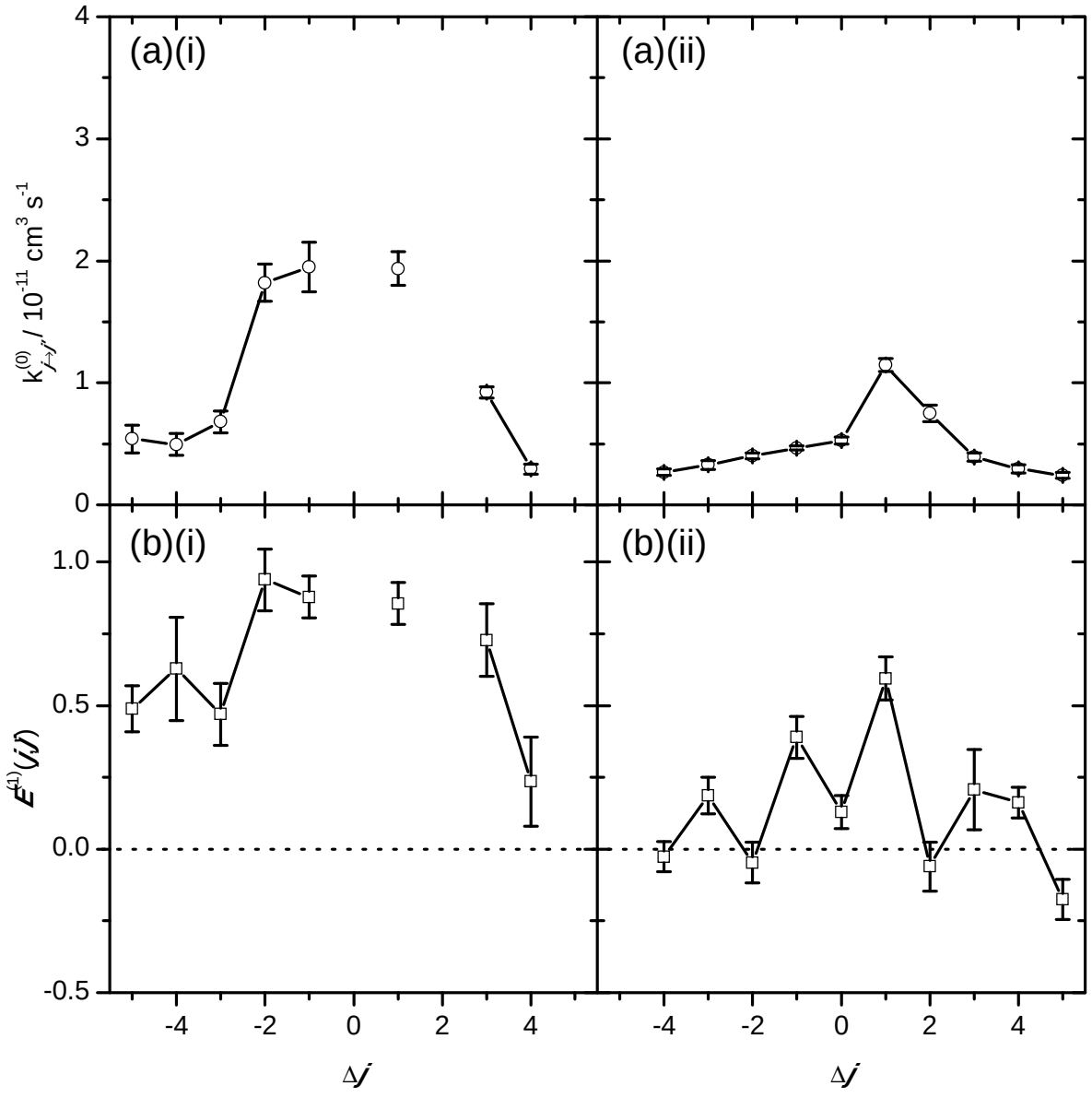

Figure 5.4 – (a) Bimolecular rate constants, $k^{(0)}_{j\to j'}$, for the transfer of population from the j = 10.5 F_2f level. (i) Fε-conserving collisions to j´ F_2f levels and (ii) Fε-changing collisions to j´ F_1e levels as a function of $\Delta j = j' - j$. (b)(i) and (b)(ii) The orientation MTE, $E^{(1)}(j, j')$, for the same transitions. Data points are averages of 4 – 5 experimental measurements together with the standard error of the mean. A dotted line marks where $E^{(1)}(j, j') = 0$.

Evident from Figure 5.3 and Figure 5.4 are substantial alternations in $k^{(0)}_{j\to j'}$ with even/odd-Δj that are superimposed on a 'volcano'-type effect of decreasing magnitude with increasing Δj. The rate constants are typically slightly larger for transfer out of j = 6.5 F_1e. The $F\varepsilon$-conserving transitions have larger state-to-state RET rate constants

relative to a smooth trend than those for the odd-Δj $F\varepsilon$-conserving transitions. The opposite is true for the $F\varepsilon$-changing transitions, where odd-Δj are favoured and the oscillations are hence the opposite phase to the $F\varepsilon$-conserving transitions. This Δj-alternation reflects the preferrential conservation of total rotational parity: transfer between states of the same rotational parity is favoured over transfer that involves a change in rotational parity. There is also a general preference for spin-orbit conservation, with the rate constants for spin-orbit changing transfer being typically 1/4 – 1/3 the magnitude of the conserving transitions.

Similarly, turning to the orientation MTEs, there is stronger conservation of the initial orientation for spin-orbit conserving transitions compared to spin-orbit changing, with this propensity being more pronounced for the j = 10.5 F_2f initial state. The most striking observation though is the strong oscillations in the state-to-state MTEs as a function of Δj, which like $k^{(0)}_{j\rightarrow j'}$, depend on the rotational parity of the product level. In general, transfer that conserves the rotational parity also conserves the initially prepared orientation and results in positive MTEs, although these are less than unity reflecting some degree of depolarisation. Conversely, transfer that changes the rotational parity generally results in MTEs that are considerably smaller in magnitude, or even *negative*. This is a surprising observation, as it means single collisions in an isotropic sample prepared with an initial LAB-frame sense of rotation, are found to result in product states that are rotating with the opposite LAB-frame sense of rotation for specific combinations of the initial and final states. Overall similar behaviour is seen for both the j = 6.5 F_1e and j = 10.5 F_2f initial levels, although the lower initial j has a deeper modulation to the oscillations.

5.4.2 QS Calculations

The collaboration with the groups of Profs. Paul J. Dagdigian (Johns Hopkins University) and Millard H. Alexander (University of Maryland) is continued in this chapter for the state-to-state RET and polarisation transfer in collisions of CN($A^2\Pi$) with Ar. Complimentary exact QS calculations were performed separate to the experiments on the new Bennett-Kłos set of *ab initio* CN($A^2\Pi$)-Ar PESs that were outlined in Section 4.5.4.

The QS theory has been introduced in detail in Section 1.6.1. Energy-dependent state-to-state tensor cross-sections were computed for CN($A^2\Pi$, v = 4)+Ar for transitions out of the j = 6.5 F_1e and j = 10.5 F_2f initial levels. Close-coupling calculations were carried out with the HIBRIDON suite of programs.[53, 301] The state-to-state tensor cross-section of rank K, $\sigma^{(K)}_{jF\varepsilon\rightarrow j'F'\varepsilon'}$, for molecules in a $^2\Pi$ electronic state is given by Equation 1.55.[53, 55, 56] The K = 0 tensor cross-sections, $\sigma^{(0)}_{j\rightarrow j'}$, are related to the integral cross-sections *via* Equation 1.56.[10] In the QS calculations, care was taken to include a sufficient number of both energetically closed channels and partial waves to ensure convergence of the cross-sections. At the highest energies considered (2000 cm^{-1}), the rotational basis included all levels with $j \leq 25.5$, and the scattering calculations included all total angular momenta $J \leq 400.5$. To calculate the thermal rate constants, the cross-sections were computed over a grid of collision energies, up to total energies of 2000 cm^{-1} and averaged over a room-temperature (T = 298 K) Maxwell-Boltzmann distribution of relative velocities according to Equation 1.57.[328]

The computed energy-dependent K = 0 and K = 1 tensor cross-sections are presented in Figure 5.5 for several transitions out of the j = 10.5 F_2f initial level to $|\Delta j| \leq 2$ for all fine-structure and Λ-doublet levels. Figure 5.5(a) and Figure 5.5(c) reveal that the K = 0 tensor cross-sections for exoergic transitions have a negative collision energy dependence, being large at low collision energies and decreasing with increasing collision energy. This behaviour is similar to that for the CN($A^2\Pi$)+Ar elastic depolarisation cross-sections in Section 4.5.4,[296] although the collision energy dependence is larger for the elastic depolarisation cross-sections. The endoergic cross-sections in Figure 5.5(a), i.e. Δj = +1 and +2, grow rapidly from their respective energy thresholds. The fine-structure conserving K = 1 tensor cross-sections in Figure 5.5(b) exhibit similar collision energy dependences and magnitudes to the corresponding K = 0 tensor cross-sections in Figure 5.5(a). In contrast, the fine-structure changing K = 1 tensor cross-sections in Figure 5.5(d) show different behaviours to the corresponding K = 0 tensor cross-sections in Figure 5.5(c). The K = 1 cross-section for Δj = +1 has a much smaller magnitude than but a similar collision energy dependence to the corresponding K = 0 cross-section. The K = 1 cross-section for the Δj = –1 transition is relatively small and has a weak collision energy dependence. The even-Δj (Δj = 0 and -2) fine-structure changing cross-sections for K = 1 have a very different collision energy

dependence to the corresponding odd-Δj transitions and are mainly negative. Recall that the $K > 0$ tensor cross-sections may be positive or negative.

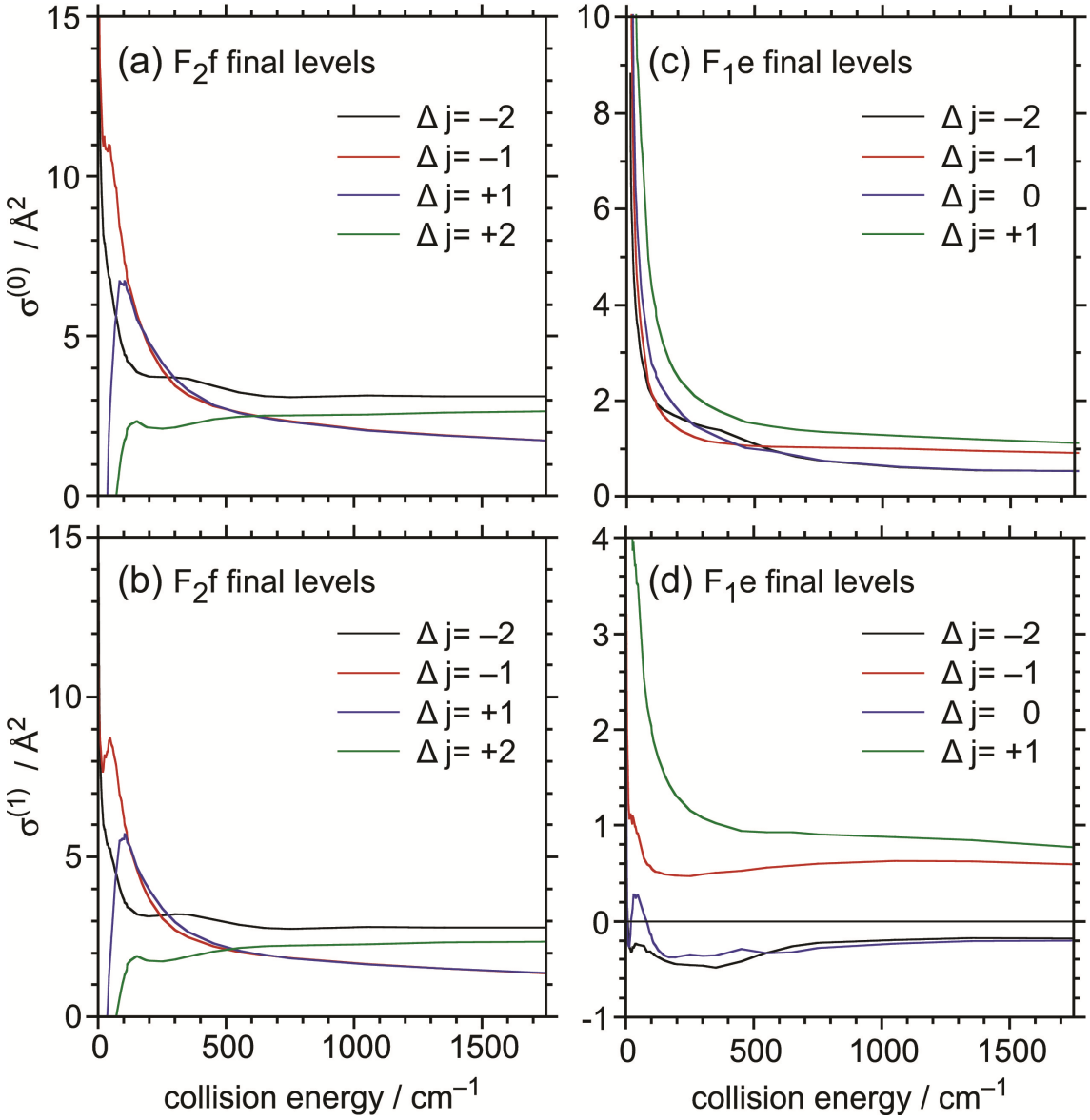

Figure 5.5 – Computed state-to-state tensor cross-sections for transitions out of the j = 10.5 F_2f initial level in collisions of CN($A^2\Pi$, v=4)+Ar as a function of the collision energy. (a) K = 0 tensor cross-sections to F_2f final levels, (b) K = 1 tensor cross-sections to F_2f final levels, (c) K = 0 tensor cross-sections to F_1e final levels, (d) K = 1 tensor cross-sections to F_1e final levels.

The state-to-state rate constants, $k^{(0)}_{j\to j'}$, and MTEs, $E^{(1)}(j, j')$, were calculated by thermally averaging the state-to-state tensor cross-sections.[328] These computed quantities are given in Table 5.4 and plotted along with the experimental results from Section 5.4.1 in Figure 5.6 and Figure 5.7, respectively. There is generally excellent, near-quantitative agreement between the experimental measurements and QS

predictions, both in overall magnitude and state-to-state propensities for $k^{(0)}_{j\to j'}$ and $E^{(1)}(j, j')$. All the observed qualitative trends are accurately reproduced by the theory, from the preference of spin-orbit conservation and the 'volcano' effect of rate constants, to, more importantly, the striking even/odd-Δj alternations in both $k^{(0)}_{j\to j'}$ and $E^{(1)}(j, j')$ that seem to depend sensitively on the rotational parity of the final state. Furthermore, the distinct change in handedness (*sign*) of product orientation in the parity-changing $F\varepsilon$-changing transitions is clearly resolved in the calculations. There are some discrepancies between experiment and theory, particularly for the positive Δj transfer from j = 6.5 F_1e, which are addressed in Section 5.4.3. To help rationalise all the results, the partial K = 1 and K = 0 transfer cross-sections (cross-sections as a function of total-J) and partial MTEs ($\sigma^{(0)}_{j\to j'}/\sigma^{(1)}_{j\to j'}$) for selected transitions out of j = 10.5 F_2f were calculated. These are presented and discussed in Section 4.5.3.

Table 5.4 – QS state-to-state population transfer rate constants, $k^{(0)}_{j\to j'}$, and orientation MTEs, $E^{(1)}(j,j')$, for CN($A^2\Pi$, v = 4)+Ar, j = 6.5 F_1e and j = 10.5 F_2f to j' = j + Δj, for both Fε-conserving and Fε-changing transitions.

Δj	$k^{(0)}_{j\to j'}$ / 10^{-11} cm^3 s^{-1}		$E^{(1)}(j,j')$	
	Conserving	Changing	Conserving	Changing
j = 6.5 F_1e				
-4	1.61	0.800	0.33	-0.24
-3	1.97	0.920	0.04	0.31
-2	3.16	0.840	0.65	-0.31
-1	2.73	1.10	0.29	0.58
0	-	0.690	-	-0.43
+1	2.41	0.640	0.28	0.51
+2	1.85	0.560	0.70	-0.40
+3	1.42	-	0.10	-
j = 10.5 F_2f				
-4	1.13	0.713	0.77	-0.26
-3	1.59	0.523	0.69	0.31
-2	2.36	0.845	0.85	-0.27
-1	2.55	0.860	0.79	0.41
0	-	0.910	-	-0.19
+1	2.27	1.44	0.82	0.56
+2	1.37	0.831	0.84	-0.03
+3	0.929	0.495	0.77	0.13
+4	0.348	0.375	0.72	-0.17
+5	-	0.183	-	-0.27

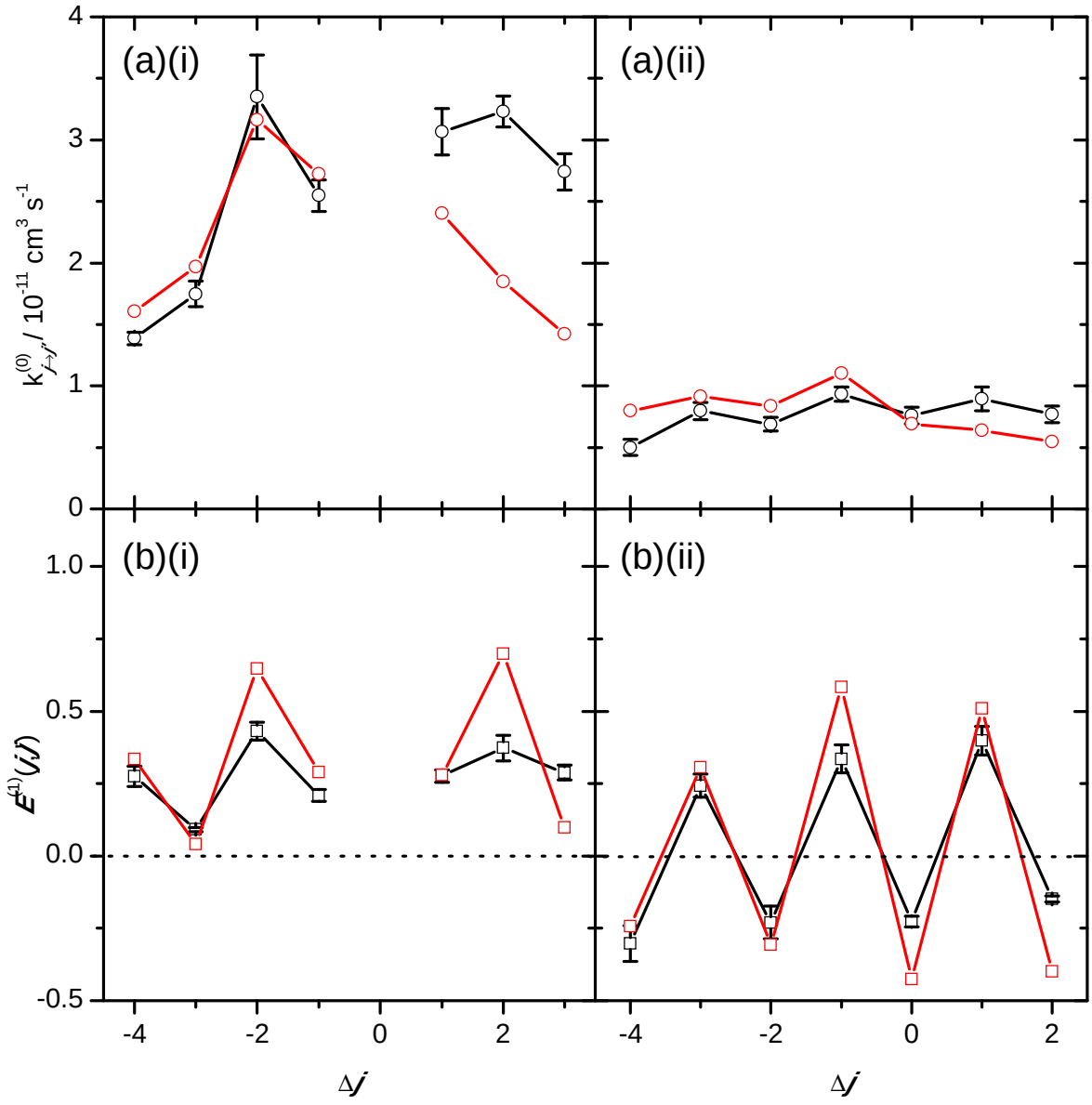

Figure 5.6 – (a) Bimolecular rate constants (circles), $k^{(0)}_{j\to j'}$, for the transfer of population from the j = 6.5 F_1e level. (i) Fε-conserving collisions to j´F_1e levels and (ii) Fε-changing collisions to j´F_2f levels, as a function of Δj = j´- j. (b)(i) and (b)(ii) The orientation MTEs (squares), $E^{(1)}(j,j')$, for the same transitions. Red data points are predictions from the full QS calculations using the B-K PESs. Black data points are averages of 4 – 5 experimental measurements together with the standard error of the mean from Section 4.5.1. A dotted line marks where $E^{(1)}(j,j') = 0$.

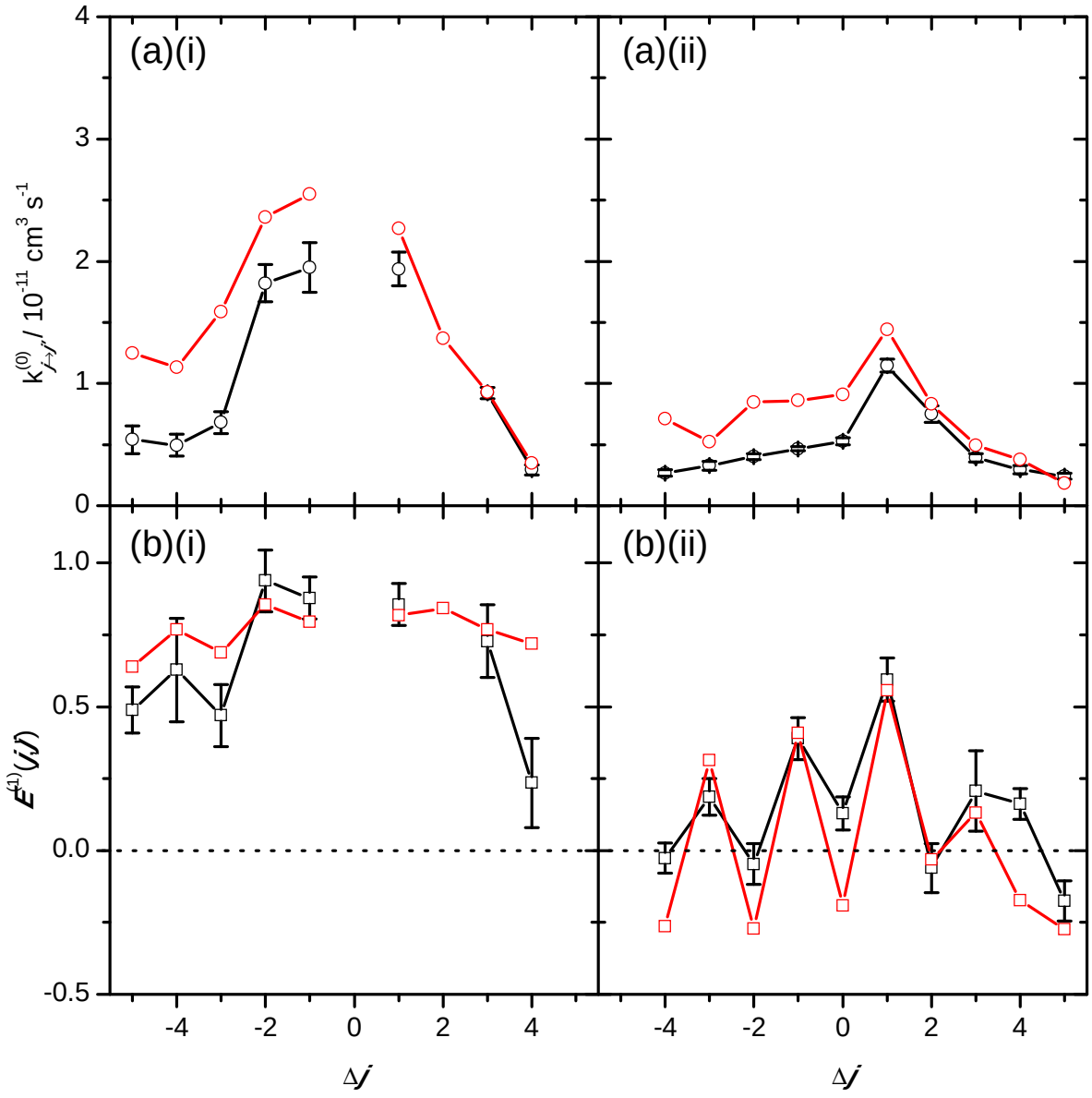

Figure 5.7 – (a) Bimolecular rate constants (circles), $k^{(0)}_{j\to j'}$, for the transfer of population from the j = 10.5 F_2f level. (i) Fε-conserving collisions to j´F_2f levels and (ii) Fε-changing collisions to j´F_1e levels, as a function of $\Delta j = j' - j$. (b)(i) and (b)(ii) The orientation MTEs (squares), $E^{(1)}(j,j')$, for the same transitions. Red data points are predictions from the full QS calculations using the B-K PESs. Black data points are averages of 4 – 5 experimental measurements together with the standard error of the mean from Section 4.5.1. A dotted line marks where $E^{(1)}(j,j') = 0$.

5.4.3 Discussion

Population transfer

The state-to-state population transfer rate constants, $k^{(0)}_{j\to j'}$, are discussed here, followed by the orientation MTEs. The results highlighted significant alternations in $k^{(0)}_{j\to j'}$ with even/odd-Δj over a smoothly declining volcano plot of rate constants arising from energy gap laws and linear-to-angular momentum restrictions.[23] The $F\varepsilon$-conserving transitions favour even-Δj transitions, whilst the $k^{(0)}_{j\to j'}$ alternations for $F\varepsilon$-changing transfer are opposite in phase, favouring odd-Δj. This Δj-alternation reflects the preferrential conservation of total rotational parity during RET, which is a general phenomenon for near-homonuclear systems,[5, 76, 318] having been previously observed in collisions of CN($A^2\Pi$) with Ar and He.[184, 197, 304] There is excellent agreement between the results from this work and the relative state-to-state RET measurements of Dagdigian, Alexander and co-workers for CN($A^2\Pi$, v = 3)+Ar, starting from the j = 6.5 F_1e level.[190] This confirms the observations to be a general feature of the CN($A^2\Pi$)+Ar scattering dynamics. The previous FMS $k^{(0)}_{j\to j'}$ rate constants from Ballingall *et al*. also agree well with this work, ranging between (1 – 3) × 10^{-11} cm^3 s^{-1} for $\Delta j = \pm 3$.[199]

There is excellent, near-quantitative, reproducibility between the experiment and theory in Figure 5.6 and Figure 5.7, with all the main observations in general accurately depicted. The only significant discrepencies are listed as follows. The measured rate constants shown in Figure 5.6(a)(i) for positive Δj from j = 6.5 F_1e are noticeably larger than those predicted by theory. This is believed, in part, to be an experimental artefact, the result of an accidental spectroscopic near-overlap in the pump step. The formation of the CN($A^2\Pi$-$X^2\Sigma^+$) (4,0) R-branch band head results in the R_1(5.5) and R_1(10.5) pump transitions being separated by only $\Delta\nu$ = 0.24 cm^{-1}. Under saturated pumping conditions, the full width at half maximum (FWHM) of the pump laser was previously measured to be $\Delta\nu \approx 0.5$ cm^{-1}.[64, 198] Therefore, when the pump laser is centred on the R_1(5.5) transition to prepare j = 6.5 F_1e, there is a slight, unavoidable, spectroscopic overlap with the R_1(10.5) transition, resulting in the preparation of a small unwanted population in the j = 11.5 F_1e level. RET from this accidentally prepared level is expected to be most probable for Δj = -1 – -3 $F\varepsilon$-conserving transitions, i.e. to j' = 7.5 –

9.5 F_1e, for which there is the largest disagreement between experiment and theory. Direct measurement of the j = 11.5 F_1e level when pumping j = 6.5 F_1e indicated a prepared population ~10% of the desired level. This confirms that its contribution to other observed product levels under these conditions is likely to be negligible with respect to the reported experimental errors in Section 5.4.1. The weighted contributions from the j = 11.5 F_1e level to either the experimental measurements or QS calculations could, in principle, have been subtracted from the results in Figure 5.6. However, the unoptimised nature of the accidental pump step to j = 11.5 F_1e is likely to have caused considerable fluctuations in the population and orientation of that level. A better approach therefore was to prepare a nearby, but isolated, level *via* an isolated spectroscopic transition, and perform appropriate complimentary QS calculations. This would also provide a deeper insight into the state-to-state scattering dynamics. The $P_2(11.5)$ transition preparing the j = 10.5 F_2f level was found to be ideal, being separated by >1 cm^{-1} from the nearest transition, and lying even further away from transitions that would prepare levels energetically near to j = 10.5 F_2f. Excitation on this transition was confirmed to uniquely prepare j = 10.5 F_2f.

Second, in Figure 5.7(a)(i) and Figure 5.7(a)(ii) there is a small but systematic disagreement between experiment and theory in the absolute magnitude of $k^{(0)}_{j\rightarrow j'}$ for transfer out of the j = 10.5 F_2f initial level. The calculations overstate the rate constants for nearly all of the observed final levels, consistent with the slight (~15%) over-prediction of the total population removal rate constants in Section 4.5.4. In Chapter 4, RET in CN($A^2\Pi$)+Ar was found to be extremely sensitive to the form of the PESs. Moreover, conversion of the total removal cross-sections to collision radii suggested that weak attractive forces strongly mediate the RET. The dominant attractive components of the B-K PESs are the isotropic λ = 0 and quadrupolar λ = 2 terms. The first of these influences which regions of the PES are sampled at a particular collision energy, producing subtle effects on the scattering ampitudes and product branching channels, and only terms with $\lambda \geq 1$ are capable of contributing to RET. The modest over-prediction of the rate constants in Figure 5.7 may therefore result from a slight over-estimation of the anisotropic range of the B-K PESs.

The parity-dependent even/odd-Δj alternations in the state-to-state RET rate constants seen in Figure 5.6 and Figure 5.7 are a consequence of the near-homonuclearity of the CN($A^2\Pi$)+Ar system. Collisions that conserve total rotational parity are enabled by the

even-λ components of the PES angular expansions, whilst collisions that change rotational parity result from the odd-λ components.[49, 52] In a symmetric homonuclear PES, the odd-λ terms must necessarily tend to zero. The near-symmetry of CN($A^2\Pi$)-Ar makes the PESs strongly even in character, as evident in Section 4.5.4. This gives rise to the strong propensity for conservation of the rotational parity and resulting even/odd-Δj oscillations in $k^{(0)}_{j\to j'}$. The very good agreement between experiment and theory therefore indicates that the PESs accurately reproduce the even/odd nature of the CN($A^2\Pi$)+Ar interaction.

A preference for spin-orbit conservation is also observed, with the rate constants for spin-orbit changing transfer being typically 1/4 – 1/3 the magnitude of the conserving transitions. Aside from the F_2 spin-orbit manifold being slightly higher in energy than the F_1 manifold, this behaviour again has a simple explanation through inspection of the angular expansions of the PESs. Seen in Section 4.5.4, the even-λ terms of the PESs have substantially greater magnitudes than the odd-λ terms at values of R (the separation between CN and Ar), which are accessible at thermal collision energies. This is another manifestation of the near-homonuclearity of CN and consequent head-tail symmetry of the PESs. The strong spin-orbit conservation is broadly consistent with the relative ranges of the V_{sum} and V_{dif} potentials, as demonstrated in Figure 4.32, within the Hund's case-(a) to case-(b) limits of the CN($A^2\Pi$) rotational states and non-Born limit range of thermal collision energies involved. In the pure Hund's case-(a) limit, spin-orbit conserving transitions are enabled exclusively by the V_{sum} PES, while spin-orbit changing transitions are enabled only by the V_{dif}. As the system departs from this limit, both the V_{sum} and V_{dif} potentials influence the dynamics. The role of the V_{dif} PES can be approximated from Figure 4.38, which shows the ratio of the coefficients quantifying the contributions from the λ = 2 components of the V_{sum} and V_{dif} PESs due to the departure from the Hund's case-(a) coupling limit. This shows that for the rotational levels studied, there is a small but significant contribution from V_{dif}, and so the majority of collisions are spin-orbit conserving.

In comparison to the electronically and kinematically similar NO($X^2\Pi$)+Ar system,[143, 329-331] the CN($A^2\Pi$)+Ar system has a higher probability to undergo collision-induced changes in the fine-structure label. This reflects the significance of the V_{dif} potential in the present system, again expected when comparing Figure 4.38. However, the

amplitudes of the parity-dependent oscillations in the CN($A^2\Pi$)+Ar final state populations are significantly less than for NO($X^2\Pi$)+Ar,[324, 332] indicating greater head-tail asymmetry for CN($A^2\Pi$)-Ar. Furthermore, for NO($X^2\Pi$), Alexander predicted a propensity for preferrential RET to the A'' Λ-doublet state for many rotational levels in the scattered products, even with initial equal populations of the two precollision Λ-doublet components.[324] This propensity was attributed to interference between scattered paths on the two adiabatic NO($X^2\Pi$)-Ar PESs of A' and A'' symmetry for final NO($X^2\Pi$) rotational states that have Hund's case-(b) character, where the molecular wavefunction is a mixture of $\Omega = 1/2$ and $\Omega = 1/2$ functions.[52, 143] This effect was observed by Dagdigian and co-workers for high-N collisions of CN($A^2\Pi$) with Ar, which is strongly Hund's case-(b). In this work, the low-j levels studied are close to the Hund's case-(a) limit. For these molecules, no such Λ-doublet propensity is expected, and so there should be equal population of both product Λ-doublet components. If both the initial and final states are well described in Hund's case-(a), then as seen in Equation 1.48, the magnitude of the coupling potential for spin-orbit conserving and changing transitions is symmetric with respect to changing the symmetry index, ε, of both the initial and final states. Therefore, the cross-sections for $e \rightarrow e$ and $f \rightarrow f$ transitions will be identical, and so similarly will the cross-sections for $e \rightarrow f$ and $f \rightarrow e$. The observed preference for $F\varepsilon$-conserving transfer in Figure 5.6 and Figure 5.7 should therefore only result from the spin-orbit propensity and not from any preferred Λ-doublet transition. Unfortunately, the pure Λ-doublet collisions were not measured in this study, as explained in Section 5.1, precluding futher assessment of the Λ-doublets.

Polarisation Transfer

Looking at the measured orientation MTEs in Figure 5.3 and Figure 5.4, there is overall similar behaviour for both the $j = 6.5$ F_1e and $j = 10.5$ F_2f initial levels, reaffirming the observations to be a general feature of the CN($A^2\Pi$)+Ar scattering dynamics. The trends in the MTEs follow closely those of the observed state-to-state RET rate constants. Aside from spin-orbit conserving transitions favouring the retention of initial orientation, being more pronounced for $j = 10.5$ F_2f initial state, the most striking feature is the strong oscillations in the state-to-state MTEs as a function of Δj. These oscillations reflect the preferred conservation of rotational parity in the final level. In general, parity-conserving transitions also conserve the initial orientation, resulting in

positve MTEs, whereas parity-changing transitions result in MTEs that are considerably smaller in magnitude, or even negative. That is, specific product molecules end up rotating with the opposite sense compared to the prepared rotation within an isotropic collision environment. These results suggest that the parity-dependent oscillations in the MTE as observed by Norman and Field,[105] for a small range of initial and product states in CaF($A^2\Pi$)+Ar, are in fact a fundamental feature of $^2\Pi$+Rg collisions.

The MTEs are often less than unity, supporting the conclusions from the previous chapter of inelastic depolarisation being a prominent collisional mechanism. In general, more orientation is preserved in transfer from j = 10.5 F_2f, where the average MTE across the range of product levels probed approaches unity, than from j = 6.5 F_1e, with an average MTE of ~0.5, respectievly. This fits with conservation of angular momentum arguments conveyed in Chapter 4, where a monotonic decline of the elastic depolarisation rate constants with increasing j, for the QS predictions at least, was attributed to the rotor being harder to tilt (reorient) the faster it rotates.

The results are consistent with an unrestricted change in m during inelastic transfer, contrary to the previous findings of McCaffery and co-workers for kinematically comparable rare-earth metal dimer systems,[55, 325-327] but similar to the $C_2H_2(\tilde{X}^1\Sigma_g^+, v_2 = 1, j)$+Ar and self-collision systems measured by Zacharias and co-workers.[80-82, 108] To explain their findings, Zacharias and co-workers proposed a mechanism, within an isotropic environment, where collisions perpendicular to the plane of rotation effectively destroy the polarisation, whilst collisions in the plane of rotation promote RET without loss of polarisation, i.e. sampling of particular classical impact parameters dictates the observed dynamics.[80-82, 108] The orientation MTEs from this study are further comparable to the CN($A^2\Pi$)+Ar alignment MTEs from Ballingall *et al.* measured using the previous FMS set-up.[199] There, conversion of the MTEs, $E^{(2)}(j,j')$ ≈ 0.55 – 0.32 for Δj = ±3, to classical tilt angles encouraged an interpretation of polarisation transfer within a simple scattering model, where small Δj transitions result from strong forward scattering through small scattering angles at large impact parameters.

Figure 5.6 and Figure 5.7 exhibit excellent agreement between experiment and theory in both the qualitative trends and the quantitative values of the MTEs. Furthermore, the striking parity-dependent alternations of the MTEs were correctly predicted in the

earlier theory papers of Alexander and co-workers.[53, 57] This encourages a closer look into the current calculations. Figure 5.5(a) and Figure 5.5(b) show the computed collision energy dependent $K = 0$ and $K = 1$ tensor cross-sections for parity-conserving and parity-changing transitions to a range of $F\varepsilon$-conserving product states from the $j = 10.5$ F_2f initial level. The collision energy dependences of the $K = 0$ and $K = 1$ spin-orbit conserving cross-sections have very similar forms, although the absolute magnitudes of the $K = 0$ cross-sections are slightly larger. This implies that the MTE is mostly constant and near-unity as a function of collision energy for these transitions, with no significant variation with the parity of the final state, consistent with the associated thermally averaged MTEs displayed in Figure 5.7. Conversly, there are much more significant differences in the relative $K = 0$ and $K = 1$ cross-sections for the $F\varepsilon$-changing transitions in Figure 5.5(c) and Figure 5.5(d). There, the $K = 0$ and $K = 1$ collision energy dependences for the parity-conserving final states have very similar forms, although with a substantially smaller magnitude for $K = 1$. Most noticeably, however, the parity-changing (even-Δj) $K = 1$ and $K = 0$ cross-sections have completely different shapes. The $K = 1$ cross-sections for these transitions are predominantly nearly constant and negative across the range of collision energies, implying that their MTEs are negative and largely independent of collision energy, beyond a limited range of energies that lie below the thermal average. There is no clear evidence that the orientation sign change for the $F\varepsilon$- and parity-changing cross-sections are mediated by any special collision energy range, for example trapping or orbiting collisions within the attractive range of the PESs. The orientation sign-changing behaviour instead appears to be relatively independent of collision energy for each particular product state.

There are tangible differences between the $F\varepsilon$-conserving and $F\varepsilon$-changing transitions. Notably, the MTE alternations with Δj are deeper for the $F\varepsilon$-changing collisions and even change sign. For the low-j values studied here, CN($A^2\Pi$) is relatively close to the Hund's case-(a) coupling limit, meaning that spin-orbit conserving and changing transfer is dominated by the V_{sum} and V_{dif} PESs, as discussed earlier with respect to RET.[52] Since the parity-conserving and parity-changing transitions result predominantly from the even-λ and odd-λ terms in the PES angular expansions respectively, this must be the result of the difference in the even/odd character between the V_{sum} and V_{dif} potentials. The V_{dif} PES has an inherently more even character than the V_{sum}, as by

symmetry it lacks the lowest-order (λ = 1) odd term in the angular expansions. This is clear from Section 4.5.4.

The dramatic change in sign of the orientation for a molecule rotating initially in j = 10.5 F_2f necessitates a large transfer of angular momentum during the collision. An important consideration is whether the parity-conserving and parity-changing transfer arise from collisions at different classical impact parameters, as hinted at in previous studies of inelastic depolarisation.[80-82, 108, 199] For example, could a large impact parameter '*glancing*' collision preserve the orientation for the parity-conserving transfer, whereas a low impact parameter '*hard*' collision reorient the polarisation for the parity-changing transfer? Insight into the contributing range of impact parameters (b) and atom-diatom separations (R) can be gained from examining the tensor cross-sections as a function of total-J (total angular momentum), termed the *partial tensor opacity functions*. [53, 57] The tensor cross-sections, $\sigma^{(K)}_{jF\varepsilon\to J'F'\varepsilon'}$, are related to the partial tensor cross-sections, $\sigma^{(K)}_{jF\varepsilon\to J'F'\varepsilon'}(J)$, *via* Equation 5.5, i.e. they are the sum of the cross-sections over all possible J or b, since the two are related through Equation 1.28 and Equation 1.29. Figure 5.8(a) displays the computed K = 0 and K = 1 partial tensor opacity functions for $F\varepsilon$-changing transfer from j = 10.5 F_2f to j' = 10.5 F_1e (Δj = 0) and j' = 9.5 F_1e (Δj = -1), which are parity-changing and parity-conserving transitions respectively, at a collision energy of 300 cm^{-1}. The conversion of J to b is shown in Table 5.5.

$$\sigma^{(K)}_{jF\varepsilon\to J'F'\varepsilon'} = \sum_J \sigma^{(K)}_{jF\varepsilon\to J'F'\varepsilon'}(J)$$

Equation 5.5

Table 5.5 – Conversion of J to b for CN($A^2\Pi$)+Ar using Equation 1.28 and Equation 1.29, where v_{rel} = 675m s^{-1} assuming a collision energy of 300 cm^{-1}.

J / $\hbar$	b / Å
0	0.00
20	1.19
40	2.39
60	3.58
80	4.78
100	5.97

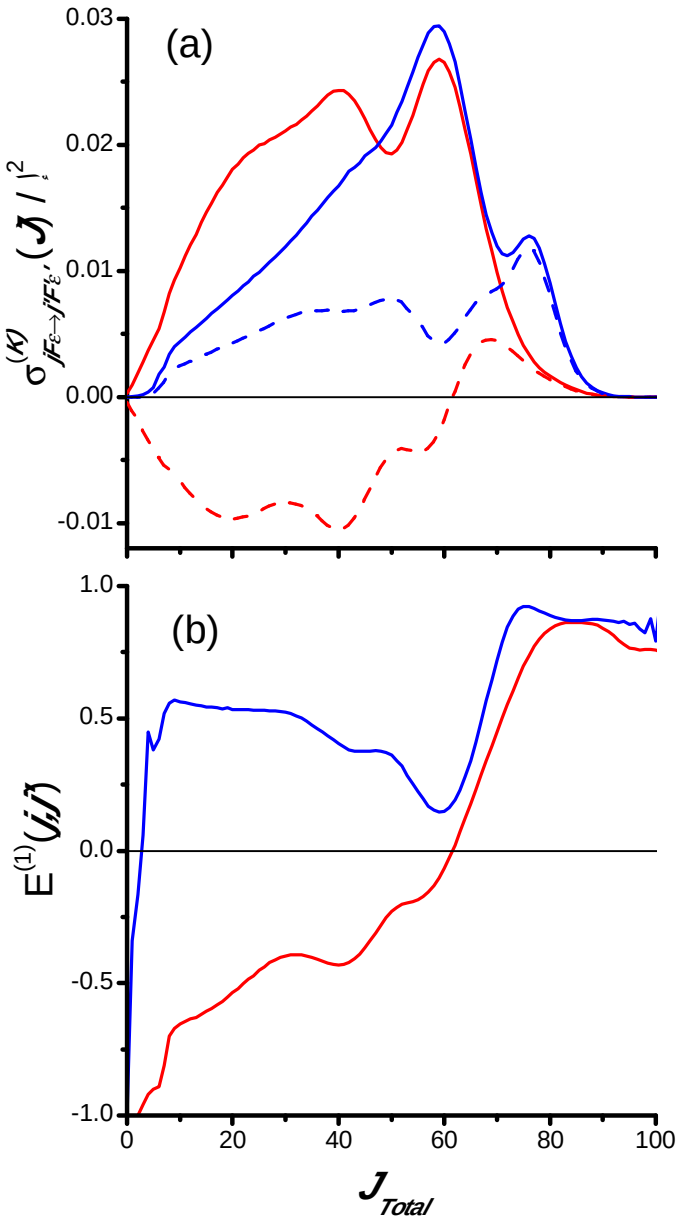

Figure 5.8 – (a) Computed partial tensor state-to-state cross sections for Fε-changing transitions from the j = 10.5 F_2f initial level for CN($A^2\Pi$,v = 4)+Ar at 300 cm^{-1} collision energy, for K = 0 (solid line) and K = 1 (dashed line) to product levels j' = 10.5 F_1e (red) and j' = 9.5 F_1e (blue), which are Δj = 0 parity-changing and Δj = -1 parity-conserving, respectively. (b) Resulting partial MTEs, $E^{(1)}(j,j') = \sigma^{(K=1)}_{jF\varepsilon\to J'F'\varepsilon'}(J)/\sigma^{(K=0)}_{jF\varepsilon\to J'F'\varepsilon'}(J)$, from j = 10.5 F_2f to j' = 10.5 F_1e (red) and j' = 9.5 F_1e (blue).

There are substantial differences between both the K = 0 and K = 1 partial tensor cross-sections for the parity-conserving and parity-changing transitions in Figure 5.8. A high-J peak (J = 70 - 80) is observed in the parity-conserving K = 0 transition that is absent for the parity-changing transition. On the other hand, the parity-changing transition

clearly has a larger K = 0 cross-section across the lower-J range (J = 0 – 50). This suggests that on average, the parity-changing collisions generally occur at lower impact parameters than the parity-conserving collisions. However, the K = 1 partial cross-sections illustrate that it is not simply this different range of contributing total-J that cause the observed polarisation oscillations. The K = 1 parity-conserving cross-section is positive for all total-J, whilst the corresponding parity-changing cross-section is negative across almost the entire range of total-J. This is evident from the partial MTEs inn Figure 5.8(b), which are the ratios of the relevant partial cross-sections from Figure 5.8(a). Across the contributing ranges of total-J for each transition, the parity-conserving MTE is positive, whilst the parity-changing MTE is almost always negative. Even at J = 50, which corresponds to a classical impact parameter of ~3 Å, near the attractive minimum of the V_{sum} potential (Section 4.5.4), the K = 0 cross-sections are almost identical, but the resulting partial MTEs are still opposite in sign. The partial cross-sections here clearly demonstrate that the dynamics of parity-conserving and parity-changing encounters must be fundamentally different for reasons other than their opacity functions alone. A major contributing factor must presumably be from the angular expansions of the PESs.

The most relevant recent work to address this problem has been the joint crossed-beam experimental measurements and theory presented by Aoiz, Brouard, Stolte and co-workers for the NO($X^2\Pi$)+Ar, He and D_2 systems.[34-36, 45, 153-158] As outlined in Section 1.7, they measured full state-to-state rotationally inelastic DCSs for transitions from a selected single initial Λ-doublet level (*e* or *f*) of the lowest j = 0.5 F_1 rotational state. Strong parity-dependent effects were observed, with remarkably different scattering-angle distributions for final states of the same j' but different parity. QS calculations were in quantitative agreement with the experimental results. Decomposition of the calculations revealed that the different scattering distributions not only arise from different partial cross-sections, but also that scattering from the same range of total-J gives rise to different DCSs for final states of different parity.[153] The parity-dependent effects observed in the NO($X^2\Pi$)+Rg and D_2 DCSs measurements were also accurately reproduced by the semi-classical QQT model (introduced in Section 1.6.1).[34, 35] To recap, this model treats the scattering as defined by classical rigid ellipse-rigid sphere kinematics, but allows for quantum interferences between paths that lead to the same final state and scattering angle arising from impacts at different points on the ellipsoidal surface, as outlined in Figure 5.9.

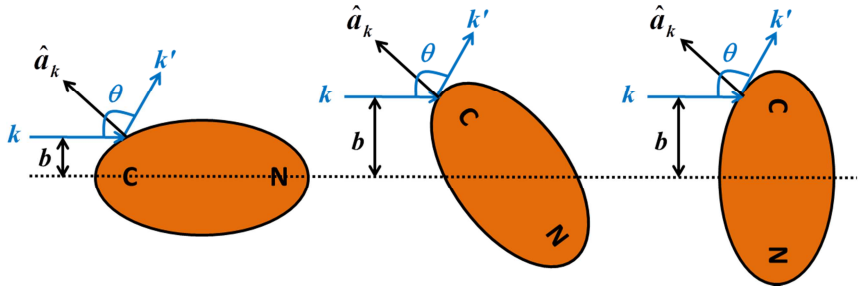

Figure 5.9 – The QQT model of different interfering scattering paths leading to the same final rotational state, j', and scattering angle, θ, arising from impacts at different points on the ellipsoidal surface. b = classical impact parameter, k = initial wavevector, k' = final wavevector, $\hat{a}_k = \frac{k'-k}{|k'-k|}$ *= kinematic apse, along which the angular momentum is conserved.*

Stolte and co-workers demonstrated that interference between trajectories from impacts at the opposite ends of the ellipse leads to parity-changing transitions, whilst interference between end-on and side-on impacts leads to parity-conserving transitions, recovering the known dependence on the even/odd angular expansions of the PESs.[154, 155, 157, 158] This interference effect may well therefore be the origin of the observed parity-dependent oscillation in the MTEs for CN(A^{2}Π)+Ar. In the QQT model, the transfer of angular momentum is essentially classical and determined by the kinematics and geometry of the collision.[28] For given initial and final states and a well-defined collision energy, the angular momentum anisotropy of the product is directly determined by the scattering angle. Experimentally observed LAB-frame *integral* alignments are different for opposite parity final-states, not because of any fundamental differences in the angular momentum transfer, but because the DCSs for the product states are different.[157, 158] Despite the differences in the nature of the observables in the NO(X^{2}Π) experiments and those presented here, the same mechanism may be responsible. In this picture of the dynamics, collisions with the kinematics required to change the sense of rotation occur at scattering angles that may result in interferences leading to the parity-changing final states, whilst those that do not significantly alter the rotational polarisation occur at scattering angles that may lead to the parity-conserving final states. If this is correct, then an extension to the QQT model might be capable of reproducing the observed MTE behaviour here when integrated over all scattering angles. This also suggests that the observed MTE oscillations should be a general property of ^{2}Π+Rg collisions, consistent with Normal and Field's observations in CaF(A^{2}Π)+Ar and the earlier predictions of Alexander and co-workers.[53, 57, 105]

Since parity-dependent oscillations in DCSs have also been observed for NO($X^2\Pi$)+D_2,[36] it is an interesting prospect whether such parity propensities manifest themselves in polarisation-resolved rotationally inelastic collisions of CN($A^2\Pi$) with molecular partners. This is investigated in the next section. Overall, it is clear that current scattering theory is capable of providing essentially near-quantitative agreement with experiment for this benchmark $^2\Pi$+Rg system.

5.4.4 Summary

The key conclusions from this section are listed below.

i. The first ever systematic experimental and theoretical investigation of state-to-state RET and polarisation transfer in CN($A^2\Pi$, v = 4, $jF\varepsilon$)+Ar has been performed.

ii. The ns-pulsed FMS cw-probe OODR technique was employed to prepare a rotational population and orientation in either j = 6.5 F_1e or j = 10.5 F_2f and monitor the collisional transfer to nearby $j'F'\varepsilon'$ product states for $\Delta j \leq |5|$ $F\varepsilon$-conserving and $F\varepsilon$-changing transitions.

iii. The initial level population and orientation time-traces were fitted to the three-level kinetic model outlined in Chapter 4 and the collisional product levels to single exponential functions in order to obtain the state-to-state RET rate constants, $k^{(0)}_{j\rightarrow j'}$, and orientation MTEs, $E^{(1)}(j, j')$.

iv. There has been continued collaboration with other research groups to perform complementary full QS calculations.

v. Typically excellent agreement exists between experiment and QS theory in both the qualitative trends and quantitative values for $k^{(0)}_{j\rightarrow j'}$ and $E^{(1)}(j, j')$.

vi. Inelastic depolarisation is shown to be a significant pathway for this collision system, consistent with the conclusions from Chapter 4.

vii. A “volcano” distribution of rate constants arises from energy-gap and linear-to-angular momentum constraints.

viii. Substantial parity-dependent even/odd-Δj alternations in $k^{(0)}_{j\rightarrow j'}$ reflect the near-symmetry of the CN($A^2\Pi$)-Ar PESs due to the near-homonuclearity of the CN molecule and the spherical nature of the partner. The interaction is described as strongly even in character, with the dominance of even-λ

components in the PES angular expansions through symmetry constraints, as seen in Section 4.5.4. Within a weak coupling limit, parity-conserving transitions are enabled by even-λ terms and parity-changing transitions by odd-λ terms.

ix. A preference for spin-orbit conservation in $k^{(0)}_{j\to j'}$ and $E^{(1)}(j, j')$ is a consequence of the relative ranges of the V_{sum} and V_{dif} PESs at thermal collision energies. At the Hund's case-(a) limit, V_{sum} controls spin-orbit conservation and V_{dif} controls spin-orbit transfer. As the system departs from this limit, both PESs mediate fine-structure collisions.

x. Striking oscillations in $E^{(1)}(j, j')$ as a function of Δj are again a manifestation of the rotational parity propensity. Parity-conserving collisions generally also conserve the initially prepared orientation, resulting in positve MTEs, although these are often less than unity, due to inelastic depolarisation. Parity-changing collisions generally result in MTEs that are considerably smaller in magnitude or, in the case of $F\varepsilon$-changing transitions, even negative. The deeper modulation of the $F\varepsilon$-changing oscillations is due to the more even character of the V_{dif} PES that by symmetry lacks the lowest odd-λ term.

xi. A closer look into the QS calculations and comparison to available literature indicates that the dynamics of collisions which lead to parity-conserving and parity-changing transitions must be fundamentally different and the oscillations may result from interferences between collisions at different impact parameters that sample the even-λ and odd-λ terms of the PESs.

xii. This may be better rationalised by extension of the semi-classical QQT model, where scattering is defined by rigid ellipse-rigid sphere kinematics, with interferences between scattering paths that lead to the same j' and scattering angle arising from different impacts on the ellipsoidal surface.

xiii. Parity effects have also been observed and predicted in other $^2\Pi$+Rg systems, inferring that they are in fact a general feature of $^2\Pi$+Rg collisions.

xiv. It is clear that current scattering theory provides essentially near-quantitative agreement for this benchmark $^2\Pi$+Rg system.

5.5 CN($A^2\Pi$)+N_2, O_2 and CO_2 State-to-State RET and Polarisation Transfer

5.5.1 Results

Representative data and fits for the stimulated emission FM line shapes are shown for the j = 6.5 F_1e prepared states and example Δj = -2 $F\varepsilon$-conserving and $F\varepsilon$-changing population transfer product states, respectively, in Figure 5.10. For the purposes of presentation the first 100 ns post-pump signal has been averaged. In all cases the fits represent the data well. The large difference between the two experimental geometries (co-rotating and counter-rotating) in the prepared levels indicates that a significant rotational orientation has been created. The overall signal sizes of the product levels are considerably smaller than those of the initial levels, indicating that only a small fraction of the initial population is transferred to any particular product level. The $F\varepsilon$-conserving product states appear to be more collisionally populated than the $F\varepsilon$-changing product states. The difference between the product geometries shows that some of the prepared orientation has been transferred during RET. The magnitude of the transferred orientation is however never equal to that of the initial level, demonstrative of inelastic depolarisation. For each collider, the amount of transferred orientation clearly depends on the product fine-structure and Λ-doublet label, and hence on the final rotational parity. The $F\varepsilon$-conserving transitions in general appear to conserve both a larger fraction and the sign of the initial orientation, whilst the $F\varepsilon$-changing transitions result in much smaller product orientations, that in the case of the N_2 and CO_2 partners, even change sign. This behaviour so far is consistent with that of CN($A^2\Pi$)+Ar from the previous section.

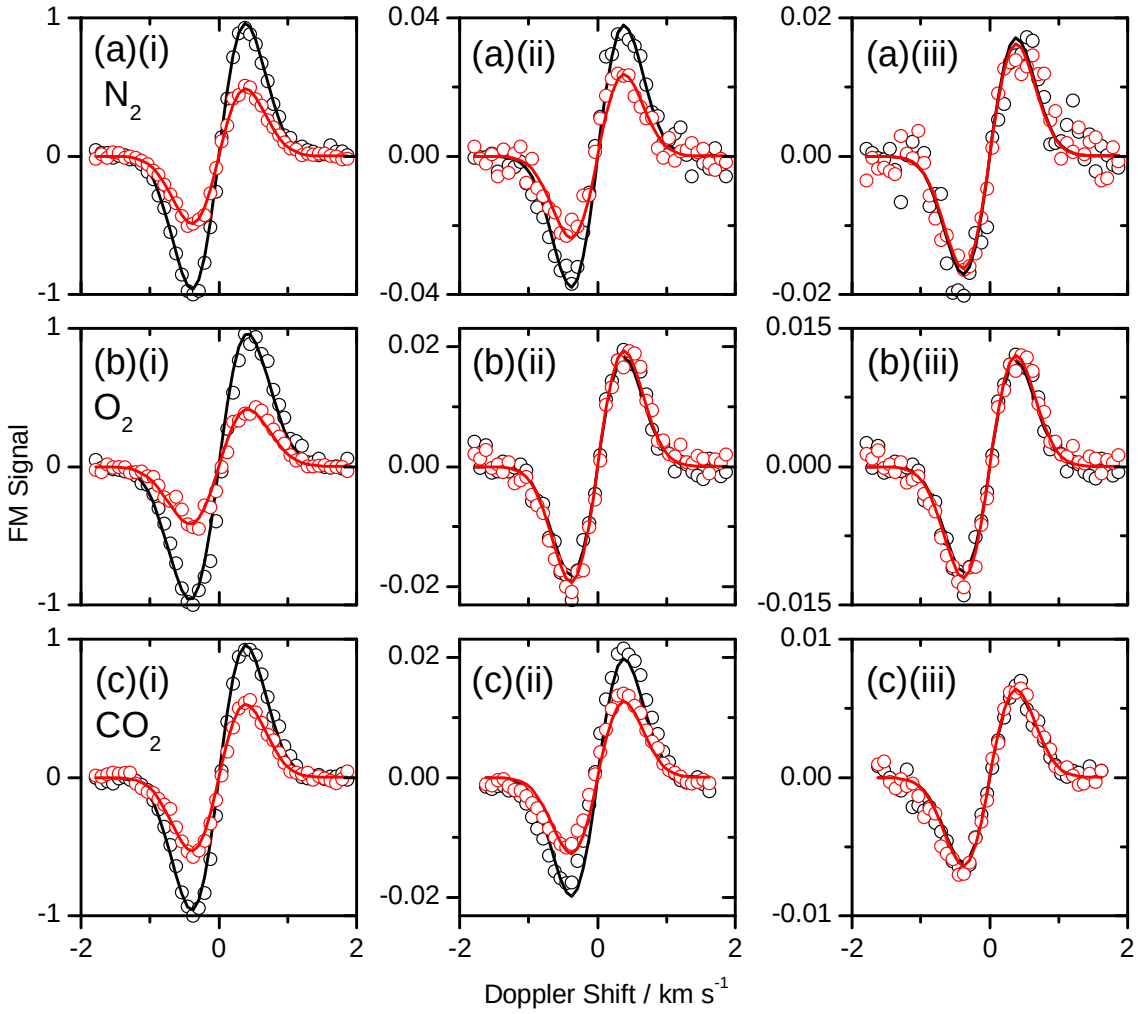

Figure 5.10 – Representative data (circles) and fits (lines) for the stimulated emission FM line shapes for co-rotating (black) and counter-rotating (red) geometries. (i) j = 6.5 F_1e initial state; (ii) Δj = -2 $F\varepsilon$-conserving; (iii) Δj = -2 $F\varepsilon$-changing product states for (a) N_2, (b) O_2 and (c) CO_2 colliders. For the purposes of presentation the first 100 ns post-pump signals have been averaged and experimental uncertainties removed.

Figure 5.11 shows representative kinetic traces and fits for the total removal of population from the initial level j = 6.5 F_1e and the state-to-state population transfer for Δj = -1 and -2, $F\varepsilon$-conserving and $F\varepsilon$-changing, respectively, for each collider. The prepared population decay was fitted to the three-level kinetic model (Equation 4.23) and the population transfer fitted to a single exponential according to Equation 5.1. In each case, the fits represent the data well. The initial population removal traces in Figure 5.11(a)-(c)(i) show the same behaviour as observed in Chapter 4, with similar total removal kinetics for N_2 and O_2, although close inspection reveals that the trace for O_2, as with CO_2, tends to zero at long times, whilst a constant non-zero background is

present for N_2. This is consistent with the larger $\sigma^{(0)}_{j\to j_x}$ cross-sections seen in the three-level fitting to O_2 and CO_2, and suggests that the rates between RET and other removal processes, for example quenching, are different for O_2 and CO_2 compared with N_2. Comparing the rate of state-to-state RET for each collider gives N_2 > O_2 > CO_2, reaffirming the notion of extra loss channels for O_2 and especially CO_2, as this has the fastest total removal yet the slowest state-to-state RET. In all cases shown, except for CO_2 Δj = -1, the $F\varepsilon$-conserving population transfer is faster than the $F\varepsilon$-changing. This is consistent with the spin-orbit propensity discussed in Section 5.4 for CN($A^2\Pi$)+Ar, which represents the contributions from the V_{sum} and V_{dif} PESs close to the Hund's case-(a) limit.

The initial and product orientation traces and kinetic fits according to Equation 4.28 and Equation 5.3 are shown in Figure 5.12 for the same initial and final levels as Figure 5.11, specifically Δj = -1 and Δj = -2 for both $F\varepsilon$-conserving and $F\varepsilon$-changing transitions from j = 6.5 F_1e. The general trends appear similar to those for the Ar collision partner, with marked parity-dependences reproduced in both the data and fits. Overall, there is little variation between collider species. The circular pump step prepares a negative orientation in the initial levels that decays towards zero relative to the loss of population. For Δj = -1, the $F\varepsilon$-conserving and $F\varepsilon$-changing transfer traces retain the sign of the prepared orientation at early times but differ in initial magnitude before decaying at finite rates. The initial $F\varepsilon$-changing transferred orientation for Δj = -2 has clearly changed sign, whilst preserving less of the initial magnitude. The Δj = -2 $F\varepsilon$-conserving transitions strongly conserve both the sign and magnitude of the initial state orientation. This seemingly indicates that the rotational parity propensity is ubiquitous to CN($A^2\Pi$), regardless of collision partner species. The orientation MTE for each transfer level was obtained by taking the ratio of the t = 0 product orientation (found by extrapolation in the single exponential fits) to the t = 0 orientation of the prepared level (from the three-level fits), according to Equation 5.2.

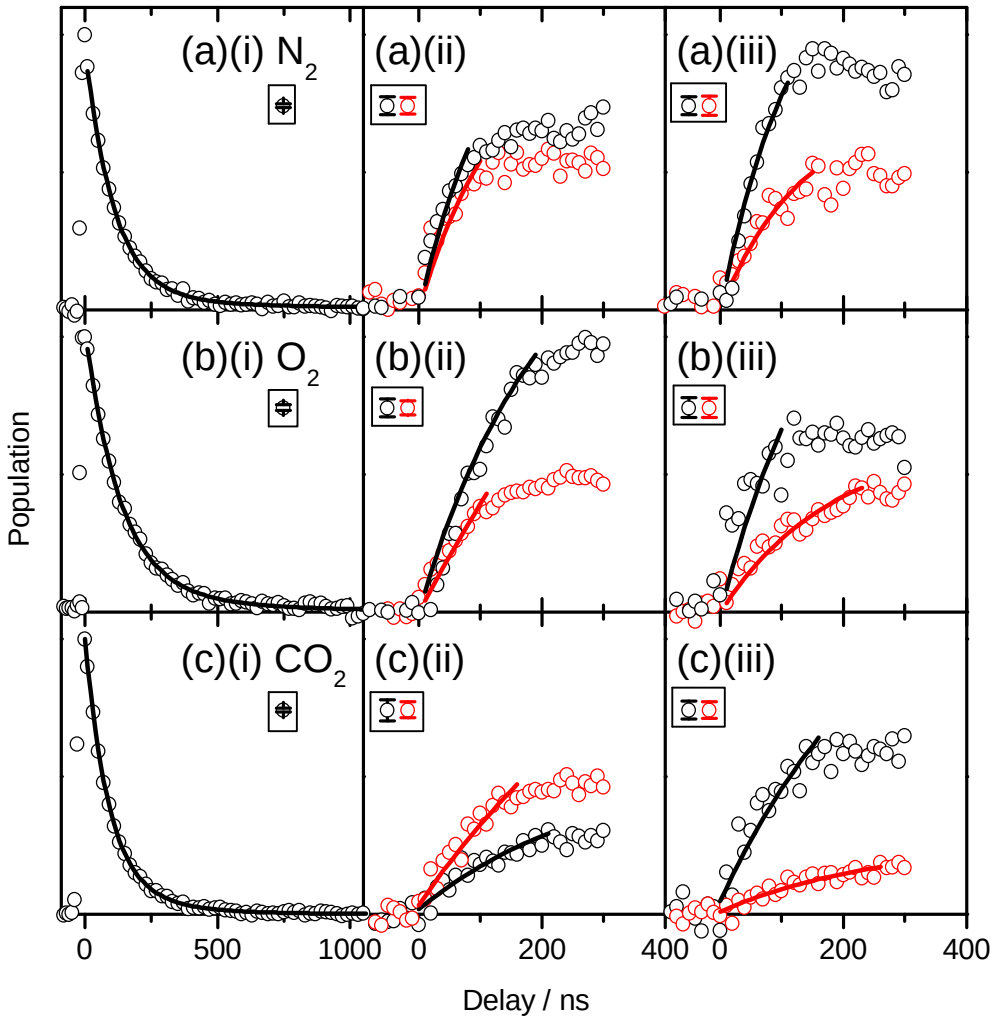

Figure 5.11 – Typical population kinetic traces (circles) and fits (solid lines) according to Equation 4.23 and Equation 5.1 for the three molecular colliders: (a) N_2,(b) O_2 and (c) CO_2. (i): Direct line total population removal from j = 6.5 F_1e at ~200 mTorr for CO_2 and ~400 mTorr for N_2 and O_2. (ii) State-to-state population transfer (multiplied by a factor of 30) for Δj = -1 and (iii) Δj = -2. (Black) Fε-conserving transitions, (red) Fε-changing transitions, at 400 mTorr pressure for N_2 and O_2 and 200 mTorr for CO_2. Representative average 2σ error bars are displayed within the inset of each panel. Error bars for individual data points have been omitted for visual clarity.

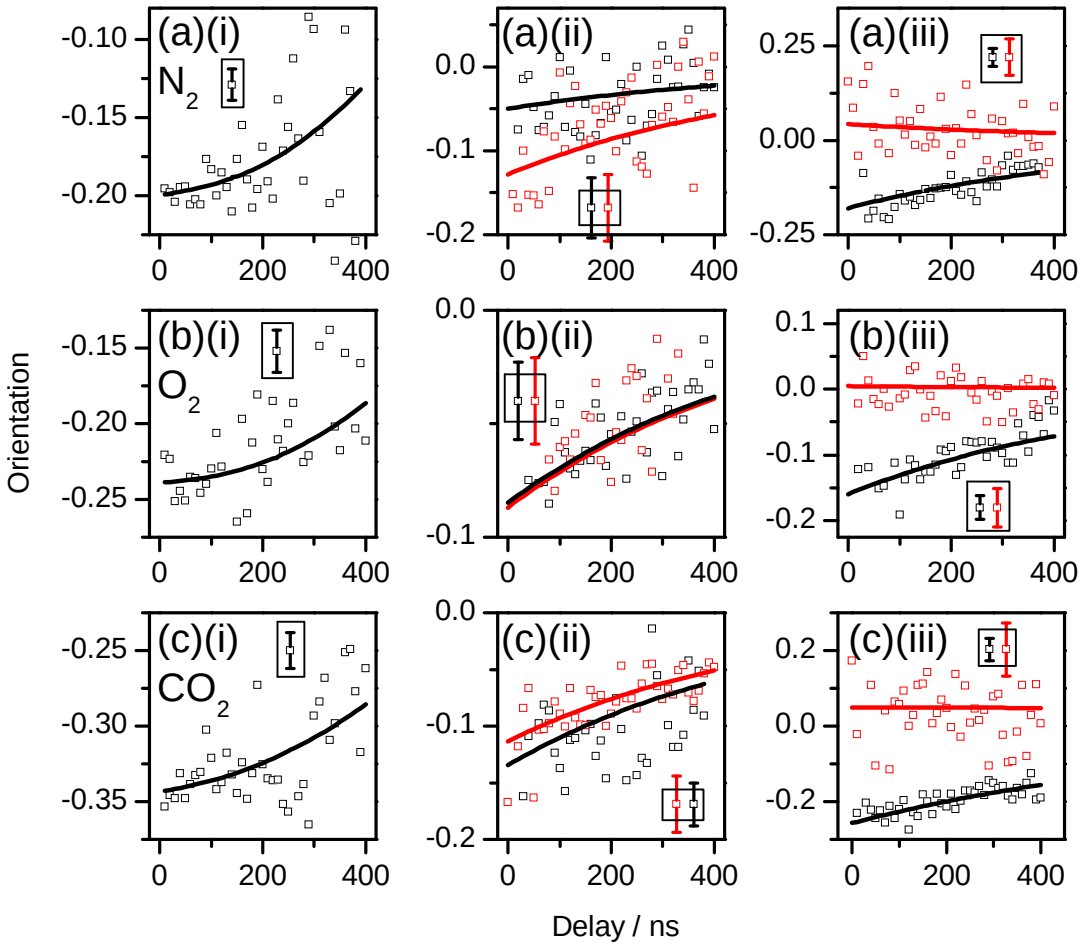

Figure 5.12 – Typical orientation kinetic traces (squares) and fits (solid lines) according to Equation 4.28 and Equation 5.3 for the three molecular colliders: (a) N_2,(b) O_2 and (c) CO_2. (i): Direct line total orientation removal from j = 6.5 F_1e at ~200 mTorr for CO_2 and ~400 mTorr for N_2 and O_2. (ii) State-to-state orientation transfer for Δj = -1 and (iii) Δj = -2. (Black) Fε-conserving transitions, (red) Fε-changing transitions, at 400 mTorr pressure for N_2 and O_2 and 200 mTorr for CO_2. Representative average 2σ error bars are displayed within the inset of each panel. Error bars for individual data points have been omitted for visual clarity.

The average state-to-state RET rate constants and orientation MTEs for each collider were determined from multiple independent measurements for each product state, performed on different days and fitted independently, as outlined in Section 5.3. The rate constants were turned into thermally averaged cross-sections to allow for comparison of each collider. The state-to-state population transfer cross-sections and MTEs are listed in Table 5.6 and compared for the different collision partners in Figure 5.13, including the previously determined results for Ar from Section 5.4.

Table 5.6 – Measured (average) thermal state-to-state population transfer cross-sections, $\sigma^{(0)}_{j\to j'}$, and MTEs, $E^{(1)}(j,j')$, for CN($A^2\Pi$, v = 4) j = 6.5 F_1e to j' = j + Δj, for both Fε-conserving and Fε-changing transitions, for N_2, O_2 and CO_2 collision partners. Uncertainties are the standard error of the mean. In all cases, Δj = 0 Fε-conserving is the direct line that prepares the initial level.

Δj	$\sigma^{(0)}_{j\to j'}$ / Å^2		$E^{(1)}(j,j')$	
	Conserving	Changing	Conserving	Changing
N_2				
-4	1.41 ± 0.14	0.93 ± 0.07	0.31 ± 0.02	-0.16 ± 0.05
-3	2.17 ± 0.18	1.40 ± 0.23	0.23 ± 0.03	0.57 ± 0.07
-2	6.55 ± 0.62	1.45 ± 0.16	0.71 ± 0.08	-0.31 ± 0.002
-1	3.38 ± 0.50	3.05 ± 0.36	0.35 ± 0.01	0.90 ± 0.03
0	-	2.03 ± 0.04	-	0.33 ± 0.004
+1	3.24 ± 0.26	2.72 ± 0.43	0.59 ± 0.03	0.65 ± 0.07
+2	5.90 ± 0.55	1.83 ± 0.18	0.69 ± 0.13	0.39 ± 0.02
+3	4.06 ± 1.06	-	0.65 ± 0.03	
O_2				
-4	1.27 ± 0.19	0.63 ± 0.07	0.40 ± 0.07	-0.22 ± 0.03
-3	1.75 ± 0.10	1.15 ± 0.09	0.23 ± 0.04	0.46 ± 0.03
-2	4.09 ± 0.11	1.11 ± 0.07	0.53 ± 0.03	0.08 ± 0.05
-1	2.96 ± 0.55	1.51 ± 0.17	0.36 ± 0.02	0.48 ± 0.02
0	-	0.98 ± 0.07	-	0.24 ± 0.02
+1	2.87 ± 0.52	1.51 ± 0.10	0.50 ± 0.01	0.43 ± 0.03
+2	4.53 ± 0.14	1.03 ± 0.12	0.60 ± 0.02	0.32 ± 0.02
+3	2.39 ± 0.09	1.22 ± 0.09	0.57 ± 0.01	0.23 ± 0.02
+4	2.65 ± 0.22	-	0.71 ± 0.03	-
CO_2				
-4	1.43 ± 0.09	0.75 ± 0.11	0.35 ± 0.02	-0.16 ± 0.01
-3	1.32 ± 0.09	1.24 ± 0.14	0.24 ± 0.02	0.19 ± 0.01
-2	4.01 ± 0.18	0.85 ± 0.07	0.71 ± 0.01	-0.09 ± 0.04
-1	1.86 ± 0.14	2.54 ± 0.19	0.38 ± 0.02	0.44 ± 0.01
0	-	0.88 ± 0.06	-	0.27 ± 0.02
+1	1.80 ± 0.08	1.69 ± 0.14	0.50 ± 0.02	0.29 ± 0.01
+2	3.43 ± 0.93	0.70 ± 0.13	0.68 ± 0.03	0.26 ± 0.03
+3	2.58 ± 0.08	1.09 ± 0.02	0.51 ± 0.05	0.30 ± 0.01
+4	2.85 ± 0.19	-	0.31 ± 0.01	-

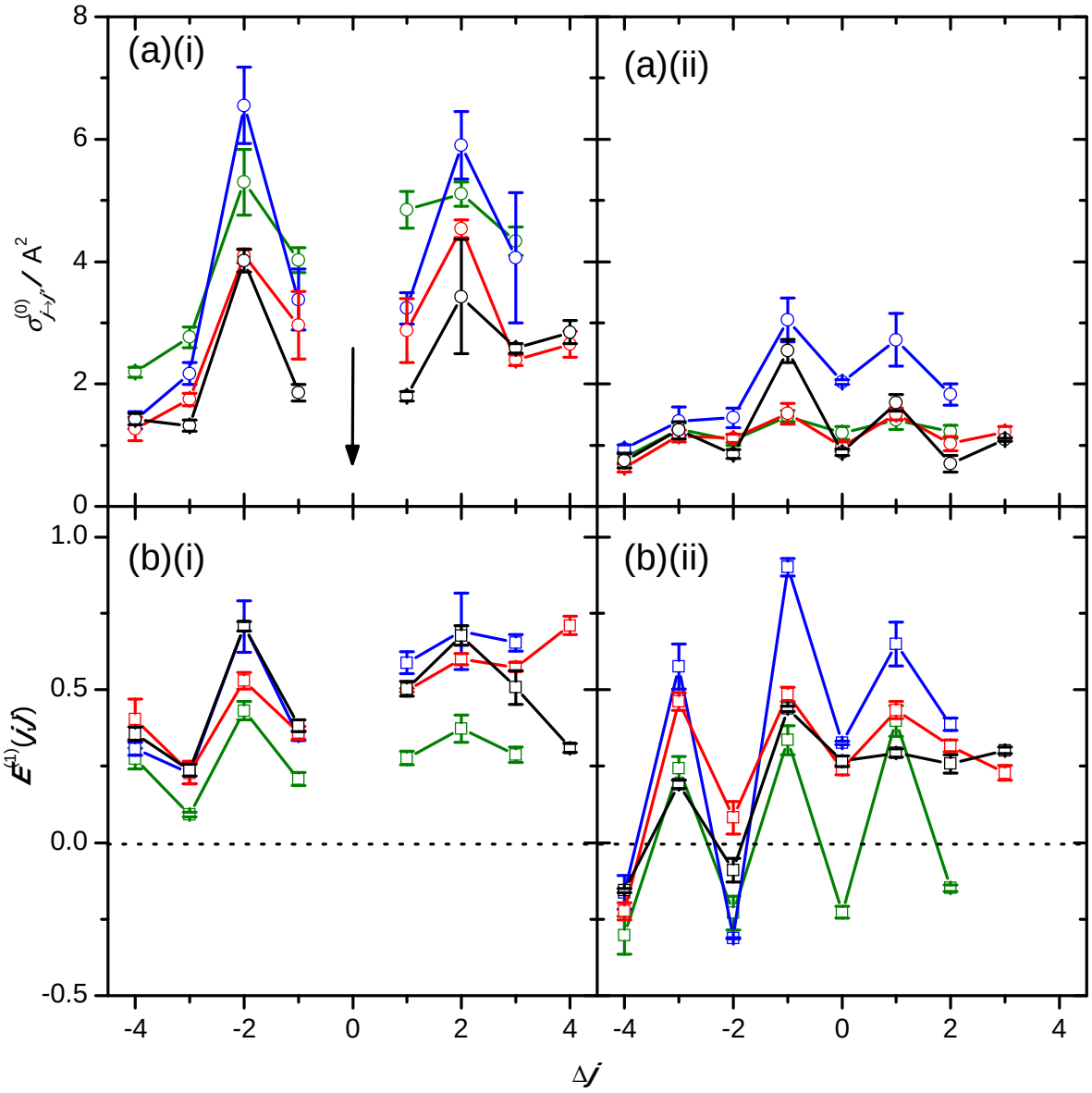

Figure 5.13 – (a) Thermally averaged cross-sections (circles), $\sigma^{(0)}_{j\to j'}$, for the transfer of population from the CN($A^2\Pi$, v = 4) j = 6.5 F_1e initial level, which is marked by an arrow. (b) The orientation MTE (squares), $E^{(1)}(j,j')$, for the same transitions. (i) Fε-conserving collisions to j´ F_1e levels and (ii) Fε-changing collisions to j´ F_2f levels as a function of Δj = j´ - j. Data points are averages of 4 – 5 separate experimental measurements together with the standard error of the mean. Collision partners: olive = Ar (from Section 5.5), blue = N_2, red = O_2, black = CO_2.

The results in this section are in qualitative agreement with those from the previous section for CN($A^2\Pi$)+Ar. The state-to-state RET cross-sections for both Fε-conserving and Fε-changing transitions for all four colliders (Ar, N_2, O_2, and CO_2) display a

marked even/odd-Δ*j* alternation, with even-Δ*j* favoured for $F\varepsilon$-conserving transfer and odd-Δ*j* favoured for $F\varepsilon$-changing transitions. This reflects the preferred conservation of rotational parity, as described in Section 5.4.3. Similar overall transfer cross-sections for the $F\varepsilon$-conserving transitions are observed for Ar and N_2, although with detailed differences. Considerably smaller cross-sections were measured for O_2 and CO_2. In all cases the cross-sections for $F\varepsilon$-changing collisions are on average half the size of those for $F\varepsilon$-conserving transfer, indicating a propensity for spin-orbit conservation. Although a similar effect is seen for Ar in Section 5.4, there the equivalent ratio is smaller, at around 1/3. Likewise, the N_2 partner typically experiences moderately to significantly larger parity-conserving $F\varepsilon$-changing cross-sections than the other colliders.

The MTEs for the molecular partners show overall very similar behaviour to Ar. There is a preference to conserve the initial orientation in the $F\varepsilon$-conserving transitions compared to $F\varepsilon$-changing. Out of all the colliders for the $F\varepsilon$-conserving transitions, Ar retains the least amount of the initial orientation followed approximately by $O_2 < CO_2 < N_2$, and none of the MTEs change sign. The parity-conserving even-Δ*j* transfer conserves more of the initial orientation, although often less than unity, reflecting some depolarisation. The parity-dependent oscillations are of opposite phase for $F\varepsilon$-changing transfer, with odd-Δ*j* parity-conserving transitions conserving the the initial orientation, resulting in positive MTEs, whereas even-Δ*j* parity-changing transitions result in MTEs that are considerably smaller in magnitude or even negative. The lower Δ*j* have the strongest sign-changing alternations, which are most apparent for N_2, although as Δ*j* increases the oscillations smooth out, especially for O_2 and CO_2. More orientation is retained for collisions with N_2 in the $F\varepsilon$-changing manifold, followed by O_2, CO_2 and Ar. In fact, for N_2, the parity-conserving MTEs are equal to or larger than their $F\varepsilon$-conserving parity-conserving counterparts. The molecular colliders generally retain more orientation in both probed $F\varepsilon$-manifolds compared to Ar, and the difference in magnitude between the two manifolds is less than that for Ar.

5.5.2 Discussion

Population Transfer

The substantial even-odd Δj oscillations in Figure 5.13 for all of the molecular colliders, as observed for CN($A^2\Pi$)+Ar in Section 5.4, represents a preference for conservation of total parity. As discussed in Section 5.1, within a weak coupling limit, parity-conserving RET is enabled by the even-λ terms in the angular expansion of the PES, while parity-changing transfer is enabled by the odd-λ terms. The strong parity-conservation propensity in CN($A^2\Pi$)+Ar was attributed to the dominance of even-λ terms in the angular expansion of the PESs that results from the near-symmetry of the interaction, which itself is a consequence of the near-homonuclear character of the CN molecule. The strong parity propensity observed here for N_2, O_2 and CO_2 must then presumably reflect a similar dominance of the even-λ terms in their respective PESs arising from near-symmetry. This comes despite the additional dimensions introduced from the non-spherical nature of these molecular colliders. Indeed, the *ab initio* CN($A^2\Pi$)-N_2 PESs of Dagdigian and co-workers display a marked even order, with the associated QS calculations following the behaviour of CN($A^2\Pi$)+Ar from Section 5.4.[206] This is addressed in more detail below. Similar effects have been observed in related systems, such as in self-collisions of $C_2H_2\left(\tilde{X}^1\Sigma_g, v_2 = 1, j\right)$, which exhibited exclusively Δj = even RET transitions, resulting from the total wavefunction parity and the nuclear spin symmetry of acetylene.[333] A preference for parity-conserving transfer was noted by Heaven and co-workers in low-temperature (7 K) collisions of CN($A^2\Pi$) with H_2,[204] which suggests that strongly even interactions with CN($A^2\Pi$) are not uncommon for at least small, centrosymmetric, molecules. However, in related predissociation measurements of the CN($X^2\Sigma^+$)-H_2 van der Waals complex *via* electronic excitation to the $A^2\Pi$ state, Heaven and co-workers saw no such parity propensity.[203, 204] This was ascribed to the limited range of initial geometries introducing asymmetry to the system. This clearly demonstrates how specific symmetry components of the PES are responsible for the parity-conservation.

Comparison of each collider's ability to conserve or change spin-orbit label upon RET in Figure 5.13 also reveals detailed information about the interaction with CN($A^2\Pi$). Species with unpaired electronic spins are routinely found to be more effective at

causing a change in spin-orbit label compared to closed-shell systems.[331, 334-339] This has often been attributed to the multiple PESs required to properly represent open-shell–open-shell encounters and an effect of long-range intermolecular interactions. As the isolated molecules approach one another, they correlate to and evolve on one or more of these surfaces, then dissociate back to the isolated molecules in different product spin-orbit states. Recent examples of open-shell molecular collision systems involving multiple PESs include van der Meerakker and co-workers' CMB measurements of rotationally resolved stark-decelerated OH($X^2\Pi$, v = 0, j = 1.5, F_1f) scattered with hexapole-focussed NO($X^2\Pi$) radicals.[334] Quantum-coupled channels calculations using a set of multiple coupled PESs revealed that the measured product spin-orbit excitations result from long-range electrostatic forces and non-adiabatic couplings between different PESs.[334] In separate related studies, Vonk *et al*. measured the DCSs of rotationally inelastic self-collisions of NO($X^2\Pi_{1/2}$, $j' \leq 2.5$) in a CMB-REMPI setup and Bacon *et al*. recorded DCSs for NO($X^2\Pi_{1/2}$, $j' \leq 2.5$)+CO and O_2.[335, 336] All three targets presented a high probability for spin-orbit transfer, although overall, NO+O_2 produced a considerably higher spin-orbit transfer ratio. For the spin-orbit conserving transitions, the DCS intensity maxima for NO+O_2 were shifted towards larger scattering angles than for spin-orbit changing transitions, making the latter more effective at RET. This was postulated to be an effect of spin-pairing producing a deep attractive well in the intermolecular potential. Crossed-beam inelastic scattering of NO($X^2\Pi$) with rare gases and a variety of molecular colliders, including N_2, O_2 and CO_2, by Bieler *et al*. also showed a strong collider dependence to the spin-orbit populations, but no additional Λ-doublet selectivity.[338]

A difference in spin-orbit transfer may then be expected in this work when comparing collisions of CN($A^2\Pi$) with closed-shell Ar, N_2 and CO_2 to open-shell O_2. The relative spin-orbit changing cross-sections in Figure 5.13 are larger for each of the molecular colliders compared to Ar from Section 5.4. This is exemplified in Table 5.7, which shows the respective sums of the $F\varepsilon$-conserving and $F\varepsilon$-changing cross-sections and their ratio ($F\varepsilon$-changing/$F\varepsilon$-conserving) for each collider. Also shown in Table 5.7 are the net sum of the state-to-state RET cross-sections for each collider that includes all the probed $F\varepsilon$-conserving and $F\varepsilon$-changing transitions compared to the total removal σ_{pop} cross-sections from Section 4.6, for discussion later.

Table 5.7 – The summed Fε-conserving and Fε-changing $\sigma^{(0)}_{j\to j'}$ cross-sections and the ratio of changing/conserving for each collider. Also shown are the net sum of all the measured $\sigma^{(0)}_{j\to j'}$ for each collider and the σ_{pop} total removal cross-sections from Section 4.6. Errors are 2σ uncertainties.

Collider	$\sum\sigma^{(0)}_{j\to j'}$ / Å^2		Ratio	Sum[b]	σ_{pop} / Å^2
	Conserving[a]	Changing[a]		$\sum\sigma^{(0)}_{j\to j'}$ / Å^2	
Ar	24.23 ± 2.97	8.44 ± 1.52	0.35	37.00 ± 4.96	61.71 ± 1.61
N_2	22.65 ± 4.50	13.41 ± 2.91	0.59	40.12 ± 9.54	82.31 ± 0.64
O_2	19.86 ± 3.43	9.15 ± 1.55	0.46	31.66 ± 5.41	69.77 ± 1.37
CO_2	16.42 ± 3.19	9.74 ± 1.72	0.59	29.01 ± 5.29	121.56 ± 1.38

[a] *Includes only common j′ probed.*

[b] *Includes all j′ probed.*

The spin-orbit ratio for Ar is approximately 1/3, which in Section 5.4 was explained in terms being close to the Hund's case-(a) limit, where the V_{sum} PES mediates spin-orbit conservation and the V_{dif} PES enables spin-orbit transfer. As the system departs from the Hund's case-(a) limit, both V_{sum} and V_{dif} contribute to spin-orbit conserving and changing transitions. The molecular colliders all appear to be more efficient at changing the spin-orbit label than Ar, each with a spin-orbit ratio of roughly 1/2. If collisions of CN($A^2\Pi$) with the molecular partners are represented in a diabatic basis, as previously done by Dagdigian and co-workers for CN($A^2\Pi$)-N_2,[206] this suggests that the V_{dif} is of larger magnitude in the regions accessible at thermal collision energies for the molecules. The higher spin-orbit ratio from collisions with N_2, O_2 and CO_2 compared to Ar is in agreement with the findings of van der Meerakker and co-workers, Vonk *et al*., Bacon *et al*. and Bieler *et al*. cited above, who explained their results partly with respect to long-range intermolecular forces. The relative order of the spin-orbit ratios for the colliders is $CO_2 \approx N_2 > O_2 >$Ar, which loosely follows the magnitudes of the polarisabilities and quadrupole moments in Table 4.9.

However, the above-cited papers also draw on the importance of the different contributing PESs to molecule-molecule encounters, especially where each species is open-shell. In the case of CN($A^2\Pi$)+O_2, the CN($A^2\Pi$) and $O_2\left(X^3\Sigma_g^-\right)$ molecules come together to form (likely strongly attractive) doublet and quartet surfaces of the NC-OO complex, resulting in six available PESs. As stated in Section 1.8.2, one out of three of

these meetings can quench CN($A^2\Pi$). Long-range spin-pairing interactions and collision-induced non-adiabatic transfer between the multiple PESs should allow for efficient spin-orbit excitation. However, the spin-orbit ratio for O_2 in Table 5.7 is in fact slightly smaller than for the kinematically similar, but closed-shell, N_2, indicating that O_2 does not particularly favour spin-orbit transfer over N_2. This may imply that those molecules that do strongly interact disappear through quenching and so only the weakly interacting regions of the surfaces are being explored, where the coupling is not strong enough to enable the excitation. Clearly, the molecules in this study are good at spin-orbit transfer, although despite its open-shell nature, O_2 does not appear to be any more efficient at this process than the rest of the colliders.

As introduced in Section 1.7, Huennekens and co-workers employed PS-OODR to measure the collisional transfer of population and orientation in NaK($A^1\Sigma^+$)+Ar and K.[137] This provides another convenient comparison between open-shell and closed-shell partners. Collisions with K were found to be more efficient at causing RET and very effective at destroying the polarisation during inelastic transfer compared to Ar. No parity propensity was observed for NaK+K, but instead a preference for Δj = positive. Conversely, RET with Ar exhibited a strong Δj = even propensity attributed to near-homonuclear symmetry. As well as NaK($A^1\Sigma^+$)+K being strongly attractive and reactive, the results were credited to the non-zero angular momentum of the K atom's loosely bound outer valence electron and the difference in polarisabilities between K and Ar.[137] Contrasting those results with this work, O_2 still has a marked parity propensity compared to the close-shell colliders, specifically N_2, with no preference for either positive or negative Δj. In fact, looking at Figure 5.13, N_2 appears to be better at both state-to-state RET and polarisation transfer than O_2. This could again be attributed to exploring the weakly interacting regions of the CN($A^2\Pi$)-O_2 PESs, alongside competing quenching channels

The order of the collider net summed state-to-state RET efficiencies in Table 5.7 is N_2 > Ar > O_2 > CO_2, showing that overall, N_2 and Ar are better at RET. This is in accordance with state-selected experiments of ter Meulen and co-workers who found N_2 to behave similarly to Ar in collisions with OH($X^2\Pi$).[78, 95] The larger cross-section for N_2 compared to O_2, as is also the case for the total removal cross-sections, could be linked to the relative magnitude of the N_2 quadrupole moment compared to that of O_2. Jörg *et al*. found N_2 to be more efficient at RET than CO_2 in collisions with OH($X^2\Pi$),

measuring cross-sections around a third larger for N_2, analogous to Table 5.7.[101] The range of Δj in the state-to-state RET for the molecular colliders here is not noticeably larger than for Ar, despite the possible added molecular rotational inelasticity that could channel away angular momentum and energy.

The total removal cross-sections from Section 4.6 indicated substantial electronic quenching channels for O_2 and CO_2, whereas the results for N_2 were very similar to those for Ar, with both partners being dominated by RET. Comparison of the partner-dependence of the state-to-state cross-sections from this section, shown in Figure 5.13, with the total removal cross-sections from Figure 4.44, across the range of j studied and more specifically for j = 6.5 F_1e, reinforces the conclusions from the previous chapter regarding the behaviour of the different colliders. Substantial differences between the total removal and state-to-state cross-sections for CO_2 and O_2 again demonstrate that another process is also removing the population. For a particular initial level, if every state-to-state product level is probed, then the sum of the individual RET cross-sections should be analogous to the total RET cross-section out of that level. Since not all the possible state-to-state product levels have been probed in this study, a direct comparison between the two sets of measurements cannot be made. However, the majority of the significant open channels in the pure $F\varepsilon$-conserving and $F\varepsilon$-changing transitions have been probed and so an approximate comparison can still be drawn.

Without any other available information, the sum of the measured channels, $\sum\sigma^{(0)}_{j\rightarrow j'}$, would be expected to represent around half of the total RET cross-sections, σ_{pop}, assuming roughly equal combined populations in the unobserved F-conserving/ε-changing and F-changing/ε-conserving channels. This assumes that conservation of rotational parity and spin-orbit label are the prevalent propensities at low j, as is apparent from Figure 5.13 and discussed above, as well as previously observed and predicted for CN($A^2\Pi$)+Ar in Section 5.4 and elsewhere in references [15, 206]. In Table 5.7, there appears to be excellent agreement with this assumption for Ar and very good agreement for N_2, with $\sum\sigma^{(0)}_{j\rightarrow j'}$ around half the size of σ_{pop}. These two partners possess very small quenching rate constants, as detailed in Table 4.11 and discussed in Section 4.6. This reaffirms that RET is the dominant population removal pathway for these colliders. In contrast, for O_2 and much more so for CO_2, $\sum\sigma^{(0)}_{j\rightarrow j'}$ is less than half of σ_{pop}. This is again consistent with another collisional process removing the prepared

population, namely electronic quenching, as seen in the comparison of the quenching rate constants in Table 4.10 and discussed further in Section 4.6. However, the implied quenching efficiencies from the difference between $\sum\sigma^{(0)}_{j\to j'}$ and σ_{pop} for O_2 and CO_2 are respectively smaller and much larger than the quenching rate constants determined from the three-level kinetic fitting and reported from the literature in Table 4.11. Substantial uncertainties in $\sum\sigma^{(0)}_{j\to j'}$ arise from unobserved levels within the measured $F\varepsilon$-conserving and $F\varepsilon$-changing manifolds, as well as from the assumption regarding the unobserved F-conserving/ε-changing and F-changing/ε-conserving pathways. Therefore, although the state-to-state RET cross-sections do support the proposal of enhanced quenching for O_2 and CO_2, the quenching rate constants reported in Table 4.11 present more reliable estimates of this channel.

The total removal results from Section 4.6 also hinted at a preferred quenching geometry for O_2 and CO_2, similar to the combined experimental and theoretical work of Brouard and co-workers on the OH($A^2\Sigma$)+Kr system.[316, 317] The state-to-state RET cross-sections in Figure 5.13 do not provide any further evidence of this, with no discernible difference between each of the colliders other than the overall breakdown between RET and quenching. In fact, such an anisotropic interaction would be expected to wash out any parity-dependent oscillations that arise from the near-symmetry of the system. Clearly this is not the case, as strong Δj-dependent alternations still persist for O_2 and CO_2. This could simply mean that the complexation is very weak in these cases, or sampled at different regions of the PESs. Very few full parity-resolved studies for RET of $^2\Pi$ species with molecular collision partners exist with which to compare, especially those involving potentially reactive and unreactive partners, as is the case here. Other than Heaven and co-workers' low temperature studies of CN($X^2\Sigma^+$)+H_2,[203, 204] Stolte and co-workers observed parity-dependent effect in DCS measurements of NO($X^2\Pi$)+D_2.[36] Ter Meulen and co-workers utilised hexapole state-selection in fully state-resolved CMB measurements for RET in OH($X^2\Pi$, j = 1.5, F_1f)+CO, N_2 and CO_2.[78, 95] Although all three colliders saw a preference for conservation of total parity for Δj = +1 $F\varepsilon$-conserving and Δj = -1 $F\varepsilon$-changing transitions, in general there was a lack of any distinct parity propensity. This could result from the much more heteronuclear nature of OH($X^2\Pi$) and the consequent loss of near-head-tail symmetry in the PESs. Despite the presence of a strongly attractive reactive pathway for OH($X^2\Pi$)+CO compared to OH($X^2\Pi$)+N_2, no obvious differences between the two

systems were noted. In all cases, a significant probability to populate the upper fine-structure manifold was observed, in agreement with the earlier discussion on spin-orbit effects.

The general form of the state-to-state RET cross-sections for CN($A^2\Pi$, v, $jF\varepsilon$)+N_2 and CO_2 in this section can be compared to those previously reported by Dagdigian and co-workers.[206, 224] Although they prepared different initial states, namely v = 3, j = 7.5 F_1f and v = 3, j = 9.5 F_2f, such a minor change has previously had no significant effect on the relative cross-sections, as observed for the total removal in Chapter 4. The rotational levels are still near the peak of the Boltzmann distribution and have similar angular momenta and energies. The LIF-OODR technique employed also means that both sets of experiments were performed within an isotropic bath set-up at thermal collision energies. The total removal cross-sections from Section 4.6 were in excellent agreement with the results from reference 206, however the state-to-state RET cross-sections here are in remarkable disagreement. The measurements in Figure 5.13 generally follow the same qualitative trends as for Ar. Conversely, Dagdigian and co-workers observed a very strong preference for spin-orbit conservation with negligible spin-orbit transfer and unusual ranges of Δj. Whilst their $F\varepsilon$-conserving cross-sections do show a similar decrease with Δj, they do not exhibit the characteristic parity-dependent even/odd alternation reported here.

Instead, the results in this work are in much better agreement with the QS calculations performed by Dagdigian and co-workers on the geometrically-averaged PESs of CN($A^2\Pi$)-N_2.[206] Theory predicted Δj distributions consistent with CN($A^2\Pi$)+Ar,[15] centred energetically on the initially prepared level and with a spin-orbit ratio of around a 1/4. Importantly, the alternations from parity-conservation were still present. Contrary to the conclusions of the previous authors, the approximate QS method therefore appears to illuminate the essential features of the collision dynamics well. The high signal-to-noise of the FMS measurements, as evident in Figure 5.11 and Figure 5.12, reproducibility of the experiment and the high purity of the collider gases (99.9995% N_2, O_2; 99.999% CO_2), along with the minimisation of any possible sources of contamination give confidence in the results of this thesis. As do the careful kinetic processing and analysis procedures and the excellent agreement of the CN($A^2\Pi$)+Ar measurements in Section 5.4 with QS theory. As also addressed in that section, the slight spectroscopic near-overlap of the R_1(5.5) pump transition with the close-by

R_1(10.5) (4,0) line is likely to have made a negligible contribution to the reported cross-sections for each collision partner, since the same experimental protocol was implemented throughout. This is apparent from the absence of any prompt signals in the RET product kinetic traces in Figure 5.11 and is again supported by the exceptional level of agreement between experiment and theory in Section 5.4. The surprising experimental results of Dagdigian and co-workers in references 206 and 224, and the remarkable disagreement with theory are therefore likely to have risen from some undetected experimental artefact in their measurements, rather than failures of theory or any issues with the FMS experiment.

The results from Chapter 4 and this chapter indicate that, aside from differences in competing removal channels, the interactions of N_2, O_2 and CO_2 with CN($A^2\Pi$) are somewhat similar in form to that of Ar. The good agreement of the N_2 results with the QS calculations in reference 206 provides further support of this. It is therefore intuitive at this point to examine the spherically-averaged CN($A^2\Pi$)-N_2 PESs from reference 206 and contrast them with the CN($A^2\Pi$)-Ar PESs in Section 4.5.4. Unfortunately, there are no PESs for O_2 or CO_2 with which to compare.

The method employed to construct the CN($A^2\Pi$, v = 3)-N_2 PESs is as follows. Firstly, the CN and N_2 molecules were frozen at their respective internuclear distances, so that the PESs are functions of $\boldsymbol{R}$, the distance between the centres-of-mass of the two diatomics; two polar angles $\boldsymbol{\theta}$ and $\boldsymbol{\theta'}$, which are the orientations with respect to R of the CN and NN bonds, respectively; and $\boldsymbol{\phi}$, the dihedral angle. The N_2 was then assumed to be a spherical target by averaging over three limiting high-symmetry geometries of CN-N_2 by varying θ' and ϕ, as shown in Figure 5.14. Then, for each of the geometries, whilst holding the arrangement of the N_2 molecule constant, θ and R were varied in the *ab initio* calculations. As with a $^2\Pi$-Rg interaction, the approach of the target lifts the degeneracy of the singly occupied π-orbital, meaning that two PESs of A' and A'' symmetry are needed to describe the encounter for each limiting case. Arithmetic averages of the three A' PESs and the three A'' PESs were then taken and linear combinations of these averaged PESs according to Equation 1.12 and Equation 1.13 produced the conventional diabatic $V_{sum}(R, \theta)$ and $V_{dif}(R, \theta)$ representations. The corresponding A' and A'' PESs for each limiting geometry are displayed in Figure 5.14 and the V_{sum} and V_{dif} potentials are shown in Figure 5.15. The QS calculations were

constructed using analytic representations of V_{sum} and V_{dif} in the same manner as for CN($A^2\Pi$)+Ar. The exact details of the PESs and calculations are found in reference 206.

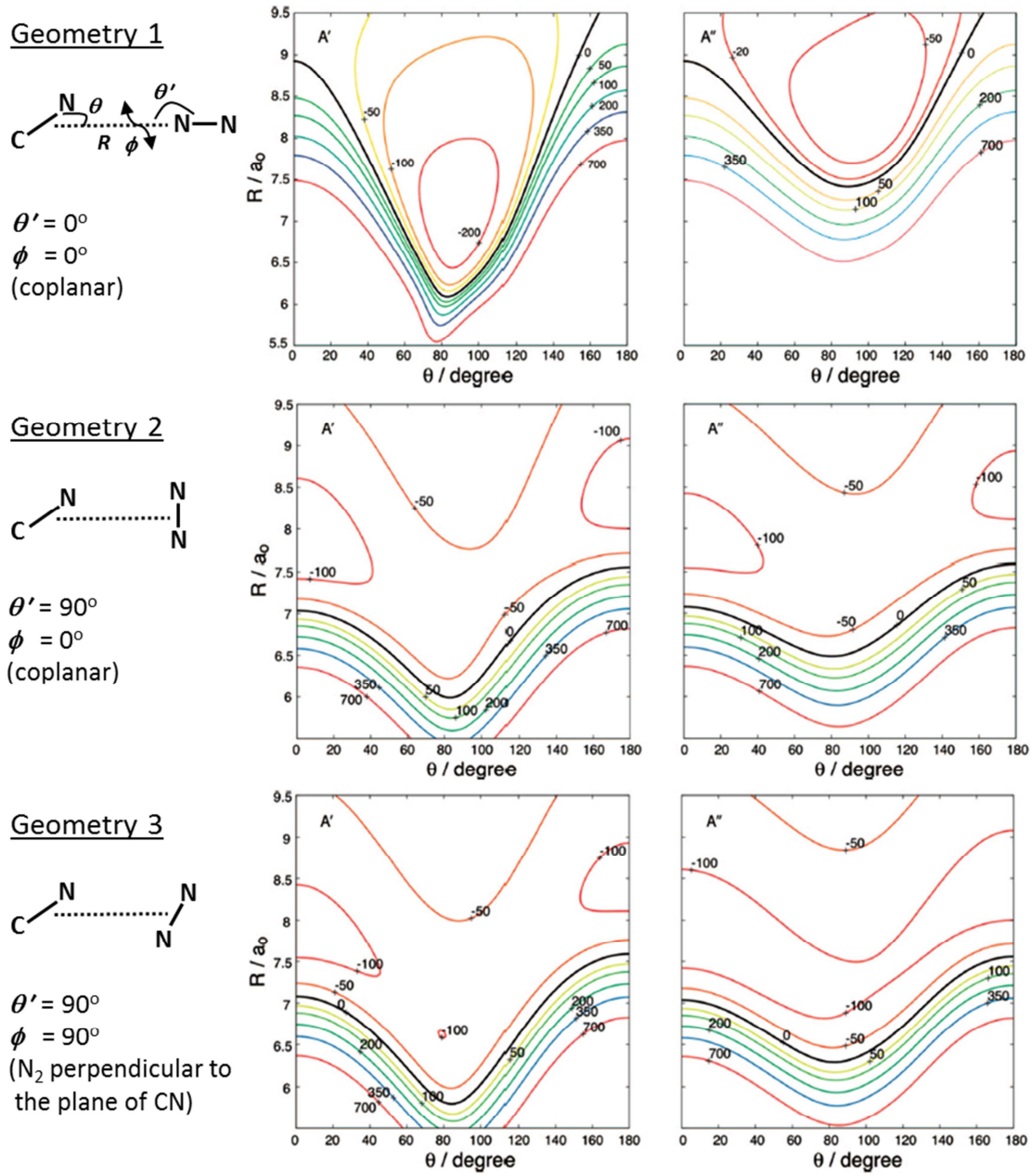

Figure 5.14 – The three limiting high-symmetry geometries at which ab initio calculations were performed by Dagdigian and co-workers for CN($A^2\Pi$, v = 3)-N_2. The arrangement of the N_2 molecule was held fixed in each case, while the separation R between the diatomics and the angle θ between CN and R were varied. PES contour plots (in cm^{-1}) of A′ and A″ reflection symmetry for each geometry are shown as a function of R and θ. In geometry 1, N_2 is fixed at a linear geometry coplanar with CN; in geometry 2, N_2 is fixed at a perpendicular geometry lying in the CN plane of rotation; in geometry 3, N_2 is fixed a perpendicular geometry that is

perpendicular to the CN plane of rotation. The $\theta = 0^o$ angle corresponds to the N-end of the CN molecule pointing towards the N_2 molecule, which for geometry 1 gives a linear CN-NN arrangement. Note that for collinear CN ($\theta = 0^o$ or 180^o), geometries 2 and 3 are degenerate. The zero-energy heavy black contours separate the attractive and repulsive regions of the surfaces. This figure was adapted from Figures 6 to 9 in reference 206.

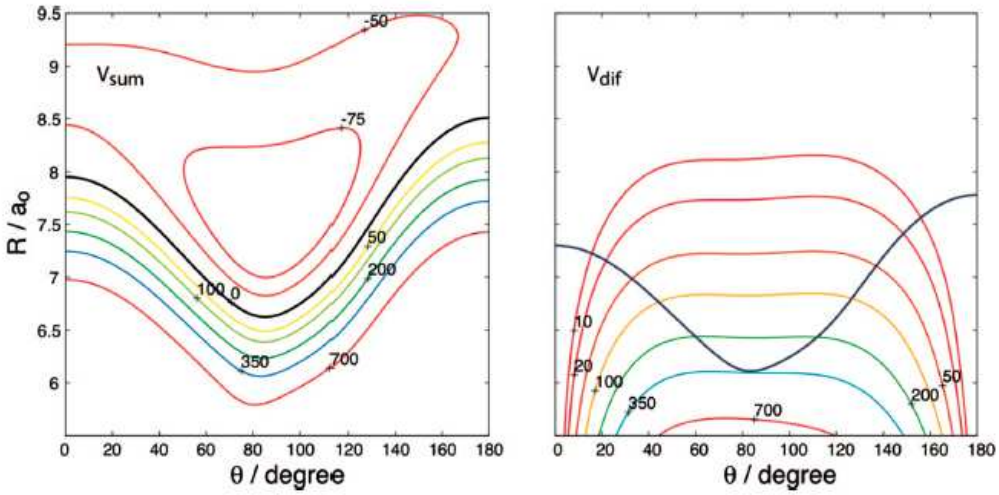

Figure 5.15 – Contour plots (in cm^{-1}) of the CN($A^2\Pi$, v = 3)-N_2 V_{sum} and V_{dif} PESs derived from the averaged A′ and A″ PESs in the previous figure. The $\theta = 0^o$ angle corresponds to the N-end of the CN molecule pointing towards the N_2 molecule. The heavy black contour in the V_{sum} PES separates the attractive and repulsive regions. The heavy blue contour in the V_{dif} PES corresponds to 300 cm^{-1}, which delineates the classical turning point at a collision energy of 300 cm^{-1}. Adapted from reference 206.

All three geometries in Figure 5.14 possess substantial anisotropy in the repulsive wall that favours a bent CN orientation. This is greater for the *A′* PESs and is more noticeable for geometry 1, where CN points directly towards N_2. The attractive minimum for geometry 1 is in a bent arrangement, whereas geometries 2 and 3 are linear. In each case this corresponds to a T-shaped geometry. The averaged V_{sum} and V_{dif} PESs mirror the angle-dependences of the individual interactions reasonably well and overall appear similar in general form to the CN($A^2\Pi$)-Ar PESs in Section 4.5.4. There is a deep T-shaped minimum and even character with near-symmetry. This results in the parity-dependent even/odd-Δj alternations predicted in reference 206 and observed in this study. A predominantly even PES is in accord with the argument of Dagdigian and co-workers of a leading quadrupole-quadrupole interaction for CN($A^2\Pi$)-N_2. This interaction has $\lambda = 4$ anisotropy, which induces both spin-orbit conserving and spin-orbit changing transitions within a given fine-structure manifold. It also couples Λ-

doublets of the same symmetry for even-Δj and opposite symmetry for odd-Δj, reproducing the measured $F\varepsilon$-propensities in Figure 5.13. In the Hund's case-(a) limit, spin-orbit changing transitions are enabled by the difference between the A' and A'' surfaces, which as seen in Figure 5.14 are quite different. Accordingly, the V_{dif} in Figure 5.15 has appreciable magnitude in regions accessible at thermal collisions energies. This again accounts for the sizeable fine-structure changing cross-sections predicted in the QS calculations and observed here. Clearly, the additional dimensions and asymmetry of the partner do not remove specific symmetry properties of the PESs or destroy any symmetry-related effects in the collision cross-sections (or MTEs). Nor does averaging over the orientation of N_2 appear to significantly reduce the anisotropy of the interaction.

The apparent insensitivity of inelastic scattering to the N_2 orientation is in contrast to recent findings of Kalugina *et al*. on the related CN($X^2\Sigma^+$)-H_2 system.[340] The full four-dimensional PES including all angles describing the relative orientation of the molecules was required to accurately reproduce the experimental state-to-state RET cross-sections. Similarly, Lester and co-workers found that the angular motions of OH and N_2 in the OH($X^2\Pi$)-N_2 complex are strongly correlated through dipole-quadrupole interactions.[341] Dagdigian and co-workers adopted their approximation for geometrical averaging in CN($A^2\Pi$)-N_2 from the previous work of Alexander and co-workers on the SiS-*para*-H_2 system.[207] There, PESs for three limiting orientations of the H_2 molecule in its lowest rotational state were constructed and spherically averaged to form a single PES on which coupled state calculations were then performed. To ascertain the error introduced by this averaging and from neglecting any rotational excitation of the H_2 molecule, the results were compared to several SiS de-excitation cross-sections determined from a PES that retained the angular dependence of the encounter and from QS calculations with H_2-(j = 2). The gross difference between the two sets of results amounted to less than 10%, leading the authors to conclude that the simplified angle-averaging approach does in fact provide an accurate description of the dynamics. The SiS-*para*-H_2 results were found to closely resemble calculations on the equivalent SiS-He system, which provides further evidence of how a small symmetric molecule can be approximately treated as a spherical target. Clearly, the ability of calculations on averaged PESs to reproduce experiment is not universal and may depend on the nature of the system.

In summary, the state-to-state RET cross-sections in this section, like the results from Chapter 4, indicate weakly interacting molecular systems that interplay between RET and quenching through an intricate balance between kinematic and potential effects, including long-range attractive forces. Contrary to previous experimental work[206, 224] and despite the additional dimensions and PESs available, small centrosymmetric molecules such as N_2, O_2 and CO_2, behave similarly to Ar in collisions with CN($A^2\Pi$) and can be broadly treated as spherical targets. This is supported by recent QS calculations for CN($A^2\Pi$)+N_2 on averaged PESs, which in this case appear to successfully characterise the interaction.[206] Further insight may be drawn from the more dynamically sensitive polarisation transfer measurements that are discussed next.

Orientation Transfer

The MTEs for the molecular colliders in Figure 5.13 closely resemble the general features of the state-to-state RET cross-sections and are very similar in form to the MTEs for Ar. Inelastic depolarisation is seen to be a significant pathway in these systems, compared to the much weaker elastic depolarisation observed in Section 4.6. The polarisation transfer results here must then further reflect the key discussion points that have been addressed so far for the molecular colliders. Strong parity-dependent even/odd-Δj oscillations persist for each collision system, where parity-conserving transitions preserve more of the initially prepared orientation, rotating with the same sense, whereas parity-changing transitions produce smaller MTEs. Like Ar, The $F\mathcal{E}$-changing Δj-oscillations exhibit deeper modulations that in some cases even change sign. This again demonstrates the near-symmetry of the interactions and the different radial dependences of the even-λ and odd-λ terms. In Section 5.4, through comparison of the experimental results to full QS calculations and literature QQT models, the events that lead to the parity-conserving and parity-changing transfer were shown to be fundamentally different, arising from interferences between collisions that sample the even-λ and odd-λ terms of the PESs at particular impact parameters. These same collision mechanisms must be responsible for the parity effects observed with the molecular partners.

The oscillations are typically weaker for the molecular colliders and appear to smooth out as Δj increases from negative to positive, especially for $F\mathcal{E}$-changing transitions, where the parity-changing MTEs have less tendency to change sign as Δj increases.

This implies that there is less difference in the even/odd character of the PESs. The blurring effect is much more apparent for O_2 and CO_2, and could be a result of averaging over the additional dimensions of the molecular partners introducing asymmetry, with O_2 (r_{OO} = 1.21 Å) and CO_2 (r_{OCO} = 2.32 Å) having larger stereochemical sizes compared compared to N_2 (r_{NN} = 1.10 Å). It could also be another manifestation of the inelastic quenching pathways of O_2 and CO_2, where a preferred interaction geometry averages over particular transitions. Although there was no immediate evidence of this when looking at the elastic depolarisation cross-sections in Section 4.6, it may effect more strongly the MTEs here that represent inelastic polarisation removal.

There is a preference to conserve polarisation with conservation of fine-structure, with the $F\varepsilon$-conserving transitions generally preserving more orientation than the $F\varepsilon$-changing transitions for all colliders. This again comes from being near the Hund's case-(a) limit. From looking at Figure 5.13, the order of orientation for each collider during RET appears to be N_2 > CO_2 > O_2 > Ar. For $F\varepsilon$-changing RET, this order becomes N_2 > O_2 > CO_2 > Ar. Therefore, N_2 is consistently the best collider at preserving the initial orientation, whilst Ar is the worst. The differences between polarisation transfer abilities could be due to subtle differences in the interaction potentials and exploring different regions of the PESs, long-range intermolecular forces and the availability of multiple inelastic removal channels, as has already been addressed in detail for the rest of the results in this thesis. For example, the comparison of RET for N_2 and O_2 is often attributed to the relative magnitudes of their quadrupole moments.[88, 134, 306-309] The distinctly similar behaviour of the CO_2 and O_2 systems more than likely comes from the competition between RET and total quenching, where strongly interacting molecules may irreversibly disappear down a hole to the ground state, or possibly react.

The polarisation transfer results in this section present further evidence of how N_2, O_2 and CO_2 behave similarly to Ar in collisions with CN($A^2\Pi$), reproducing the general trends observed in Section 5.4. This further implies that they have similar interaction potentials to CN($A^2\Pi$)-Ar and supports the theoretical work and approximations made by Dagdigian and co-workers for CN($A^2\Pi$)-N_2 in reference 206. The NO($X^2\Pi$)+D_2 DCS measurements of Stolte and co-workers demonstrate how it is certainly not uncommon to see molecular species act as rare gases during molecular collisions, and

indeed there are other notable examples of RET studies.[36, 203, 204] Parity effects may therefore be a dynamically fundamental property of $^2\Pi$ systems.

5.5.3 Summary

The key conclusions from this section are listed below.

i. The experimental investigation of state-to-state RET and polarisation transfer in CN($A^2\Pi$) has been extended to molecular partners, namely N_2, O_2 and CO_2.

ii. The collisional evolution of the prepared rotational population and orientation from j = 6.5 F_1e to j' F_1e and j' F_1f product levels for $\Delta j \leq |4|$ was followed using the same experimental protocol and kinetic analysis methods as for CN($A^2\Pi$)+Ar. The RET rate constants were converted to thermal cross-sections, $\sigma^{(0)}_{j\rightarrow j'}$ to allow for absolute comparison of the colliders.

iii. The molecular partners exhibit overall very similar behaviour to Ar, with inelastic depolarisation again shown to be significant.

iv. The relative magnitudes of the $\sigma^{(0)}_{j\rightarrow j'}$ are broadly N_2 > Ar > O_2 > CO_2. There is further evidence of enhanced quenching channels for O_2 and CO_2 when comparing the results to Chapter 4. The MTEs possibly hint at a preferred quenching geometry.

v. Substantial parity-dependent even/odd-Δj alternations in $\sigma^{(0)}_{j\rightarrow j'}$ and $E^{(1)}(j, j')$ are prominent for all colliders, reflecting the preferred conservation of total parity. The alternations are again much more pronounced for the MTEs, even changing sign for particular $F\varepsilon$-changing parity-changing transitions.

vi. The Δj-alternations imply a dominance of even-λ terms in the PESs from near-symmetrical interactions, despite the additional molecular degrees of freedom.

vii. The alternations are generally weaker than for Ar, appearing to blur out as Δj increases from negative to positive. This is more noticeable for the $F\varepsilon$-changing MTEs and especially for O_2 and CO_2. This could be an effect of

averaging over the molecular geometries, but also of quenching for O_2 and CO_2.

viii. The collision mechanisms that lead to parity-conserving and parity-changing transitions must ultimately be the same as for CN($A^2\Pi$)+Ar.

ix. The molecular colliders are efficient at causing spin-orbit transfer ($F\varepsilon$-changing transitions), more so than Ar. This suggests that the molecular V_{dif} potentials have larger magnitudes in the regions accessible at thermal collision energies.

x. Despite its open-shell electronic structure and availability of multiple coupled PESs, O_2 is no better at spin-orbit excitation than the rest of the colliders, especially N_2.

xi. The larger N_2 RET cross-sections compared to O_2 and differences in MTEs could be due to the larger quadrupole moment of N_2 *versus* O_2 and the influence of quenching in the latter.

xii. The results suggest weakly interacting systems that balance between potential and kinematic effects with competing inelastic pathways and possible influences from long-range intermolecular forces. Strongly attractive anisotropic interactions that may be expected with O_2 and CO_2 could be removed through quenching.

xiii. The overall similar behaviour of the molecular partners to Ar suggests that in general, small centrosymmetric molecules, such as N_2, O_2 and CO_2, may be treated as spherical targets. This is in stark disagreement with previous experiments of Dagdigian and co-workers, but in good agreement with their CN($A^2\Pi$)+N_2 QS calculations on spherically-averaged PESs, which have been outlined here.[206, 224]

xiv. Therefore, despite the previous conclusions of Dagdigian and co-workers, it is proposed that approximate QS calculations do in fact work well. However, such angle-averaging approaches have been shown not to be universal and may depend on the nature of the system.

xv. Parity effects may be ubiquitous to $^2\Pi$ systems of near-homonuclear symmetry.

Chapter 6

Conclusions and Future Directions

6.1 Conclusions

This thesis set out to correlate the transfer and removal mechanisms of polarised rotational angular momentum in the CN($A^2\Pi$) radical upon collisions with Ar and molecular colliders N_2, O_2 and CO_2. To achieve this, the novel and highly sensitive FMS cw-probe technique was employed in a ns-pulsed pump OODR configuration within a thermalised experimental cell. The results for the CN($A^2\Pi$)+Ar system were compared to complementary exact QS calculations on *ab initio* PESs to provide a deeper dynamical insight into the fundamental collision processes and vigorously test the latest state-of-the-art scattering theory. The study was divided into two main parts.

Firstly, the total removal and depolarisation of rotational angular momentum in CN($A^2\Pi$, v = 4, j, F_1e)+Ar was interrogated. Fitting the carefully processed experimental data to a single exponential model failed to properly reproduce the observed near-exponential population and multimodal polarisation decays. Instead, a three-level kinetic model gave the minimum required complexity, which accounted for reversible transfer of population, orientation and alignment between the initial (prepared) level and nearby product states, with depolarisation permissible in both. Irreversible loss to unobserved levels could also occur. Whilst the measured collisional depolarisation was fast on the timescale of population removal, most of this actually comprised inelastic depolarisation. Elastic depolarisation was concluded to be a relatively minor process in comparison.

Complementary full QS calculations were performed by collaborators on the best previous CN($A^2\Pi$, v = 3)-Ar (B-W) and new CN($A^2\Pi$, v = 4)-Ar (B-K) PESs. There was overall good agreement between experiment and theory, with a ~10% – 15% over-prediction of the population removal rate constants from the B-K PESs and slightly slower computed elastic depolarisation rate constants that possess an experimentally unobserved monotonic *j*-depenedence. Conversion of the measured total removal rate constants to collision radii, and the negative collision energy dependence of the theoretical predicted cross-sections indicated that RET is enabled by the attractive regions of the PESs. The primary difference between the B-W and B-K PESs is the considerably deeper attractive well in the latter, specifically the isotropic V_{00} term. The better agreement of the older PESs with the experimental population removal was concluded to be fortuitous, whilst the slight over-prediction of the B-K PESs demonstrates how even highly averaged quantities are extremely sensitive to the form of the potential. In general, the B-K PESs were concluded to represent the system well. Faster predicted elastic depolarisation at higher *j* suggested slight imperfections in the anisotopy of the attractive regions of the PESs.

A complete ME simulation using the B-K QS results for j = 6.5 F_1e closely reproduced the observed experimental behaviour, confirming inelastic depolarisation to be a significant channel and highlighting the importance of multiple collisional effects in this type of measurement when sensitive to both polarised and unpolarised molecules. It was proposed that the observed behaviour in CN($A^2\Pi$)+Ar draws from a simple balance between kinematic and potential effects, mediated by weak attractive forces, with a small but significant contribution from the V_{dif} PES.

The collisional removal and depolarisation of rotational angular momentum in CN($A^2\Pi$) by N_2, O_2 and CO_2 was then experimentally monitored. The optimised three-level kinetic model was used to derive thermally averaged total removal and orientation elastic depolarisation cross-sections. The CN($A^2\Pi$) population removal efficiency for all the colliders studied lay in the order CO_2 > N_2 > O_2 > Ar, which approximately correlated with the long-range attractive interactions of each collision pair, determined by the relative magnitudes of the polarisabilities and lowest-order electrostatic forces. Further evidence of this came from the consistently larger depolarisation cross-sections for N_2 compared to O_2. Decomposition of the kinetic analysis and comparison to literature quenching rate constants revealed additional rapid removal channels for O_2

and CO_2, likely to be EET to $CN(X^2\Sigma^+)$, which may proceed *via* a preferred quenching geometry, although there was no clear signature of this in the depolarisation data. The quenching channels were found to be supressed for Ar and N_2, which were instead dominated by reversible RET to nearby rotational levels. Overall, elastic depolarisation by the molecular partners was very similar to that by Ar, with no *j*-dependence and very slow in competition with much stronger inelastic pathways. This seems to be a common observation in the kinematically related molecule-molecule systems. As such, the molecular colliders were suggested to have similar $CN(A^2\Pi)$ interaction potentials to Ar, supported by recent orientation-averaged $CN(A^2\Pi)$-N_2 PESs of Dagdigian and co-workers and corresponding total removal cross-sections.[206] It was therefore proposed that small centrosymmetric molecules, such as N_2, O_2 and CO_2, colliding with $CN(A^2\Pi)$, could approximately be treated as spherical targets.

In the second part of this work, the FMS OODR technique was re-employed in the first ever systematic experimental and theoretical investigation of state-to-state RET and transfer of orientation in $CN(A^2\Pi, v = 4)$+Ar. Three-level fits to the initially prepared states (j = 6.5 F_1e and j = 10.5 F_1f) and single exponential fits to the collisionally populated product states ($\Delta j \leq |5|$, $F\varepsilon$-conserving and $F\varepsilon$-changing) revealed the time-dependence of the population and orientation, from which the state-to-state RET rate constants and MTEs were derived. Full QS calculations on the B-K PESs exhibited typically excellent, near-quantitative agreement with experiment. This again demonstrates the level of accuracy of the PESs. The results were consistent with the previous conclusions that inelastic depolarisation is a significant channel in $CN(A^2\Pi)$+Ar.

Parity-dependent alternations with even/odd-Δj in the observed and predicted $k^{(0)}_{j\rightarrow j'}$, and most strikingly in $E^{(1)}(j,j')$ (often accompanied with a change in *sign* of orientation for $F\varepsilon$-changing parity-changing transitions), were attributed to the near-homonuclear nature of the $CN(A^2\Pi)$-Ar PESs. Expansion of the PESs into radial and angular terms facilitates inspection of the symmetry properties of the interaction, where it becomes apparent that parity-conserving transitions are enabled by the even-λ terms and parity-changing transitions by the odd-λ terms. The near-symmetry of the interaction constrains the surfaces to be predominently even in character, leading to very different radial dependencies of the even-λ and odd-λ components and a preference for parity-

conservation. The excellent agreement between experiment and theory implies that the PESs reproduce the even/odd character of the interaction well. The QS calculations indicated that the dynamics of the collisions that produce these different outcomes are fundamentally different. The origin of the Δj-alternations were suggested to result from intereferences between collisions that sample the even-λ and odd-λ angular terms of the PESs. A semi-classical QQT approach to the scattering dynamics may help to rationalise the angular dependencies of the different contributing trajectories.[34-36, 45, 153-158] A noticeable propensity in both $k^{(0)}_{j\rightarrow j'}$ and $E^{(1)}(j,j')$ to conserve spin-orbit label was attributed the relative ranges of the V_{sum} and V_{dif} PESs close to the Hund's case-(a) coupling limit, where the V_{sum} PES enables spin-orbit conservation and the V_{dif} mediates spin-orbit transfer. The V_{dif} potential by symmetry lacks the lowest order odd-λ term in the PES angular expansions, resulting larger modulated Δj-alternations for $F\varepsilon$-changing transitions.

The oscillatory structure in the MTEs of $^2\Pi$ systems was first predicted in the 1980s by Alexander and co-workers.[20, 56] Similar parity-dependent behaviour was later reported in the measurements and calculations of state-to-state RET, polarisation transfer and DCSs in a variety of closely related $^2\Pi$+Rg systems, such as CN($A^2\Pi$, v = 3)+Ar, CaF($A^2\Pi$)+Ar and NO($X^2\Pi$)+Ar, He (and D_2).[15, 34-36, 45, 105, 153-158, 190, 194] This suggests that the marked parity effects are in fact a general feature of $^2\Pi$+Rg collisions. Current scattering theory is clearly capable of providing essentially near-quantitative agreement with experiment for this benchmark $^2\Pi$+Rg system.

The experimental study of state-to-state RET and polarisation transfer in CN($A^2\Pi$) was then extended to collisions with N_2, O_2 and CO_2. The time-dependence of the initial level (j = 6.5 F_1e) and collisionally populated product levels ($\Delta j \leq |4|$) for both $F\varepsilon$-conserving and $F\varepsilon$-changing transitions were fitted to three-level and single exponential kinetic models, respectively, to determine the thermal state-to-state RET cross-sections and orientation MTEs. Substantial parity-dependent even/odd-Δj alternations prevailed throughout, causing sign changes of the MTEs for particular transitions, although typically with weaker modulations than for Ar. This demonstrated the near-symmetry of the interactions, despite the added dimensions of the molecular partners, where even-λ terms still dominate due to the near-homonuclearity of the CN molecule. The same scattering mechanisms as for CN($A^2\Pi$)+Ar must then be involved, where parity-

conserving collisions are intrinsically different to parity-changing collisions, which may imply interferences between different scattering paths along the PESs.

The molecular colliders were efficient at spin-orbit excitation in $CN(A^2\Pi)$, implying that the V_{dif} is of larger magnitude in the regions accessible at thermal collision energies for these systems compared to Ar. However even with its open-shell electronic structure, O_2 was less efficient at spin-orbit transfer than N_2. This could be an effect of exploring the weakly interacting regions of the PESs and removal of strongly interacting molecules by quenching. Comparison of the state-to-state results of Chapter 5 with the total removal results of Chapter 4 provided more evidence about the quenching pathways of CO_2 and O_2 and the preferred RET channels of N_2 and Ar, as well as further gauging the influences of long-range intermolecular forces.

The results from Chapter 5 supported the findings that in general, small centrosymmetric molecules such as N_2, O_2 and CO_2 approximately act as spherical targets. This is in marked disagreement with the previous experimental observations of Dagdigian and co-workers for $CN(A^2\Pi)+N_2$ and CO_2 but is in good agreement with their QS calculations on spherically-averaged $CN(A^2\Pi)$-N_2 PESs.[206, 224] The asymmetry and inelasticity of the molecular partner do not greatly reduce the symmetry or anisotropy of the PESs, nor introduce further complexities. The QS calculations on approximate surfaces in this case appear to work well, although from other literature examples this was shown not to be universal and may depend on the nature of the system. Overall, the state-to-state RET and polarisation transfer results indicated weakly interacting systems with competing inelastic channels that balance between potential energy and kinematic effects. The observed parity-propensities appear to be a fundamental property of $CN(A^2\Pi)$ collisions, if not $^2\Pi$ systems in general.

In summary, collisions involving the $CN(A^2\Pi)$ radical are dominated by symmetry effects and are typically inelastic in nature. They are not purely repulsive and the attractive part of the PES is therefore important. Successful comparison to QS calculations on *ab initio* PESs has been central to understanding the $CN(A^2\Pi)+Ar$ system and interpreting the experimental results. Aside from different preferred population removal channels, the N_2, O_2 and CO_2 molecular colliders behave somewhat similarly to Ar. This work has demonstrated the capability and powerful nature of the FMS technique in studying the scalar and vector properties of molecular collisions. It

has also attested the synergism between experiment and theory in $^2\Pi$+Rg encounters, encouraging future application to $^2\Pi$+molecule systems. The research presented here has direct significance to combustion, atmospheric and astrochemical environments, allowing for example the input of collision rate constants into kinetic models. The research additionally impacts at a more fundamental level of chemistry and physics, providing a glimpse into the dynamical world of molecular collisions and interactions through correlation of nuclear motions.

6.2 Future Directions

The results from thesis have opened up future avenues of research into the collision dynamics of the CN($A^2\Pi$) radical. Using the current FMS experimental set-up, the role of long-range electrostatic forces and stereochemical size can be further investigated by measuring collisions with heteronuclear diatomics and polyatomics, for example CN($A^2\Pi$)+CO, NO, H_2O or $CHCl_3$. This would also provide a convenient route for comparing different partner RET *versus* quenching preferences, the effects of partner electronic structure, and perhaps most importantly the ubiquity of symmetry properties, particularly parity conservation. It would be interesting to see to what extent larger and more asymmetric colliders may be approximately treated as spherical targets. This will hopefully spur the computation of more refined molecular PESs and QS calculations.

There was substantial evidence for preferred quenching of CN($A^2\Pi$) by O_2 and CO_2, most likely occuring *via* EET to CN($X^2\Sigma^+$), compared to the dominant RET pathways for Ar and N_2. The next obvious step is therefore to prepare and probe a polarised rotational angular momentum in the CN($X^2\Sigma^+$) electronic ground state. Aside from the different electronic structure, namely the zero orbital angular momentum and resulting Hund's case-(b) rotational levels, CN($X^2\Sigma^+$) also has a relatively large dipole moment (1.3 D),[178] again making it interesting to compare the effect of stronger long-range interactions. There is no electronic quenching pathway available from CN($X^2\Sigma^+$), however the experiment may be sensitive to the flow of (depolarised) rotational angular momentum from the CN($A^2\Pi$) state. This has set the scene for a new international collaboration between the McKendrick-Costen group at Heriot-Watt University and the Halpern group at Howard University, USA.[342] The plan is to add a fourth laser, an Nd:YAG pumped dye laser, to the FMS experiment in order to implement stimulated

emission pumping (SEP) to prepare a rotational population and polarisation in an isolated CN($X^2\Sigma^+$, v'' = 1, $jf\varepsilon$) level. An example spectroscopic scheme (as displayed in Figure 6.1) would be to firstly photolyse ICN at 266 nm to generate nascent CN($X^2\Sigma^+$), then after thermal equilibration, employ polarised optical pumping on the $A^2\Pi \leftarrow X^2\Sigma^+$ (4,0) band to create a sample of polarised CN($A^2\Pi$, v' = 4, $jF\varepsilon$). After an optimised small time delay, a polarised dump laser in stimulated emission on the $A^2\Pi \rightarrow X^2\Sigma^+$ (4,1) band would then generate considerable population and rotational anisotropy in the desired CN($X^2\Sigma^+$, v'' = 1, $jf\varepsilon$) level. Finally, the tunable FMS cw-diode laser in absorption on the $A^2\Pi \leftarrow X^2\Sigma^+$ (5,1) band can sensitively probe the collisional evolution of the prepared ground state level. The new experiment would make use of equipment already available to each group, such as the correct diode laser head to work in the desired probe wavelength range, as well as a spare dye laser and necessary polarisation optics.

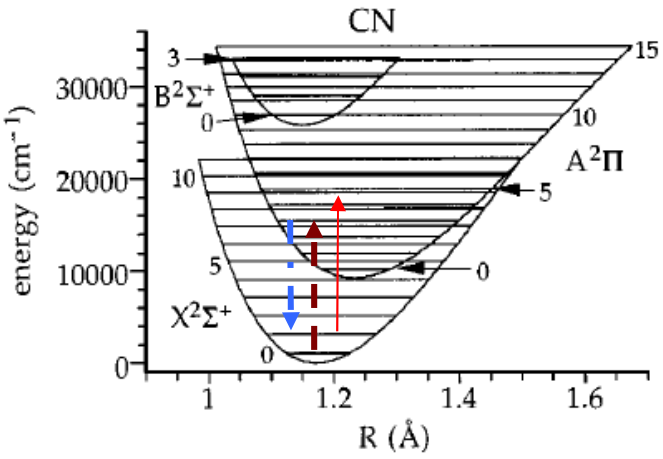

Figure 6.1 – An example SEP spectroscopic scheme displayed on low lying potential energy curves of the CN radical. The dashed arrows indicate SEP of $X^2\Sigma^+$, followed by cw-FM probing.[342]

The range of states that may be populated and probed is limited by the oscillator strength and effective Franck-Condon factors for the $A^2\Pi - X^2\Sigma^+$ band. This limits the suitable $A^2\Pi$ state vibrational levels to essentially v' = 3, 4 or 5. A preliminary set of experiments would involve optimising the new dump laser and checking that population is effectively removed from the CN($A^2\Pi$, v' = 4) state by monitoring the FM signal in stimulated emission on the $A^2\Pi \leftarrow X^2\Sigma^+$ (4,2) band, in the same manner as used in this thesis. One of the key advantages of using a resonant intermediate state is the fine-

structure and parity selectivity, as shown in Figure 6.2.[342] Measurements of $CN(X^2\Sigma^+)$+Ar could be further compared to high level QS calculations.

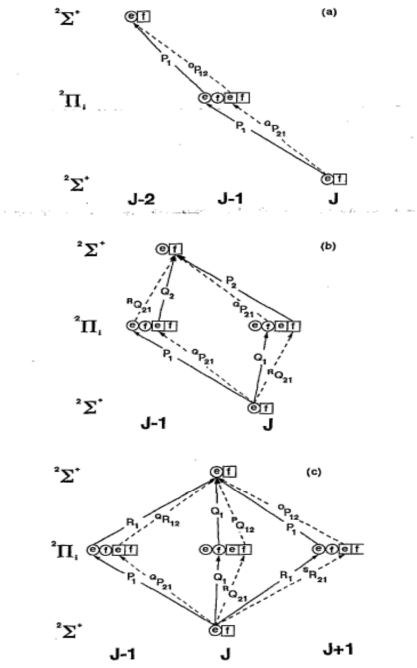

FIG. 2. Schematic illustration of allowed one-photon pathways for a $^2\Sigma^+ \leftarrow ^2\Sigma^+$ two-photon transition through a $^2\Pi_i$ intermediate state. F_1 levels are symbolized by circles, F_2 levels by squares; e/f indicates the parity of the level. (a) O_1 transitions. (b) $^QP_{21}$ transitions. (c) Q_1 transitions.

Figure 6.2 – One-photon paths for a $^2\Sigma$-$^2\Pi$-$^2\Sigma$ SEP transition, demonstrating fine-structure and parity selectivity. The F_1 levels are represented by circles and the F_2 levels by squares.[342]

Lastly, the FMS experiment could be reconfigured back to the multi-pass laser set-up to measure fully state-selected DCSs of nascent $CN(X^2\Sigma^+)$ or $CN(A^2\Pi)$ collisions, similar to what has been done previously in our group (see for example references 63, 64, 161 and 198). Although this is limited to linear laser polarisations, specific combinations of $jF\varepsilon \rightarrow j'F'\varepsilon'$ could be measured in order to check for scattering angle-resolved parity properties, such as the parity pair effect of adjacent Δj transitions ending in the same final parity, as observed by Stolte and co-workers in $NO(X^2\Pi)$+Rg systems,[34, 153-156, 158] first discussed in Section 1.7. The QQT model could then be invoked to help rationalise the results. This would follow nicely from the state-to-state RET and polarisation transfer studies presented in Chapter 5 and help answer remaining questions.

Bibliography

1. P. J. Dagdigian, in *Chemical Dynamics and Kinetics of Small Free Radicals*, edited by K. Liu and A. Wagner (World Scientific, Singapore, 1995), pp. 315-364.

2. R. D. Levine, *Molecular Reaction Dynamics*. (Cambridge University Press, Cambridge, UK, 2009).

3. G. Paterson, PhD Thesis, Heriot-Watt University (2010).

4. P. W. Atkins and J. C. de Paula, *Atkins' Physical Chemistry*. (Oxford University Press, Oxford, UK, 2006).

5. A. Schiffman and D. W. Chandler, *Int. Rev. Phys. Chem.* **14**, 371 (1995).

6. M. L. Costen, S. Marinakis and K. G. McKendrick, *Chem. Soc. Rev*. **37**, 732 (2008).

7. M. R. S. McCoustra, Lecture Series, Heriot-Watt University, Edinburgh, UK (2008).

8. H. J. Werner, P. J. Knowles, R. Lindh, F. R. Mandy, M. Schutz, P. Celani, T. Korona, G. Rauhut, R. D. Amos, A. Bernhardsson, A. Berning, D. L. Cooper, M. J. O. Deegan, A. J. dobbyn, F. Eckert, C. Hampel, G. Hetzer, A. W. Lloyd, S. J. McNicholas, W. Meyer, M. E. Mura, A. Nicklas, P. Palmieri, R. Pitzer, U. Schumann, H. Stoll, A. J. Stone, R. Tarroni and T. Thorsteinsson, MOLPRO version 2006.3, a package of *ab initio* computer programs, 2006, see http://www.molpro.net.

9. J. Kłos, M. H. Alexander, M. Brouard, C. J. Eyles and F. J. Aoiz, *J. Chem. Phys.* **129**, 054301 (2008).

10. R. N. Zare, *Angular Momentum: Understanding Spatial Aspects in Chemistry and Physics*. (John Wiley & Sons, Inc., New York, 1988).

11. A. Degli Esposti, A. Berning and H.-J. Werner, *J. Chem. Phys*. **103**, 2067 (1995).

12. G. Paterson, M. L. Costen and K. G. McKendrick, *Int. Rev. Phys. Chem*. **31**, 69 (2012).

13. H. J. Werner, B. Follmeg and M. H. Alexander, *J. Chem. Phys*. **89**, 3139 (1988).

14. H. J. Werner, B. Follmeg, M. H. Alexander and D. Lemoine, *J. Chem. Phys.* **91**, 5425 (1989).

15. M. H. Alexander, X. Yang, P. J. Dagdigian, A. Berning and H. J. Werner, *J. Chem. Phys*. **112**, 781 (2000).

16. A. J. Orr-Ewing and R. N. Zare, *Annu. Rev. Phys. Chem.* **45**, 315 (1994).

17. K. Blum, *Density Matrix Theory and Applications*, Second ed. (Plenum Press, New York, 1996).

18. F. J. Aoiz, M. Brouard, C. J. Eyles, J. Kłos and M. P. de Miranda, *J. Chem. Phys.* **130**, 044305 (2009).

19. G. Paterson, M. L. Costen and K. G. McKendrick, *Mol. Phys.* **109**, 2565 (2011).

20. M. H. Alexander and T. Orlikowski, *J. Chem. Phys.* **80**, 1506 (1984).

21. P. Beaud, T. Gerber, P. P. Radi, M. Tulej and G. Knopp, *Chem. Phys. Lett.* **373**, 251 (2003).

22. V. E. Bondybey and T. A. Miller, *J. Chem. Phys.* **69**, 3597 (1978).

23. N. K. Dabkara and P. M. Agrawal, *Chem. Phys. Lett.* **299**, 125 (1999).

24. D. A. Hostutler, T. C. Smith, G. D. Hager, G. C. McBane and M. C. Heaven, *J. Chem. Phys.* **120**, 7483 (2004).

25. T. C. Smith, D. A. Hostutler, G. D. Hager, M. C. Heaven and G. C. McBane, *J. Chem. Phys.* **120**, 2285 (2004).

26. M. A. Osborne and A. J. McCaffery, *J. Chem. Phys.* **101**, 5604 (1994).

27. A. J. McCaffery, Z. T. Alwahabi, M. A. Osborne and C. J. Williams, *J. Chem. Phys.* **98**, 4586 (1993).

28. V. Khare, D. J. Kouri and D. K. Hoffman, *J. Chem. Phys.* **74**, 2275 (1981).

29. V. Khare, D. J. Kouri and D. K. Hoffman, *J. Chem. Phys.* **76**, 4493 (1982).

30. S. Clare, A. J. Marks and A. J. McCaffery, *J. Chem. Phys.* **111**, 9287 (1999).

31. A. J. McCaffery and R. J. Marsh, *J. Chem. Phys.* **115**, 9771 (2001).

32. A. J. McCaffery, M. J. Proctor and B. J. Whitaker, *Annu. Rev. Phys. Chem.* **37**, 223 (1986).

33. M. H. Alexander, Personal Communication (2013).

34. A. Gijsbertsen, H. Linnartz, C. A. Taatjes and S. Stolte, *J. Am. Chem. Soc.* **128**, 8777 (2006).

35. A. Gijsbertsen, H. Linnartz, G. Rus, A. E. Wiskerke, S. Stolte, D. W. Chandler and J. Kłos, *J. Chem. Phys.* **123**, 224305 (2005).

36. A. Gijsbertsen, H. Linnartz and S. Stolte, *J. Chem. Phys.* **125**, 133112 (2006).

37. R. N. Porter, *Annu. Rev. Phys. Chem.* **25**, 317 (1974).

38. F. J. Aoiz, V. J. Herrero and V. S. Rabanos, *J. Chem. Phys.* **94**, 7991 (1991).

39. F. J. Aoiz, V. J. Herrero and V. S. Rabanos, *J. Chem. Phys.* **97**, 7423 (1992).

40. F. J. Aoiz, L. Bañares and V. J. Herrero, *J. Chem. Soc. Faraday Trans.* **94**, 2483 (1998).

41. F. J. Aoiz, J. E. Verdasco, V. J. Herrero, V. S. Rabanos and M. A. Alexander, *J. Chem. Phys.* **119**, 5860 (2003).

42. W. F. Hu and G. C. Schatz, *J. Chem. Phys.* **125**, 132301 (2006).

43. J. Kłos, G. Chalasinski, M. T. Berry, R. Bukowski and S. M. Cybulski, *J. Chem. Phys.* **112**, 2195 (2000).

44. M. Brouard, A. Bryant, Y. P. Chang, R. Cireasa, C. J. Eyles, A. M. Green, S. Marinakis, F. J. Aoiz and J. Kłos, *J. Chem. Phys.* **130**, 044306 (2009).

45. F. J. Aoiz, M. Brouard, C. J. Eyles, J. Kłos and M. P. d. Miranda, *J. Chem. Phys.* **130**, 044305 (2009).

46. M. Brouard, H. Chadwick, Y. P. Chang, R. Cireasa, C. J. Eyles, A. O. La Via, N. Screen, F. J. Aoiz and J. Kłos, *J. Chem. Phys.* **131**, 104307 (2009).

47. M. Brouard, H. Chadwick, Y. P. Chang, R. Cireasa and C. J. Eyles, *Phys. Scr.* **80**, 048120 (2009).

48. M. L. Costen, R. Livingstone, K. G. McKendrick, G. Paterson, M. Brouard, H. Chadwick, Y. P. Chang, C. J. Eyles, F. J. Aoiz and J. Kłos, *J. Phys. Chem. A* **113**, 15156 (2009).

49. M. H. Alexander, *J. Chem. Phys.* **76**, 5974 (1982).

50. M. H. Alexander, *Chem. Phys.* **92**, 337 (1985).

51. R. N. Dixon and D. Field, *Proc. Roy. Soc. London A* **368**, 99 (1979).

52. P. J. Dagdigian, M. H. Alexander and K. Liu, *J. Chem. Phys.* **91**, 839 (1989).

53. P. J. Dagdigian and M. H. Alexander, *J. Chem. Phys.* **130**, 094303 (2009).

54. P. J. Dagdigian and M. H. Alexander, *J. Chem. Phys.* **131**, 229902 (2009).

55. M. D. Rowe and A. J. McCaffery, *Chem. Phys.* **43**, 35 (1979).

56. M. H. Alexander and S. L. Davis, *J. Chem. Phys.* **78**, 6754 (1983).

57. P. J. Dagdigian and M. H. Alexander, *J. Chem. Phys.* **130**, 164315 (2009).

58. E. Hecht, *Optics*, 3rd ed. (Addison Wesley, 1997).

59. http://www.arnoldsat.com/polarizations.jpg, (2013).

60. W. R. Gentry, *Atomic and Molecular Beam Methods*. (Oxford University Press, Oxford, U.K., 1988).

61. L. Scharfenberg, J. Kłos, P. J. Dagdigian, M. H. Alexander, G. Meijer and S. Y. T. Van De Meerakker, *Phys. Chem. Chem. Phys.* **12**, 10660 (2010).

62. J. J. Gilijamse, S. Hoekstra, S. Y. T. van der Meerakker, G. C. Groenenboom and G. Meijer, *Science* **313**, 1617 (2006).

63. A. Alagappan, PhD Thesis, Heriot-Watt University (2007).

64. A. Alagappan, I. Ballingall, M. L. Costen and K. G. McKendrick, *J. Chem. Phys.* **126**, 041103 (2007).

65. R. J. Gordon and G. E. Hall, *Adv. Chem. Phys.* **96**, 1 (1996).

66. S. Rudic, C. Murray, D. Ascenzi, H. Anderson, J. N. Harvey and A. J. Orr-Ewing, *J. Chem. Phys.* **117**, 5692 (2002).

67. C. Murray and A. J. Orr-Ewing, *Int. Rev. Phys. Chem.* **23**, 435 (2004).

68. J. K. Pearce, C. Murray, P. N. Stevens and A. J. Orr-Ewing, *Mol. Phys.* **103**, 1785 (2005).

69. C. Murray, J. K. Pearce, S. Rudic, B. Retail and A. J. Orr-Ewing, *J. Phys. Chem. A* **109**, 11093 (2005).

70. K. L. Reid, A. J. McCaffery and B. J. Whitaker, *Phys. Rev. Lett.* **67**, 1937 (1991).

71. A. J. McCaffery, K. L. Reid and B. J. Whitaker, *Phys. Rev. Lett.* **61**, 2085 (1988).

72. A. J. McCaffery, *Chem. Soc. Rev.* **25**, 49 (1996).

73. K. P. Liu, *Annu. Rev. Phys. Chem.* **52**, 139 (2001).

74. A. Teslja and J. J. Valentini, *J. Chem. Phys.* **125**, 132304 (2006).

75. P. A. Barrass, P. Sharkey and I. W. M. Smith, *Phys. Chem. Chem. Phys.* **5**, 1400 (2003).

76. P. J. Dagdigian, *Annu. Rev. Phys. Chem.* **48**, 95 (1997).

77. M. C. van Beek and J. J. ter Meulen, *J. Chem. Phys.* **115**, 1843 (2001).

78. M. C. van Beek, J. J. ter Meulen and M. H. Alexander, *J. Chem. Phys.* **113**, 628 (2000).

79. M. C. van Beek, J. J. ter Meulen and M. H. Alexander, *J. Chem. Phys.* **113**, 637 (2000).

80. J. B. Halpern, R. Dopheide and H. Zacharias, *J. Phys. Chem.* **99**, 13611 (1995).

81. A. D. Rudert, J. Martin, W. B. Gao, J. B. Halpern and H. Zacharias, *J. Chem. Phys.* **111**, 9549 (1999).

82. A. D. Rudert, J. Martin, W. B. Gao, H. Zacharias and J. B. Halpern, *J. Chem. Phys.* **112**, 9749 (2000).

83. N. A. Jackson, C. J. Randall and K. G. McKendrick, *Chem. Phys.* **233**, 45 (1998).

84. N. A. Jackson, C. W. Watson and K. G. McKendrick, *Chem. Phys. Lett.* **243**, 564 (1995).

85. S. Singleton and K. G. McKendrick, *J. Phys. Chem.* **97**, 1389 (1993).

86. K. G. McKendrick, *J. Chem. Soc. Faraday Trans.* **94**, 1921 (1998).

87. http://www.forbrf.lth.se/english/research/measurement_methods/laser_induced_fluorescence_lif/, (2008).

88. D. A. V. Kliner and R. L. Farrow, *J. Chem. Phys.* **110**, 412 (1999).

89. A. Moise, R. Cireasa, D. H. Parker and J. J. ter Meulen, *J. Chem. Phys.* **125**, 204315 (2006).

90. A. Moise, D. H. Parker and J. J. ter Meulen, *J. Chem. Phys.* **126**, (2007).

91. R. Cireasa, A. Moise and J. J. ter Meulen, *J. Chem. Phys.* **123**, 64310 (2005).

92. R. Cireasa, M. C. van Beek, A. Moise and J. J. ter Meulen, *J. Chem. Phys.* **122**, 074319 (2005).

93. J. Kłos, F. J. Aoiz, R. Cireasa and J. J. ter Meulen, *Phys. Chem. Chem. Phys.* **6**, 4968 (2004).

94. M. C. van Beek, G. Berden, H. L. Bethlem and J. J. ter Meulen, *Phys. Rev. Lett.* **86**, 4001-4004 (2001).

95. M. C. van Beek, K. Schreel and J. J. ter Meulen, *J. Chem. Phys.* **109**, 1302 (1998).

96. K. Schreel and J. J. ter Meulen, *J. Phys. Chem. A* **101**, 7639 (1997).

97. K. Schreel and J. J. terMeulen, *J. Chem. Phys.* **105**, 4522 (1996).

98. K. Schreel, J. Schleipen, A. Eppink and J. J. Ter meulen, *J. Chem. Phys.* **99**, 8713 (1993).

99. C. F. Kaminski, B. Lofstedt, R. Fritzon and M. Alden, *Opt. Commun.* **129**, 38 (1996).

100. E. A. Brinkman and D. R. Crosley, *J. Phys. Chem. A* **108**, 8084 (2004).

101. A. Jorg, U. Meier, R. Kienle and K. Kohse-Hoinghaus, *Appl. Phys. B* **55**, (1992).

102. A. Degli Esposti and H.-J. Werner, *J. Chem. Phys.* **93**, 3351 (1990).

103. B. Abel, N. Lange, F. Reiche and J. Troe, *J. Chem. Phys.* **110**, 1389 (1999).

104. C. D. Pibel and C. B. Moore, *J. Chem. Phys.* **93**, 4804 (1990).

105. J. B. Norman and R. W. Field, *J. Chem. Phys.* **92**, 76 (1990).

106. S. J. Silvers, R. A. Gottscho and R. W. Field, *J. Chem. Phys.* **74**, 6000 (1981).

107. M. Brouard, A. Bryant, I. Burak, S. Marinakis, F. Quadrini, I. A. Garcia and C. Vallance, *Mol. Phys.* **103**, 1693 (2005).

108. J. B. Halpern, R. Dopheide and H. Zacharias, *Astrophys. Space Sci.* **236**, 19 (1996).

109. T. G. A. Heijmen, R. Moszynski, P. E. S. Wormer, A. van der Avoird, A. D. Rudert, J. B. Halpern, J. Martin, W. B. Gao and H. Zacharias, *J. Chem. Phys.* **111**, 2519 (1999).

110. Y. H. Huang, R. C. Lu and J. B. Halpern, *Appl. Opt.* **32**, 981 (1993).

111. G. O. Sitz and R. L. Farrow, *J. Chem. Phys.* **101**, 4682 (1994).

112. G. O. Sitz and R. L. Farrow, *J. Chem. Phys.* **103**, 489 (1995).

113. J. W. Walewski, K. Nyholm, A. Dreizler and M. Alden, *Appl. Spectrosc.* **58**, 238 (2004).

114. K. Danzmann, K. Grutzmacher and B. Wende, *Phys. Rev. Lett.* **57**, 2151 (1986).

115. W. G. Tong and E. S. Yeung, *Anal. Chem.* **57**, 70 (1985).

116. G. Zizak, J. Lanauze and J. D. Winefordner, *Appl. Opt.* **24**, 3319 (1985).

117. K. Nyholm, *Opt. Commun.* **111**, 66 (1994).

118. K. Nyholm, R. Fritzon and M. Alden, *Opt. Lett.* **18**, 1672 (1993).

119. K. Nyholm, R. Fritzon and M. Alden, *Appl. Phys. B* **59**, 37 (1994).

120. K. Nyholm, R. Fritzon, N. Georgiev and M. Alden, *Opt. Commun.* **114**, 76 (1995).

121. K. Nyholm, M. Kaivola and C. G. Aminoff, *Appl. Phys. B* **60**, 5 (1995).

122. K. Nyholm, R. Maier, C. G. Aminoff and M. Kaivola, *Appl. Opt.* **32**, 919 (1993).

123. S. Mukamel, *Principles of Nonlinear Optical Spectroscopy*. (Oxford University Press, Oxford, 1995).

124. M. L. Costen, H. J. Crichton and K. G. McKendrick, *J. Chem. Phys.* **120**, 7910 (2004).

125. M. L. Costen and K. G. McKendrick, *J. Chem. Phys.* **122**, 164309 (2005).

126. S. Marinakis, G. Paterson, J. Kłos, M. L. Costen and K. G. McKendrick, *Phys. Chem. Chem. Phys.* **9**, 4414 (2007).

127. S. Marinakis, G. Paterson, G. Richmond, M. Rockingham, M. L. Costen and K. G. McKendrick, *J. Chem. Phys.* **128**, 121101 (2008).

128. G. Paterson, S. Marinakis, M. L. Costen and K. G. McKendrick, *Phys. Chem. Chem. Phys.* **11**, 8813 (2009).

129. G. Paterson, S. Marinakis, M. L. Costen and K. G. McKendrick, *Phys. Scr.* **80**, 048111 (2009).

130. G. Paterson, S. Marinakis, M. L. Costen, K. G. McKendrick, J. Kłos and R. Tobola, *J. Chem. Phys.* **129**, 074304 (2008).

131. G. Paterson, S. Marinakis, M. L. Costen, K. G. McKendrick, J. Kłos and R. Tobola, *J. Chem. Phys.* **131**, 159901 (2009).

132. G. Paterson, S. Marinakis, J. Kłos, M. L. Costen and K. G. McKendrick, *Phys. Chem. Chem. Phys.* **11**, 8804 (2009).

133. H. J. Crichton, M. L. Costen and K. G. McKendrick, *J. Chem. Phys.* **119**, 9461 (2003).

134. A. Schiffman and D. J. Nesbitt, *J. Chem. Phys*. **100**, 2677 (1994).

135. S. Benec'h, J. Buldyreva and A. Chrysos, *J. Mol. Spectrosc*. **210**, 8 (2001).

136. G. Paterson, A. Relf, M. L. Costen, K. G. McKendrick, M. H. Alexander and P. J. Dagdigian, *J. Chem. Phys*. **135**, 234304 (2011).

137. C. M. Wolfe, S. Ashman, J. Bai, B. Beser, E. H. Ahmed, A. M. Lyyra and J. Huennekens, *J. Chem. Phys*. **134**, 174301 (2011).

138. P. H. Vaccaro, F. Temps, S. Halle, J. L. Kinsey and R. W. Field, *J. Chem. Phys*. **88**, 4819 (1988).

139. R. J. Wilson and A. J. McCaffery, *Chem. Phys. Lett*. **261**, 195 (1996).

140. A. J. McCaffery and R. J. Wilson, *J. Phys. B* **30**, 5773 (1997).

141. S. Antonova, A. Lin, A. P. Tsakotellis and G. C. McBane, *J. Chem. Phys*. **110**, 2384 (1999).

142. S. Antonova, A. Lin, A. P. Tsakotellis and G. C. McBane, *J. Chem. Phys*. **110**, 11742 (1999).

143. A. Lin, S. Antonova, A. P. Tsakotellis and G. C. McBane, *J. Phys. Chem. A* **103**, 1198 (1999).

144. K. T. Lorenz, D. W. Chandler and G. C. McBane, *J. Phys. Chem. A* **106**, 1144 (2002).

145. G. C. McBane and S. M. Cybulski, *J. Chem. Phys*. **110**, 11734 (1999).

146. S. L. Davis and M. H. Alexander, *J. Chem. Phys*. **78**, 800 (1983).

147. M. N. R. Ashfold, N. H. Nahler, A. J. Orr-Ewing, O. P. J. Vieuxmaire, R. L. Toomes, T. N. Kitsopoulos, I. A. Garcia, D. A. Chestakov, S. M. Wu and D. H. Parker, *Phys. Chem. Chem. Phys*. **8**, 26 (2006).

148. K. Thomas Lorenz, D. W. Chandler, J. W. Barr, W. Chen, G. L. Barnes and J. I. Cline, *Science* **293**, 2063 (2001).

149. E. A. Wade, K. T. Lorenz, D. W. Chandler, J. W. Barr, G. L. Barnes and J. I. Cline, *Chem. Phys*. **301**, 261 (2004).

150. J. J. Kay, G. Paterson, M. L. Costen, K. E. Strecker, K. G. McKendrick and D. W. Chandler, *J. Chem. Phys*. **134**, 091101 (2011).

151. J. J. Kay, J. D. Steill, J. Kłos, G. Paterson, M. L. Costen, K. E. Stecker, K. G. McKendrick, M. H. Alexander and D. W. Chandler, *Mol. Phys*. **110**, 1693 (2012).

152. J. D. Steill, J. J. Kay, G. Paterson, T. R. Sharples, J. Kłos, M. L. Costen, K. E. Strecker, K. G. McKendrick, M. H. Alexander and D. W. Chandler, *J. Phys. Chem. A* **117**, 8163 (2013).

153. C. J. Eyles, M. Brouard, H. Chadwick, F. J. Aoiz, J. Kłos, A. Gijsbertsen, X. Zhang and S. Stolte, *Phys. Chem. Chem. Phys*. **14**, 5420 (2012).

154. C. J. Eyles, M. Brouard, H. Chadwick, B. Hornung, B. Nichols, C. H. Yang, J. Kłos, F. J. Aoiz, A. Gijsbertsen, A. E. Wiskerke and S. Stolte, *Phys. Chem. Chem. Phys*. **14**, 5403 (2012).

155. C. J. Eyles, M. Brouard, C. H. Yang, J. Kłos, F. J. Aoiz, A. Gijsbertsen, A. E. Wiskerke and S. Stolte, *Nature Chem*. **3**, 597 (2011).

156. J. Kłos, F. J. Aoiz, J. E. Verdasco, M. Brouard, S. Marinakis and S. Stolte, *J. Chem. Phys*. **127**, 031102 (2007).

157. M. Brouard, H. Chadwick, C. J. Eyles, B. Hornung, B. Nichols, F. J. Aoiz, P. G. Jambrina and S. Stolte, *J. Chem. Phys*. **138**, 104310 (2013).

158. M. Brouard, H. Chadwick, C. J. Eyles, B. Hornung, B. Nichols, F. J. Aoiz, P. G. Jambrina, S. Stolte and M. P. de Miranda, *J. Chem. Phys*. **138**, 104309 (2013).

159. M. L. Costen, S. W. North and G. E. Hall, *J. Chem. Phys*. **111**, 6735 (1999).

160. S. W. North and G. E. Hall, *Annu. Rev. Phys. Chem*. **51**, 243 (2000).

161. A. Alagappan, M. L. Costen and K. G. McKendrick, *Spectrochim. Acta Part A* **63**, 910 (2006).

162. G. Hancock, G. Richmond, G. A. D. Ritchie, S. Taylor, M. L. Costen and G. E. Hall, *Mol. Phys*. **108**, 1083 (2010).

163. W. H. Fisher, T. Carrington, S. V. Filseth, C. M. Sadowski and C. H. Dugan, *Chem. Phys*. **82**, 443 (1983).

164. W. Krieger, J. Hager and J. Pfab, *Chem. Phys. Lett*. **85**, 69 (1982).

165. M. D. Morse and K. F. Freed, *J. Chem. Phys*. **78**, 6045 (1983).

166. Y. Amatatsu, S. Yabushita and K. Morokuma, *J. Chem. Phys*. **100**, 4894 (1994).

167. M. L. Costen and G. E. Hall, *Phys. Chem. Chem. Phys*. **9**, 272 (2007).

168. Y. F. Wang and C. X. W. Qian, *J. Chem. Phys*. **100**, 2707 (1994).

169. I. Nadler, D. Mahgerefteh, H. Reisler and C. Wittig, *J. Chem. Phys*. **82**, 3885 (1985).

170. J. F. Black, E. Hasselbrink, J. R. Waldeck and R. N. Zare, *Mol. Phys*. **71**, 1143 (1990).

171. M. L. Costen and G. E. Hall, *Phys. Chem. Chem. Phys*. **7**, 1408 (2005).

172. D. H. Katayama, T. A. Miller and V. E. Bondybey, *J. Chem. Phys*. **71**, 1662 (1979).

173. R. C. Lu, Y. H. Huang and J. B. Halpern, *Astrophys. J*. **395**, 710 (1992).

174. M. R. Taherian and T. G. Slanger, *J. Chem. Phys*. **81**, 3814 (1984).

175. C. Snedden and D. L. Lambert, *Astrophys. J*. **259**, 381 (1982).

176. N. Duric, P. Erman and M. Larsson, *Phys. Scr*. **18**, 39 (1978).

177. M. Jeunehomme, *J. Chem. Phys*. **42**, 4086 (1965).

178. P. J. Knowles, H. J. Werner, P. J. Hay and D. C. Cartwright, *J. Chem. Phys.* **89**, 7334 (1988).

179. D. C. Cartwright and P. J. Hay, *Astrophys. J.* **257**, 383 (1982).

180. M. Larsson, P. E. M. Siegbahn and H. Agren, *Astrophys. J.* **272**, 369 (1983).

181. H. Lavendy, G. Gandara and J. M. Robbe, *J. Mol. Spectrosc.* **106**, 395 (1984).

182. C. W. Bauschlicher, S. R. Langhoff and P. R. Taylor, *Astrophys. J.* **332**, 531 (1988).

183. B. Nizamov, X. Yang, P. J. Dagdigian and M. H. Alexander, *J. Phys. Chem. A* **106**, 8345 (2002).

184. N. Furio, A. Ali and P. J. Dagdigian, *J. Chem. Phys.* **85**, 3860 (1986).

185. M. H. Alexander and G. C. Corey, *J. Chem. Phys.* **84**, 100 (1986).

186. W. M. Gelbart and K. F. Freed, *Chem. Phys. Lett.* **18**, 470 (1973).

187. G. Jihua, A. Ali and P. J. Dagdiagian, *J. Chem. Phys.* **85**, 7098 (1986).

188. A. Ali, G. Jihua and P. J. Dagdigian, *J. Chem. Phys.* **87**, 2045 (1987).

189. P. J. Dagdigian, D. Patelmisra, A. Berning, H. J. Werner and M. H. Alexander, *J. Chem. Phys.* **98**, 8580 (1993).

190. X. Yang, P. J. Dagdigian and M. H. Alexander, *J. Chem. Phys.* **112**, 4474 (2000).

191. R. Fei, H. M. Lambert, T. Carrington, S. V. Filseth, C. M. Sadowski and C. H. Dugan, *J. Chem. Phys.* **100**, 1190 (1994).

192. R. Fei, D. E. Adelman, T. Carrington, C. H. Dugan and S. V. Filseth, *Chem. Phys. Lett.* **232**, 547 (1995).

193. J. Z. Guo, C. M. Sadowski, Q. Gao and F. J. Morgan, *J. Chem. Phys.* **113**, 7276 (2000).

194. X. Yang and P. J. Dagdigian, *Chem. Phys. Lett.* **297**, 506 (1998).

195. J. Han, M. C. Heaven and U. Schnupf, *J. Chem. Phys.* **128**, 224309 (2008).

196. J. D. Han, M. C. Heaven, U. Schnupf and M. H. Alexander, *J. Chem. Phys.* **128**, 104308 (2008).

197. B. Nizamov, P. J. Dagdigian and M. H. Alexander, *J. Chem. Phys.* **115**, 8393 (2001).

198. A. Alagappan, I. Ballingall, M. L. Costen, K. G. McKendrick and G. Paterson, *Phys. Chem. Chem. Phys.* **9**, 747 (2007).

199. I. Ballingall, M. F. Rutherford, K. G. McKendrick and M. L. Costen, *Mol. Phys.* **108**, 847 (2010).

200. M. B. Yang and M. H. Alexander, *J. Chem. Phys.* **107**, 7148 (1997).

201. W. G. Lawrence, Y. L. Chen and M. C. Heaven, *J. Chem. Phys.* **107**, 7163 (1997).

202. S. Fei and M. C. Heaven, *J. Chem. Phys*. **98**, 753 (1993).

203. Y. L. Chen and M. C. Heaven, *J. Chem. Phys*. **109**, 5171 (1998).

204. Y. L. Chen and M. C. Heaven, *J. Chem. Phys*. **112**, 7416 (2000).

205. A. L. Kaledin, M. C. Heaven and J. M. Bowman, *J. Chem. Phys*. **110**, 10380 (1999).

206. A. Khachatrian, P. J. Dagdigian, D. I. G. Bennett, F. Lique, J. Kłos and M. H. Alexander, *J. Phys. Chem. A* **113**, 3922 (2009).

207. F. Lique, R. Tobola, J. Kłos, N. Feautrier, A. Spielfiedel, L. F. M. Vincent, G. Chalasinski and M. H. Alexander, *Astron. Astrophys*. **478**, 567 (2008).

208. M. R. Taherian and T. G. Slanger, *J. Chem. Phys*. **82**, 2511 (1985).

209. C. Conley, J. B. Halpern, J. Wood, C. Vaughn and W. M. Jackson, *Chem. Phys. Lett*. **73**, 224 (1980).

210. D. Lindackers, M. Burmeister and P. Roth, presented at the 2nd International Conference on Chemical Kinetics, Maryland, USA, 1989 (unpublished).

211. D. L. Yang and M. C. Lin, *The Chemical Dynamics and Kinetics of Small Molecules*, Part I, edited by K. Liu and A. Wagner (World Scientific, Singapore, 1995).

212. N. S. Wang, D. L. Yang, M. C. Lin and C. F. Melius, *Int. J. Chem. Kinet*. **23**, 151 (1991).

213. R. J. Balla and K. H. Casleton, *J. Phys. Chem*. **95**, 2344 (1991).

214. W. H. Feng and J. F. Hershberger, *J. Phys. Chem. A* **113**, 3523 (2009).

215. K. T. Rim and J. F. Hershberger, *J. Phys. Chem. A* **103**, 3721 (1999).

216. L. F. Phillips, *J. Phys. Chem. A* **102**, 31 (1998).

217. L. F. Phillips, I. W. M. Smith, R. P. Tuckett and C. J. Whitham, *Chem. Phys. Lett*. **183**, 254 (1991).

218. D. G. Sauder, D. Patelmisra and P. J. Dagdigian, *J. Chem. Phys*. **95**, 1696 (1991).

219. R. G. Macdonald, K. P. Liu, D. M. Sonnenfroh and D. J. Liu, *Can. J. Chem*. **72**, 660 (1994).

220. D. M. Sonnenfroh, R. G. Macdonald and K. P. Liu, *J. Chem. Phys*. **93**, 1478 (1990).

221. S. M. K. Brunet, J. Z. Guo, T. Carrington, S. V. Filseth and C. M. Sadowski, *J. Chem. Phys*. **116**, 3617 (2002).

222. K. M. Hickson, C. M. Sadowski and I. W. M. Smith, *Chem. Phys. Lett*. **372**, 443 (2003).

223. R. V. Olkhov and I. W. M. Smith, *Phys. Chem. Chem. Phys*. **8**, 5643 (2006).

224. A. Khachatrian and P. J. Dagdigian, *J. Phys. Chem. A* **113**, 13390 (2009).

225. S. M. Miller and D. C. Clary, *J. Chem. Phys*. **98**, 1843 (1993).

226. W. P. Hess and S. R. Leone, *J. Chem. Phys.* **86**, 3773 (1987).

227. R. S. Ram, L. Wallace and P. F. Bernath, *J. Mol. Spectrosc.* **263**, 82 (2010).

228. P. W. Atkins and R. S. Friedman, *Molecular Quantum Mechanics*, 4 ed. (Oxford University Press, Oxford, UK, 2008).

229. A. J. Alexander, M. Brouard, K. S. Kalogerakis and J. P. Simons, *Chem. Soc. Rev.* **27**, 405 (1998).

230. D. Cerny, R. Bacis, G. Guelachvili and F. Roux, *J. Mol. Spectrosc.* **73**, 154 (1978).

231. N. Banwell, *Fundamentals of Molecular Spectroscopy*, 3 ed. (McGraw-Hill Education, Maidenhead, UK, 1972).

232. J. Brown and A. Carrington, *Rotational Spectroscopy of Diatomic Molecules*. (Cambridge University Press, Cambridge, UK, 2003).

233. K. S. Song and E. C. Jung, *Appl. Spectrosc. Rev.* **38**, 395 (2003).

234. A. Yariv, *Optical Electronics*, 4 ed. (Oxford University Press, Oxford, 1990).

235. G. Bonfiglioli and P. Brovetto, *Appl. Opt.* **3**, 1417 (1964).

236. E. I. Moses and C. L. Tang, *Opt. Lett.* **1**, 115 (1977).

237. G. C. Bjorklund, *Opt. Lett.* **5**, 15 (1980).

238. G. C. Bjorklund, M. D. Levenson, W. Lenth and C. Ortiz, *Appl. Phys. B* **32**, 145 (1983).

239. M. Gehrtz, G. C. Bjorklund and E. A. Whittaker, *J. Opt. Soc. Am. B* **2**, 1510 (1985).

240. J. C. Bloch, R. W. Field, G. E. Hall and T. J. Sears, *J. Chem. Phys.* **101**, 1717 (1994).

241. B. C. Chang and T. J. Sears, *J. Chem. Phys.* **102**, 6347 (1995).

242. W. E. Moerner and L. Kador, *Phys. Rev. Lett.* **62**, 2535 (1989).

243. C. L. Tang and J. M. Telle, *J. Appl. Phys.* **45**, 4503 (1974).

244. S. A. Akhmanov, Y. D. Golyaev and S. V. Lantratov, Sov. *J. Quantum Electron* **8**, 758 (1978).

245. S. E. Harris, M. K. Oshman, B. J. McMurtry and E. O. Ammann, *Appl. Phys. Lett.* **7**, 185 (1965).

246. R. G. Brewer, *Physics Today* **30**, 50 (1977).

247. G. L. Eesley, M. D. Levenson and W. M. Tolles, *IEEE J. Quantum Electron.* **14**, 45 (1978).

248. A. Owyoung, *IEEE J. Quantum Electron.* **14**, 192 (1978).

249. J. E. Bjorkholm, E. H. Turner and D. B. Pearson, *Appl. Phys. Lett.* **26**, 564 (1975).

250. A. Abramovici, W. E. Althouse, R. W. P. Drever, Y. Gursel, S. Kawamura, F. J. Raab, D. Shoemaker, L. Sievers, R. E. Spero, K. S. Thorne, R. E. Vogt, R. Weiss, S. E. Whitcomb and M. E. Zucker, *Science* **256**, 325 (1992).

251. P. Fritschel, G. Gonzalez, B. Lantz, P. Saha and M. Zucker, *Phys. Rev. Lett.* **80**, 3181 (1998).

252. J. Ye, L. S. Ma and J. L. Hall, *J. Opt. Soc. Am. B* **15**, 6 (1998).

253. R. Wynands and A. Nagel, *Appl. Phys. B* **68**, 1 (1999).

254. T. C. Steimle, M. L. Costen, G. E. Hall and T. J. Sears, *Chem. Phys. Lett.* **319**, 363 (2000).

255. B. C. Chang, M. L. Costen, A. J. Marr, G. Ritchie, G. E. Hall and T. J. Sears, *J. Mol. Spectrosc.* **202**, 131 (2000).

256. J. Deppe, G. Friedrichs, H. J. Romming and H. G. Wagner, *Phys. Chem. Chem. Phys.* **1**, 427 (1999).

257. M. Votsmeier, S. Song, D. F. Davidson and R. K. Hanson, *Int. J. Chem. Kinet.* **31**, 445 (1999).

258. W. E. Sinclair, D. Pfluger, H. Linnartz and J. P. Maier, *J. Chem. Phys.* **110**, 296 (1999).

259. J. T. Bahns, C. C. Tsai, B. Ji, J. T. Kim, G. Zhao, W. C. Stwalley, J. C. Bloch and R. W. Field, *J. Mol. Spectrosc.* **186**, 222 (1997).

260. M. L. Costen, H. Katayanagi and G. E. Hall, *J. Phys. Chem. A* **104**, 10247 (2000).

261. W. Demtröder, *Laser Spectroscopy*. (Springer-Verlag, Berlin, 1981).

262. R. D. L. Kronig, *J. Opt. Soc. Am. Rev. Sci. Instrum.* **12**, 547 (1926).

263. H. A. Kramers, *Atti. Congr. Intern. Fis.* **2**, 545 (1927).

264. J. A. Silver, *Appl. Opt.* **31**, 707 (1992).

265. D. S. Bomse, A. C. Stanton and J. A. Silver, *Appl. Opt.* **31**, 718 (1992).

266. J. M. Supplee, E. A. Whittaker and W. Lenth, *Appl. Opt.* **33**, 6294 (1994).

267. S. W. North, X. S. Zheng, R. Fei and G. E. Hall, *J. Chem. Phys.* **104**, 2129 (1996).

268. H. Meyer and S. R. Leone, *J. Chem. Phys.* **105**, 5858 (1996).

269. U. Fano and J. H. Macek, *Rev. Mod. Phys.* **45**, 553 (1973).

270. R. Uberna, R. D. Hinchliffe and J. I. Cline, *J. Chem. Phys.* **103**, 7934 (1995).

271. A. J. Bain and A. J. McCaffery, *J. Chem. Phys.* **83**, 2632 (1985).

272. I. R. Sims, J. L. Queffelec, A. Defrance, C. Rebrionrowe, D. Travers, P. Bocherel, B. R. Rowe and I. W. M. Smith, *J. Chem. Phys.* **100**, 4229 (1994).

273. A. J. Orr-Ewing, W. R. Simpson, T. P. Rakitzis and R. N. Zare, *Isr. J. Chem.* **34**, 95 (1994).

274. M. Brouard, H. Chadwick, Y. P. Chang, C. J. Eyles, F. J. Aoiz and J. Kłos, *J. Chem. Phys.* **135**, 084306 (2011).

275. M. L. Hause, G. E. Hall and T. J. Sears, *J. Mol. Spectrosc.* **253**, 122 (2009).

276. G. E. Hall, Personal Communication (2010).

277. A. J. Alexander, *J. Chem. Phys.* **123**, 194312 (2005).

278. G. Herzberg, *Molecular Spectra and Molecular Structure, Vol. I - Spectra of Diatomic Molecules*. (Van Nostrand Reinhold, New York, 1950).

279. K. P. Huber and G. Herzberg, *Constants of Diatomic Molecules*. (Van Nostrand Reinhold, New York, 1979).

280. M. D. Rowe and A. J. McCaffery, *Chem. Phys.* **34**, 81 (1978).

281. J. McCormack, A. J. McCaffery and M. D. Rowe, *Chem. Phys.* **48**, 121 (1980).

282. S. L. Coy, S. D. Halle, J. L. Kinsey and R. W. Field, *J. Mol. Spectrosc.* **153**, 340 (1992).

283. C. J. Randall, C. Murray and K. G. McKendrick, *Phys. Chem. Chem. Phys.* **2**, 461 (2000).

284. R. A. Kendall, T. H. Dunning Jr and R. J. Harrison, *J. Chem. Phys.* **96**, 6796 (1992).

285. T. H. Dunning Jr, *J. Chem. Phys.* **90**, 1007 (1989).

286. H. J. Werner and P. J. Knowles, *J. Chem. Phys.* **82**, 5053 (1985).

287. P. J. Knowles and H. J. Werner, *Chem. Phys. Lett.* **115**, 259 (1985).

288. H. J. Werner, *Adv. Chem. Phys.* **49**, 1 (1987).

289. H. J. Werner and P. J. Knowles, *J. Chem. Phys.* **89**, 5803 (1988).

290. P. J. Knowles and H. J. Werner, Chem. *Phys. Lett.* **145**, 514 (1988).

291. H. J. Werner and P. J. Knowles, *Theor. Chim. Acta* **78**, 175 (1990).

292. E. R. Davidson and D. W. Silver, *Chem. Phys. Lett.* **52**, 403 (1977).

293. S. F. Boys and F. Bernardi, *Mol. Phys.* **19**, 553 (1970).

294. A. Berning and H. J. Werner, *J. Chem. Phys.* **100**, 1953 (1994).

295. I. P. Hamilton and J. C. Light, *J. Chem. Phys.* **84**, 306 (1986).

296. S. J. McGurk, K. G. McKendrick, M. L. Costen, D. I. G. Bennett, J. kłos, M. H. Alexander and P. J. Dagdigian, *J. Chem. Phys.* **136**, 164306 (2012).

297. P. J. Knowles, C. Hampel and H.-J. Werner, *J. Chem. Phys.* **99**, 5219 (1993).

298. T. S. Ho and H. Rabitz, *J. Chem. Phys.* **104**, 2584 (1996).

299. T. Hollebeek, T. S. Ho and H. Rabitz, *Annu. Rev. Phys. Chem.* **50**, 537 (1999).

300. M. H. Alexander, G. E. Hall and P. J. Dagdigian, *J. Chem. Educ.* **88**, 1538 (2011).

301. HIBRIDON, a package of programs for the time-independent quantum treatment of inelastic collisions and photodissociation, written by M. H. Alexander, D. E. Manolopoulos, H. J. Werner, B. Follmeg, P. F. Vohralik, D. Lemoine, G. Corey, R. Gordon, B. Johnson, T. Orlikowski, A. Berning, A. Delgi-Esposti, C. Rist, P. J. Dagdigian, B. Pouilly, G. van der Sanden, M. Yang, F. de Weerd, S. Gregurick and J. Kłos.

302. I. W. M. Smith, *Kinetics and Dynamics of Elementary Gas Reactions.* (Buttersworths, London, 1980).

303. P. J. Dagdigian and M. H. Alexander, *J. Chem. Phys.* **130**, 204304 (2009).

304. J. H. Guo, A. Ali and P. J. Dagdigian, *J. Chem. Phys.* **85**, 7098 (1986).

305. M. P. deMiranda and D. C. Clary, *J. Chem. Phys.* **106**, 4509 (1997).

306. S. Lee, J. Luque, J. Reppel, A. Brown and D. R. Crosley, *J. Chem. Phys.* **121**, 1373 (2004).

307. K. V. Chance, D. A. Jennings, K. M. Evenson, M. D. Vanek, I. G. Nolt, J. V. Radostitz and K. Park, *J. Mol. Spectrosc.* **146**, 375 (1991).

308. K. Park, L. R. Zink, K. V. Chance, K. M. Evenson and I. G. Nolt, *J. Quant. Spectrosc. Radiat. Transfer* **61**, 715 (1999).

309. K. Park, L. R. Zink, K. M. Evenson, K. V. Chance and I. G. Nolt, *J. Quant. Spectrosc. Radiat. Transfer* **55**, 285 (1996).

310. C. Graham, D. A. Imrie and R. E. Raab, *Mol. Phys.* **93**, 49 (1998).

311. A. D. Buckingham, R. L. Disch and D. A. Dunmur, *J. Am. Chem. Soc.* **90**, 3104 (1968).

312. T. N. Olney, N. M. Cann, G. Cooper and C. E. Brion, *Chem. Phys.* **223**, 59 (1997).

313. C. S. Parmenter and M. Seaver, *J. Chem. Phys.* **70**, 5458 (1979).

314. H. M. Lin, M. Seaver, K. Y. Tang, A. E. W. Knight and C. S. Parmenter, *J. Chem. Phys.* **70**, 5442 (1979).

315. H. Chadwick, M. Brouard, Y. P. Chang, C. J. Eyles, T. Perkins, S. A. Seamons, J. Kłos, M. H. Alexander and F. J. Aoiz, *J. Chem. Phys.* **137**, 154305 (2012).

316. J. H. Lehman, M. I. Lester, J. Kłos, M. H. Alexander, P. J. Dagdigian, D. Herraez-Aguilar, F. J. Aoiz, M. Brouard, H. Chadwick, T. Perkins and S. A. Seamons, *J. Phys. Chem. A* **117**, 13481 (2013).

317. H. Chadwick, M. Brouard, Y.-P. Chang, C. J. Eyles, G. McCrudden, T. Perkins, S. A. Seamons, J. Kłos, M. H. Alexander, P. J. Dagdiagian, D. Herraez-Aguilar and F. J. Aoiz, *J. Chem. Phys*. **140**, 054306 (2014).

318. C. Dufour, B. Pinchemel, M. Douay, J. Schamps and M. H. Alexander, Chem. Phys. **98**, 315 (1985).

319. S. Green and P. Thaddeus, *Astrophys. J*. **205**, 766 (1976).

320. G. Jihua, A. Ali and P. J. Dagdiagian, *J. Chem. Phys*. **85**, 7098 (1986).

321. H. Meyer, *J. Chem. Phys*. **102**, 3151 (1995).

322. A. V. Smith and A. W. Johnson, *Chem. Phys. Lett*. **93**, 608 (1982).

323. T. Orlikowski and M. H. Alexander, *J. Chem. Phys*. **79**, 6006 (1983).

324. M. H. Alexander, *J. Chem. Phys*. **99**, 7725 (1993).

325. S. R. Jeyes, A. J. McCaffery and M. D. Rowe, *Mol. Phys*. **36**, 845 (1978).

326. S. R. Jeyes, A. J. McCaffery and M. D. Rowe, *Mol. Phys*. **36**, 1865 (1978).

327. A. J. McCaffery, S. R. Jeyes, M. D. Rowe and H. Kato, *Bunsen-Gesel. Phys. Chem. Chem. Phys*. **81**, 225 (1977).

328. J. I. Steinfeld, J. S. Francisco and W. L. Hase, *Chemical Kinetics and Dynamics*. (Prentice Hall, Upper Saddle River, NJ, 1998).

329. J. J. van Leuken, F. H. W. Vanamerom, J. Bulthuis, J. G. Snijders and S. Stolte, *J. Phys. Chem*. **99**, 15573 (1995).

330. M. Drabbels, A. M. Wodtke, M. Yang and M. H. Alexander, *J. Phys. Chem. A* **101**, 6463 (1997).

331. P. L. James, I. R. Sims, I. W. M. Smith, M. H. Alexander and M. B. Yang, *J. Chem. Phys*. **109**, 3882 (1998).

332. M. H. Alexander, *J. Chem. Phys*. **111**, 7426 (1999).

333. R. Dopheide, W. Cronrath and H. Zacharias, *J. Chem. Phys*. **101**, 5804 (1994).

334. M. Kirste, X. A. Wang, H. C. Schewe, G. Meijer, K. P. Liu, A. van der Avoird, L. M. C. Janssen, K. B. Gubbels, G. C. Groenenboom and S. Y. T. van de Meerakker, *Science* **338**, 1060 (2012).

335. J. A. Bacon, C. F. Giese and W. R. Gentry, *J. Chem. Phys*. **108**, 3127 (1998).

336. M. T. Vonk, J. A. Bacon, C. F. Giese and W. R. Gentry, *J. Chem. Phys*. **106**, 1353 (1997).

337. M. T. Nguyen, R. Sumathi, D. Sengupta and J. Peeters, *Chem. Phys*. **230**, 1 (1998).

338. C. R. Bieler, A. Sanov and H. Reisler, *Chem. Phys. Lett*. **235**, 175 (1995).

339. P. Sharkey, I. R. Sims, I. W. M. Smith, P. Bocherel and B. R. Rowe, *J. Chem. Soc. Faraday Trans.* **90**, 3609 (1994).

340. Y. Kalugina, J. Kłos and F. Lique, *J. Chem. Phys.* **139**, 074301 (2013).

341. M. D. Marshall, B. V. Pond, S. M. Hopman and M. I. Lester, *J. Chem. Phys.* **114**, 7001 (2001).

342. M. L. Costen and J. B. Halpern, Personal Communication (2014).

Appendix I

Published Papers

1. Stephen J. McGurk, Kenneth G. McKendrick, Matthew L. Costen, Dorian I. G. Bennett, Jacek Kłos, Millard H. Alexander and Paul J. Dagdigian, *Journal of Chemical Physics*, **136**, 164306 (2012).

"*Depolarization of Rotational Angular Momentum in CN($A^2\Pi$, v = 4) + Ar Collisions*".

2. Stephen J. McGurk, Kenneth G. McKendrick, Matthew L. Costen, Millard H. Alexander and Paul J. Dagdigian. *Journal of Chemical Physics*, **139**, 124304 (2013).

"*Parity-Dependent Oscillations in Collisional Polarization Transfer: CN($A^2\Pi$, v = 4) + Ar*".

3. Stephen J. McGurk, Joshua B. Halpern, Kenneth G. McKendrick and Matthew L. Costen. *Journal of Physical Chemistry A*, **118**, 2007 (2014).

"*Parity-Dependent Rotational Energy Transfer in CN($A^2\Pi$, v = 4, j F_1e) + N_2, O_2 and CO_2 Collisions*".

4. Stephen J. McGurk, Joshua B. Halpern, Kenneth G. McKendrick and Matthew L. Costen. *Journal of Physical Chemistry A*, (In Preparation).

"*Collisional Depolarization and Parity-Dependent Polarization Transfer in CN($A^2\Pi$, v = 4, j F_1e) + N_2, O_2 and CO_2*".

Appendix II

Conferences and Meetings Attended

- Heriot-Watt University and University of Edinburgh Meetings on Physical Chemistry and Chemical Physics, UK, 2009 – 2013.
- Royal Society of Chemistry Spectroscopy and Dynamics Group (SDG) Meetings, UK, January 2010 – 2012.
- Annual Northern Universities Meetings on Chemical Physics (ANUMOCP), UK, July 2010 – 2012.
- Gordon Research Seminar (GRS) on Atomic and Molecular Physics, Stonehill College, Massachusetts, USA, July 2012.
- Gordon Research Conference (GRC) on Atomic and Molecular Physics, Stonehill College, Massachusetts, USA, July 2012.

Appendix III

Courses Attended

- Chemistry Departmental Seminars, Heriot-Watt University, UK, 2009 – 2013.
- Physics Departmental Seminars, Heriot-Watt University, UK, 2009 – 2013.
- Postgraduate Academic Enhancement Courses (Educational Development Unit), Heriot-Watt University, UK, 2009 – 2013.
- Physical Chemistry Enhancement Week, Firbush Outdoor Centre, UK, March 2011.
- Vitae National Gradschool, Windemere, UK, November 2012.